Nanosources and Manipulation of Atoms Under High Fields and Temperatures: Applications

NATO ASI Series

Advanced Science Institutes Series

A Series presenting the results of activities sponsored by the NATO Science Committee, which aims at the dissemination of advanced scientific and technological knowledge, with a view to strengthening links between scientific communities.

The Series is published by an international board of publishers in conjunction with the NATO Scientific Affairs Division

A Life Sciences **B Physics**	Plenum Publishing Corporation London and New York
C Mathematical and Physical Sciences **D Behavioural and Social Sciences** **E Applied Sciences**	Kluwer Academic Publishers Dordrecht, Boston and London
F Computer and Systems Sciences **G Ecological Sciences** **H Cell Biology** **I Global Environmental Change**	Springer-Verlag Berlin, Heidelberg, New York, London, Paris and Tokyo

NATO-PCO-DATA BASE

The electronic index to the NATO ASI Series provides full bibliographical references (with keywords and/or abstracts) to more than 30000 contributions from international scientists published in all sections of the NATO ASI Series.
Access to the NATO-PCO-DATA BASE is possible in two ways:

– via online FILE 128 (NATO-PCO-DATA BASE) hosted by ESRIN, Via Galileo Galilei, I-00044 Frascati, Italy.

– via CD-ROM "NATO-PCO-DATA BASE" with user-friendly retrieval software in English, French and German (© WTV GmbH and DATAWARE Technologies Inc. 1989).

The CD-ROM can be ordered through any member of the Board of Publishers or through NATO-PCO, Overijse, Belgium.

Series E: Applied Sciences - Vol. 235

Nanosources and Manipulation of Atoms Under High Fields and Temperatures: Applications

edited by

Vu Thien Binh
Department of Material Physics,
Université Claude Bernard Lyon I,
Villeurbanne, France

N. Garcia
Department of Condensed Materials,
Universidad Autonoma de Madrid,
Madrid, Spain

and

K. Dransfeld
Faculty of Physics,
Universität Konstanz,
Konstanz, Germany

Springer Science+Business Media, B.V.

Proceedings of the NATO Advanced Research Workshop on
Manipulations of Atoms Under High Fields and Temperatures: Applications
Lyon, France
6–10 July 1992

Library of Congress Cataloging-in-Publication Data

Nanosources and manipulation of atoms under high fields and
temperatures : applications / edited by Vu Thien Binh, N. Garcia,
and K. Dransfeld.
p. cm. -- (NATO ASI series. Series E, Applied sciences ; vol.
235)
Includes index.
ISBN 978-94-010-4758-6 ISBN 978-94-011-1729-6 (eBook)
DOI 10.1007/978-94-011-1729-6
1. Nanostructure materials--Congresses. 2. Nanotechnology-
-Congresses. I. Vu, Thien Binh, 1946- . II. García, N.
(Nicolás) III. Dransfeld, K. (Klaus) IV. Series: NATO ASI series.
Series E, Applied sciences ; no. 235.
TA418.9.N35N35 1993
620.1'12--dc20 93-18976

ISBN 978-94-010-4758-6

Printed on acid-free paper

All Rights Reserved
© 1993 Springer Science+Business Media Dordrecht
Originally published by Kluwer Academic Publishers in 1993
Softcover reprint of the hardcover 1st Edition 1993
No part of the material protected by this copyright notice may be reproduced or utilized in any form or by any means, electronic or mechanical, including photocopying, recording or by any information storage and retrieval system, without written permission from the copyright owner.

This book contains the proceedings of a NATO Advanced Research Workshop held within the programme of activities of the NATO Special Programme on Nanoscale Science as part of the activities of the NATO Science Committee.

Other books previously published as a result of the activities of the Special Programme are:

Nastasi, M., Parking, D.M. and Gleiter, H. (eds.), *Mechanical Properties and Deformation Behavior of Materials Having Ultra-Fine Microstructures.* (ASIE 233) 1993 ISBN 0-7923-2195-2

CONTENTS

Preface ix

Introduction

Local Probe Methods and Miniaturization..... 1
H. Rohrer

Nanosources and Applications

Low Energy Electron Microscopy..... 13
E. Bauer

Nanotips and Transmission Low Energy Electron Diffraction..... 19
J.C.H. Spence

Lensless Low Energy Electron Point Source Microscopy..... 35
H.J. Kreuzer, A. Wierzbicki, M.G.A. Crawford and C.B. Roald

Electron Focusing: Computer Simulation..... 45
H. De Raedt and K. Michielsen

Nanotip Fashioning and Nanosource Characteristics..... 59
Vu Thien Binh, N. Garcia, S.T. Purcell and V. Semet

Electron Emission from Nanometer-Size Metallic Clusters:
Electronic States and Structural Stability of Supported Au Clusters..... 77
M.E. Lin, A. Ramachandra, R.P. Andres and R. Reifenberger

On the Energy Dissipation in Field Emission and Tunneling Microscopy..... 89
J. Xu, R. Möller, K. Läuger, K. Dransfeld and C.C. Williams

Miniaturized Electron Microscope..... 101
U. Staufer, L.P. Muray, D.P. Kern and T.H.P. Chang

Direct Observation of the Motion of Individual Surface Atoms
on a Picosecond Timescale..... 111
H. Heinzelmann, G.M. McClelland and Fumiya Watanabe

Single-Electron Manipulation Under High-Field at Room Temperature..... 115
H. Nejoh, S. Watanabe, M. Nakamura and M. Aono

Focused Ion Beams and their Applications in Microfabrication..... 121
P.D. Prewett

Miniaturized Liquid Metal Ion Sources (MILMIS)..... 139
J. Mitterauer

Integrated Microtips: Application to Flat Displays..... 165
R. Baptist

Tip-Surface Interactions and Applications

Field-Induced Transfer of an Electropositive Atom Between Two Closely Spaced Electrodes..... 177
N.D. Lang

Molecular Dynamics Simulations of Metal Surfaces: Surface Melting and Non-Melting, and Tip-Surface Interactions..... 185
F. Ercolessi, O. Tomagnini, S. Iarlori and E. Tosatti

Atomic Manipulation Using Field Evaporation..... 207
N.M. Miskovsky, Tien T. Tsong and Ching Ming Wei

What is Underneath ? Moving Atoms and Molecules to Find Out..... 213
P.S. Weiss and D.M. Eigler

Local Experiments Using Nanofabricated Structures in STM..... 219
J.K. Gimzewski, R. Berndt and R.R. Schlittler

Quantum Atom Switch: Tunneling of Xe Atoms..... 229
J.J. Saenz and N. Garcia

The Eigler Xe Switch: Its Atomic Structure from Xe Energy Minimization and STM Image Calculations..... 239
C. Joachim, X. Bouju and C. Girard

Friction and Forces on an Atomic Scale..... 253
O. Marti, J. Colchero and J. Mlynek

Atomic-Scale Adhesion..... 271
U. Dürig and O. Züger

Local Modification of Langmuir-Blodgett Films by Atomic Force Microscopy 287
L.F. Chi and H. Fuchs

Layered Semiconductors as Materials for (Sub)Nanometer Scale Surface Modification with the STM..... 293
H. Fuchs, Th. Schimmel, S. Akari, L.M. Eng, M. Anders, M. Lux-Steiner and K. Dransfeld

Micromachined Silicon Tools for Nanometer-Scale Science..... 311
J. Brugger, V.P. Jaecklin, R.A. Buser, C. Linder and N.F. De Rooij

List of Participants..... 319
Index..... 323

PREFACE

This volume contains the proceedings of the NATO-Advanced Research Workshop (ARW) "Manipulation of atoms under high fields and temperatures: Applications", sponsored by the NATO Scientific Affairs Division, Special Programme on Nanoscale Science. This ARW took place in Summer '92, in the pleasant surroundings of the Hotel des Thermes at Charbonnières les Bains - Lyon, France.

Gathering some fifty experts from different fields, the ARW provided an opportunity to review the basic principles and to highlight the progress made during the last few years on the nanosources and the interactions between atomic-scale probes and samples. The motivation is to use the novel properties attached to the atomic dimensions to develop nanoscale technologies.

The perception of the atomic-scale world has greatly changed since the discovery and development, in the early 80's, of Scanning Tunneling Microscopy (STM) by Binnig and Rohrer. Beyond the observation of individual atoms, which is now routine, the concept of playing with atoms has become commonplace. This has lead to the fashioning of tools at the atomic scale, to the deposition, the displacement and the creation of atomic structures and also to the knowledge of interactions and contacts between atoms. Nanotips ending with a single atom are sources of ultra-fine charged beams. They can be unique tools for high resolution observations, for micro-fabrications by micro-machining and deposition at a scale not previously attainable, with a working distance less stringent than with STM devices. These tips should then be the starting point for the development of high-performance miniature devices. For all the subjects mentioned above, new laws have been identified and circumscribed during the ARW. This meeting marked the shift of emphasis from a passive attitude of analysis towards a more active role of the scientist in the creation and use of atomic configurations.

The ARW was also supported by several French scientific and governmental agencies (CNRS, DRET...). I would like to take this opportunity to express my gratitude to all the participants, coming from some ten countries, for contributing to the excitement and success of the ARW. I am indebted to my co-organisers and co-editors, N. Garcia and K. Dransfeld, and to the NATO officials whose help was indispensable in organising this meeting.

Vu Thien Binh
December 1992.

LOCAL PROBE METHODS AND MINIATURIZATION

H. ROHRER
IBM Research Division
Zurich Research Laboratory
CH-8803 Rüschlikon
Switzerland

1. Introduction

Miniaturization was one of the key elements for the tremendous development and wide dissemination of microtechnology. Miniaturization is at present mainly seen in the context with data processing, communication and consumer electronics. Therefore, microtechnology predominately means microelectronics. Micromechanics on the other hand still burns on a modest flame and does not receive the same attention, neither in science nor in technology circles. There is not yet a vast hungry industry pressing for progress. Nevertheless, there are very promising beginnings. The overall importance of mechanics, especially nanomechanics, might eventually very well match that of nanoelectronics.

Miniaturization naturally carries us far beyond microtechnology, it carries us to science and technology on the nanometer scale — into the nanometer world. In the following I would like to discuss some aspects of the next big step of miniaturization, the one from the micrometer to the nanometer, in which local probe methods will play a most important role. I am not going to make predictions, I am not going to make evaluations and I am also not really concerned with "realities". I cannot give you any reasonable business case for the nanometer world, I just can give possibilities. Business cases lie in recognizing and realizing possibilities by those who want to do business. Remember, nobody could have made and did make a business case for the micrometer age fifty years ago. New developments happen on the basis of possibilities and not vice versa.

The motivation for continuing miniaturization is manifold: in science to study phenomena and effects below characteristic length or time scales, to learn about processes such as melting, corrosion, nucleation, etc. etc., down to atomic scales, to analyze and understand properties of composite materials of ever finer granularity; in technology to fabricate smaller, faster and less expensive components for microelectronics and quite generally to create new possibilities with miniaturized sensors, tools and instrumentation. Ten years ago nanoscience and technology were not yet commonly used terms. But it was foreseeable already at that time that in advancing into the world of the ever smaller, miniaturization would not stop at the micrometer, the measure of today's microelectronics and micromechanics. In those times, nanotechnology mostly meant something of the order of one tenth of a micrometer although selected struc-

V.T. Binh et al. (eds.),
Nanosources and Manipulation of Atoms Under High Fields and Temperatures: Applications, 1–12.
© 1993 *Kluwer Academic Publishers.*

tures of nanometer size were accessible to electron microscopy nearly down to the atomic level. But no wide basis existed to work on a nanometer scale. With work I mean observing an individual, specially selected object of nanometer size, e.g., an atom or a molecule or an aggregate of atoms and molecules, together with its immediate surrounding, to be able to measure and understand its properties, to manipulate and change it, and finally to control its possible functions and processes related to them.

2. Progress of Miniaturization

Figure 1 gives some examples of the progress of miniaturization taken from the data processing industry where miniaturization has achieved the most impressive overall level [1]. It progressed steadily and exponentially during the past few decades and there is no reason to believe that it should not continue to do so in the near future.

The step from the millimeter to the micrometer was technologically undoubtedly a great achievement. However, it was scientifically straight forward in the sense that the major important scientific knowledge, methods and techniques, and instrumentation were developed by and in science well in advance. Quantum mechanics existed long before, electron microscopy dates also back to the twenties, and the properties of semiconductors, the basic material for microelectronics, had already been widely studied for decades before scientists invented the transistor.

The material properties and effects are essentially the same on the micrometer and on the millimeter scale. The micrometer, therefore, appears in many ways as simply downscaling the millimeter. This will continue for a while, say to somewhere around

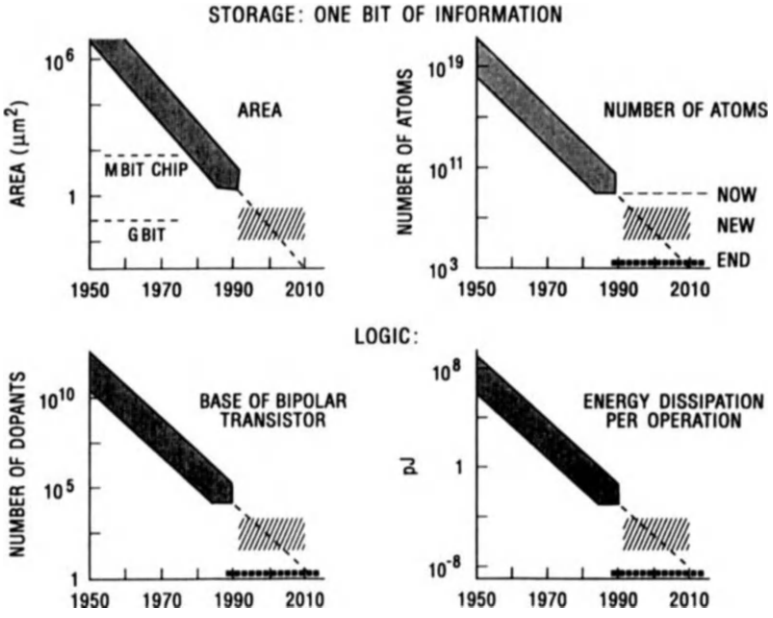

Fig. 1. Progress of miniaturization in information processing. Adapted from Ref. 1.

50 nanometers or one twentieth of a micrometer. Unfortunately, this lead to the widespread belief that science is not really needed for further progress in microtechnology. As a consequence, too much of secure, foreseeable and no-risk science is done and science is loosing its comfortable but necessary lead on technology. We should remember that neither quantum mechanics, electron microscopy, lasers, etc., were invented, nor semiconductor materials were studied because of microtechnology. But microtechnology exists because of said scientific progress achieved well in advance. Likewise, science on the nanoscale should create nanotechnology, not vice versa.

3. The New Nanometer World

Miniaturization becomes a totally new game when we reach dimensions where physical laws and effects assume a different appearance, where size becomes comparable to characteristic length scales, where transport follows different laws, where surface and interface effects become dominant, and where concepts like dimensionality and symmetry are no longer readily useful or significant. This means in a certain sense the end of a specific type of miniaturization but, at the same time, these scientific challenges offer new possibilities.

In today's lecture I would like to talk mainly about possibilities rather than limits — to talk about limits is a) not very interesting and b) even less instructive since the limits of today very often do not survive tomorrow. After all, the essence of science is

	MACRO / MICRO	**NANO**
MECHANICAL PROPERTIES	BULK CONSTANTS	CHEMICAL BONDS
	10^8 - 10^{-8} N	10^{-7} - 10^{-14} N
	0 - 10^7 Pa	10^4 - 10^{12} Pa
	Hz - MHz	MHz - < THz
		< 10 kT
	NANO MECHANICS/"CHEMICS"	
ELECTRICAL	< 10^5 V/cm	> 10^8 V/cm (dc)
		> 10^7 V/cm (ac)
	10^6 A/cm^2	10^8 A/cm^2
	MANIPULATION/MODIFICATION NONLINEARITIES	
	TRANSISTORS	BALLISTIC DEVICES SET
THERMAL RELAX.	> μs	< nsec
NUMBERS	MEGA / GIGA	TERA / PETA
APPROACHES	MINIATURIZATION CHIPS	ASSEMBLIES MICRO LABORATORIES

Fig. 2. The new nanometer age.

to circumvent or overcome limits and obstacles, not to be preoccupied or even stopped by them. Scientific and technical feasibility is unlimited in the sense that we do not see any general limitations. This does not mean that we can do everything in a given way and at a given time, but that we will find ways to accomplish whatever we set out to do. Scientific progress is like water seeping through soil. Each individual grain of sand is impermeable, and yet water finds its way through the soil to form springs, brooks, streams and rivers. It is a lengthy and unpredictable process.

Figure 2 gives a few examples of what is new in the nanometer regime.

Take a look at mechanical properties. We have to deal with chemical bonds and no longer with bulk properties. Forces are extremely small — down to 10^{-12} N, yet strains and pressures can be very high, e.g. pressures up to 10^{12} Pa. Eigenfrequencies of mechanical systems can approach terahertz. Such systems, therefore, might offer a valid alternative and could well complement electronic approaches, in particular also because mechanical displacements and distortions are shielded over one to a few nm and because the energies involved are readily in the range of a few kT. Nanomechanics and "nanochemics" — also chemistry can be a very local affair — appear, therefore, to be a promising route. A first example is the mechanical detection of magnetic resonance [2].

Take interaction intensities. Local electric fields of several volts per angstrom can readily be reached in a scanning tunneling microscope configuration. They are strong and local enough to tear individual atoms and atom clusters out of compact surfaces, as shown in Figs. 3 [3].

Electronic transport will be dominated by quantum effects, and interference effects should play an important role. The progress made in recent years in understanding transport on a mesoscopic scale is crucial to its extension to the nanometer scale and molecular-sized systems. Single-electron tunneling (SET) could bring also electronics closer to the kT range. Thermal relaxation times can be well below nanoseconds, and, finally, we will have to use new concepts to deal reasonably with Tera and Peta quantities.

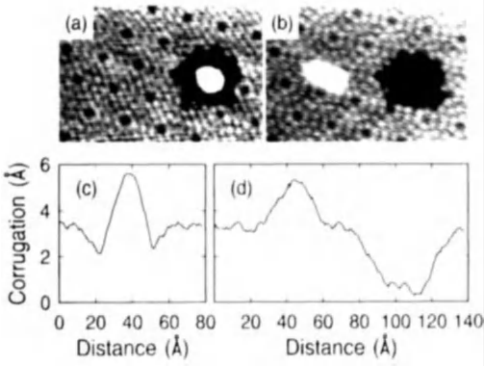

Fig. 3. Surface modification. (a) Creation of a silicon cluster on a silicon (111) 7×7 surface together with the STM profile in (c). (b) Displacement and deposition of the cluster and corresponding STM profile in (d). The same can be done with atoms instead of atom clusters. From Ref. 3. Copyright 1991 by AAAS.

4. Local Probe Methods

Local probe methods [4,5] can be considered in a way as miniaturization of experimentation, a down-scaling of the active part of the experiment to nanometer dimension. The properties of objects are sensed, conditioned or changed by an interaction between the local probe and the object, see Fig. 4. The "localization" of the experiment is given by the active size of the local probe and the distance between probe and object. For atomic resolution both have to be of atomic dimension. In case of a sufficiently rapid decay of the interaction with distance, the experiment is performed with these two atomic size regions of probe and object, respectively, which are closest to each other. The active part of the experiment has shrunk down to atomic dimension.

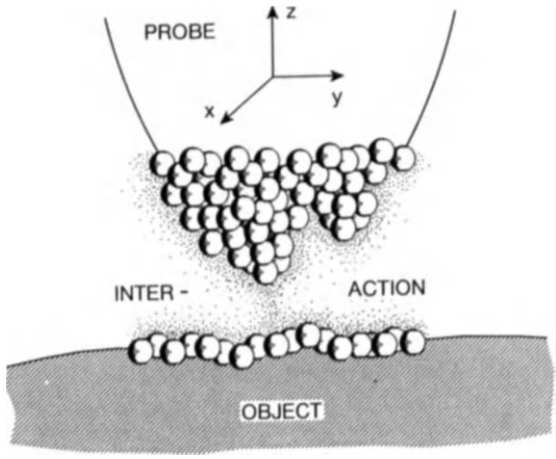

Fig. 4. Schematic of local probe methods. The circles represent atoms of the parts of probe and object, respectively, closest to each other. The probe is moved in the x, y and z-direction.

Local probe methods have many attractive features.
— The variety of interactions gives access to a large variety of properties. The overlap of electron wave-functions of probe and object is the interaction for scanning tunneling microscopy and spectroscopy (STM) [4]; electronic states of the object are probed by electronic states of the probe. Scanning the probe at constant interaction across the object yields an image which reflects in the simplest case the objects topography. Figure 5 is an STM image of a GaAs-AlGaAs interface [6], Imaged are the filled states; the corrugation observed is, therefore, associated with the As atoms. The interface between GaAs and AlGaAs appears atomically sharp, the apparent roughness of the AlGaAs is an "electronic" roughness due to fluctuation in the Al distribution. Forces as interaction lead to force microscopy. Figure 6 is a combined structural and magnetic image of a magnetic track [7]. The art of local probe methods in general is to separate and use the various interactions; e.g. in Fig. 6 to separate the magnetic force from the others such as Coulomb, adhesive, and van der Wahl's forces, respectively, and to produce a topographic and magnetic image.

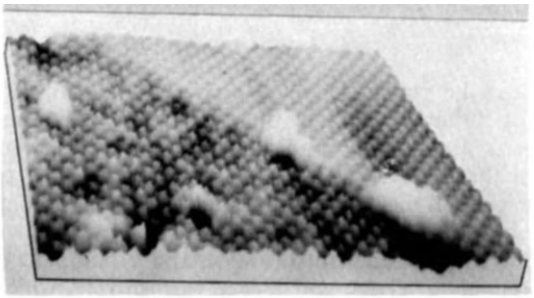

Fig. 5. Interface of a GaAs (top right) — AlGaAs (bottom left) heterostructure. It appears atomically sharp. Image area: 5 × 8 nm². Image courtesy of H.W.M. Salemink.

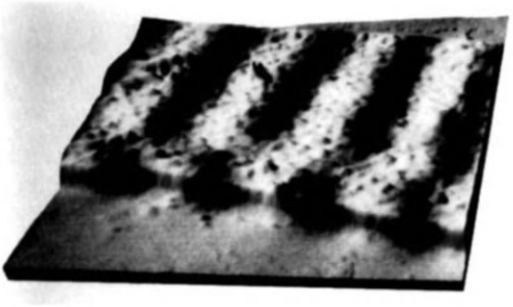

Fig. 6. Force image of a magnetic track. In bright and dark stripes, the magnetization points in opposite directions. The magnetic pattern was imaged by magnetic forces, the topography of the track by electrostatic forces. Image area: 6 × 6 μm². Image courtesy of Ch. Schönenberger and S.F. Alvarado.

— Local probe methods can be performed in a variety of environments ranging from ultrahigh vacuum to electrolytes. This is particularly important since properties and particularly functions of nanometer sized object are usually quite sensitive to a specific environment. Biological macromolecules are a vivid example.
— A particular local probe-object configuration can lead to local "conditioning" of properties. An example is the photon emission in an STM configuration shown in Fig. 7 [8]. Close proximity of local probe and object give rise to localized plasmon modes which can be exited by the tunneling electron. The decay of the excitation results in the emission of a photon. The photon map of Fig. 7 can be considered as optical microscopy with subnanometer resolution. Another example is the "microwave microscopy", also with subnanometer resolution. Nonlinearities in the tunnel junction — be they caused by the nonlinear *I-V* characteristic or nonlinear dielectric properties — give rise to third harmonic generation. Figure 8 is a constant third harmonic contour of an oxidized silicon surface, showing a monolayer step with subnanometer resolution [9].

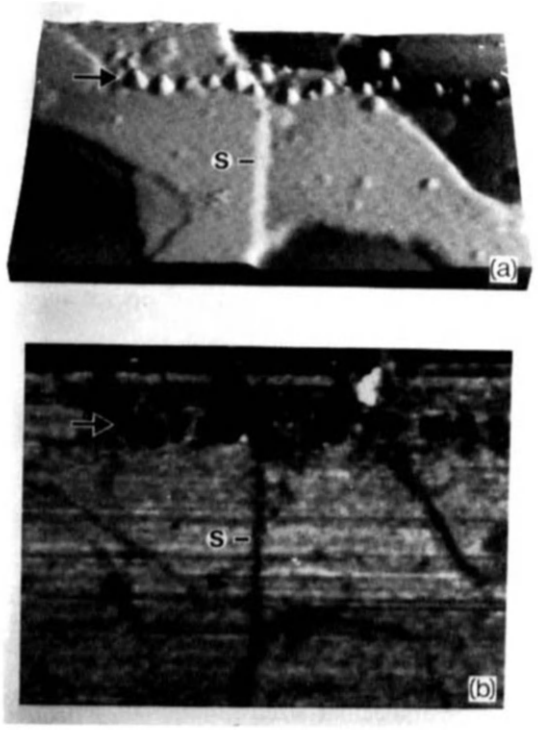

Fig. 7. (a) STM images of topography and (b) corresponding photon map of a Cu(111) surface exhibiting terraces separated by steps (see marker S for instance) and small structures indicated by arrows which were created by a series of electric field pulses at positive tip polarity. Area = 50 × 30 nm². An example of "optical microscopy" with subnanometer resolution. Image courtesy of J.K. Gimzewski.

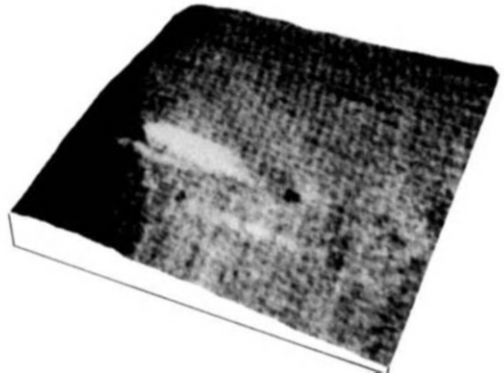

Fig. 8. Image of constant third harmonic generation at 3 GHz of an oxidized silicon surface. At left a monolayer step. At the bright spots, a small dc current flows. Area: 9 × 9 nm².

— For a sufficiently strong interaction, the local probe becomes a nanotool for nanometer sized manipulation and modification. Figure 3 is an example.
— The local probes can act as a sort of interface between the macroscopic and nanoscopic worlds, respectively, in order to address and control specific functions of individual nanometer-sized functional elements.
— Functionalized local probes will allow performance of "intelligent" experiments. The local probe becomes in a sense a miniaturized laboratory. Molecular recognition with a particular molecule attached to the local probe is an example, still futuristic though.
— Local probe instruments lend themselves for miniaturization. Arrays of a large number of miniaturized local probe instruments which are operated simultaneously offer interesting prospects.

These examples show that we are indeed learning to "work" with nanometer sized objects, an absolutely necessary prerequisite to advance miniaturization into the nm regime.

5. Post-Miniaturization

Figure 1 also shows that miniaturization meaning the division into ever smaller and simpler blocks, or "smaller, faster, cheaper" will come to an end in two or three decades – of which "cheaper will quite probably be the first. Progress after miniaturization could be based on increased complexity. A promising route could be to assemble molecular-sized functional elements to create complex functional units. A primary task of science is to find appropriate self-assembling techniques and ways to interface the macroscopic world with molecular-sized functional elements for communication and control or modification of their functions. This will lead to an extremely fruitful interdisciplinary effort which is expected to add new dimensions to biology and supramolecular chemistry as well. In this context, it is interesting to note that while solid-state science has moved down from the millimeter to the nanometer scale, chemistry has independently progressed from the level of small, few-atom molecules to macromolecules of biological size (see Fig. 9). Supra-molecular chemistry might eventually provide the functional elements for the assembly scenario in the post-miniaturi-

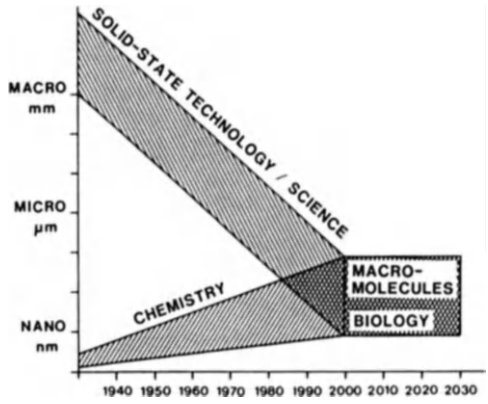

Fig. 9. Development of chemistry and solid state science/technology. From Ref. 5b.

zation period. Biological elements might generally be impractical, but biological concepts will guide us to new ways of thinking and doing things. Finally, numerical approaches will be of great importance in understanding properties, functions and processes on the nanometer scale since theory has little symmetry and no fixed dimensionality to build on and since functions and processes depend critically on the nano-object's environment. Here we also find a striking development which is complementary to that in solid-state science and technology (Fig. 10).

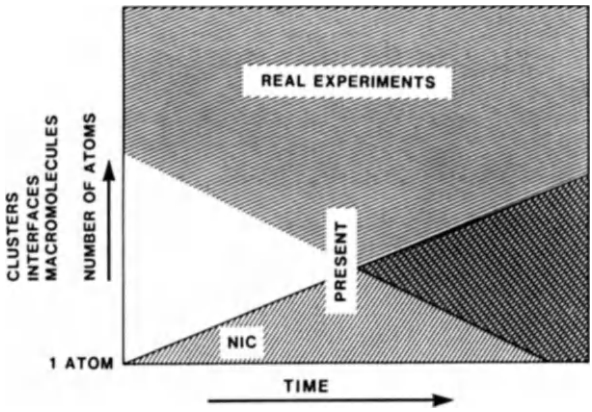

Fig. 10. Development of real experiments and numerically intensive computation (NIC). From Ref. 5b.

6. Outlook

The first decade of local probe methods dealt mainly with imaging down to the atomic scale. Progress in understanding depends to a great extent on the possibility of using various interactions: in scanning tunneling microscopy, for example, spectroscopy exploits the different interaction strengths between different states. The full power of spectroscopy, however, only comes to bear if it can be performed in a reasonable energy range. This is the case for clean or well-ordered surface structures in UHV. Most often, however — for example in ambient conditions, in electrolytes, or when large electric fields irreversibly affect the structure as in the case of Cs diffusion on GaAs [10] — the energy range to perform spectroscopy is very limited. Of increasing importance, therefore, are experiments which exploit different kinds of interactions. Examples given above are the combined structural magnetic image of a magnetic track (Fig. 6), the tunneling microscopy combined with photon emission (Fig. 7) or with third harmonics generation (Fig. 8). Figure 11a shows a constant tunnel current image of a self-assembled monolayer with the characteristic pattern of depressions. As was shown recently [11], topography can be separated from distortions and gap variations due to changes in electronic properties by simultaneously measuring tunnel current, force, and force gradient. Indeed, in the convolution of Fig. 11a the depressions practically disappear, Fig. 11b. Such combined imaging methods should play an important role in gaining a better understanding of soft and easily deformable and electronic inhomogeneous materials like organic and biological macromolecules.

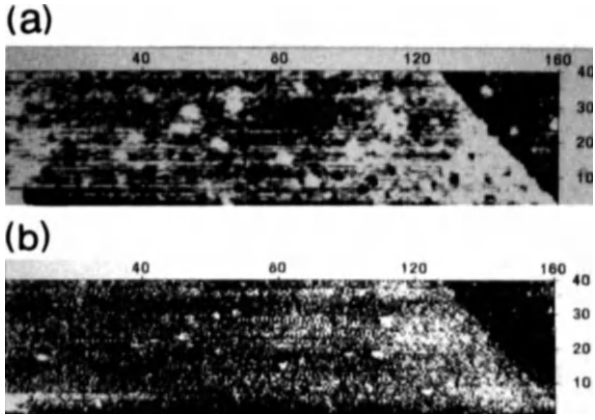

Fig. 11. (a) A constant current image of a mixed self-assembled monolayer. Besides the characteristic depression pattern, protrusions of larger lateral dimensions are also seen. In (b), the topography of the same area is presented. Depressions and protrusions are hardly visible. Lateral dimensions are given in nm; the range from black to white is 6 Å in both cases. From Ref. 11b.

The period of producing images has to be followed now by understanding more complex systems.

Manipulation and modification on the atomic and molecular scale have also opened a new, highly interesting direction with a large set of challenging questions. High fields and temperatures, the topic of this workshop, is one of them. Here we can fortunately draw on the expertise developed over many years in the field emission community, whose contributions were an important and refreshing element of this workshop.

In the general trend of miniaturization, the next big step after manipulation and modification will be understanding, controlling, and modifying functions of molecular-sized functional elements, the door to the assembly scenario. To "smaller" will be added "more complex," so to speak a new dimension in Fig. 1.

7. Beyond the Technical Aspects

The nanometer age, or the "age of interdisciplinarity" poses formidable challenges beyond issues of purely scientific and technical nature. The scientific community can only meet the challenge of interdisciplinarity if it finds its way back to scientific values and beliefs. Necessary are cooperation and openness, not competition and barriers; communication practices which serve the exchange of scientific information, not the establishment of personal profiles; standards based on novelty, ingenuity, elegance and simplicity, not on claims, promises, trends and sensations; open minds and alertness for new developments, not programs and plans; the solution of the problem counts, not the methods or techniques we learned or the scientific discipline. But also scientific bodies have to rethink their objectives and practices seriously and to find ways and means to enhance the science-technology relation without depriving science of its freedom and without endangering its mission for the future.

The nanometer age will also be of tremendous impact on society at large. The fact that we might be able to manipulate, modify and compose matter atom by atom, molecule by molecule, opens fantastic, but also frightening perspectives. It will become an existential question whether society can regain its confidence in scientific and technical developments. Whether science and technology see again their ultimate mission to serve for the benefit of mankind and whether they will be accepted again for their positive contributions and not rejected for their possible abuse, whether society will shoulder its responsibility for the proper use of the practically unlimited possibilities offered by science — not by controlling science but by controlling its exploitation.

And finally, the unavoidable globalization of science and technology has also to include all those countries and areas where technical sciences and technology are either not yet existent or on a very moderate level. This is not just a problem of integrating the vast intellectual potential of the "Third World" into the science and technology community in order to satisfy its increasing demand for brain power. It is above all a question of science and technology for humanity. The gap between industrial nations and the Third World is constantly increasing. Science and technology accelerates this process dramatically. To advance in science and technology is unequally more demanding than to improve the global standard of living. It is much more difficult to activate the intellectual and technical potential and to create the skills necessary for today's and tomorrow's science and technology than to simply draw increasingly and more effectively on existing natural resources. The more complex the technological problems, the more serious is the issue. We often talk about the imbalance of give and take between industrial nations. Is this really the problem of the decades to come? The real issue is, how we can let the vast majority of humanity participate actively in scientific and technical developments, not just as cheap labor and/or consumers — an issue of a completely different dimension than the present technology conflicts and disputes between those who already have. And also of much greater dimension than the scientific and technical challenges per se. Science and technology have changed the world; they also have created new responsibilities.

Acknowledgment

I would like to thank my colleagues for many enlightening discussions.

References

[1] R.W. Keyes, IBM J. Res. Develop. 32, 24 (1988).
[2] J.A. Sidles, J.L. Garbini and G.P. Drobny, Rev. Sci. Instrum. 63, 1124 (1992); D. Rugar, C.S. Yannoni and J.A. Sidles, to be published.
[3] I.-W. Lyo and Ph. Avouris, Science 253, 173 (1991).
[4] G. Binnig and H. Rohrer, IBM J. Res. Develop. 30, 355 (1986); P.K. Hansma and J. Tersoff, J. Appl. Phys. 61, RI (1987).
[5] a) *Scanning Tunneling Microscopy I*, Springer Series in Surface Science 20, edited by H.J. Güntherodt and R. Wiesendanger (Springer Verlag, 1991); b) Proc. 6th Int'l. STM Conference, STM '91, Interlaken, Switzerland, Aug. 12-16, 1991, in Ultramicroscopy 42-44, 1 (1992).
[6] O. Albrektsen, D.J. Arent, H.P. Meier and H.W.M. Salemink, Appl. Phys. Lett. 57, 31 (1990).

[7] C. Schönenberger, S.F. Alvarado, S.E. Lambert and I.L. Sanders, J. Appl. Phys. 67, 7278 (1990); C. Schönenberger and S.F. Alvarado, Z. Phys. B 80, 373 (1990).
[8] R. Berndt, J.K. Gimzewski and P. Johansson, Phys. Rev. Lett. 67, 3796 (1991).
[9] B. Michel, W. Mizutani, R. Schierle, A. Jarosch, W. Knop, H. Benedickter, W. Bächtold and H. Rohrer, Rev. Sci. Instrum., September 1992); W. Mizutani, B. Michel, R. Schierle and H. Rohrer, to be published.
[10] L.J. Whitman, J.A. Stroscio, R.A. Dragoset, and R.J. Celotta, Phys. Rev. Lett. 66, 1338 (1991).
[11] a) D. Anselmetti, Ch. Gerber, B. Michel, H.J. Güntherodt and H. Rohrer, Rev. Sci. Instrum. 63, 3003 (1992); b) *idem*, to be published.

LOW ENERGY ELECTRON MICROSCOPY

E. BAUER
Physikalisches Institut
Technische Universität Clausthal
D 3392 Clausthal-Zellerfeld Germany

ABSTRACT. The basic principles and some applications of low energy electron microscopy (LEEM) are briefly described. The relationship between LEEM and other topics of this conference are pointed out.

1. Introduction

STM and LEEM are complementary surface imaging techniques inasmuch STM has high spatial and low temporal resolution while for LEEM the opposite is true. There are also many other differences between the two techniques, one of which is very relevant in the context of the conference: STM requires high *local* fields which makes the manipulation of atoms possible, LEEM needs only relatively low *average* fields which precludes atomic manipulation. Nevertheless, there are some important connections between LEEM and the other topics discussed in this book. This brief account will try to point them out. We will first discuss the most important foundations of LEEM and illustrate its potential by some examples, then indicate how nanotips could be useful in LEEM and finally make some comparisons with the other surface imaging techniques described in this book.

2. LEEM basics.

LEEM is based on the high reflectivity which crystals have for electrons in the energy range up to about 50 eV. At some energies, mainly below 10 eV, more than 50% of the electrons are elastically specularly reflected. This gives very intense images and, consequently, short image acquisition times, i.e. high time resolution. Slow electrons are very sensitive to electric and magnetic disturbances. Therefore, fast electrons, typically with 20 keV energy are used in the illumination and imaging system. Only immediately before the specimen they are decelerated in a cathode lens to the desired low energy and re-accelerated after interaction with the surface. The deceleration / acceleration field which may be considered to be homogeneous immediately in front of a flat surface, limits the resolution of the instrument to at best a few nm, independent of the quality of the lens following this field. Present instruments are still far away from this limit, reaching resolutions of about 20 nm.

The image contrast is mainly determined by diffraction in the topmost layers of the crystal but other contrast mechanisms are also important: i) topography contrast due to the field distortions associated with deviations from a flat surface and ii) geometric phase contrast which is caused by optical path differences of the electron waves reflected from

V.T. Binh et al. (eds.),
Nanosources and Manipulation of Atoms Under High Fields and Temperatures: Applications, 13–18.
© 1993 *Kluwer Academic Publishers.*

neighbouring surfaces differing in height (step contrast) or from thin layers differing in thickness (quantum size contrast). With spin polarised electrons one can obtain, in addition, magnetic contrast from ferromagnetic materials because the reflectivity of the surface depends upon relative orientation of electron spin and magnetisation. It is this versatility and the wide temperature range -limited only by vapour pressure and outgassing at high temperatures- which make LEEM such a powerful surface and thin film analysis tool.

3. LEEM applications.

Figs. 1-3 illustrate the potential of LEEM.

Fig.1a is one of first images of monoatomic steps obtained in the early eighties [1], more than 20 years after the conception of the method [2]. It was obtained with a field emission gun operated in the Schottky emission mode. The geometric phase contrast of the steps is converted into an amplitude contrast by slight defocusing. In the original two Fresnel fringes are visible. Fig. 1b [3] is from a Si(111) surface onto which was deposited at 800 K and annealed at about 1300 K. Co had reacted with the Si surface and formed large flat $CoSi_2$ crystals, a process which was recorded on video tape. The still photograph was taken after rapid quenching which partially froze in the high temperature state, except for the decoration of the sublimation steps by (7x7) structure nuclei and the formation of (7x7) islands on the terraces which otherwise have (1x1) structure. $CoSi_2$ sublimes slower than Si. Therefore, the Si sublimation steps propagate -in Fig. 1b from the top to bottom- between the $CoSi_2$ crystals (left and right side of Fig. 1b).

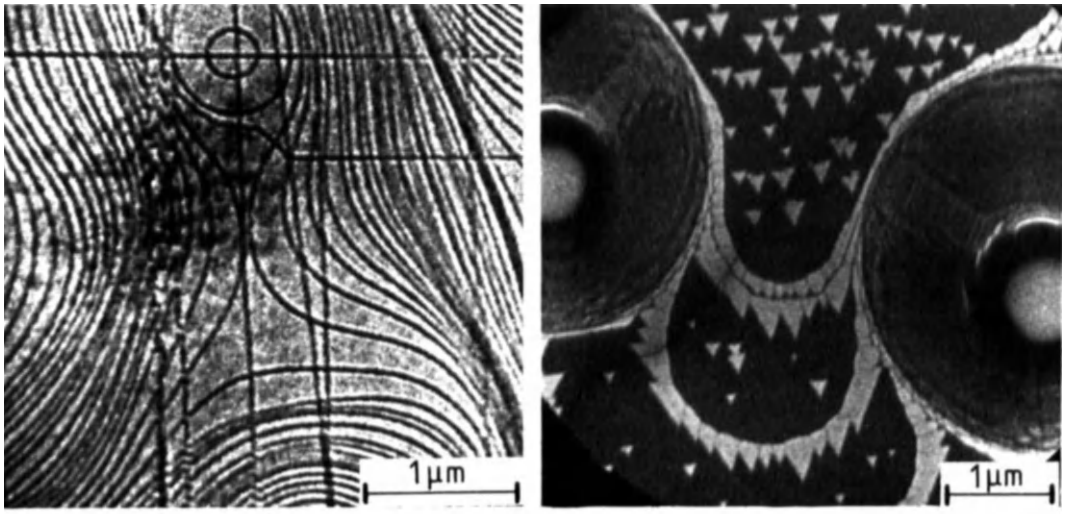

Fig. 1: (a) Monoatomic steps on a Mo(110) surface [1] , (b) $CoSi_2$ - induced hillcocks during sublimation of a Si(111) surface [3] . For explanation see text.

A third example is the homoepitaxy of Si on the Si(100) which is illustrated in Fig. 2 by a sequence of images taken from a video recording [4]. The Si(100) surface has a (2x1) structure consisting of dimer rows. The direction of these rows alternates by 90° from one terrace to the next which differ in height by one monolayer. The strong binding anisotropic connected with the dimerization causes large differences in the step energies and, therefore, a very anisotropic equilibrium and growth shape of the 2D Si islands. The anisotropy, alternating from one monolayer to the next can clearly be seen in the figure.

A final example (Fig. 3) illustrates the use of spin-polarised electrons in LEEM. Fig. 3a shows an ordinary LEEM image of a Co layer on W(110) with average thickness of 11 monolayers [5]. At the growth temperature of 790 K Co forms on W(110) flat (0001)-oriented 3D islands on the top of a Co monolayer. These islands are the elongated features, many of which originate at round W mesas. In addition to these mesas, which were formed during desorption of a previous Co deposit as a consequence of Co agglomeration and alloying, the step structure of the Co monolayer-covered substrate is visible. If a second image is taken with opposite spin-polarisation and two images are subtracted and contrast-enhanced, then the polarisation asymmetry image of Fig. 3b is obtained. The black / white contrast shows that the 3D Co islands are magnetised in-plane and that most of them are mono-domains. The grey-level between the islands is the same as in the corners outside the image, demonstrating the absence of magnetisation in the monolayer, at least parallel to the surface. Fig. 3 is also part of a video sequence. Thus spin-resolved LEEM can also monitor kinetics of magnetic processes. Many more examples can be found in several review papers [6,7,8] and in the original papers reviewed in them.

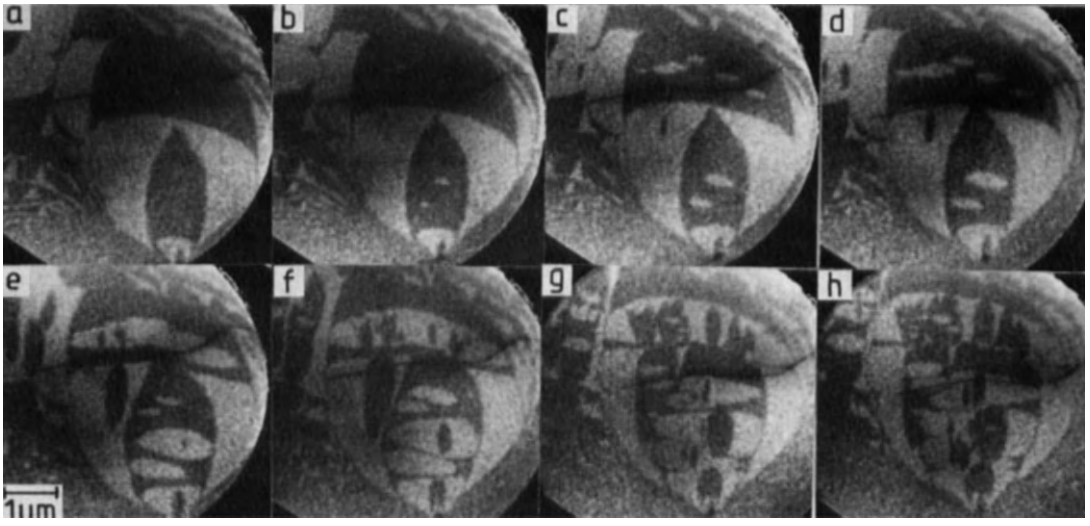

Fig. 2: Homoepitaxial growth of Si on a Si(100) surface. Excerpts from a video recording [4]. For explanation see text.

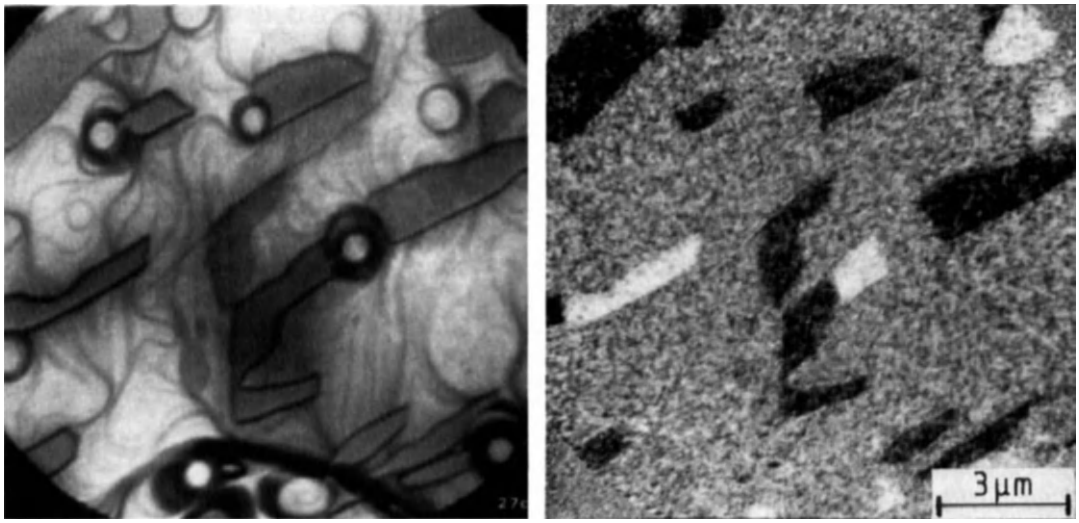

Fig. 3: Ferromagnetic Co islands on a W(110) surface [5]. (a) ordinary LEEM image, (b) Difference image between two images taken with opposite spin polarisation.

4. Nanotips in LEEM.

In order to understand the usefulness of nanotips for LEEM we have to take a somewhat closer look at the optics of this microscope. An essential feature of electron microscopes in general is that they allow to observe not only the image of the object but also its diffraction pattern which is created in the back focal plane of the objective if the specimen is illuminated by a parallel beam. The diffraction pattern gives valuable information on the average atomic structure -the lateral periodicity of the surface including disturbances to it such as steps and, with much more effort, the atomic positions- in the area illuminated or selected by an aperture in the first image plane. The quality of the information depends upon the so-called transfer width of the system which is a measure for spatial coherence. Obviously, a point source is the ideal source for coherent electron waves provided that three conditions are met: i) it must supply enough current so that the high intensity of LEEM images is not lost, ii) the gain in spatial coherence may not be compensated by the loss of temporal coherence due to a wide energy spread of the emitted electrons or due to space charge effects, and iii) the lifetime and stability of the source must allow extended LEEM and LED studies.

To illustrate the third condition, the useful lifetime of LaB_6 and well-treated conventional field-emitters are nowadays of the order of 1000 hours and they work so reliably that the microscopist pays little attention to them. If the teton tips discussed in several contributions to this book fulfil these conditions they will be ideal sources for LEEM. This can be seen as follows. The coherence width ω is given by the condition $\omega \sin \alpha \leq \lambda/2$, where α is the start angle of the electrons and λ the wavelength at the start energy eV. Electrons leaving the surface at the angle α intersect the back focal plane of the objective lens at the distance $r \approx f(V/U_0)^{1/2} \sin \alpha$ where f is the focal length and U_0 the acceleration potential. Likewise, electrons from the electron gun which are imaged by the

illumination system in the back focal plane at the distance r from the axis arrive at the surface at the angle α. α determines the coherence width which is, thus, given by

$$\omega \leq \frac{\lambda}{2\sin\alpha} \approx \frac{\lambda}{2}\frac{f}{r}\sqrt{\frac{V}{U_0}} = \frac{1}{2}\sqrt{\frac{150}{V}}\sqrt{\frac{V}{U_0}}\frac{f}{r} = \frac{1}{2}\sqrt{\frac{150}{U_0}}\frac{f}{r} \text{ (Å)}$$

For U_0 = 15 kV and f = 5 mm, which are typical values used in LEEM $\omega < r / 4$ (Å, r in mm). For a given low aberration illumination optics the source size determines the radius of its image in the back focal plane and, thus, the coherence. For LaB_6 emitters $r \approx 1$ µm, that is $\omega < 250$ Å, are realistic; for a conventional field emitter r = 100 nm, that is $\omega <$ 2500 Å; for a teton tip r = 10 nm, that is $\omega < 25000$ Å appear feasible, provided the LEED pattern is magnified high enough by the imaging optics so that the spot profiles can be measured with sufficient accuracy.

While high coherence is very desirable in LEED, it is frequently undesired in LEEM, e.g. for imaging steps which requires slight defocusing in order to convert the phase contrast into amplitude contrast (see Fig. 1a). The many Fresnel fringes which form then make image interpretation difficult, in particular if the steps are so closely spaced that their Fresnel diffraction patterns overlap. For holography, however, coherence is needed and point sources such as teton tips become useful. There are two reasons why low energy electron reflection holography is interesting. The first one is resolution improvement via correction of the spherical aberration and of the astigmatism of the objective lens [9]. This procedure needs a beam splitter to produce a coherent reference wave and the knowledge of the wave aberration which is needed for numerical processing of the hologram. This is a major undertaking which appears premature of the present state of LEEM.

The other possibility is to use a perfect surface as a low energy reflector, to deposit object on it and to use the wave reflected from the uncovered part of the surface as a reference wave for holography. This application would be interesting with organic objects such as macromolecules which are sensitive to electron bombardment. With LEEM energies below 10 eV damage is negligible but resolution is limited because of the long wavelength $\lambda = \sqrt{150/V} \geq 4$Å and reconstruction is complicated by the field distortion caused by the non planar object. Compared to lensless low-energy electron holography [10] this method appears much more difficult and has a lower resolution because of the lower energy, but has the advantage of no specimen damage.

There are other limitations to low-energy transmission microscopy [11] but the high inelastic cross-sections of the outer electron shells in the 100 eV range are certainly the most serious handicaps. As pointed out in ref. (11), electron microscopy or holography with conventional electron microscopes below the atomic displacement threshold is much more suitable in this respect. It remains to be seen whether or not low energy electron transmission or reflection holography will become viable methods.

5. Summary.

LEEM and STM are not only complementary for the reasons given in the introduction but also in their interaction with the *atoms* in the specimen: STM can be used to manipulate atoms, LEEM cannot. STM and LEEM are similar in their interactions with the *electrons* in the specimen: they do not cause specimen damage due to electronic excitations, if LEEM is used below the excitation/ionisation threshold. Combination of nanotip technology and

science with LEEM is promising not only for combined STM-LEEM studies but also for improvements and extensions of LEEM such as high resolution LEED or LEEM holography.

Acknowledgement: This work was supported by the Deutsche Forschungsgemeinschaft and by the Volkswagen Foundation. The experimental results used as illustrations here were obtained by W. Telieps, M. Mundschau, W. Swiech, H. Pinkvos and H. Poppa. Discussions with H.J. Kreuzer and J. Spence are also acknowledged.

REFERENCES

1 W. Telieps and E. Bauer, Ultramicroscopy **17**, 51 (1985)

2 E. Bauer, in Electron Microscopy, Vol. 1, Edit. by Breese,Jr. (Acad. Press, New York 1962), p. D-11

3 E. Bauer, M. Mundschau, W. Swiech and W. Telieps, J. Vac. Sci. Technol. **A9**, 1007 (1991)

4 W. Swiech and E. Bauer, Surf. Science **255**, 219 (1991)

5 H. Pinkvos, H. Poppa, E. Bauer and J. Hurst, in *Magnetism and Structure in Systems of Reduced Dimensions,* NATO - ARW, Corsica, June 1992

6 E. Bauer and W. Telieps, in*Surface and Interface Characterizzation by Electron Optical Methods,* edit. by A. Howie and U. Valdrè (Plenum Press, New York 1988) p. 195

7 E. Bauer in*Chemistry and Physics of Solid Surfaces VIII,* edit. by R. Vanselow and R.F. Howe (Springer, Berlin, 1990), p. 267

8 E. Bauer in: Int. Phys. Conf. Ser. No. 119, Sec. 1 (IOP Publishing Ltd, 1991), p. 1

9 H. Litche, private communication

10 H.W. Fink, H. Schmid, H. Kreuzer and A. Wierbicki, Phys. Rev. Lett. **67**, 1543 (1991)

11 W. Quian, J.C.H. Spence and J.M. Zuo, Acta Cryst. A, to be published

NANOTIPS AND TRANSMISSION LOW ENERGY ELECTRON DIFFRACTION

J.C.H.SPENCE
Dept. of Physics and Astronomy
Arizona State University
Tempe, AZ. 85287
U.S.A.

ABSTRACT. A field-emission nanotip is a lens, which forms an image of a virtual source. The results of recent calculations for the aberration coefficients of these sources are given, and found to be of sub-nanometer dimensions. The use of these sources in field-emission guns is discussed. The relationship between Fourier imaging, shadow imaging and in-line holography at sub-kilovolt electron energies is discussed, using a nanotip field emitter. The results of recent multiple electron scattering computations for the transmission of 100 - 1000 volt electrons through thin gold films are summarised.

1. INTRODUCTION.

The exciting prospect of manipulating individual atoms by STM and related methods has brought together at this conference researchers from diverse fields, all with a common interest in the behaviour of atoms in the high fields generated at sharp tips. These fields include scanning tunnelling microscopy (STM), atomic force microscopy (AFM), field electron microscopy (FEM) and field ion microscopy (FIM) and the atom probe.

But these nano-tips promise equally exciting spin-offs in other areas. In particular, the ability to fabricate nanotips reproducibly from a range of materials can be expected to have a large impact on all electron-optical imaging and analytical instruments which use field-emission electron guns, in addition to their obvious benefits for STM, AFM and FIM work. The fine structure in their electron energy-loss distribution has also attracted much attention. Most recently, we have also seen the dramatic transmission Fourier images recorded at about 300 volts by Fink and co-workers [1], in which the atomic resolution detail obtained in the patterns is approximately equal to the nanotip source size.

The formation of atomically sharp tips has a long history, beginning in the field of field emission microscopy. A variety of sharpening techniques,

V.T. Binh et al. (eds.),
Nanosources and Manipulation of Atoms Under High Fields and Temperatures: Applications, 19–33.
© 1993 *Kluwer Academic Publishers. Printed in the Netherlands.*

including sputtering, oxygen etching and thermally assisted field desorption have been tried over the years (see [2] for a review). Tips have been observed in electron microscopes, using special holders. There remains, however, an urgent need for the development of better methods for forming and characterising these tips, since so many areas of science now depend on their development. For example, it may be said that the STM works, not because the tip is sharp, but because the surface is flat. Most tips, when used on undulating surfaces, produce image artifacts such as "domain boundaries" of atomic width. These image artifacts appear when the tip switches from one emission point to another, which may be hundreds of Angstroms apart, so that two widely separated regions of surface appear adjacent in the image. Better tips would elliminate these artifacts and allow rougher surfaces to be studied. The Atomic Metallic Ion Emission (AMIE) method, described elsewhere in this volume, appears to be a promising method of tip preparation for UHV based imaging methods, while lithographic techniques are used for improved AFM tips. Transmission Fourier imaging provides one simple method of tip characterisation for STM, whereas FIM is perhaps the ideal method.

In this paper we summarise the results of some recent calculations for the aberrations of nanotips and their coherence properties. If such a nanotip is used in a simple low voltage shadow image microscope, an in-line electron hologram or shadow image is formed on a distant screen. We also discuss the multiple scattering, Fourier imaging and optical potential corrections involved in the interpretation of these interferograms. We commence, however, with some comments on the use of nanotips in electron optical instrumentation.

2. NANOTIPS IN FIELD-EMISSION GUNS.

The design of field-emission guns has a long history, involving problems of electron-optical design optimization, which, for many-lens systems, are nowdays handled by ray-tracing computer programs. The design must consider the choice of extractor voltage (which depends on tip sharpness), the aberrations of all the lenses including the accelerator and probe-forming lenses, and any loss of intensity due to limiting apertures. Given adequate electronic and mechanical stability, the ultimate probe size depends on *both* wavelength and aberrations, which scale roughly with lens dimensions. The advantage of reducing wavelength and accepting moderate aberrations (for the same probe size) is that a focal length of millimeter dimensions then allows space for many detectors and sample manipulation, heating, cooling and tilting devices. An off-axis X-ray detector, for example, may then subtend a sufficently large solid angle at the probe to be used. In addition, the ray bundle may be kept paraxial. For lens apertures of micron dimensions the aperture tends to be filled, so that the outer non-paraxial rays are severely aberrated.

While detailed calculations have yet to be done, the use of a nanotips in high voltage electron guns may have several advantages, even if the brightness of these tips is the same as for conventional cold field-emitters.

(For a given tip, brightness is, by definition, independent of source size). Departures from Fowler-Nordheim behaviour, fine structure in emission energy loss spectra and much higher brightnesses have all been claimed for nanotips, as discussed elsewhere in this book. For applications in Scanning Transmission Electron Microscopes (STEM), the increased probe current at lower extraction voltage, narrower emission energy distribution, higher coherence and increased lifetime and stability of these tips may have advantages. Since an extraction voltage of a few hundred volts is used with nanotips, the energy of backscattered ions from the anode is greatly reduced, which may account for the increased stability of emission. Recent experiments have confirmed some of these attributes for a sharpened tip fitted to a Vacuum Generators HB501 STEM instrument [3]. In this application, the magnification for the probe-forming lens must be reduced from about 0.02 to perhaps unity for a nanotip. The results of calculations to be reported below show that the asymptotic emission semiangle for a nanotip is about seven degeres. The Helmholtz-Lagrange conservation of phase space gives $E_i A_i S_i$ as a constant along the electron beam, where E is the beam energy, A its area and S the local solid angle. At unity magnification, acceleration to 100 kV then results in an angular compression from seven degerees to 12 milliradians, if E_1 = 1000 V (the extraction voltage appropriate to the *virtual* source size of 0.23 nm given below) . This almost fills the 18 milliradian optimum objective aperture needed for atomic resolution imaging at 100 kV in the latest VG high resolution STEM instrument (Cs = 1.3 mm).

3. ABERRATION COEFFICIENTS FOR NANOTIPS.

A nanotip is a lens. As shown in figure 1, the emission appears to come from a virtual source of radius R_0 inside the tip in the gaussian image plane (defined by paraxial rays). This virtual source might be thought of as the focus formed by a preceeding virtual lens. Points on this virtual source are conjugate to those on the emitting surface, with magnification M. The rearward extension of the asymptote to rays leaving the tip at different angles do not meet at a point in the gaussian image plane. This allows aberration coefficients to be defined.

Ray-tracing computations have recently been completed for the case of field-emission from a nanotip of radius 1 nm [4]. These computations solve Posson's equation for the fields, then use a differential form of the Lorentz force law and the equation of motion to solve for the trajectory of the emitted electron. Intensities are found from a statistically weighted sum of trajectories using the Fowler Nordheim equation.

We define our nanotip as a hemispherical cap of radius R = 1 nm atop a larger hemisphere of radius 100 nm, capping a shank. We find that, if the anode is well separated from the tip, the electric field at the tip is E = V/(KR) where K = 30 for R = 10 A and K = 1.4 for R =1000 A, if E is in volts per Angstrom. The onset of field emission occurs at about 0.5 V/A. By definition, the intersection of a ray with the gaussian image plane occurs at

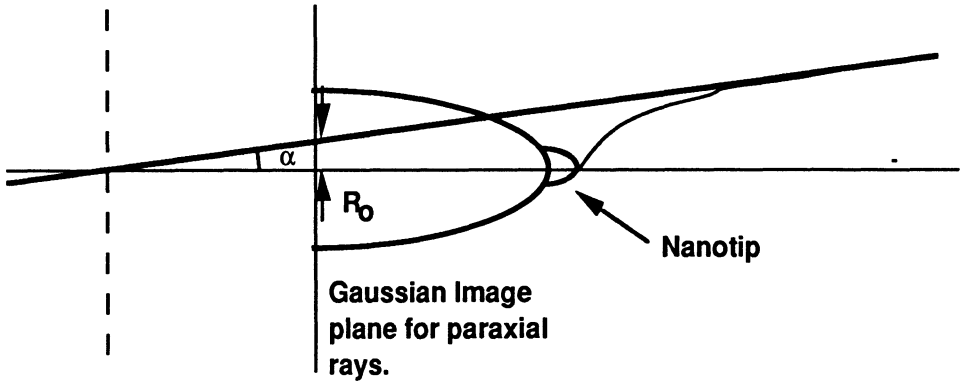

Figure 1. Aberrations and rays for a nanotip. The rearward asymptotic extension of rays from the sample cross the axis at the gaussian image plane at a distance R_0 from the axis which depends on α.

$$R_0 = M\, C_s \sin^3 \alpha$$

if its asymptote makes an angle α with the axis. By ray tracing, we find from a plot of $\sin^3\alpha$ against R_0 that for the nanotip M = 0.531 and C_s (R = 1 nm) = 0.236 nm. For a larger tip, we find C_s (R = 100 nm) = 0.271 with M = 0.647.

Chromatic aberration coefficients can be found similary; our calculations give C_c (R = 1 nm) = 0.142 nm and C_c (R = 100 nm) = 0.24 nm. The virtual source was modelled as a gaussian, and found to have fallen to 1/e of its maximum value at a half-width of 0.23 nm for the nanotip. (The 100 nm tip had a half width of 22 nm). Both are smaller than the emission areas on the tip surface.

The asymptotic angular emission spectrum was also computed, and found to have a halfwidth of 7.4 degrees for the nanotip and 18 degrees for the 100 nm tip. The coherence of the emission can be calculated using the van-Cittert-Zernike theorem (applied to the virtual source), and this gives, for example, a coherence width at a sample or anode placed 370 nm away as 65 nm, and a width of 1.7 cm on a screen 10 cm from the source.

These calculations confirm the general trend by which aberrations scale with lens dimensions, in this case with the tip itself forming the lens. However, by comparing these results with closed-form expressions, it is possible to show that the total aberrations in this case are controlled not by the nanotip shape, but rather by that of the supporting boss [4]. It may be that the tip-

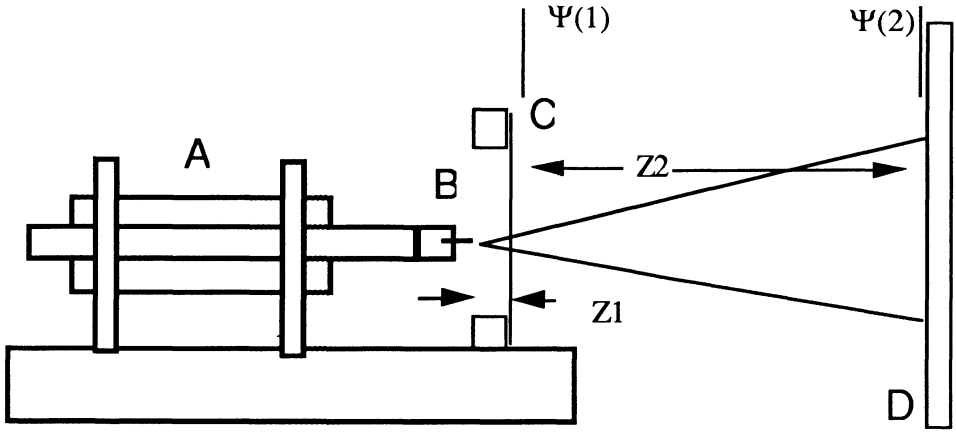

Figure 2 Geometry of a point source projection microscope. A - Inchworm positioning device. B - STM tube scanner, with tip at high negative potential. C - Thin, semitransparent grounded crystal of thickness t. D - Microchannel plate detector. Image wavefunction $\Psi(1)$ and detector wavefunction $\Psi(2)$ are shown.

support system acts as a two-lens system - a strong first lens (the nanotip) and a weaker second lens (the support). We measure only the asymptotic aberrations of the combined system. The effect of the nanotip is to reduce the potential needed for field-emission. These calculations do not include space-charge effects. Figure 2 shows a geometry similar to that used by Fink et al [1]

We may conclude that the aberrations of nanotips are negligibly small compared to those of minilens apertures. Nanotips may therefore be used as an essentially aberration-free high brightness source of electrons for energies up to the threshold for field desorption (perhaps 500 volts, depending on tip sharpness). At higher voltages, additional lenses used to accelerate the beam will introduce much larger aberrations. For point-projection imaging, the significance of this is that Fourier images and holograms formed using nanotips will be free of the distortions of field which are seen in Ronchigrams obtained on STEM instruments.

4. COHERENT SHADOW IMAGING AND HREM.

Lensless shadow imaging using a field emission source was first attempted before the war by Morton and Ramberg [5], and later developed by Muller and Tsong, and Melmed and Smit [7]. The geometry of figure 2 produces a simple shadow image of magnification $M = z_2/z_1$. If we assume that the nanotip emits a perfect spherical wave, we may now relate this shadow image to a conventional high resolution electron microscope (HREM) image formed with plane wave illumination, as shown in figure 3. For the

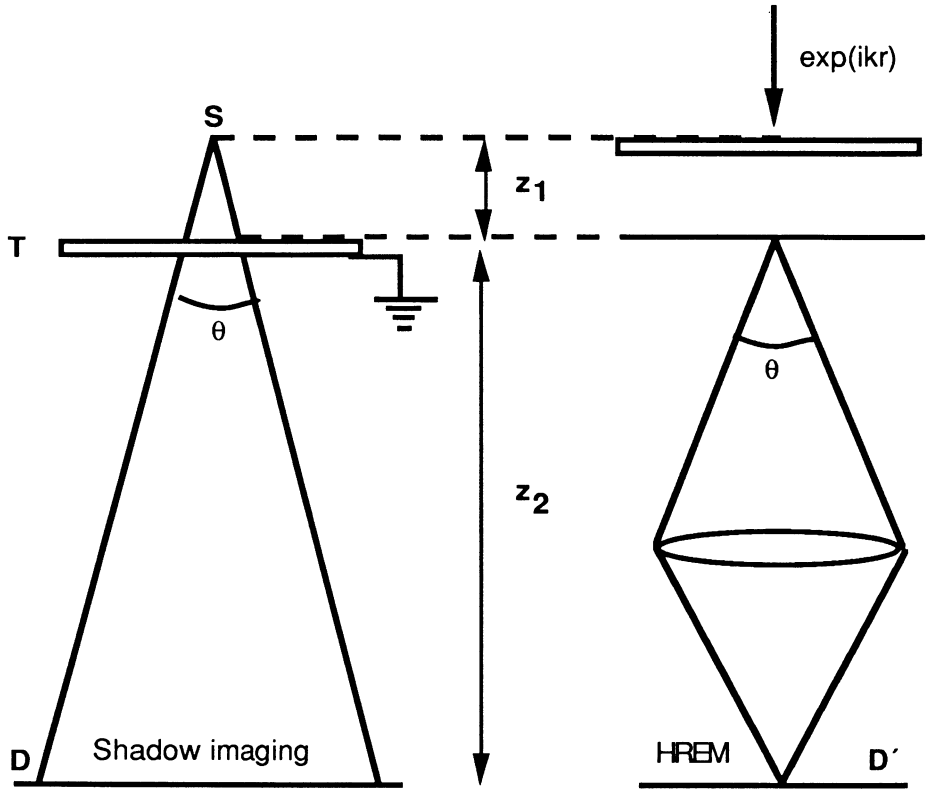

Figure 3. Equivalence of shadow image D formed with spherical wave S, and high resolution electron microscope image, out-of- focus by z_1, at D´ formed with plane wave illumination. For equal magnifications, the images at D and D´ are identical in the absence of aberrations for thin samples.

present we assume complete coherence, an unlimited illumination angle θ, and a negligible coefficient of spherical aberration C_S .

We consider first the high voltage case, where the transmission function q(x) for the sample may be given in the phase object approximation. Then, in one dimension, $q(x) = \exp(-i \sigma \phi_p(x))$ (with Fourier transform T(U)) , where $\sigma = \pi / \lambda V_0$, with λ the electron wavelength and $\phi_p(x)$ the projected sample potential. We choose cartesian coordinates with z along the beam path. Let the electron wavefunction across the downstream side of the slab be $\Psi_i(x)$, and let the spherical wave incident on the sample be represented in the

parabolic approximation by $t_{z1}(x) = \exp(-i \pi x^2/z_1 \lambda)$ (with transform $T(U) = \exp(i \pi z_1 \lambda U^2)$). Then, with $U = \Theta/\lambda$, where Θ is the scattering angle,

$$\Psi_i (x) = q (x) t_{z1}(x) \qquad 1.$$

The detected wavefield in the far-field is

$$\Psi_D (X) = Q (U) * T(U) \qquad 2.$$

Evaluating the convolution in 2, and ignoring unimportant phase factors gives

$$\Psi_D (X = z_2 \lambda U) = q (X/M) * t_{z1}(X/M) \qquad 3.$$

This important result establishes that for thin samples, if the emission angle from the tip is not limited, then the shadow image consists of an "ideal" image which is out of focus by the tip (or probe)-to-sample distance z_1. Equation 3 is identical to the expression for an out-of-focus high resolution transmission electron microscope (HREM) image (with $C_S = 0$) formed using plane-wave illumination (as shown at D'), with the exception that the point-projection image at D has been magnified by $M = z_2/z_1$ without the use of lenses (apart from the tip itself). As may readily be confirmed using an optical laser and a slide transparency, increasing z_2 increases the overall magnification of a shadow image, but not the focus defect, which is fixed by z_1. No assumption of periodicity has been made for the sample. The effects of limiting the emission angle from the tip (or the beam divergence θ) are equivalent to limiting the semiangle subtended by the objective aperture in HREM. The resolution of the shadow image is approximately equal to the effective source size if it is extended, and is limited by the angular range over which emission from the tip or probe is coherent [7].

An in-focus image can only be obtained using 3 if $z_1 = 0$, in which case M is infinite and, if a physical emitter is used, field emission then becomes impossible. In addition, if $z_1 = 0$, zero contrast is predicted for the image of a phase object.

The arrangement of figure 3 also corresponds to the formation of an out-of-focus convergent-beam electron diffraction pattern (CBED) with an illumination aperture much larger than the Bragg angle. The source S' may be either the effective virtual source within a physical field-emission tip of sub-nanometer dimensions (as in the recent experiments of Fink et al [1]), or the focussed image of a field emitter S. In the first case, T, the transmission sample, acts as a grounded anode, and the accelerating voltage V_o is unlikely to exceed a kilovolt. Sample thickness must be limited to a few Angstroms, but spherical aberration is negligible. In the second case, by using an accelerator, it has recently become possible to make field-emission STEM instruments which operate at accelerating voltages up to about 300 kV

(Vacuum Generators HB603). Then S' is the out-of-focus probe used to form a nanodiffraction pattern at D, whose diffraction orders overlap if θ is large. Spherical aberration is appreciable ($C_S \approx 1$mm), but sample thicknesses may be a few hundred Angstroms. We first consider a thin transmission sample in a high voltage machine, in order to relate the shadow image formed at D to the conventional HREM image shown at D'.

It is important to clarify the conditions under which this idealised analogy between HREM and shadow imaging holds. Apart from the assumptions of complete coherence and C_s=0, there is an important limitation on the strength of multiple scattering for the analogy to hold. This is that the same transmission function q(x) can be used for spherical wave and plane-wave illumination. The analysis fails for a general thick dynamically scattering object, since then the transmission function used in equation 1 (for spherical wave incidence) cannot be interpreted in equation 3 for plane-wave incidence [24]. Thus the analogy fails if the phase object approximation fails.

At low voltages, transmission samples are not weak phase objects, and the three-dimensional dynamical theory of transmission low energy electron diffraction (TLEED) must be used to interpret the results of the experiments of Fink et al [1] (see [8]). The projected charge density approximation (further discussed below) cannot therefore be used .

Although the focus error in a point-projection shadow image cannot be compensated for by using additional lenses, it can be removed holographically, as we now describe.

5. IN-LINE ELECTRON HOLOGRAPHY.

While most electron holography has been based on the Mollenstedt-Ducker biprism using the off-axis geometry there has also been continuous development of the in-line technique. There are two cases:

1. For a sufficiently small object of size d (which may be strongly scattering or opaque), that portion of the wavefunction which travels around the object may provide a strong reference wave, so that the total dynamical wave-function at the detector may be written as

$$\Psi_D(X,Y) = 1 + \varepsilon(X,Y) \qquad \varepsilon << 1 \qquad 4.$$

Then, following well established principles, the out-of-focus shadow "image" Ψ_D may be interpreted as an in-line electron hologram [9]. The reconstruction process retrieves the multiply scattered wave-function Ψ_D which, in general, bears no simple relationship to the atomic structure of the object apart from that imposed by symmetry. Under single scattering conditions, an intuitive interpretation may be possible. A further complication occurs at low energies, where exchange and virtual inelastic scattering effects destroy any simple relationship between the optical potential needed in the scattering theory, and the distribution of charge density in the sample [8, 10].

The famous "twin-image problem" must also be resolved - the most successful method for the in-line geometry appears to be Fraunhofer holography [11], in which the hologram is recorded in the far-field of the object. This requires $z_2 > d^2/\lambda$. Then, for a small object, the virtual image is sufficiently far out of focus to avoid interference with the real image. Optical holography of macroscopic objects does not normally satisfy this far-field condition, and is thus mostly near-field holography, whereas a focus defect of only z_2 = 300 nm is sufficient to obtain far-field conditions for electron holography of a Buckyball molecule (C60) at 100 kV. The first experimental attempts at this form of electron holography were those of Haine and Mulvey [12], whose lack of success could be traced to lack of source brightness. Following the application of field emission sources to electron microscopy by Crewe [13] , more satisfactory results were obtained by Munch [14] and Saxton [15]. Experimental results in this geometry have also been reported ([16] , [17]) using nearly collimated illumination, and for the near-field case [18] . More recently, in line electron holograms have been recorded in STEM instruments, where a variety of schemes have been described for reconstruction and for avoiding the twin image problem [19].

If the reconstruction of a point-projection electron hologram is performed using a point source of light of wavelength λ' and optical distances z_1' and z_2', then the lateral magnification M_L is

$$M_L = m \; [1 - (z_2/(z_1 + z_2)) - m^2 \, z_2/\mu \, z_1' \,]^{-1}$$

where $m = \lambda'/\lambda$ and m is the photographic enlargement of the hologram. The longitudinal magnification is

$$M_z = M_L^2/\mu$$

In order to obtain a faithful three-dimensional reconstruction we require $M_z = M_L$. This can be obtained if $m = 1$, $z1 \ll z2$ and $z_1' \approx z_2$. Then for the case of visible light in-line reconstruction of a point-projection electron hologram, the overall magnification is

$$M_L = \mu$$

If an observer views the virtual image of a reconstructed hologram, his or her eye selects a particular plane to focus on from within the reconstructed optical volume. Despite rapid progress in methods for presenting three-dimensional data by computer using special viewing devices, the process of numerically reconstructing a three-dimensional scene still requires large amounts of computing time and memory. No truly satisfactory methods of presenting three-dimensional "gray-scale" information (such as crystal charge density) appears to have been so far devised.

We emphasis that electron holography cannot allow one to "see inside" a crystal. (The preceeding discussion refers to electron holograms which delineate the external shape of a small object, such as an MgO cube). All reconstruction methods deal with free-space propagation, whereas the propagation of electrons in crystals or molecules is governed by the Schroedinger equation, which includes additional dynamical dispersion effects due to the variation of potential within the sample. Nevertheless, holograms recorded at low voltage are sensitive to the coordinates of the atoms along the beam path, so that trial and error reconstruction methods might be used to obtain the three-dimensional optical potential from the hologram.

2. For laterally extended objects wider than the beam, the required reference wave exists only for weakly scattering objects. This case has been studied in detail theoretically and experimentally (using a field-emission STEM instrument) by Cowley (see [19] for a review). Methods have been proposed for resolving the twin image problem in this case, based on translation of the probe and on the differences in magnification of the conjugate images. Since the contrast is zero for an in-focus, unaberrated reconstruction of a phase object, a 90^{o} phase shift must also be introduced in the reconstruction process to compensate for the 90^{o} phase shift which occurs on scattering. (This phase shift, given by the first-order expansion of q (x), is not normally included in the first Born approximation, because of the different boundary conditions used). An alternative method of reconstruction has also been proposed, based on scanning the in-line hologram over a matched filter, which performs a deconvolution in real time [20]. Extensive computations have recently been reported [8] for this transmission low energy diffraction (TLEED) case, using the Bloch wave method. These treat the case of 600 volt electrons traversing, and backscattered by, a thin film of gold. Single scattering conditions are found to exist for a thicknesses of less than about 0.3 nm. The total transmitted intensity falls to 0.37 of the incident intensity at a thickness of about 0.8 nm. These calculations must be based on a complex optical potential V'(x,y) rather than the coulomb potential V(x,y). The two potentials differ as a result of corrections due to exchange, virtual inelastic scattering and an imaginary absorption term, introduced to account for depletion of the elastic wavefield by inelastic scattering.

6. FOURIER IMAGES.

If the sample is laterally extended and periodic, such that a square lattice of side *a* can be chosen, it is a remarkable fact that the magnified shadow images form a perfect unaberrated image of the crystalline sample on certain special downstream planes. (Lattice images are also formed for certain other two-dimensional lattices). These lattice images have been named Fourier images by their discoverers [21]. They are formed by interference between rays leaving the tip at angles differing by multiples of the Bragg angle which interfere after diffraction on passing through the crystal.

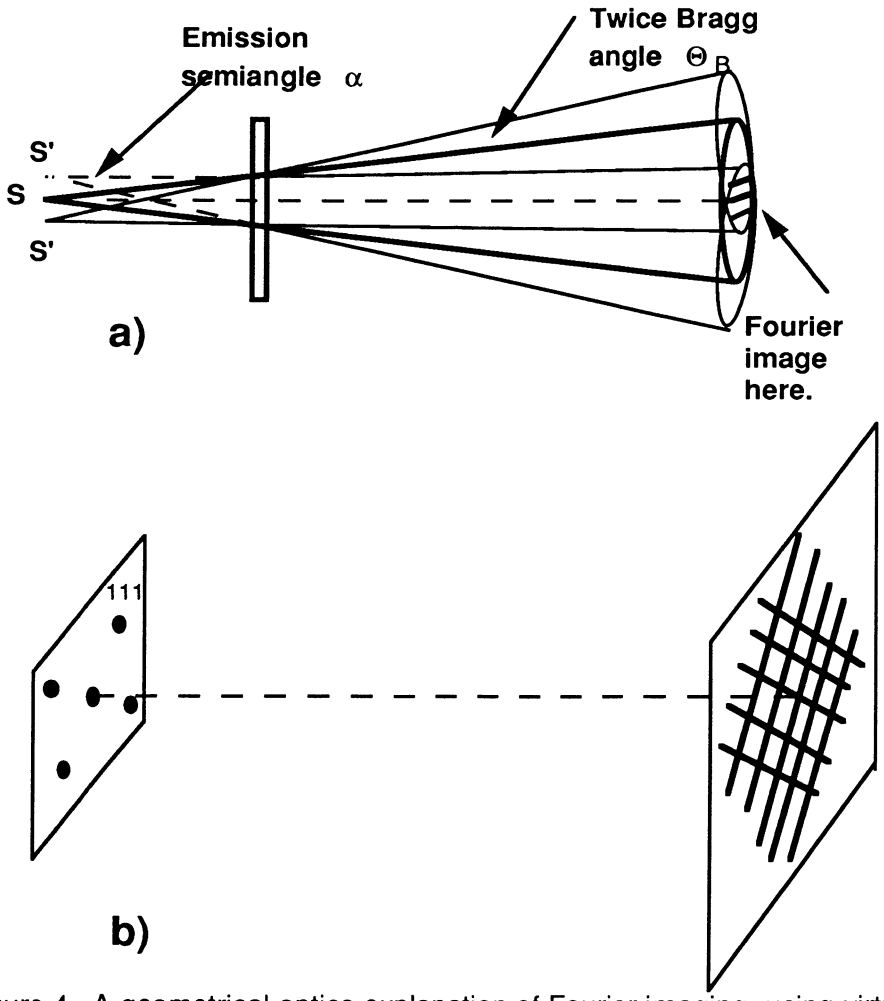

Figure 4. A geometrical optics explanation of Fourier imaging, using virtual sources. The diverging cone of rays from S is Bragg diffracted to form additional cones. If these Bragg cones are extended backwards they define virtual sources S´. As shown in figure 4(b), these sources lie on the reciprocal lattice. Exactly as for Young´s pin-hole experiment, a lattice fringe image is thus formed without lenses or scanning due to interference between the diffracted orders.

Figure 4 shows a simplified explanation of the effect using geometric optics. According to Fourier imaging theory (and neglecting unimportant phase factors), magnified copies Ψ_n of Ψ_D are formed on planes z_2 satisfying

$$\frac{1}{z_1(n)} + \frac{1}{z_2} = \frac{\lambda}{2na^2} \qquad 5$$

where n is an integer and *a* the lattice constant. Aberration - free lensless imaging then occurs with magnification M = z_2/z_1 if the source is a true point. Only periodic components of Ψ_D appear "in focus" for tip positions $z_1(n)$; non-periodic detail always remains out of focus. Each image point contains contributions from many object points, related by translational symmetry. Patterns are periodic in z, but if few beams are excited, this periodicity will not be observed experimentally, since a sinusoidal grating is always in focus. Although the contrast of the Fourier image of a phase object is zero, it was possible to show that, at high energies where the projected charge density (PCD) approximation applies [22] , faithful images of the thin crystal charge density could be obtained in the neighborhood of the Fourier image planes. Thus if a total focussing error $z_1 = \Delta f$ is introduced which is sufficiently small to allow a first order expansion of $t_{\Delta f}(x,y)$, then the final image intensity may be shown to be [22]

$$I(x,y) = 1 - (\frac{\Delta f \lambda \sigma}{2\pi}) \nabla^2 \phi_p(x,y)$$
$$= 1 + (\frac{\Delta f \lambda \sigma}{2\pi\varepsilon_o \varepsilon}) \rho_p(x,y) \qquad 6$$

Thus the image can be expected to reveal the atom positions as maxima in the projected total charge density $\rho_p(x,y)$. In order for 6 to apply, a sufficiently energetic beam must be used to ensure that corrections to $\phi_p(x,y)$ due to virtual inelastic scattering and exchange effects are negligible - only under these conditions does Poisson's equation relate the Hartree potential $\phi_p(x,y)$ to $\rho_p(x,y)$ [8]. This condition is not satisfied at LEED energies.

Experimental electron Fourier lattice images were first observed by Cowley ([23], see also [19] for a review) using a STEM instrument . His experimental point-projection lattice image (from the 0.8 nm lattice planes of thin crystals of beryl) are confined to the region near the optic axis, and the image becomes severely distorted by the effects of spherical aberration away from the axis, unlike the low voltage Fourier images observed by Fink et al (1991).

Resolution in Fourier images is limited in practice by the size of the effective source, which limits the semi-angular range ϕ over which emission is coherent, and by the electron wavelength. In one dimension, the number of beams contributing to the image is thus approximately ϕ / Θ_B, where Θ_B is the Bragg angle. The low voltage Fourier images clearly demonstrate that the

emission from the tip is occuring from regions of atomic dimensions. (An atomic resolution image would also be obtained if a matched tip and sample were used, so that multiple tip emission points lay on the same lattice as the sample).

At these low voltages, the Ewald sphere radius is not much larger than a reciprocal lattice vector, so that the theory of transmission low energy electron diffraction (TLEED) must be used to interpret the images [8], and the PCD approximation (which assumes a "flat" Ewald sphere) cannot therefore be used. For a general dynamically scattering thin crystal it can be shown that Fourier images still occur near the optic axis, but these images now become modulated by the crystal rocking curve [7]. The number of lattice fringes occuring within the Bragg angle α (subtended by the detector at the sample) is equal to the order of the Fourier image. Faithful images are only obtained at large z_1 values, where the extent over which the image is periodically averaged increases. The lattice fringes are severly distorted in the region of the Bragg angle α. The effects of the Higher Order Laue Zone (HOLZ) reflections would cause the Fourier lattice image to be crossed by a distinctive pattern of fine lines (as in LACBED and CBIM [26]). Although the difficulties of interpretation would be considerable, such an image comes close to the ideal of providing simultaneous strain and periodically averaged atomic position measurements.

7. DISCUSSION.

A close similarity exists between the techniques of microdiffraction in STEM (for which $z_1 = 0$ and a small objective aperture is used), Fourier imaging (z1 small, no limiting aperture), Ronchigrams, STEM lattice imaging and in-line electron holography. STEM lattice images are formed by displaying a portion of the intensity in the region where the coherent diffraction orders overlap as a function of probe position [24]. At low energies, transmission LEED theory must be used to interpret the images.

The question then arises as to what is the best electron beam energy at which to obtain interpretable atomic resolution images of defects in the geometry of figure 2. This involves a compromise between the following beam-energy dependent factors: 1. Difficulty of image interpretation. 2. Radiation damage. 3. Source brightness. 4. Detector efficiency. 5. Penetration. A simple image interpretation or holographic reconstruction of the sample potential V(x,y) rather than the optical potential V'(x,y)) or charge density $\rho(x,y)$ is only possible under single scattering or PCD conditions, which occur at hundreds of kilovolts for sample thicknesses of a few nanometers, or more for light atoms [22]. In simplest form, the image interpretation question reduces to a determination of whether the atoms appear as dark or bright spots in the image - this alone can be a very difficult question to answer. Radiation damage due to ionization and radiolysis decreases with accelerating voltage according to the Bethe stopping power law, while ballistic "knock-on" damage rises rapidly above a threshold to an approximately constant value. The ionization process, which causes sample

damage, is essential for efficient detection, which therefore becomes less efficient with increasing voltage. (A thicker detector can be used). Thus the ratio R of elastic scattering (carrying wanted information) to inelastic scattering (producing background) controls all the most important parameters. For coherent imaging, R is proportional to the electron velocity. Source brightness increases with voltage. In summary, interpretability, source brightness, ionization damage conditions and lens performance (controlled by C_S and λ) all improve with increasing accelerating voltage, whereas ballistic damage increases and detector efficiency decreases. Distortion-free images are only produced in the point-projection geometry if C_S is negligible (otherwise Ronchigrams are produced), requiring micron sized lenses.

The best all-round compromise would thus appear to consist of a field-emission point projection instrument operating just below the knock-on threshold, at, say 200 kV. Then penetration is maximised, damage minimized and image interpretability maximized. The use of a physical tip and anode sample is attractive because this arrangement essentially eliminates spherical aberration. However such a design cannot be expected to operate much above 1 kV. Samples for such machines must also be prepared for an uncompromising ultra-high vacuum environment, and must be conducting. The addition of a single diverging aperture lens of tenth-micron diameter allows the sample to lie in field-free space, while having little affect on the aberrations of the tip. The use of electrostatic mini-lenses of micron sized dimensions [2] as the accelerator and probe-forming objective lens may have advantages for such an atomic resolution point projection instrument . The alignment of the optical elements may then require piezoelectric positioning devices. However the overall electron optical design must be considered in detail, and this can be done using optimization techniques [25]. The design problem is similar to that of conventional cold field emission guns [13], and the intensity reductions caused by limiting apertures must also be considered. An imaging omega energy filter might be fitted following the sample [26], to provide elastic energy filtering with parallel detection.

Such an instrument would offer three important advantages over conventional HREM machines. First, if spherical aberration effects could be made negligible so that the distortions seen in current Ronchigrams were absent, images could be straightforwardly interpreted using the PCD approximation in terms of sample charge density (by suitable choice of z_1). Resolution is likely to be limited by electronic and mechanical instabilities (tip vibration) rather than spherical aberration. Secondly, the arrangement is well suited to chemical analysis at the atomic level using energy-loss spectroscopy. Recent advances in data analysis in this field suggest that it is now more sensitive than X-ray analysis for light elements, and that energy filtered images of chemically identified species can be formed from clusters of just a few atoms. Finally, for crystalline samples, if the illumination aperture θ is limited, a CBED pattern can be formed and interpreted quantitatively.

Acknowledgment.

This work was supported by NSF grant DMR91-12550. I am grateful to W. Qian and Drs. Scheinfien and Kasper for useful discussions.

References.

1. Fink, H-W., Schmid, H., Kreuzer, H. J. and Wierzbicki, A. (1991) Phys. Rev. Letts. 67, 1543 - 1545.
2. Staufer,U., Muray,L., Kern,D. and Chang,T. (1991) J. Vac. Sci. Tech. B9, 2962
3. Bleloch, A. L., Walls M.G., and Howie, A. Proc. Eurem 92. in press.
4. Scheinfien, M. Qian, W. and Spence, J.C.H. (1992) J. Appl. Phys. in press.
5. Morton, G.A. ,Ramberg, E.G Phys. Rev. 56, (1939) 705 .
6. Melmed , A.J. (1991). Appl. Phys. Letts. 12, 100.
7. Spence, J. W., Qian, W. Phys. Rev. B45, (1992) 10271.
8. Qian, W, Spence, J.C. H. Zuo, J.M. Acta Cryst. A, (1992) in press .
9. Gabor, D. Proc. Roy. Soc. (London) A197, (1949) 454 .
10. Smart, D.J , Humphreys, C.J. in Inst. Phys. Conf. Ser. No. 41, Chapter 3 1978),
11. DeVelis, J.B. Parrent, G.B., Thompson, B.J. J. Opt. Soc. Am. 56, (1966) 423 .
12. Haine, M.E. , Mulvey, T. J. Opt. Soc. Am. 42, (1952) 763 .
13. Crewe, A. Eggenberger, D.N., Wall, J., Welter, L.M. Rev. Sci. Instr. 39, (1968) 576 .
14. J. Munch, J. Optik 43, (1975) 79 .
15. G. Saxon, G. Optik 35, (1972) 359 .
16. Zhang, X, and Joy, D. in Poc. 49th meeting of EMSA. G. Bailey, Ed. (San Francisco Press, San Francisco) 1991
17. Tonomura, A. Fukuhara, A., Watanabe, H., Komoda, T. Jap. J. Appl. Phys. 7, (1968) 295 .
18. Hibi, T. J. Electronmicroscopy 4, (1956) 10 .
19. J. M. Cowley, J.M. J. Electr. Mic. Tech. 3, (1986) 25 .
20. L. H. Veneklasen, L.H. Optik 44, (1975) 447 .
21. Cowley, J.M. Moodie, A.F. Proc. Phys. Soc. B 70, (1957) 486 .
22. Lynch, D.F., Moodie, A.F., O'Keefe, M. Acta Cryst. A31, (1975) 300 .
23. Cowley, J.M.Ultramic. 4, (1979) 435 .
24. Spence, J.C. Cowley, J. M. 50, (1978) 129.
25. Scheinfein, M. Galantai, A. Optik 74, (1986) 154 .
26. Mayer, J. Spence, J.C.H., Mobus, G. in Proc. Electr. Micros. Soc. Am. G. Bailey, Eds. San Jose, 1991), pp. 786.

LENSLESS LOW ENERGY ELECTRON POINT SOURCE MICROSCOPY

H.J. Kreuzer, A. Wierzbicki, M.G.A. Crawford and C.B. Roald
Department of Physics, Dalhousie University
Halifax, N.S. B3H 3J5 Canada

ABSTRACT. The theory of the point source low energy electron microscope is reviewed. Images are calculated for a double helix of carbon atoms and for small clusters of atoms for which multiple scattering can be accounted for exactly. A Kirchoff-Helmholtz transform is used for reconstruction. Depth resolution is improved by using a range of electron energies or employing tilted geometries.

1. Introduction

More than 40 years ago, D. Gabor [1] proposed a new principle of microscopy to overcome the limitations of lenses. Using a coherent ensemble of particles with wave nature, the fraction of the beam elastically scattered by an object is made to interfere with a coherent reference wave at some two-dimensional detector creating a hologram that contains information on both the amplitude and the phase of the scattered wave. The laser provides such a coherent source of photons for light holography. Only recently has electron holography been demonstrated in electron microscopy [2,3], in photoemission electron holography [4], and in lensless low energy electron microscope [5-8].

In the lensless low-energy electron microscope an ultrathin metal tip with one or a few atoms at its apex serves as a "point" source for electrons which, after accelaration to energies in the range of 20 - 200 eV, scatter off the atoms of an object film a distance of 0.1 - 1 μm away. On a screen some 10 cm away an image is formed by the unscattered and the scattered electrons. If the object film only blocks a small fraction of the incoming electron beam, most electrons arrive on the screen unscattered and we have the typical situation of an in-line hologram, as demonstrated explicitly with the images of carbon fibres. On the other hand, if the object film is extended, images are obtained with structures of length scales that correspond to the lattice of the object film. These structures are, however, not geometric shadow images but interference patterns.

V.T. Binh et al. (eds.),
Nanosources and Manipulation of Atoms Under High Fields and Temperatures: Applications, 35–44.
© 1993 *Kluwer Academic Publishers.*

In the point source electron microscope lenses to produce a reduced image of the beam source have been made obsolete by the fact that an atomic size metal tip generates an abberation-free virtual source whose dimensions can be estimated to be less than 0.5 Å. Because it is the point-like character of the electron source that distinguishes this microscope from others we propose to name it the kendroscope from the greek kendron meaning sharp tip or spine. Imaging with the kendroscope we will refer to as kendroscopy, and the images we will call kendrograms. We will show below that kendrograms are composed of two contributions, a modified hologram or holographic diffraction pattern and a classical diffraction pattern.

The theory of the kendroscope has been developed recently [9] that allows the simulation of kendrograms to aid in the interpretation of experimental images. A modified Fourier transform of the Kirchhoff-Helmholtz type was also advanced that allows to reconstruct the spatial structure of the object film from the image or kendrogram. Further work on the theory of the kendroscope has been published by Spence *et al.* [10-11]

In this paper we will report on some new developments since the submission of the theory paper. In particular we will outline a matrix method to deal with multiple scattering in small clusters. We will also show some interesting kendrograms, e.g. of a double helix structure for which we also do the reconstruction. Doing the latter for a small MgO cluster we will see that element-specific information can be obtained. Lastly, we show that depth resolution in reconstruction can be enhanced significantly from a series of images obtained by tilting the object.

2. Scattering Theory

The theory of the kendroscope uses a scattering approach based on the Lippmann-Schwinger equation. One models the electron source as emitting a wave of mostly spherical symmetry by writing (for large distances from the source, i.e. $kr>>1$)

$$\psi^{(in)}(\mathbf{r}) = \langle \mathbf{r} | \psi^{(in)} \rangle = r^{-1}\exp(ikr)\left[1+\sum_{\ell=1}^{\infty}\sum_{m=-\ell}^{\ell} c_{\ell m}\,(-i)^{\ell}\,Y_{\ell}^{m}(\mathbf{r}/r)\right] \tag{1}$$

For the object film this represents the incoming electron beam (which in LEED is a plane wave). The deviations of the incoming wave from perfect spherical symmetry can be intrinsic to the source itself or might arise from the accelerating electric field between the source and the object. To account for the energy spread in the incoming electron beam, we can sum the final result over different wave numbers k due to the linearity of the Schrödinger equation.

The scattered wave emanating from the object film is given by

$$|\psi^{(+)}> = |\psi^{(in)}> + G^{(+)} T |\psi^{(in)}> \tag{2}$$

where $G^{(+)}$ is the free Green's function, and the T-matrix satisfies the Lippmann-Schwinger equation

$$T = V + VG^{(+)} T \tag{3}$$

Next we assume that the scattering potential of the object film can be written as a constant inner potential, V_0, and a sum of pseudo-potentials centered at the positions, $\mathbf{r}_i$, of the atoms or ions of the object, i.e.

$$V(\mathbf{r}) = V_0 + \sum_i V(\mathbf{r}-\mathbf{r}_i) \tag{4}$$

Expressing the full T-matrix in terms of the T-matrices, T_i, of single atoms, one eventually finds for the scattering solution for a cluster of identical atoms

$$\psi^{(+)}(\mathbf{r}) = \frac{\exp(ikr)}{r}\left[1 + \sum_{\ell=1}^{\infty}\sum_{m=-\ell}^{\ell} c_{\ell m}(-i)^{\ell} Y_{\ell}^{m}(\mathbf{r}/r)\right]$$

$$+ \sum_{i\ell m} \frac{\exp(ik\rho_i)}{\rho_i} \tau_{\ell} Y_{\ell}^{m}(\hat{\rho}_i) F_{\ell}^{m}(\mathbf{r}_i) \tag{5}$$

where $\rho_i = |\mathbf{r}-\mathbf{r}_i|$ and

$$\tau_{\ell} = k^{-1}\sin\delta_{\ell}\exp(i\delta_{\ell}) \tag{6}$$

contains the scattering phase shifts δ_{ℓ}. We also defined a structure factor

$$F_{\ell}^{m}(\mathbf{r}_i) = \Phi_{\ell}^{m}(\mathbf{r}_i) + \sum_{j\ell' m'} M(\mathbf{r}_j-\mathbf{r}_i;\ell,m,\ell',m')\Phi_{\ell'}^{m'}(\mathbf{r}_j)$$

$$+ \sum_{j\ell m j'\ell' m'} \mathbf{M}(\mathbf{r}_j-\mathbf{r}_i;\ell,m,\ell',m')M(\mathbf{r}_{j'}-\mathbf{r}_j;\ell',m',\ell'',m'')\Phi_{\ell''}^{m''}(\mathbf{r}_{j'})$$

$$+ \ldots \tag{7}$$

with

$$\Phi_\ell^m(\mathbf{r}) = 4\pi Y_\ell^{m*}(\hat{r}) r^{-1} \exp(ikr) \left[1 + \sum_{\ell=1}^{\infty} \sum_{m=-\ell}^{\ell} c_{\ell m} (-i)^\ell Y_\ell^m(\mathbf{r}/r) \right] \tag{8}$$

$$M(\mathbf{a}_n; \ell, m, \ell', m') = 4\pi Y_\ell^{m*}(\hat{a}_n) \tau_{\ell'} Y_{\ell'}^{m'}(\hat{a}_n) \exp(ika_n)/a_n \tag{9}$$

Factoring out a spherical wave

$$\psi^{(+)}(\mathbf{r}) = \frac{\exp(ikr)}{r} \left[1 + \sum_{\ell=1}^{\infty} \sum_{m=-\ell}^{\ell} c_{\ell m} (-i)^\ell Y_\ell^m(\mathbf{r}/r) + \bar{\psi}_s^{(+)}(\mathbf{r}) \right] \tag{10}$$

one gets for the contrast image on a screen

$$I(\mathbf{r}) = \hat{I}(\mathbf{r}) - \frac{L}{r^3} = \frac{L}{r^3} [2Re\bar{\psi}_s^{(+)}(\mathbf{r}) + |\bar{\psi}_s^{(+)}(\mathbf{r})|^2] \tag{11}$$

We will refer to the first term as the "holographic diffraction pattern" because it arises from the superposition of the interference terms between the reference wave and the scattered wave from any one of the atoms. The second term in (11) contains the interference between the scattered waves. We will refer to it as the "classical diffraction pattern". Neither term, holographic or classical diffraction, is meant to be exclusive but simply is coined to refer to the terms in (11) linear and quadratic in the scattered waves. Because both holographic and classical diffraction are present to a larger or lesser degree, we feel that a new name, namely a kendrogram, is appropriate for these images.

Holographic diffraction dominates the kendrograms for thin objects that are semi-transparent to electrons; examples are carbon fibres, C_{60} and similar carbon clusters and thin metal clusters of a few atomic layers. As the scattered wave function grows due to multiple scattering in thicker films, classical diffraction becomes more important. When it eventually dominates the image, we are in the regime of classical wave optics. At this stage objects become opaque and information about the atomic structure of the object is lost. Image formation can then be described as diffraction around macroscopic objects.

In our discussion so far we have not dealt with inelastic electron scattering. In the experimental setup inelastically scattered electrons are prevented from reaching the detector by applying the

negative of the accelarating voltage (between the tip and the object) to the detector. Thus at a given energy the effect of inelastic scattering is to reduce the flux of detected electrons. This implies that in our theory we can restrict ourselves to elastic scattering as well. The overall reduction of the scattered signal as a function of energy can then be adjusted by multiplying the calculated flux with an overall damping factor involving the mean free path. For energies between 30 and 200 eV the latter varies from 5 to 10 $\mathring{A}$ for most metals. This suggests that kendroscopy is possible on metallic films of thicknesses of the order of a few atomic layers.

3. Matrix Approach to Multiple Scattering

Multiple scattering enters the scattering wave function (5) via the structure factor defined in (7). This equation can be written as an inhomogeneous matrix equation for a vector

$$\mathbf{F}^T = (F^0{}_0(\mathbf{r}_1), F^{-1}{}_1(\mathbf{r}_1), F^0{}_1(\mathbf{r}_1), F^1{}_1(\mathbf{r}_1), \ldots, F^L_L(\mathbf{r}_1) \ldots, F^L_L(\mathbf{r}_N)) \tag{12}$$

consisting of the structure factors for all relevant partial waves (up to L) at all atomic positions. A similar vector, $\boldsymbol{\phi}$, is constructed from $\phi_\ell{}^m(\mathbf{r}_n)$. We then get from (7)

$$\mathbf{F} = \boldsymbol{\phi} + M\mathbf{F} \tag{13}$$

where the matrix M contains the elements (9). The solution of the multiple scattering problem is thus reduced to a matrix inversion, i.e.

$$\mathbf{F} = (\mathbf{1} - M)^{-1}\boldsymbol{\phi} \tag{14}$$

Spatial symmetries in the atomic cluster imply block form for the matrix M aiding in its inversion or diagonalization. We demonstrate this with a square cluster of four atoms perpendicular to the optical axis, scattering in s-waves only. The lengths of the vectors $\mathbf{r}_i$ from the source are then equal. Thus all components of $\mathbf{F}$ and $\boldsymbol{\phi}$ are equal and M has the simple structure

$$M = \begin{pmatrix} 0 & M_n & M_n & M_{nn} \\ M_n & 0 & M_{nn} & M_n \\ M_n & M_{nn} & 0 & M_n \\ M_{nn} & M_n & M_n & 0 \end{pmatrix} \tag{15}$$

where $M_n = \tau_0 a^{-1}\exp(ika)$ and $M_{nn} = \tau_0 \exp(i\sqrt{2}ka)/\sqrt{2}a$ with $a = |\mathbf{r}_i - \mathbf{r}_j|$. The

four components of **F**, all equal, are then given by

$$F(r_i) = \frac{1+2M_n+M_{nn}}{(1+M_{nn})^2(1-4M_n{}^2-M_{nn}{}^2)} 2\sqrt{\pi} \frac{\exp(ikr_i)}{r_i} \tag{16}$$

It is estimated that multiple scattering in clusters of several hundred atoms (depending on the number of partial waves included) can be treated exactly by this method.

4. Theory of Reconstruction

The r-dependence in the scattering wave function (5) suggests that reconstruction of the object from the kendrograms can be achieved

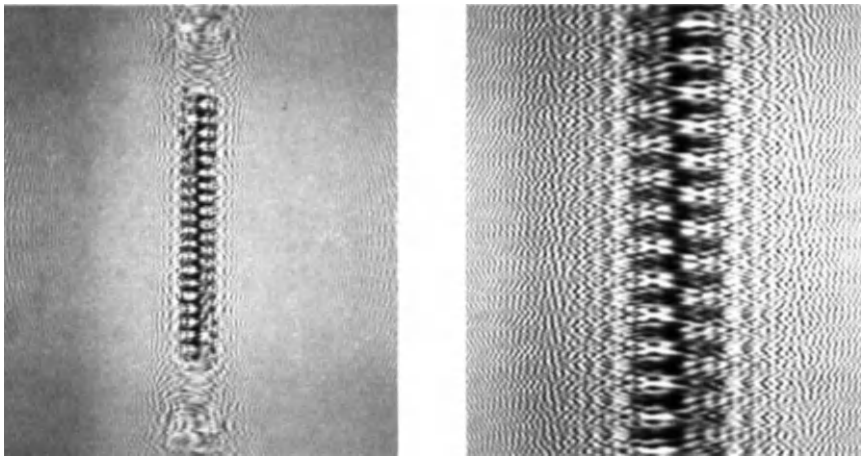

Fig.1: Kendrogram of a double helix of carbon atoms at an electron energy of 95eV and a source to atom distance $d=1000\mathring{A}$. Diameter of the double helix is $60\mathring{A}$; its pitch is $40\mathring{A}$ per turn. The images cover an angular opening of $\pm 35^0$ (left) and $\pm 15^0$ (right), repectively.

via a Kirchoff-Helmholtz transform

$$K(\mathbf{r}) = \frac{1}{4\pi} \int_S d\xi \, I(\xi) \exp(ik\xi \cdot \mathbf{r}/\xi) \tag{17}$$

where the integration extends over the 2-dimensional surface S of the screen with coordinates $\xi=(X,Y,L)$, a distance L from the source. Such a transform has also been used in photoemission electron hol-

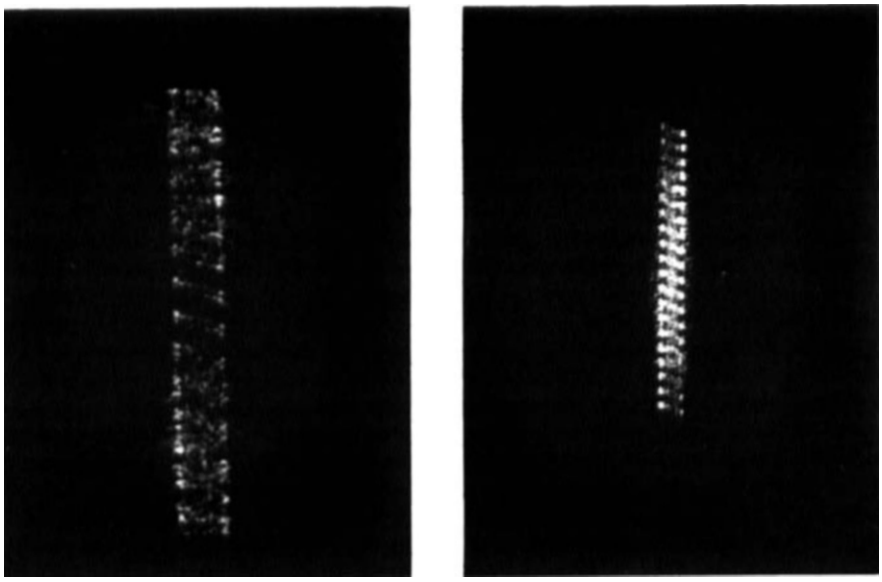

Fig.2: Reconstruction from the kendrograms of a double helix, Fig.1.

ography [4]. The applicability of this transform to kendroscopy has been demonstrated in detail by inverting theoretical kendrograms. As a further demonstration we have calculated, in the single scattering approximation, the kendrogram of a double helix of carbon atoms, as a rather crude model for a DNA molecule, shown in Fig.1 on a screen larger than the shadow projection of the object (left panel). The right panel of Fig.1 shows an enlargement of the central section. The respective reconstructions are shown in Fig.2. With the full image, left panel of Fig.1, as input, atomic resolution can be achieved in the reconstruction including depth resolution (left panel of Fig.2). However, the limited information contained in the right image in Fig.1 is only sufficient to indicate the secondary structure of the double helix without atomic resolution, see the right panel in Fig.2. Depth resolution is equally reduced in this case.

The question arises whether reconstruction with atomic resolution can yield information as to the chemical composition of the object. To demonstrate that this is possible we have used the theoretical kendrogram of a small MgO cluster, taken at an electron energy of 95eV over a half angle of 35^0, and reconstructed the object. We find that the *Mg* spots in the reconstruction have about twice the height as the *O* spots. Higher energies and multiple scattering enhance the contrast. Thus although one cannot readily identify the chemical nature of a particular spot in the reconstruction, one can still differentiate between different atomic species.

It has been suggested, both for kendroscopy and for photoemission electron holography, that lateral and, more importantly depth resolution can be improved if images obtained at several electron energies are used in the reconstruction.[9,12-16] Because spurious structures in the reconstruction are strongly energy dependent, one hopes that a superposition of reconstructed pictures for several energies will enhance the real atomic structures and smear out the spurious ones. Still one cannot circumvent limiting factors of apertured optical systems [18]. In Fig.3 we show the results of energy averaging for a double cluster of 5x5 carbon atoms. Although averaging helps in locating the atoms, the procedure still needs some new ideas.

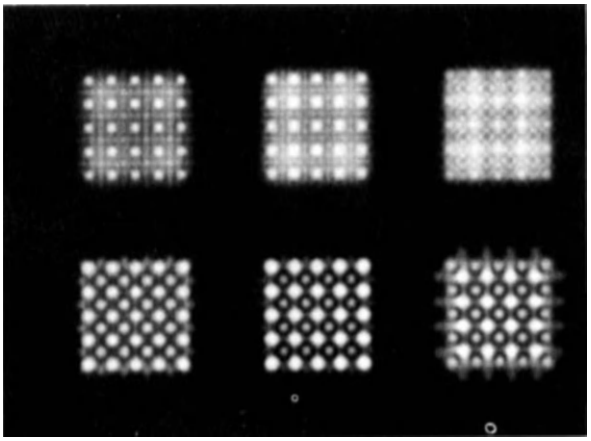

Fig.3: Reconstruction from the kendrograms of a 5x5 plus 5x5 carbon cluster (on a square lattice with a=2.5$\mathring{A}$, the first layer at d=1000$\mathring{A}$ and the second layer behind it at 1003$\mathring{A}$). First column recontructed at 1000$\mathring{A}$, second column at 1003$\mathring{A}$ and third column at 1006$\mathring{A}$ (where there were no atoms!) Top row averaged over two energies E=16 and 422eV at E=95eV, and bottom row averaged over 5 energies E= 68, 95, 122, 150 and 177 eV.

Depth resolution in reconstruction can also be enhanced significantly if kendrograms, taken for a series of tilt angles of the object, are used. This trick to obtain depth information is frequently employed in tomographic procedures [17]. We have calculated a series kendrograms from a cluster of two layers of 5x5 carbon atoms with the plane of the cluster perpendicular to the optical axis and then tilted up to 60^0 through the central row of atoms in the first layer. We then show the reconstruction in a plane along the optical axis and perpendicular to the tilt axis. For the left image the object was perpendicular to the optical axis. The long shadows are a reflection of the poor depth resolution. Superimposing the reconstructed images for the various tilt

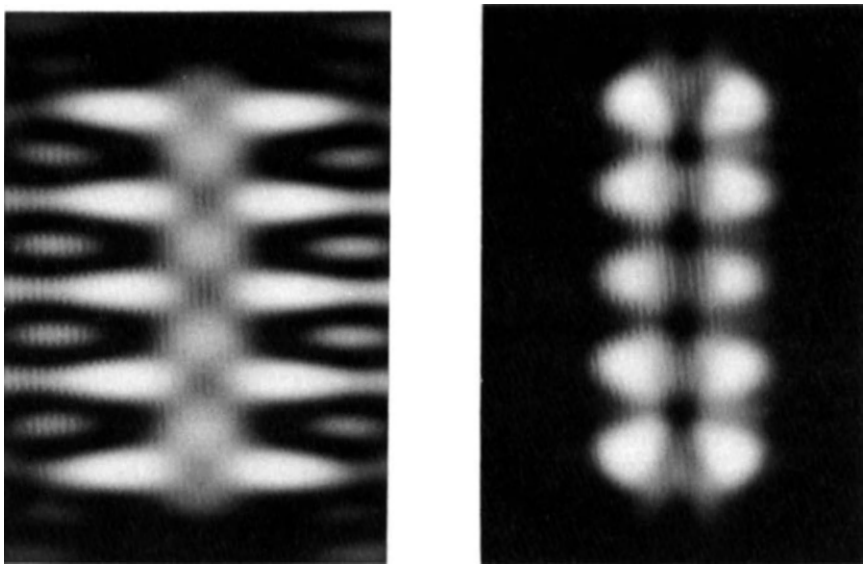

Fig.4: Reconstruction (in a plane along the optical axis and perpendicular to the tilt axis) from calculated kendrograms of a double layer of carbon atoms with 5x5 atoms in a first layer at d=1000Å arranged on a square lattice with a=2.5Å and a second layer of 5x5 atoms at d=1003Å. The electron energy is 95eV. Left image: cluster perpendicular to the optical axis. Right image: superposition of reconstructed images obtained for tilted geometries with tilt angles 0^0, $\pm 15^0$, $\pm 30^0$, $\pm 45^0$, $\pm 60^0$ and $\pm 75^0$.

angles, right panel of Fig.4, clearly resolves the ten atom positions.

5. Outlook

In this paper we have reviewed the theory to calculate electron kendrograms for the point source electron microscope including multiple scattering. Holographic diffraction and single scattering are dominant for small carbon clusters and carbon fibres. Multiple scattering becomes appreciable for large metal films for which classical diffraction also starts to play a role and eventually becomes dominant for films of more than a few atomic layers.

A Fourier-like transform can be used for the reconstruction of the object. To obtain atomic resolution in the reconstruction, the image screen must be large enough to record zero and first order Bragg diffraction. Taking images at various electron energies or at different tilt angles of the object can enhance the resolution in reconstruction.

It remains to apply the reconstruction formula to experimental data. First results for carbon fibres are very encouraging.

Acknowledgement

This work was supported by a Joint Research Agreement between Dalhousie University and the IBM Zurich Research Laboratory. Funding was also provided by the Network of Centres of Excellence in Molecular and Interfacial Dynamics, one of the fifteen Networks of Centres of Excellence supported by the Government of Canada.

References

[1] D. Gabor, Nature (London) **161**, 777 (1948).
[2] H. Lichte, Ultramicroscopy **20**, 293 (1986).
[3] A. Tonomura, Rev. Mod. Phys. **59**, 639 (1987).
[4] J.J. Barton, Phys. Rev. Lett. **61**, 1356 (1988).
[5] H.-W. Fink, Phys. Scripta **38**, 260 (1988).
[6] W. Stocker, H.-W. Fink, and R. Morin, Ultramicroscopy **31**, 379 (1989).
[7] H.-W. Fink, W. Stocker, and H. Schmid, Phys. Rev. Lett. **65**, 1204 (1990).
[8] H.-W. Fink, H. Schmid, H.J. Kreuzer, and A. Wierzbicki, Phys. Rev. Lett. **67**, 1543 (1991).
[9] H.J. Kreuzer, K. Nakamura, A. Wierzbicki, H.-W. Fink, H. Schmid, Ultramicroscopy (in press).
[10] J.C.H. Spence and W. Quian, Phys, Rev. *B* (in press).
[11] W. Quian, J.C.H. Spence and J.M. Zuo, Acta Cryst. (in press).
[12] G.R. Harp, D.K. Saldin, and B.P. Tonner, Phys. Rev. Lett. **65**, 1012 (1990).
[13] C.M. Wei, T.C. Zhao, and S.Y. Tong, Phys. Rev. Lett. **65**, 2278 (1990).
[14] S.Y. Tong, Hua *Li*, and H. Huang, Phys. Rev. Lett. **67**, 3102 (1991).
[15] J.J. Barton, Phys. Rev. Lett. **67**, 3106 (1991).
[16] D.K. Saldin, G.R. Harp, B.L. Chen, and B.P. Tonner, Phys. Rev. *B* **44**, 2480 (1991).
[17] See e.g. J. Frank (*ed.*), *Electron Tomography*, (Plenum Press, New York, 1992).
[18] J.J. Barton, J. El.Spectr. Related Phen. **51** (1990) 37.

Electron Focusing: Computer simulation

H. De Raedt and K. Michielsen

Institute for Theoretical Physics, University of Groningen, Nijenborgh 4, NL-9747 AG Groningen, The Netherlands

ABSTRACT. An overview is given of the basic mechanisms that lead to focused electron emission from very small sources. Various physical processes are investigated by analyzing the time development of wave packets obtained from the numerical solution of the time-dependent Schrödinger equation. Simplified models of atom-size tips are shown to explain the salient features of the electron emission properties observed experimentally. The computer simulation technique is also used to investigate solid-state electron-focusing devices.

1. Introduction

Recent experiments on atom-size tips [1–4] have demonstrated that they act as unusual electron beam sources, emitting electrons at fairly low applied voltages (a few thousand volts or less) with a small angular spread (of a few degrees). These properties make such electron sources very attractive for applications to electron holography and electron interferometry. [5–9] Extensive theoretical work [10, 11] revealed that tunneling through the metal-vacuum potential is the main physical mechanism determining the unusual properties of the emitted electron beams. Tunneling through a potential barrier is only one of the mechanisms for collimating an electron beam. In particular, it has been suggested [12] that adiabatic mode selection [13–15] is mainly responsible for the peculiar properties of the electron beams emitted from atom-size tips. The key ingredient of this description is the presence of a slowly varying, horn-like structure in the potential surrounding the tip and the assumption that the electron wave propagates adiabatically in this structure. However, the application of these ideas to the atom-size tips seems unjustified. [16, 17]

V.T. Binh et al. (eds.),
Nanosources and Manipulation of Atoms Under High Fields and Temperatures: Applications, 45–57.
© 1993 *Kluwer Academic Publishers.*

Recent progress in manufacturing nanometre structures in two-dimensional electron gas (2DEG) systems have made it possible to perform "electron-optics" experiments in solid state devices. [18] In an ideal device the motion of the electrons is not affected by interactions with impurities, phonons etc., i.e. the electrons travel ballistically, just as they would do in ultra-high vacuum. In real devices, typical distances for ballistic motion can be as large as $250\lambda_F$, λ_F being the Fermi wavelength of the electrons. [19] From the viewpoint of field-electron emission, motion in the vacuum region is replaced by ballistic motion in the solid. Just as for the electron-beam sources, it is of great interest to explore the possibility of focusing (collimating) electrons in the solid. [20] It has been demonstrated that magnetic fields [19–22] or an electrostatic lens [23] can be used to focus the electrons. Furthermore it has been argued [19, 24] that the rounding of the entrance/exit plane of a quantum point contact may act as a horn, leading to the collimation of the electron waves. It is important to recognize that electron waves emitted by atom-size tips are collimated to a much greater extent (a few degrees) than those produced by quantum point contacts. This is only partially due to the presence of the applied electric field which accelerates the electron when it emerges from the tip over a macroscopic distance.

Many important applications of optics heavily rely on the availability of sources that produce coherent and focused beams of light. Evidently, for a wide variety of applications, it is of great interest to have sources that emit coherent and focused beams of electrons. In this paper we present the results of a comprehensive computer-simulation study of various mechanisms to focus electrons emitted by extremely small sources.

2. Computer Simulation

By definition, a small source has an emission area of dimensions comparable to the wavelength (denoted by λ_F) of the particles it emits. A classical, "billiard-ball" treatment of the motion of the electrons is no longer valid. To explore the properties of electron transport through such small structures a proper, wave-mechanical, description is required. Our approach is to simulate the motion of the electron waves by numerically solving the time-dependent Schrödinger equation (TDSE) by means of an accurate and unconditionally stable numerical technique. [25] The TDSE approach is flexible in the sense that it can handle arbitrary geometries and potentials and therefore provides a unified framework to investigate and compare various focusing mechanisms. Incident waves were chosen to be Gaussians of width $6\lambda_F \times 6\lambda_F$, sufficiently large to mimic a plane wave front impinging on the emission area.

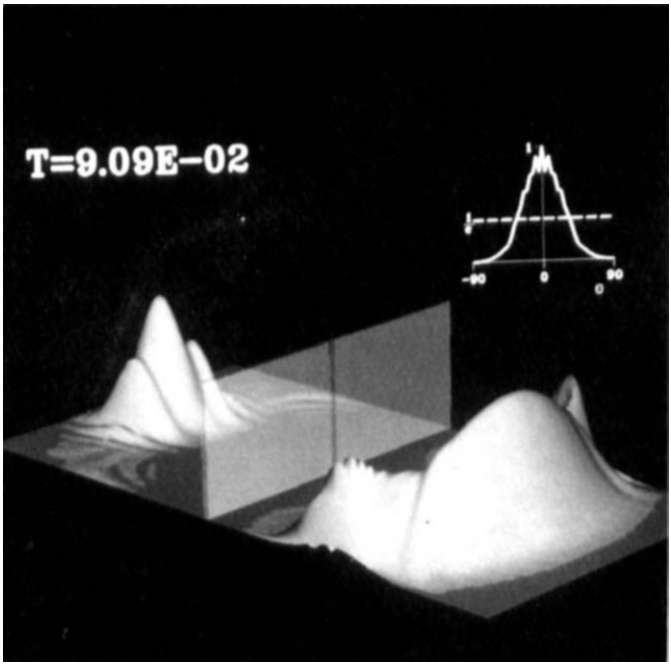

Figure 1. Intensity of the wave packet reflected and transmitted by a λ_F-wide aperture. The length of the constriction is λ_F. Also shown are the transmitted intensity T and the angular distribution of intensity of the transmitted wave. The angular spread $\theta_s \approx 35°$. The emitted beam is not focused.

The focusing capability of a source is characterized as follows. Imagine a wave, with a well-defined direction, wavelength λ_F and energy E_F, leaving the source. A detector is placed far away from the latter. The (normalised) transmitted intensity $P(\theta)$ recorded by this detector is plotted as a function of the angle (θ) with respect to the normal to the exit plane of the source. The angular distribution of intensity of the transmitted wave $P(\theta)$ is calculated by the method described in Ref.17. The collimation is characterized by determining the largest angles for which $P(\theta_{1,2}) = 1/e$. We define the angular spread $\theta_s \equiv |\theta_1 - \theta_2|/2$.

3. Computer Simulation results

The simplest model of a small source consists of a hard wall, reflecting the wave, with a small aperture in it. Such a constriction acts as a waveguide. Waves emerging from the small opening scatter strongly. This is illustrated in Fig.1 for

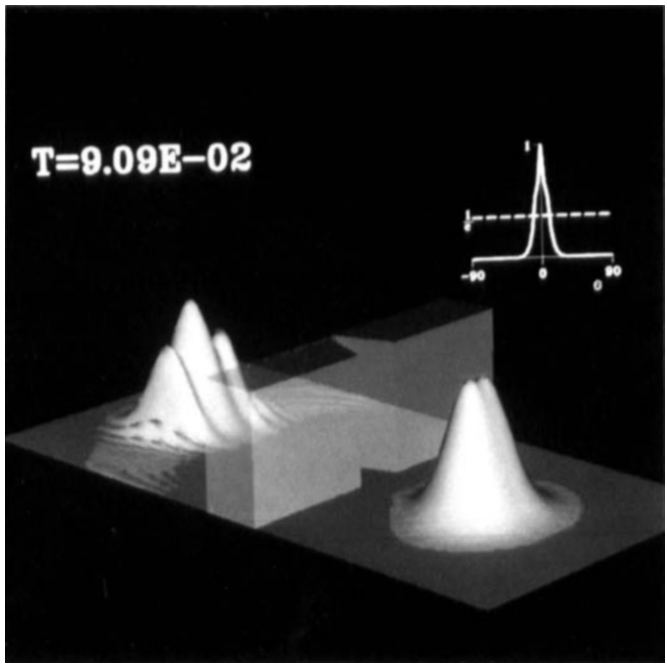

Figure 2. Intensity of the wave packet reflected and transmitted by a horn. The entrance plane is λ_F wide, the exit plane is $7.8\lambda_F$ wide, the constriction is $\lambda_F/2$ long and the total length of the device is $10\lambda_F$. Also shown are the transmitted intensity T and the angular distribution of the transmitted wave. The angular spread $\theta_s \approx 10°$.

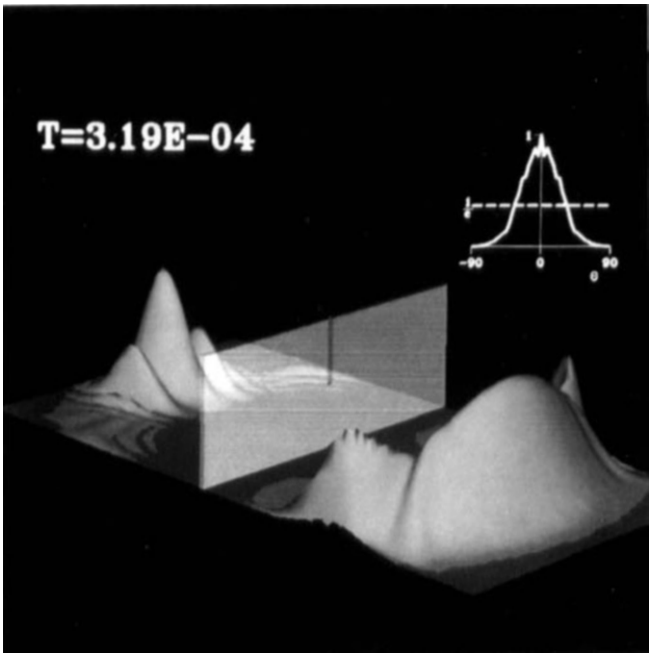

Figure 3. Intensity of the wave packet reflected and transmitted by a λ_F-wide aperture. The angle of incidence $\psi = 0°$. The length of the constriction is λ_F, the height of the potential barrier inside the constriction is $0.98E_F$. Also shown are the transmitted intensity T and the angular distribution of the transmitted wave. The angular spread $\theta_s \approx 35°$. The emitted beam is not focused.

the case where the direction of the incident wave packet ψ is perpendicular to the hard wall, i.e. $\psi = 0°$.

Gradually increasing the width of the opening in the hard wall yields a waveguide that looks like a horn. As illustrated in Fig.2 for the case of normal incidence ($\psi = 0°$), horns collimate waves but strong focusing requires relatively long horns. [17] This focusing mechanism is of secondary importance to the case of atom-size electron-emission tips.

It has been suggested [24] that a judiciously chosen potential inside a constriction can also provide a mechanism for focusing the wave. Table 1 demonstrates that this is not the case. A potential barrier inside the constriction does not focus the emitted wave but reduces its intensity. Comparing Fig.3 with Fig.1, it is clear that the presence of a potential inside the constriction does not lead to a change of the shape of the transmitted wave packet.

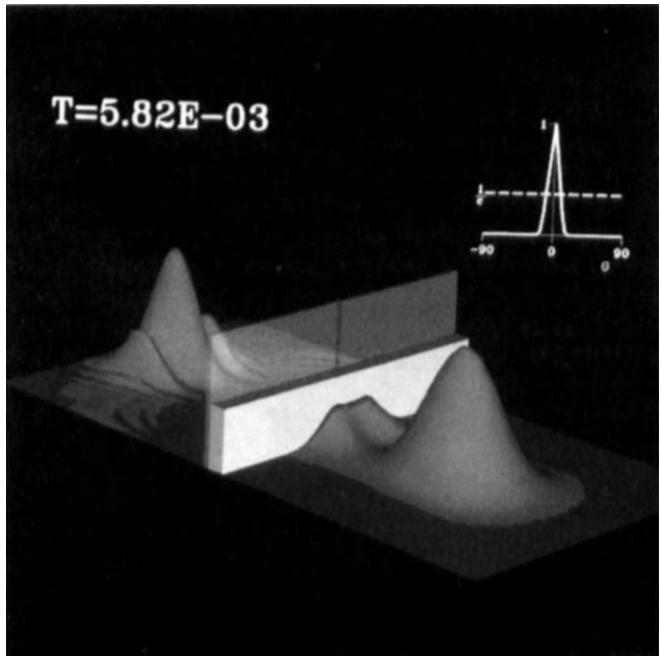

Figure 4. Intensity of the wave packet reflected and transmitted by a λ_F-wide aperture followed by a rectangular potential barrier. The length of the constriction is λ_F, the height and lenght of the potential barrier are $0.98E_F$ and $3\lambda_F$ respectively. The angle of incidence $\psi = 0°$. Also shown are the transmitted intensity T and the angular distribution of the transmitted wave. The angular spread $\theta_s \approx 10°$. The emitted beam is focused.

Table 1. Influence on the angular spread θ_s of the presence of a constant potential V inside a single λ_F-wide constriction. The angle of incidence $\psi = 0°$.

V/E_F	θ_s
0.00	$34° \pm 4°$
0.75	$34° \pm 4°$
0.98	$33° \pm 4°$
1.00	$34° \pm 4°$

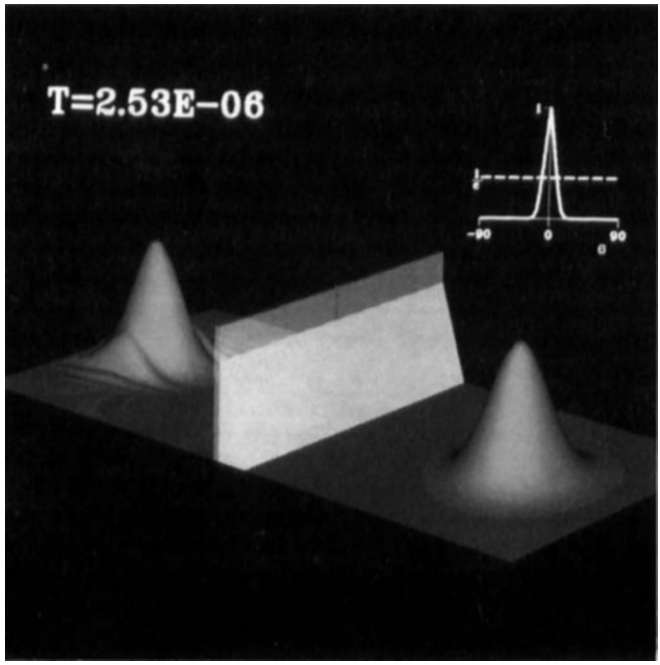

Figure 5. **Intensity of the wave packet reflected and transmitted by a** λ_F-wide aperture followed by a triangular potential barrier. The length of the constriction is λ_F, the height and lenght of the potential barrier are $1.5E_F$ and $5\lambda_F$ respectively. The angle of incidence $\psi = 0°$. Also shown are the transmitted intensity T and the angular distribution of the transmitted wave. The angular spread $\theta_s \approx 7°$. The emitted beam is strongly focused.

However, as shown in Fig.4 a rectangular barrier placed behind the constriction focuses the emitted wave at the cost of transmitted intensity. Long barriers of height slightly lower than the energy of the incident wave have optimal focusing properties and high efficiency.

The angular distribution of waves emitted by strongly focusing sources does not change much if the angle of incidence of the incident wave is varied. Comparing the simulation for the model used in Fig.4 for an angle of incidence of $\psi = 20°$ (not shown) instead of $\psi = 0°$, the outgoing waves only differ in the total transmitted intensity. The angular distributions are almost identical.

The simplest two-dimensional model of a single-atom tip consists of a constriction (the atom) followed by a triangular barrier (the metal-vacuum potential). Experimentally, the triangular barrier is higher than the energy of the waves inside the source. To leave the source the electron has to tunnel through the barrier. Fig.5

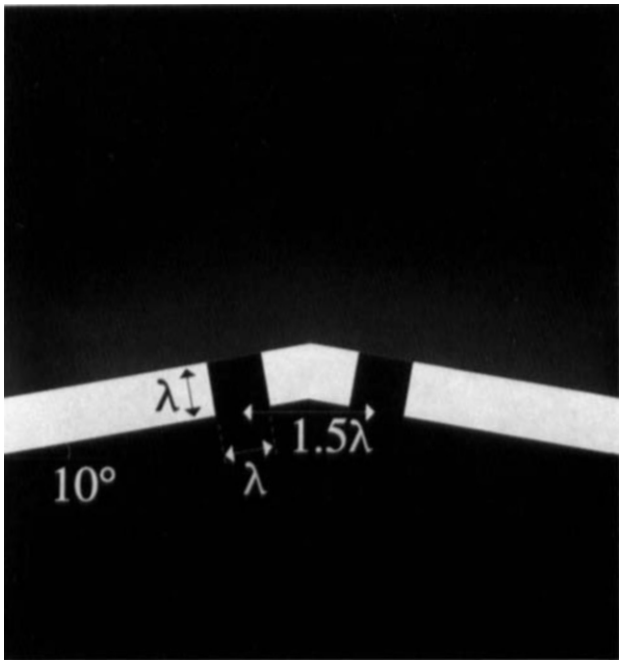

Figure 6. Two-dimensional model of a blunt tip. The white area represents a hard wall, the two openings in it the two emitting atoms. The blue-colored region indicates the triangular potential barrier.

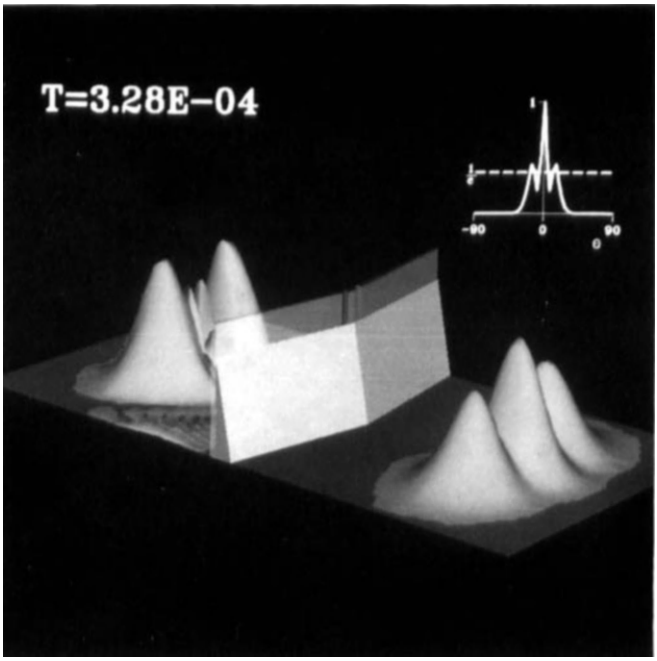

Figure 7. Intensity of the wave packet reflected and transmitted by the blunt tip shown in Fig.6. The angle of incidence $\psi = 0°$. Also shown are the transmitted intensity T and the angular distribution of the transmitted wave. The two waves emitted by the two atoms merge to form one wave packet.

demonstrates that tunneling is a very effective focusing mechanism but strongly reduces the intensity of the emitted beam.

Electron emission from three-atom tips crucially depend on the geometry of the tip. Simulations using two-dimensional models for these tips illustrate that the emission characteristics of a blunt and sharp tip are completely different. A two-dimensional blunt tip is modeled by a slightly deformed potential of two parallel constrictions (the two atoms) followed by a triangular barrier. A schematic diagram of the source is shown in Fig.6. The simulation result for the blunt tip, shown in Fig.7, illustrates that the two wave packets emerging from the two openings, merge to form one wave. According to the angular distribution on a screen placed far away from the source, this wave would give rise to a central spot and some background intensity, in qualitative agreement with experiment. [11] Further deformation of the potential modeling the blunt tip yields a potential representing a sharp (teton) tip. The schematic layout of this source is depicted in Fig.8. The wave packets emitted by this source differ considerably from those produced by the blunt tip.

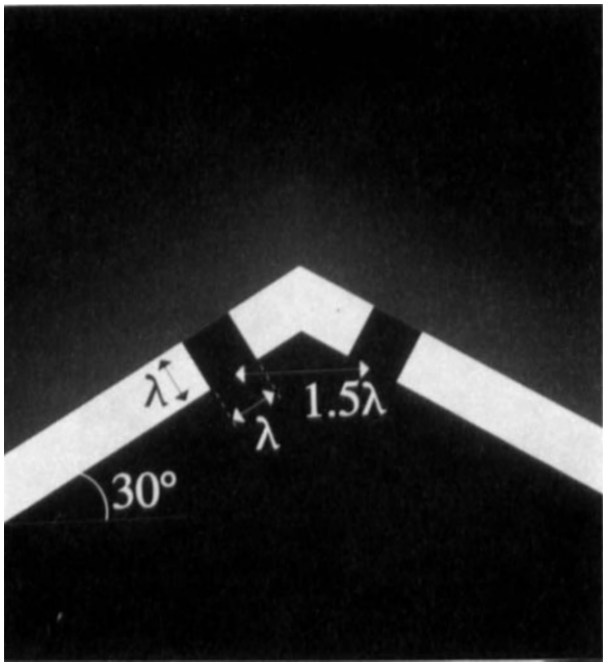

Figure 8. Two-dimensional model of a sharp tip. The white area represents a hard wall, the two openings in it the two emitting atoms. The blue-colored region indicates the triangular potential barrier.

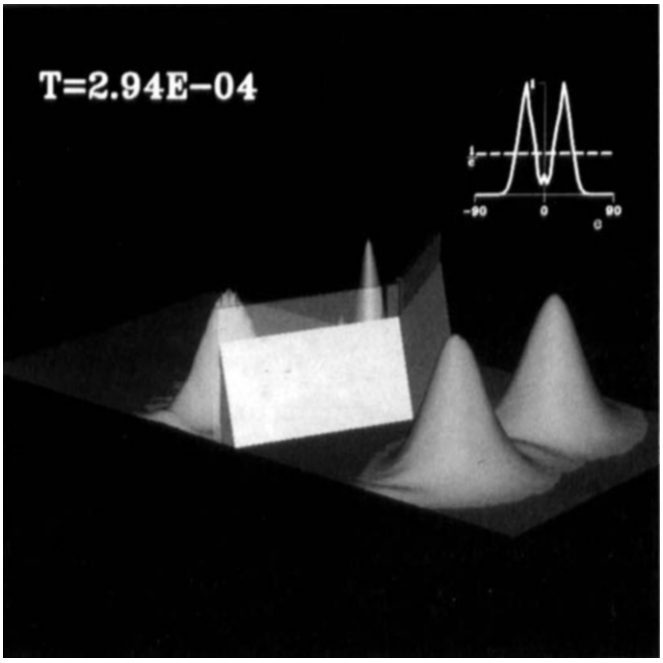

Figure 9. Intensity of the wave packet reflected and transmitted by the sharp tip shown in Fig.8. The angle of incidence $\psi = 0°$. Also shown are the transmitted intensity T and the angular distribution of the transmitted wave. The two coherent waves emitted by the two atoms do not merge. This source incorporates a beam splitter.

Indeed, Fig.9 shows that the sharp tip acts as a beam splitter, emitting two coherent electron waves. In absence of a triangular barrier, the properties of the emitted wave do not resemble those of a sharp tip, as illustrated in Fig.10. The potential barrier is the basic mechanism responsible for producing focused and well-separated but coherent waves.

This work is partially supported by the Stichting voor Fundamenteel Onderzoek der Materie (FOM), which is financially supported by the Nederlandse Organisatie voor Wetenschappelijk Onderzoek (NWO), a supercomputer grant of the NCF (The Netherlands), and the EEC Science Plan contract SC1-0395-C (MB).

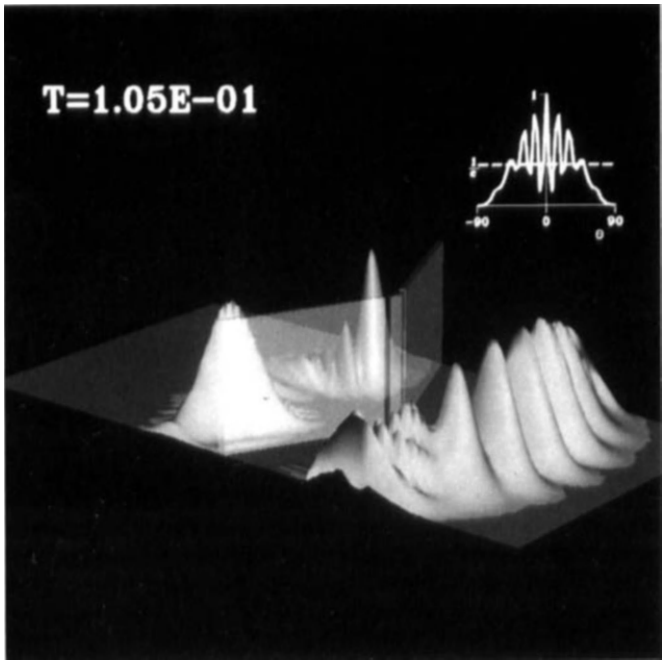

Figure 10. Intensity of the wave packet reflected and transmitted by the sharp tip shown in Fig.8, in the absence of the triangular barrier. The angle of incidence $\psi = 0°$. Also shown are the transmitted intensity T and the angular distribution of the transmitted wave.

References

1. H.-W. Fink, IBM J. Res. Develop. **30**, 460 (1986)
2. H.-W. Fink, Phys. Scr. **38**, 260 (1988)
3. Vu Thien Binh and J. Marien, Surface Science **102**, L539 (1988)
4. Vu Thien Binh, J. Microscopy **152**, 355 (1988)
5. D. Gabor, Proc. Roy. Soc. London **A454**, 197 (1949)
6. D. Gabor, Proc. Roy. Soc. London **B64**, 449 (1951)
7. A. Tonomura, Rev. Mod. Phys **59**, 639 (1987)
8. H. Lichte, Ultramicroscopy **20**, 293 (1986)
9. F.G. Missiroli, G. Pozzi, and U. Valdre, J. Phys. E **14**, 649 (1981)
10. N. García, J.J. Sáenz, and H. De Raedt, J. Phys.: Condens. Matter **1**, 9931 (1989)
11. J.J. Sáenz, N. García, Vu Thien Binh, and H. De Raedt, *Scanning Tunneling Microscopy and Related Methods*, edited by R.J. Behm et al, (Kluwer Academic, Dordrecht, 1990).
12. N.D. Lang, A. Yacobi and Y. Imry, Phys. Rev. Lett. **63**, 1499 (1989)
13. L.I. Glazman, G.B. Lesovik, D.E. Khmel'nitskii, and R.I. Shekhter, Sov. Phys. JETP. Lett. **48**, 238 (1988)
14. A. Yacobi, and Y. Imry, Europhys. Lett. **11**, 663 (1990)
15. A. Yacobi, and Y. Imry, Phys. Rev. B **41**, 5341 (1990)
16. E. Tekman, S. Ciraci, and A. Baratoff, Phys. Rev. B **43**, 7145 (1991)
17. K. Michielsen and H. De Raedt, J. Phys.: Condens. Matt. **3**, 8247 (1991)
18. H. van Houten, C.W.J. Beenakker, and B.J. van Wees, *Semiconductors and Semimetals*, edited by M.A. Reed, (New York, Academic 1990).
19. H. van Houten et al., Phys. Rev. B **39**, 8556 (1989)
20. S. Washburn, Nature **343**, 415 (1990)
21. H.U. Baranger, and A.D. Stone, Phys. Rev. Lett. **63**, 414 (1989)
22. H. van Houten, C.W.J. Beenakker, J.G. Williamson, M.E.I. Broekaart, P. van Loosdrecht, B.J. van Wees, J.E. Mooij, C.T. Foxon and J.J. Harris, Phys. Rev. B **39**, 8556 (1989)
23. U. Sivan, M. Heiblum, C.P. Umbach and H. Shtrikman , Phys. Rev. B **41**, 7937 (1990)
24. C.W.J. Beenakker and H. van Houten, Phys. Rev. B **39**, 10445 (1989)
25. H. De Raedt, Comp. Phys. Rep. **7**, 1 (1987)

NANOTIP FASHIONING AND NANOSOURCE CHARACTERISTICS

Vu Thien Binh [a], N. Garcia [b], S.T. Purcell [a] and V. Semet [a]
[a] *Département de Physique des Matériaux, UA CNRS*
Université Claude Bernard Lyon 1. 69622. Villeurbanne. France
[b] *Departamento de Fisica de la Materia Condensada,*
Universidad Autonoma de Madrid. 28049. Madrid. Spain

ABSTRACT. The fabrication by surface diffusion of tips with controlled nanoscale structures are described. Using surface diffusion, ball-shaped tips and tips with filiform-neck are obtained. Ball-shaped tips can be used for quantitative atomic force measurements. Tips with filiform-necks can be used as nano-cantilevers with extremely low spring constants and very high resonance frequencies. The field-surface-melting mechanism, which occurs under the combined use of high temperatures and high applied fields, leads to the fashioning of nanoprotrusions ending in one atom. The strong confinement of the field over the topmost atom of the protrusions allows these nanotips to be single-atom sources of electrons and metallic ions. The corresponding emitted beams present properties specific to the atomic dimension of the sources. The electron energy distribution and local heating during field emission from such tips are reported and discussed.

1. Introduction

The structuring and study of materials on a nanoscale require tools and probes also of nanoscale dimensions. The tools must be manipulated by macroscopic systems, and thus they are mostly macroscopic tips ending with controlled nanoscale structures. We refer to such tips as nanotips. Controlled fashioning of nanotips at atomic level precision can be done by a great variety of mechanisms. Among these is surface diffusion. It is the main mechanism we have used for manipulating the atoms in order to create nanoscale geometries.

In this article we review how the nanoscale constructions can be made by surface diffusion under capillary and applied field gradient driving forces. This can be used to create nano-cantilever tips on one hand, and on the other hand, to reproducibly form nanoscale teton tips ending in one atom.

The nano-cantilever tips could be used in atomic force microscopy (AFM) and the teton tips act as sources of self-collimated beams of electrons or metallic ions. The properties of these field-emitted ultra-fine beams are analyzed and related to the atomic size of the sources.

The uses of the nanotips, such as probes for AFM, metallic sources for nano-deposition, and highly coherent ion and electron beams for new analytical systems, are discussed in correlation with the other contributions to the meeting.

V.T. Binh et al. (eds.),
Nanosources and Manipulation of Atoms Under High Fields and Temperatures: Applications, 59–76.
© 1993 *Kluwer Academic Publishers.*

2. Surface diffusion mechanisms.

The fashioning of nanocrystals by surface diffusion mechanisms means a morphological modification by mass transport of the surface atoms. The surface diffusion transport flux, J, is governed by the surface diffusion coefficient and the applied driving force [1]. This is described by the Nernst-Einstein relation:

$$J = -\frac{n D}{k T} \text{ grad } (\mu) \qquad (1)$$

where n is the concentration of surface diffusing atoms, D is the surface diffusion coefficient, k is the Boltzmann constant, T is the temperature and grad (μ) represents the driving force.

Equation (1) shows how J can be controlled by the temperature and applied field, F. The temperature influences J through the concentration of adatoms, n. The surface diffusion coefficient is dependant on the temperature and F through it's influence on the activation energy. Due to surface screening of metal surface and polarization of the surface atoms, F reduces the activation energy for surface diffusion of the surface atoms [2].

The driving force controls the direction of the flux of the surface atoms. Among different possibilities, we have chosen to use the capillary and the field strength gradient as driving forces to control the shape evolution of the tips at the atomic scale during the fashioning process. The capillary force moves atoms from regions of high curvature to regions of lower curvature. In presence of an electric field gradient, the atoms move from regions of low fields towards regions to high fields.

Thus three parameters - T, F and initial tip geometry - are used to shape the tip towards the desired geometry.

3. Fashioning using temperature and tip geometry.

3.1. BALL-TIPS

The evolution of the tip shape, when heated in vacuum without applied electric field, is basically governed by the surface diffusion law (Herring's law) [1]. The surface atoms, at high temperatures, move from regions of high curvature towards regions of low curvature in order to minimize the total energy of the system. For a conical tip with an angle greater than 6°, the surface diffusion will blunt the tip, but for small angle tips (< 6°) a constriction will develop just under the apex region. The diameter of this constriction will decrease with the heating time, ending in the detachment of a solid drop. This has been studied theoretically and confirmed experimentally [3,4]. In Fig. 1(a) we show the morphological evolution in 3D of a 0° angle tip calculated by using only the surface diffusion law. Experimentally, by stopping the heating before the detachment of the solid drop, we can then obtain a stable tip presenting a nearly spherical ball at its end: a "ball-tip". Fig. 1(b) is a scanning electron microscopy image of Cu ball-tips obtained by heating under vacuum. The dimension of the solid drop will depend on the initial dimension of the tip, but it is usually around a few hundreds of nanometers. The differences that exist between the experimental profiles and the calculated ones could be explained by extra experimental conditions (uniformity of the heating along the tip, base vacuum pressure, etc.). However, it is important to note that the basic features of solid drop formation is governed by the surface diffusion law. The fabrication of such a tip is then reproducible and available for any material.

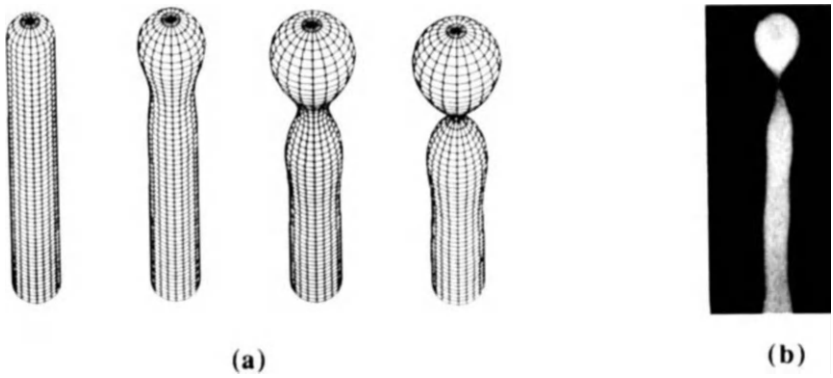

Figure 1. (a) Computer simulation using Herring's law of the evolution of a ball-tip during heating. (b) Scanning electron microscope image of a Cu ball-tip formed in vacuum.

Goodman and Garcia [5] have presented a theory for van der Waals (vdW) force acting on spherical body due to the presence of a dielectric surface and its effects on cantilever displacements used in AFM [6] . This theory is exact for spherical bodies and therefore should be used only with spherical tips. We therefore propose to use the ball-tips for AFM experiments when quantitative determinations of the analysis are required. It could be argued that the model described in reference 5 for a spherical tip is not the geometry of the tips presented in Fig. 1 due to the neck which connects the ending ball and the shank. However, the mass of the neck is negligible compared to the ball and the neck is farther away from the sample than the ball for any possible configuration between the tip and the surface. Therefore, the neck has negligible contribution to the vdW forces and ball-tips are quite good experimental approximations of a spherical tip [7].

3.2. NANO-CANTILEVER TIPS

By introducing a differential evaporation at the neck region, the morphological evolutions lead to the formation of a filiform neck. This means that the constriction region could have typical length of 200 to 400 nm with a section of 10 to 20 nm. The fabrication of these nanostructures strictly obeys thermodynamic laws and is therefore reproducible. Numerical simulations taking into account evaporation and surface diffusion give, under certain conditions, the formation of filiform necks. This is exemplified by the calculated tip form displayed in Fig. 2(a). Examples of the experimental realizations of such tips are presented in Fig.2(b-c).

As a nanotool, such a tip could be used as a very sensitive AFM sensor. The neck would be a cantilever, and due to its very small dimensions, in particular the masses, the mechanical characteristics of this nano-cantilever could be very specific. As a first approximation, by using the classic equations given for a macroscopic cylindrical cantilever [8], we have estimated the spring constant, k, and the resonance frequency, ω_0, of the nano-cantilever. The values obtained give for values of k from 0.05 N/m to 100 N/m, with a resonance frequencies varying from ~10^7 Hz to ~10^8 Hz. The combination of such low values for k and high values for ω_0, exists only in the case of the nano-cantilevers.

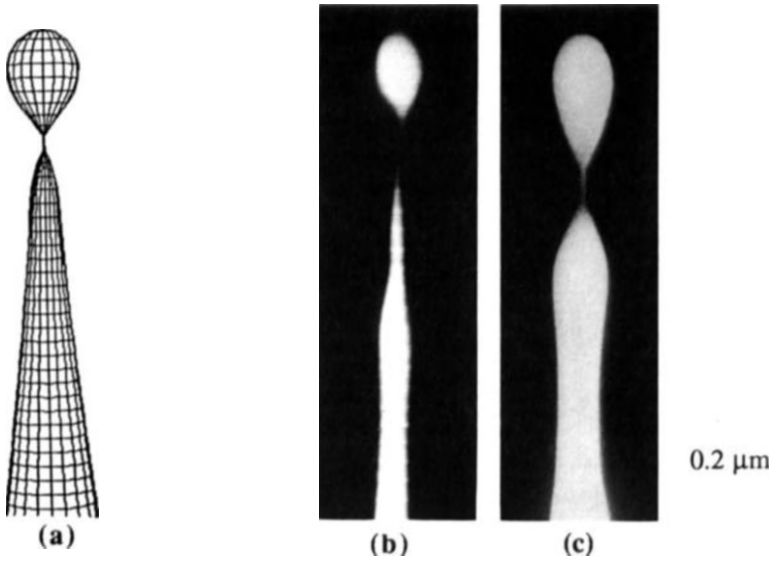

Figure 2. (a) Computer simulation of a nano-cantilever tip; (b-c) Scanning electron microscope images of different W nano-cantilever tips formed in vacuum.

4. Fashioning using temperature and electric field.[9]

4.1. FIELD-SURFACE-MELTING MECHANISM.

A metallic surface very effectively screens an applied electric field so that even for large fields the second layer of atoms does not feel the field. This can lead to important consequences. One of them is to produce surface melting at temperatures T much smaller than the bulk melting temperature T_m. To control field-surface-melting we have two parameters, T and F. T acts over the whole body, while F acts only on the surface atoms and reduces the activation barrier for surface diffusion. The effect of such a reduction was seen in early experiments and was attributed to permanent and induced dipoles in the surface atoms [2]. These effects have been used to produce built-up tips [10,11] due to the driving forces of the applied field and its gradient on the surface dipoles.

For a perfectly flat surface the effect of the field on the reduction of the activation barrier for surface diffusion is negligible even at very large fields. The reason is that the dipole induced by the applied field is small. However, if the surface is rough with adatoms, vacancies, kinks, steps, etc., the values of the permanent dipole moments are different at each point. This difference is enhanced by the spreading out of the surface charge first discussed by Smouluchowski [12]. The action of the field is then enhanced on the protruding parts of the surface. Two different behaviors could be expected. First, if for a particular T the number of defects is small, adatoms on facets will have a more reduced activation barrier for surface diffusion than other defects, with the consequence of smoothing out the surface roughness. It tends to increase the low index facets during the build-up mechanism. Second, if the surface is rougher with a large number of defects, the reduction of the activation barrier will be more important leading then to a higher surface

diffusion coefficient D. This can lead to "field-surface-melting", when D becomes large [13,14], at a temperature much lower than the bulk melting temperature. There is also a concomitant increase of the height of some existing protrusions due to the field gradient driving force over corrugations. The geometry of a nano-protrusion formed under these conditions, which could end in one atom, is then determined by the equilibrium between the pulling-out by the field gradient force and its blunting due to the capillary force. Furthermore, due to the field enhancement at the top of the protrusion [15] the probability to field evaporate the topmost atom is larger for a given value of the applied voltage to the tip. The combination of field surface melting (for atom supply) and local field evaporation can then produces stable atomic metallic ion emission (AMIE) from these nano-protrusions (see section 4.2). By fast freezing the tip at LN one can stabilize the nano-protrusion which is ended in one atom (see section 4.3). These nanotips are then single atom sources of electrons and gaz ions (see section 6). These processes are schematically represented in Fig 3.

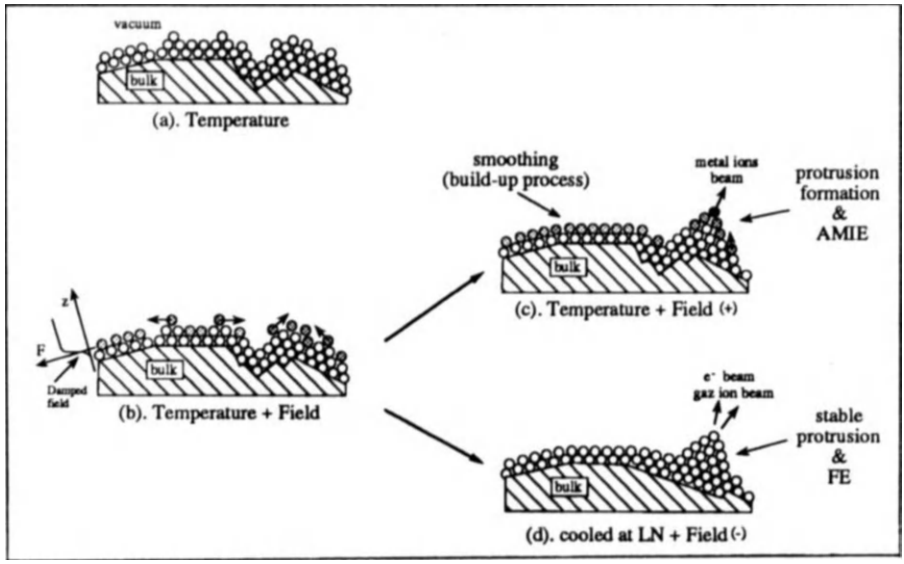

Figure 3. Schematic processes taking place at the tip under applied field and temperature.

4.2. EXPERIMENTAL STUDIES OF ATOMIC METALLIC ION EMISSION (AMIE).

We proceed by varying the applied potential V (and therefore F) and T to obtain AMIE. For W<111> tips, at 1200 K and 4 kV (F~1.2 V/Å) the AMIE started along the edges of {112} facets that follow the symmetry directions of the <111> axis. These spots can move only along these curved edges proving that the surface melting is localized along the corresponding lines. By further increasing T and V to 1500 K and 5 kV (~1.5 V/Å), we observed that the spots were then located at any point of the surface of the vicinal zone joining the facets. For higher temperatures the spots can move over the whole surface. The AMIE is reproducible and exists within a range of 1200 K to 1500 K and 4 kV to 6 kV (1.2 V/Å to 1.8 V/Å). For the lower temperatures the position of the spots are quite stable. The intensity of the emitted beams is approximately ~10^5 ions/s with the beam opening

angle of ~2°. By fast freezing the tip at liquid nitrogen and using FEM and FIM, the emitting structures can be visualized with atomic resolution. In Fig. 4(a) we present an AMIE image and the corresponding FEM and FIM images. The FIM image is composed of three sharp spots at the positions of the AMIE and FEM spots. This clearly shows that the emitting structure ends in a single atom. We have digitized the data to provide a 3D map of the emission intensity. The superimposition of the three distributions is shown in Fig. 4(b), and this confirms the association of the ion emission with the protrusions. The spot widths of ~2° and ~4° for ion and electron emissions respectively, are similar allowing for differences in T and F. The same behavior is observed experimentally with Au tips at 350 K and for applied voltage around 3.2 kV (~0.7 V/Å).

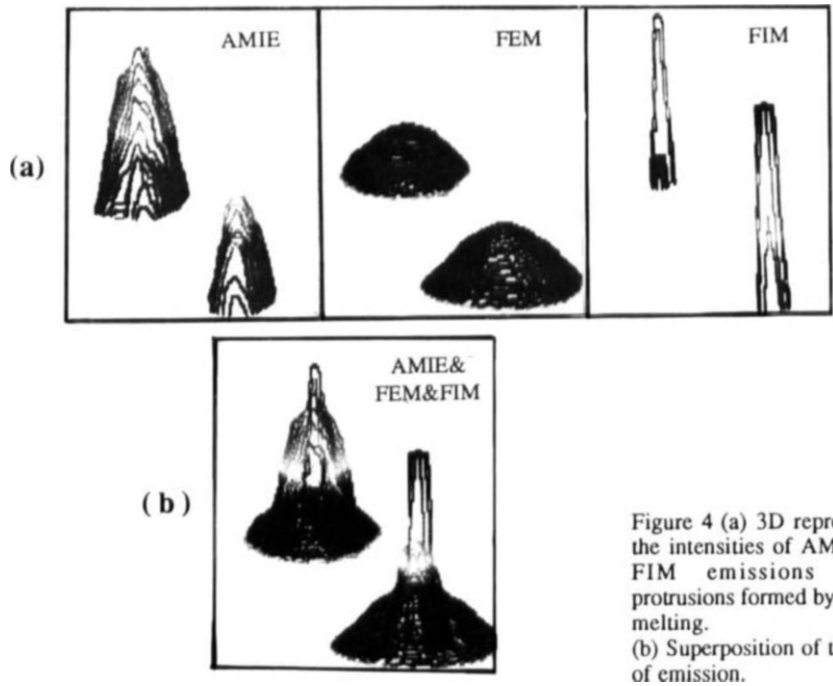

Figure 4 (a) 3D representations of the intensities of AMIE, FEM and FIM emissions from two protrusions formed by field-surface-melting.
(b) Superposition of the three types of emission.

4.3. TETON TIPS

To observe the 3D structure of the protrusions, we use field ion microscopy and field evaporation at LN to remove the different successive top layers. In Fig. 5, a sequence of four FIM frames for successive field evaporated layers is shown. The first two frames show the very first atom at the top of the protrusion and the three atoms underneath respectively. The last frame shows the structure of the protrusion near its base. It can be clearly seen that the pyramidal-like protrusion ends in one atom with dimensions estimated to about 2 nm base and height of 2 nm by counting the layers. These pyramidal structures meet at their bases in surface boundaries as revealed by further field evaporation. The four frames in Fig. 5 show an interesting point. The first layers of the protrusions are poorly ordered (frozen liquid) while the lower layers show higher order (crystalline solid).

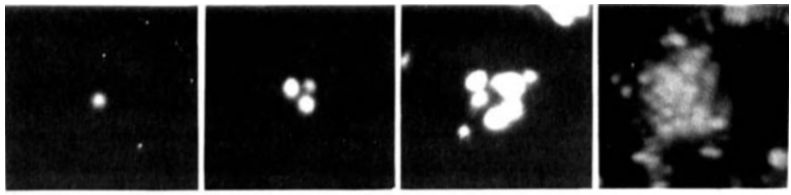

Figure 5. Successive FIM images of a teton tip at different stages of the removal of the upper atomic layers by field desorption.

5. Single-atom sources.

5.1. FIELD CONFINEMENT.

The presence of a nanoprotrusion on top of the support tip leads to a local field enhancement and confinement due to the distortion and compression of equipotentials in the apex vicinity. This distortion leads to a bunching of the lines of force resulting in a higher local magnification. In field electron emission this exceeds the magnification due to the support tip [16]. A 3D calculation of the potential and field distributions on the atomic scale of the teton tips has been made by minimizing the electrostatic energy of the tip-screen system. This system is a complex capacitor consisting of an hyperboloïd and a pyramid of spheres which are respectively the support tip and the atomic construction of

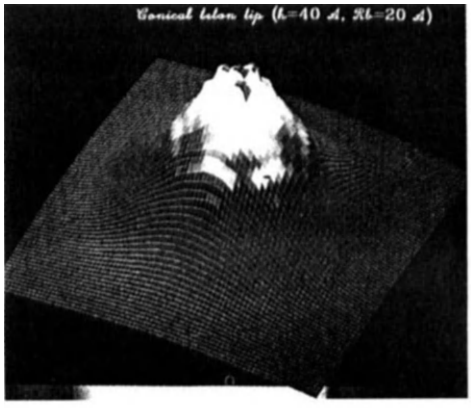

Figure 6. 3D representation of the calculated field distribution over an equipotential surface for a teton tip ending in one atom [15].

the nanoprotrusion, all at the same potential, and a plane at another fixed potential which represent the screen [15]. The results show the confinement of the field over the topmost atom of the protrusion, as is illustrated in Fig. 6. This confinement over the topmost atom allows teton tips to be single-atom sources for electrons and ions.

5.2 FIELD EMISSION ELECTRON SPECTROSCOPY

Measurement of the total energy distributions (TED's) of the field-emitted electrons gives insight into the field emission process including the tunneling barrier, the electronic structure of the tip material and the energy exchanges during emission. We have used this technique to study the differences between macroscopic and single atom sources of electrons.

The experimental setup and procedure has been described previously [17]. We have measured the TED's through a probe hole with a hemispherical energy analyzer. Measurements were made of the emission from different nanoscale protrusions formed along the main axis of a W <111> single-crystal. Control measurements were also made of the macroscopic tip without the protrusions just previous to protrusion formation and after their destruction. The protrusions were formed in ultra-high vacuum by the combined action of field and temperature using the field-surface-melting process [9].

We start by showing the TED's of the macroscopic tip in order to elucidate the well-established picture of field emission and to use this picture in comparison with the TED's of nanotips. Two example spectra, measured after the destruction of a protrusion, for different values of the applied voltage are presented in Fig. 7. The two spectra have the same general shape, are located at the same Fermi level (E_F), and show the well-known behaviors for clean W<111> tips [18]. One strong peak was observed with a sharp edge at E_F for any V_{App}. An increase of V_{App} did not change the position of the Fermi edge, only causing a broadening of the peak on the low energy side. The two spectra were fitted with the the classic equation for the tunneling current from a free electron metal which was developed by Young [19]. The fits are represented by the solid curves over the experimental points. The value of E_F for macroscopic tips was constant for all temperatures and applied fields. This was then taken as the reference level for all the spectra. The temperatures

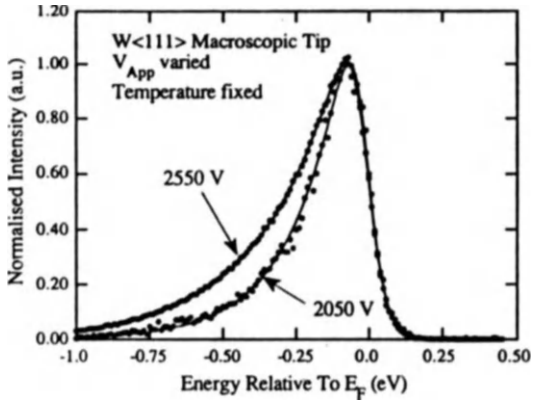

Figure 7. TED Spectra of a macroscopic tip for two V_{App} showing a broadening of the low energy side.

found by the fitting were in agreement with the known values. It is useful to note that the low energy side of the TED is controlled by the tunneling barrier and that the high energy side is controlled by the temperature because it is a reflection of the Fermi Dirac distribution. Thus the tunneling barrier and temperature can be studied independently.

In Fig. 8 we present TED spectra recorded for different V_{App} after formation of a protrusion on top of the macroscopic tip. Four features which are present for the spectra of

all nanotips at fixed temperature, and which are not present for macroscopic tips, can be discerned in the experimental observations:

- (1) The spectra are composed of well-separated peaks. In the presented example of Fig. 8 there are two peaks, labelled (a) and (b). Peak (a) is near E_F and peak (b) ~1.1 eV lower in energy. In general, the number of peaks and their relative intensities depend on the protrusion geometry and on the V_{App}. We return to point later in this section.
- (2) A linear shift of the whole spectrum is observed as a function of V_{App}. This can be seen by the two sets of spectra shown in Fig. 8. In Fig. 9 we plot the positions of the peak maxima as a function of V_{App}. All the data fall on parallel lines, with slopes of

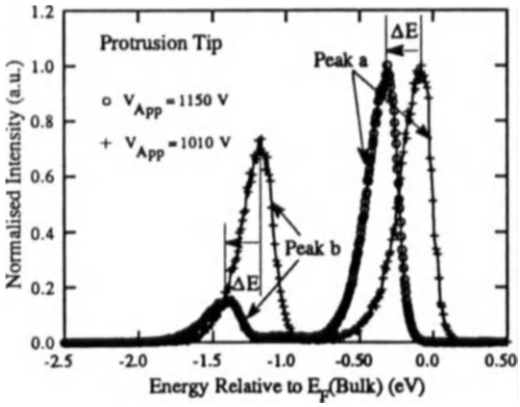

Figure 8. TED spectra of single-atom protrusion tip for two different V_{App} with the corresponding shift.

1.65±0.02 meV per applied Volt, showing that the separation between the peaks remains constant. The total shift of the peaks for the range of V_{App} in this experiment was ~0.7 eV. Note that no shift was detectable for macroscopic tips and for similar changes of V_{App}.

- (3) The shapes of the peaks vary little with V_{App}. The FWHM's are plotted in Fig. 10 for both a macroscopic and protrusion TED's. The slight increase in the FWHM's of the nanotips is due mostly to an increase in temperature (see section 6).
- (4) The peaks did not fit the Young equation. Firstly their position is not fixed at E_F. One can try to fit with the same functional form by replacing E_F with a variable energy which fixes the band position of the individual peaks. The peaks are then fitted well over the central portion but rather poorly on the tails. Such fitting does not correctly follow the increase in applied field because the FWHM's are almost field-independent. However, the temperature found from the fits, which is basically determined by the slope of the peaks of the TED's on the high energy sides, was in all cases the correct value (see section 6).

The shifts and the intensity variations of the peaks were reversible; they could be varied reproducibly by changing V_{App}. For clean single-atom protrusion tips, stable FEM patterns and FEES spectra with constant FE intensities were observed over a period of many hours. Presence of adsorption from the background gases on top of the protrusion was easily characterized by large instabilities of the emission current and strong modifications of the TED's. The adsorption could be removed by application of field and temperature after which the emission properties were again stable. The FEES spectra could be the same as before the cleaning or show changes in the positions, number and relative intensities of peaks for the same V_{App}, probably reflecting a different structure in the geometry of the protrusion.

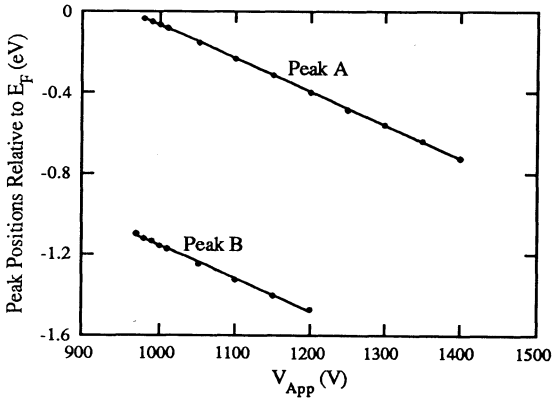

Figure 9. Positions of the peaks of Fig. 3 versus V_{App}. The slope of the lines are 1.65 ± 0.2 meV/V

The existence of the well-separated peaks in the single-atom TED's show that the electrons do not tunnel directly from the bulk Fermi level to the vacuum. The peaks suggest the presence of a localized band structure at the tip apex. This idea is supported by the constant spectra widths and energy gaps observed experimentally. The peaks in the TED spectra would then occur because the emitted electrons resonantly tunnel *only* through these bands.

Resonant tunneling through atomic energy levels of adsorbed atoms, which have been broadened due to interaction with the underneath surface, has first been introduced by Duke and Alferieff [20] and later developed more fully by Gadzuk [21]. This was used to explain the small bumps added to the energy distributions of the clean macroscopic tips observed in earlier FEES experiments [22] with chemisorbed atoms on metallic surfaces. It must be emphasized that the presence of chemisorbed atoms in these experiments only slightly modified the standard peak of a clean macroscopic tip, in contrast to the spectra from the protrusions which consist solely of well-defined peaks. This latter behavior could have its origin in the atomic size and shape of single-atom protrusion tips, and in particular on the reduced coordination number of the atom that constitutes the apex compared to a single atom on a surface.

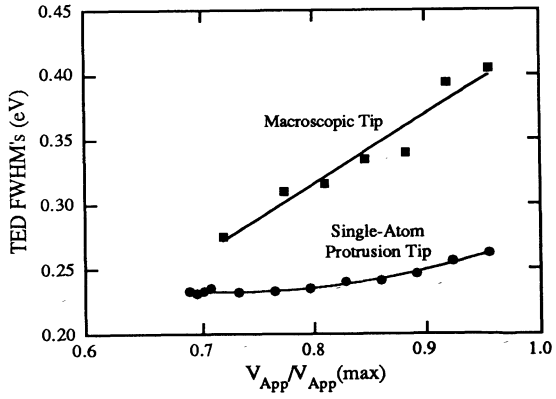

Figure 10. FWHM's of TED's from macroscopic and protrusion tips versus V_{App}.

The shifts of the peaks run counter to a metallic behavior of the topmost atom. The linearity of the shifts versus V_{App} (fig.4) means linear shifts versus applied field F at the cathode surface because $F = \beta V_{App}$. β is a geometrical factor that depends on the tip shape [23]. We propose to explain this shift and its linearity versus the applied voltage by a charge confinement in the region of the topmost atom, which implies a field penetration into the tip. It is worth pointing out that this result also implies a linear response of the tip apex to applied field for rather large values of applied field.

The charge confinement and the penetration of the field can be estimated by the Thomas-Fermi model of screening [23,24]. To our knowledge, there are no calculations which give the screening for a conical protrusion geometry. Therefore, to estimate field penetration x_0 for the protrusion we use, as a first approximation, the expression for the potential of the electric field penetration into a flat subsurface region:

$$V_F = x_0 F \exp(-\frac{r}{x_0}) \qquad (2)$$

where r is the distance from the surface to a position within the cathode. Thus the energy of the emitted electrons (r=0) varies linearly with V_{App} as:

$$\Delta E = e\, x_0\, \beta\, V_{App}. \qquad (3)$$

by taking into account the relation between F and V_{App}. e is the electron charge.

Applying eq. (3) to our experimental results of $\Delta E / V_{App} = 1.65$ meV/V and taking β as 5 to 10 $x10^6$ m^{-1} for a protrusion of 2 to 3 nm height [15], gives x_0 of 2-3 Å for the single-atom protrusion. This value should be compared to the screening length of a metal surface.which is less than 0.5 Å [23] and also with the estimation of field shift with single adsorbed Ba which is 1.3 to 1.7 Å [22]. It is also roughly the dimension of an atom and this strongly supports the idea that the observed peaks in the TED spectra are related to localized levels at the topmost atom. This estimate of x_0 is also in agreement with the fact that we can field evaporate the protrusion atom by atom [9].

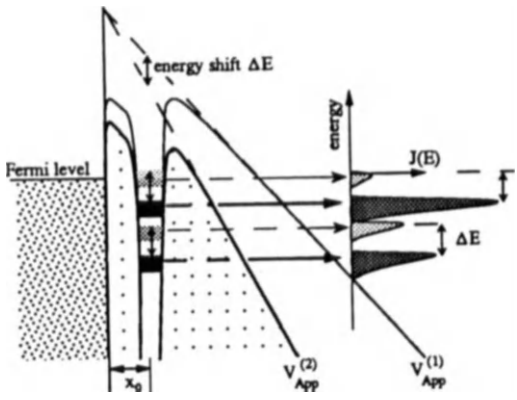

Figure 11. Simplified model of FE from single-atom tips for two V_{App}. The lightly-shaded bands signify the positions of two bands for $V_{App}^{(1)}$ and the two darkly-shaded bands are the same bands after they were shifted by increasing $V_{App}^{(1)}$ to $V_{App}^{(2)}$.

To illustrate the above hypothesis, a model for tunneling from the single atom protrusion tip is presented in Fig. 11, which shows the one-dimensional potential energy diagram in the presence of an applied field. The band structure, the field penetration, the band-shifting and the TED for field emission are all depicted. Many of these features are similar to a semiconductor, except they pertain only to the topmost atom of the protrusion.

It would appear that the model implies that a band which is significantly lower in energy than another, such as for peak (b) of Fig. 8 would have a vanishing small intensity due to the much larger tunneling barrier. However, bands with lower energy may originate from levels whose wavefunctions have greater spatial extensions. That is, a lower level may extend further into the vacuum and thus have a smaller effective tunneling barrier.

As stated above, the TED's for different protrusions vary in the number of peaks, the peak width's and relative intensities. This is a reflection of the influence of the geometry of the protrusion and the nature of the emitting atom. In Fig. 12 we show that different spectra can be obtained when one modifies the protrusion. Fig. 12 (a) and (b) show TED's with very wide (multiple peaks) and very narrow (single peak) energy spreads respectively.

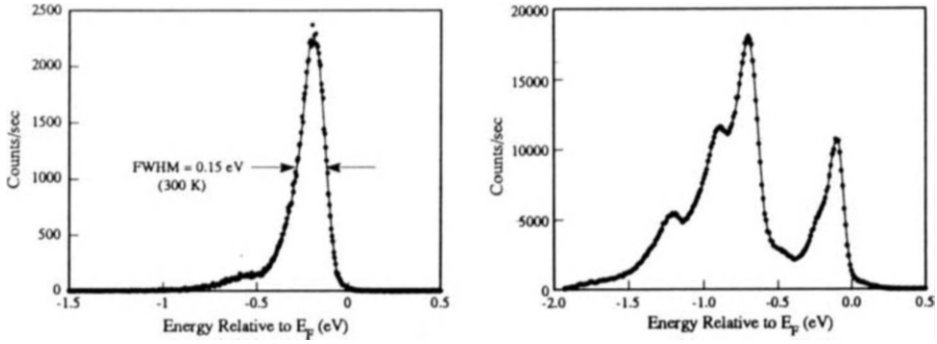

Figure 12. TED's from two different protrusions. Note the narrow energy spread of the single peak TED.

6. Atomic scale temperature measurement

6.1. NOTTINGHAM EFFECT

During the field electron emission (FE) process, energy exchanges take place between the emitted electrons and the cathode surface. These exchange processes, or so-called Nottingham effect, are important in determining the local temperature at the emitter surface. In macroscopic metallic tips, the electrons which replace the emitted electrons are assumed to come from near the bulk Fermi energy (E_F). When all the energy states above E_F are empty, all emitted electrons have less energy than E_F. The average energy of the emitted electrons is then less than that of the replacement electrons and the energy exchange, ΔE_1, then necessarily produces heating of the cathode. When energy states above E_F become populated, the average energy of replacement electrons is lower than that of emitted electrons from these levels, and the energy exchange, ΔE_2, tends to cool the cathode. The heating or cooling of the cathode is governed by the balance between $n_1.\Delta E_1$ and $n_2.\Delta E_2$, where n_1 and n_2 are the replacement rates for each process. For macroscopic tips the temperature increases caused by FE are negligible for FE current < 1 μA [25,26].

It was shown in the previous section that the TED's of single-atom protrusion tips are drastically changed from those of macroscopic tips. Referring to (Fig. 11), we see that the standard Nottingham effect mentioned above (process 1) still occurs within each band, but there are now two additional energy exchange mechanisms. The replacement electrons can now come from the higher energy levels of Fermi sea of the underneath substrate to fill the localized levels in each band that are emptied by emission (process 2) and also from the upper localized band levels to the lower (process 3). In both processes 2 & 3, energy is lost by the replacement electrons. The amount depends strongly on the number and position of the bands with respect to E_F, which also means on the protrusion geometry and the V_{App}. Moreover, since the energy exchange per emitted electron of processes 2 & 3 could have values of the order of eV, this can lead to a larger increase of the temperature at the single-atom apex compared to the standard Nottingham effect.

To check the above idea, we have set up experimental procedures to measure the temperature increases at the apex during the FE through single-atom protrusion tips. The experimental problem in the studies of such temperature increases was how to measure the local temperature at the apex of a single-atom protrusion tip during FE. This temperature may be very different from the temperature of the whole tip because of the very small emitting area. It is necessary to have a local probe of the temperature giving atomic-scale resolution. Our determination of the local temperatures was based on two effects. The first effect is that a repetitive, back-and-forth motion of a single atom between neighboring atomic sites can exist at the atomic-scale apex of a protrusion tip whose frequency is temperature dependant. The second effect is that the shape of the TED's from the protrusion tips depends on temperature. Using procedures based on these effects, we have determined the local temperatures at the apex of a nanoprotrusion for electron emissions in the 10^{-13} to 10^{-9} A range, with the whole tip at room temperature.

6.2. EXPERIMENTAL RESULTS FOR LOW CURRENTS: "FLIP-FLOP" METHOD

The first procedure we have used is based on the fluctuation method introduced by Gomer [27]. The emission current fluctuates due to the back and forth movement, or "flip-flop", of the adsorbed atom between two neighboring sites. The flip-flop frequency is directly related to the local temperature. Thus flip-flop frequency can be used to determine the temperature changes during FE. Based on this idea we have adapted the flip-flop method to measure the temperature at the apex of the single-atom protrusion tips. In the

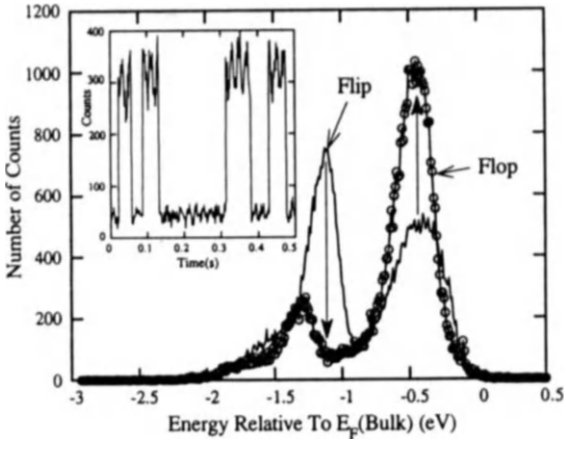

Figure 13. Effect of a flip-flop process on a TED from a single atom tip. Inset represents the change in counts for one energy.

case of Gomer the current fluctuations had to be treated statistically because they were due to the random movement of a large number of atoms. For single-atom protrusion tips, the FE comes from the topmost atom at the apex and the flip-flop then causes changes in the FE characteristics which are related only to the movement of an individual atom. During the flip-flop, the total FE current switches between two discrete values [28] which remain constant and depend on the atomic configuration of the protrusion. Their difference is typically 5 to 10 % of the total current. Moreover, each current level is associated with a particular TED. An example of two TED's measured during the two states of a flip-flop are shown in Fig. 13. The number of peaks and their relative positions are preserved during the flip-flop but the TED's shift as a whole and the relative peak intensities change. The switching between the two spectra is repetitive as long as the flip-flop continues. A consequence of the TED changes is that if the emission current is measured for one chosen energy during the flip-flop process, its variation can be very large even if the total current variation is only of a few percent. This phenomena allows very easy detection of the flip-flop even for total FE currents from the single-atom tips in the range of 10^{-13} A. This is illustrated by the inset in Fig. 13 on which we show the variation of the number of counts at a fixed energy during a flip-flop process. This technique is then used to measure the flip-flop frequency.

We have used the variation of the frequency of the flip-flop of an adsorbed atom coming from the residual gas to determine the temperature at the apex of single-atom protrusion tips. The experimental procedure for the determination of the temperature is the following:

1) The first step was the calibration of the heating loop. The local temperature of the FE area of a macroscopic tip could be deduced from the experimental TED spectra, and in particular for the high energy side, by fitting them to the tunneling equation given by Young [19]. We have checked the validity of this method for two fixed temperatures (liquid nitrogen and room temperature) and for different temperatures in the range of 1000 K to 1600 K with an optical micro-pyrometer. The temperatures from the TED's agreed to the known temperatures to better than 5%. This agreement allowed us then to calibrate the

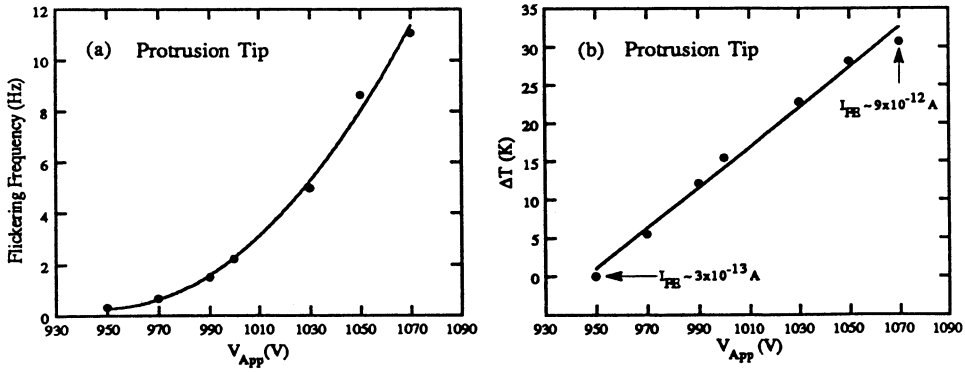

Figure 14. (a) Frequency of flip-flop vs V_{App}. (b) Temperature variation induced by FE from single-atom nanotip

heating loop current with the local temperature at the apex of a macroscopic tip for the range from 150 K to 1600 K.

2) A clean protrusion tip was then fabricated from the macroscopic tip and we waited until a flip-flop process appears, due to an adsorbed atom on the apex of the protrusion. The flip-flop frequency was then measured versus the temperature of the tip as controlled by the heating loop, at fixed V_{App}. It followed an Arrhenius function and the deduced activation energies for several flip-flop processes (~0.39 eV) were in rough agreement with former results given by Gomer for O/W (~0,55 eV). This agreement supports the validity of the calibration of the variation of the flip-flop frequency with the local temperature.

3) The last step for this experiment is the measurement of the FE current at fixed energy as a function of time of a stable flip-flop and for different values of V_{App}. We observed an increase of the flip-flop frequency with increasing V_{App} and conversely emission current (Fig. 14(a)) and by using the calibration values of steps 1 & 2 the variation of the local temperature at the apex of the protrusion is then deduced as a function of V_{App} (Fig. 14(b)). It is of ~30 K for V_{App} increase from 950 V to 1070 V, which corresponds to measured total currents from the protrusion apex respectively of ~$3x10^{-13}$ to ~$9x10^{-12}$ A.

6.3. EXPERIMENTAL RESULTS FOR HIGH CURRENTS: TED METHOD

A too large temperature causes an instability of the adsorbed atom on the protrusion. Thus, for larger temperature increases, we used another method which is based on the fitting of the experimental TED spectra by an equation derived from the classic tunneling equation [19]. This method has been set up from the following experimental observation which was note in section 5.2: the shape of the peaks in the TED from single atom protrusion tips is temperature dependant. In Fig. 15(a) we show the shape variation of the spectrum of a single-atom protrusion tip obtained for one value of V_{App} and two different controlled temperatures. It shows a broadening of the high energy edge of the spectrum with the temperature. The temperatures found from the TED's are in agreement with the known values from the calibrated heating loop. We have used this phenomenon to measure the local temperature at the apex of single-atom protrusion tips for different V_{App}. In

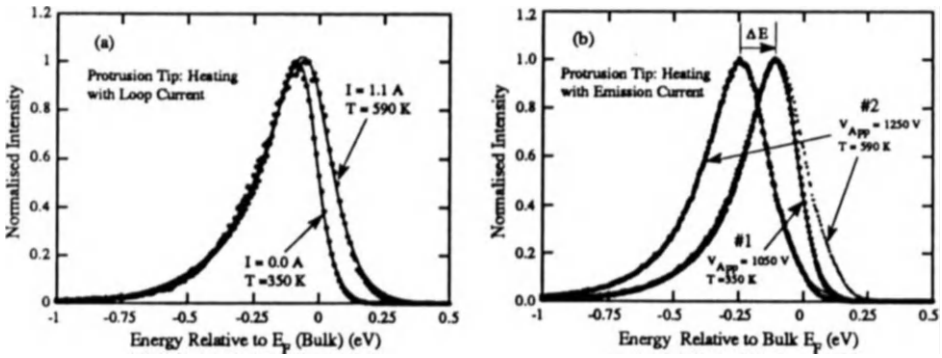

Figure 15. (a) Spectra from nanotip for room temperature and 590 K. The higher temperature is created by loop heating current. (b) Spectra from the same protrusion tip for different applied voltages and different emission currents. The spectra at higher voltage, #2, shifts to lower energy due to field penetration. We have shifted it numerically by ΔE to the position of the lower voltage peak to show the broadening of the high energy side of the spectra that is caused by the temperature increase.

Fig. 15(b) we show that, concomitant to the shift of the spectra which is characteristic of FE from single-atom protrusion tip, there is a broadening of the high energy side of the spectra as a function of V_{App}. This indicates an increase of the temperature at the apex due to FE. The local temperatures at the apex of a protrusion tip found by fitting the spectra for varying emission current are shown in Fig. 16. The temperature increase during a change in FE current from $3x10^{-11}$ to $4x10^{-9}$ A was ~210 K. The value of 210 K in the increase of the apex temperature is not a limiting value. For this experiment we have not increased V_{App} more in order to preserve the same protrusion geometry. For higher FE currents the temperature increase is indeed larger. The protrusion becomes unstable and it can be destroyed by a local melting.

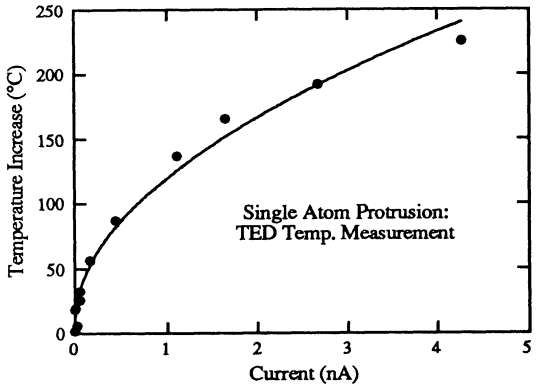

Figure 16. Changes in temperature versus emission current for a single-atom nanotip

7. Conclusions

Ball-tips, nano-cantilever tips and teton tips are fashioned by surface diffusion or the field-surface-melting mechanism. These fabrications are based on thermodynamic processes and are thus reproducible.

The nanoscale or atomic dimensions of these tips introduce new properties for their use as nanoscale probes, sources and tools. Nano-cantilevers may have resonance frequencies of ~10^8 Hz and spring constants of ~100 N/m. Teton tips act as single atom sources of electrons. The corresponding field emission spectra show a band structure which is related to the atomic size of the source. The shifting of the bands with applied field and the dependence of the spectra on protrusion geometry show that an analysis at atomic scale can be performed. To demonstrate this potential, temperature increases due to emission currents have been measured with an atomic-size probe area. This shows that in contrast to standard ideas, tunneling emission has to be associated with important energy exchanges if the tunneling region is atomic.

In general, this work shows that when experiments are performed with tools of the nanometer and atomic scales, new concepts must be developed. For example, the band structure revealed in the TED's must be considered in the analysis of Scanning Tunneling Spectroscopy or in the use of nanotips as electron or ion sources for analysis systems.

ACKNOWLEDGEMENT. This research was sponsored by an EEC "Science" project, French (MRT n° 90-S-0229 and Thomson-LCR) and Spanish scientific institutions.

REFERENCES

[1] C. Herring in "Structures and Properties of Solid Surfaces", Eds. R. Gomer and C.S. Smith, University of Chicago Press, USA (1953).

[2] For a review on the influence of applied electric field on the reduction of the activation barrier and binding energy see: E.W. Muller and T.T. Tsong, in "Field Ion Microscopy: Principles and Applications", (Elsevier, New York, 1969); Prog. Surface Sci. **1**, 1 (1974).

[3] F.A. Nichols and W.W. Mullins, J. Appl. Phys. **36**, 1826 (1965).

[4] Vu Thien Binh and R. Uzan, Surface Sci. **179**, 540 (1987).

[5] F. O. Goodman and N. Garcia, Phys. Rev. B **43**, 4728 (1991).

[6] G. Binnig, C. F. Quate and Ch. Gerber, Phys. Rev. Lett. **56**, 930 (1986).

[7] N. Garcia and Vu Thien Binh, Phys. Rev. B **46**, 7946 (1992)

[8] D. Sarid and V. Eling, J. Vac. Sci. Technol. B **9**, 431 (1991).

[9] Vu Thien Binh and N. Garcia, J. Physique I **1**, 605 (1991); Ultramicroscopy **42-44**, 80 (1992).

[10] I.L. Sokolovskaia , J. Tech. Phys. (URSS) **26**, 1177 (1956); P. Bettler and C. Charbonnier, Phys. Rev. **119**, 85 (1960). These authors were the first in applying an electric field to have build-up tips.

[11] Vu Thien Binh, J. Microscopy **152**, 55 (1988).

[12] R. Smouluchowski, Phys. Rev. **60**, 661, (1941).

[13] G. Neumann and G. M. Neumann, in "Surface Self Diffusion of Metals", Ed. F. H. Wohlbier, Diffusion Monograph Series, No. 1 (1972).

[14] J. G. Dash, Contemp. Phys. **30**, 89 (1989).

[15] D. Atlan, G. Gardet, Vu Thien Binh, N. Garcia and J.J. Saenz, Ultramicroscopy **42-44**, 154 (1992).

[16] D.J. Rose; J. Appl. Phys. **27**, 215 (1956)

[17] Vu Thien Binh, S.T. Purcell, N. Garcia and J. Doglioni, Phys. Rev. Letters, **69**, 2527 (1992)

[18] C.E. Kuyatt and E.W. Plummer, Rev. Sci. Instru. **43**, 108 (1972).

[19] R.D. Young, Phys. Rev. **113**, 110 (1959).

[20] C.B. Duke and M.E. Alferieff, J. Chem. Phys. **46**, 923 (1967).

[21] J.W. Gadzuk, Phys. Rev. B **1** (1970) 2110.

[22] E.W. Plummer and R.D. Young, Phys. Rev. B **1** (1970) 2088.

[23] R. Gomer, "Field Emission and Field Ionization", Harvard Monographs in Applied Science 9, Cambridge, USA (1961).

[24] C. Kittel, Introduction to Solid State Physics (Wiley, New York, 1968).

[25] L.W. Swanson, L.C. Crouser and F.M. Charbonnier, Phys. Rev. **151**, 327 (1966)

[26] L.W. Swanson and A.E. Bell, in Adv. Electr. Electron Phys. Vol. 32, 194 (1973), Ed L. Marton, Acad. Press New York & London. (review of energy exchanges during FE).

[27] R. Gomer, review article on the flip-flop "Surface mobilities on solid materials" pp 7-62, Ed. Vu Thien Binh, NATO-ASI Series B Vol. 86 (1983), Plenum Press, New York.

[28] J.J. Saenz, N. Garcia, Vu Thien Binh and H. De Raedt, in "Scanning Tunneling Microscopy and Related Methods", Eds. R.J. Behm, N. Garcia and H. Rohrer, NATO-ASI Series E Vol. 184, Kluwer Acad. Publ., The Netherlands, 1990.

ELECTRON EMISSION FROM NANOMETER-SIZE METALLIC CLUSTERS: ELECTRONIC STATES AND STRUCTURAL STABILITY OF SUPPORTED Au CLUSTERS

M.E. Lin, A. Ramachandra, R.P. Andres and R. Reifenberger
Purdue University
W. Lafayette IN 47907

ABSTRACT. Techniques developed to measure the thermodynamic and electronic properties of a single metallic cluster with nanometer-size dimensions are described. Using these techniques, experiments that resolve the quantized energy spectrum of electrons in a nanometer-size cluster of metallic atoms at room temperature have been performed. Studies on the stability of the electron emission current from an individual nanometer-size cluster supported on a tungsten tip have been performed to learn more about the intrinsic stability of these nanometer-size objects. The data show abrupt jumps between different emission states that are revisited as time progresses. This phenomenon is attributed to a rearrangement of the cluster structure and/or orientation on the substrate and provides new evidence of multiple 'isomeric' structures for small clusters of metallic atoms.

1. Introduction

The manipulation of atoms to fabricate nanometer-scale structures ultimately requires an understanding of the size-dependent thermodynamic, electronic, and structural properties of discrete aggregates of atoms. The properties of these aggregates differ from bulk properties and these differences will set limits on the stability and performance of structures fabricated at the nanometer length scale. In order to provide experimental information about these limits, techniques recently developed to measure the size-dependent properties of clusters of atoms supported on substrates will be reviewed. Using these techniques, the thermodynamic,[1-3] electronic, and electron emission properties of an individual nanometer-size aggregate of atoms can now be probed.

A unique feature of the structures under study is that the influence of high applied electric fields on the electronic conduction process can be performed in a natural way. This is because the techniques rely on the study of electrons field emitted from an individual cluster. To produce field emission, electric fields of order 10^9 V/m are required. In the following paper, we describe a series of experiments conducted on the electronic properties of small nanometer-size metallic clusters that provide information relevant to the above stated goals. The studies summarized below provide a unique window into the electronic structure that is important at this length scale.

V.T. Binh et al. (eds.),
Nanosources and Manipulation of Atoms Under High Fields and Temperatures: Applications, 77–88.
© 1993 *Kluwer Academic Publishers.*

2. Cluster growth and sample preparation

A description of the construction and operation of the multiple expansion cluster source (MECS) used in this study can be found in the literature.[4–6] The clusters are grown as aerosol particles in an inert gas and introduced into a vacuum chamber (10^{-6} Torr) to form a cluster beam. In previous studies, cluster samples have been captured on amorphous carbon substrates and analyzed by TEM. The isolated clusters studied in this way confirm the ability of the MECS to produce metal clusters having an approximately spherical shape, a controlled mean size, and a narrow size distribution.[4,5] This TEM size-determination method has been used in conjunction with field emission studies to determine the mean diameter and variance of the cluster-size distribution from which the clusters of interest are sampled.

To study field emission from a single cluster, a tungsten tip is exposed to the cluster beam and then transferred to a field emission chamber in a vacuum transfer cell at pressures of $\sim 5 \times 10^{-8}$ Torr.[6] Experiments are performed in the field emission chamber at typical pressures of $\sim 2 \times 10^{-10}$ Torr. A schematic of the retardation/127° energy analyzer used in these experiments is shown in Figure 1. The characterization and performance of this analyzer is described elsewhere.[7,8]

3. Size-dependent field emission spectra from supported Au clusters

The ability to measure the energy distribution of electrons emitted from a single supported Au cluster with a diameter of $\sim$ 1 nm was reported previously.[9] The observed emission spectra provided good evidence that the quantized electronic states in an individual 1 nm diameter Au cluster can survive when the cluster is supported on a W surface. A resonant-tunneling model based on first-order perturbation by the applied electric field was used to provide an estimate for the position in energy of the peaks observed in the field emission spectrum. A reasonable account for the experimental observations was obtained and a tentative identification of the cluster shell-levels responsible for the observed structure was proposed.[9,10]

As the size of the cluster increases, a number of difficulties arise in applying this resonant tunneling analysis. First, the effect of electric field penetration becomes less important since the surface to volume ratio of the cluster decreases. If the electric field does not penetrate the cluster significantly, the cluster-substrate interaction becomes the dominant perturbation. This implies that as the cluster diameter increases, the field-dependent downward shift in the electron energy spectra diminishs. Second, as the cluster size increases, increased coupling between the cluster and substrate can be anticipated since the number of cluster atoms in close proximity to the substrate increases. Since these effects are difficult to include in the resonant-tunneling model, a detailed comparison between the measured emission spectra and the model outlined in Refs. 9 and 10 has not been attempted. Rather, data on the size-dependent structure are presented to illustrate the capabilities of the technique and to illustrate any size-dependent trends that they reveal.

The emission spectra for several different cluster sizes are summarized in Figure 2.[11] The data show that the electron energy distribution shifts toward the substrate E_F with

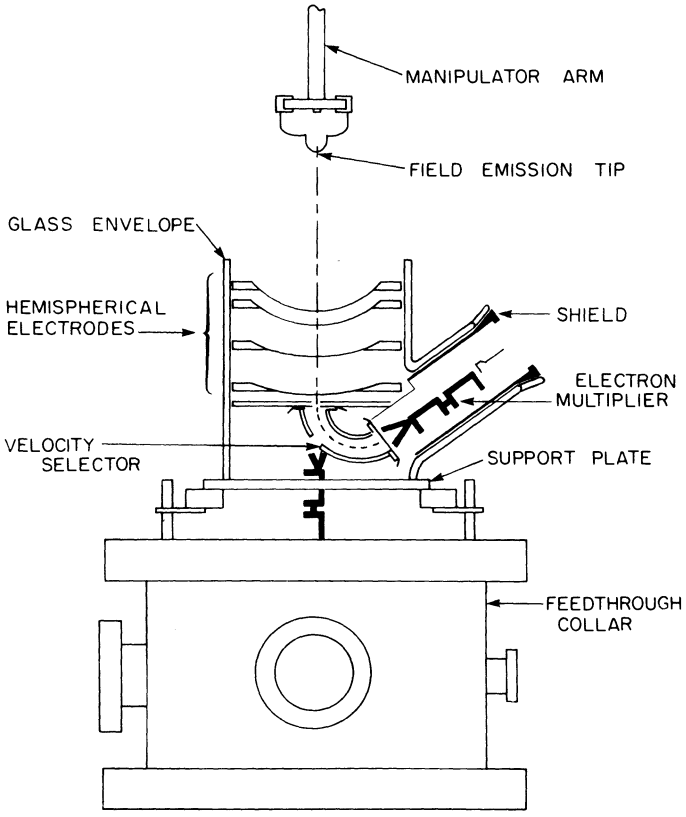

Figure 1: A schematic of the energy analyzer used in these studies. Electrons emitted from a cluster deposited on the apex of the tip are accelerated toward the first hemispherical electrode which is coated with a fluorescent screen. Those electrons passing through the probe hole in this electrode are subsequently decelerated until they reach the entrance slit of the 127° velocity selector. This analyzer has an energy resolution of 0.07 eV. Figure reproduced from Ref. 7

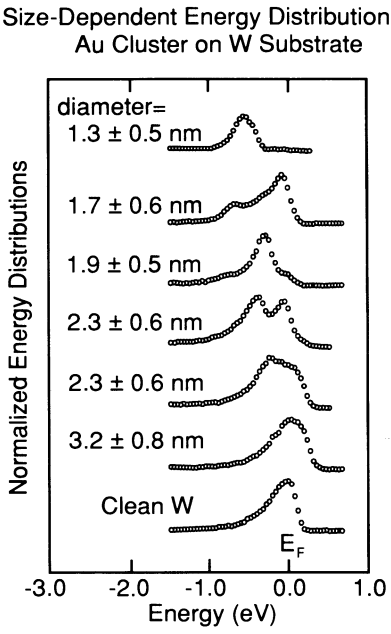

Figure 2: The size-dependent energy distribution of electrons emitted from a Au cluster supported on a W tip at room temperature. The observable features in the energy distribution mirror the quantized electronic structure of the supported Au cluster. The energy distribution obtained from a clean W tip provides a convenient method to determine the Fermi energy of the underlying substrate. Figure reproduced from Ref. 11

increasing cluster size until all structure in the distribution becomes unresolvable for clusters with diameters greater than ~3 nm.

The position in energy of the peaks in the energy distribution from an individual cluster were reproducible over a period of time spanning a few weeks. The height of the peaks changed when measured on a time scale of a few hours, a fact attributed to the time-dependent coupling of the cluster states to the substrate.[10] Different clusters with the same nominal size did not necessarily exhibit identical emission spectra, a fact which indicates the need to more accurately determine the number of atoms comprising each cluster in future studies. Similar variations in the tunneling spectra of single clusters have been reported for Si clusters supported on Au substrates.[12]

For a 1.3 ± 0.5 nm diameter cluster, a single electron emission peak was observed ~ 0.2 eV below the substrate Fermi level, indicating that the highest occupied cluster state was not pinned to the Fermi energy of the substrate. As the applied field increased, the peak moved further below the Fermi level of the substrate.

Two distinct peaks appear in the energy distribution from a 1.7 ± 0.6 nm diameter cluster and both shift to lower energies with increasing field. This shift with applied field

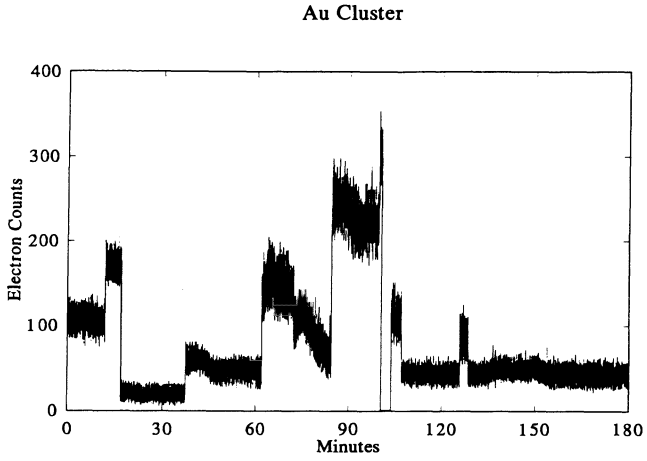

Figure 3: A typical plot of electron counts vs. time from a nominal 2.6 nm diameter Au cluster supported on the apex of a W tip. The abrupt changes in the field emitted current is found to take place only between well-defined emission states.

provides a useful way to identify cluster states[9] and indicates whether the discrete energy states are related to the supported cluster or to surface states of the substrate.

For a 1.9 ± 0.5 nm diameter cluster, three peaks are observed in the energy distribution. One peak is located at the Fermi level of the substrate and does not shift with applied field. The two other peaks are ~ 0.16 eV and ~ 0.40 eV below the Fermi level respectively. These two latter peaks were field dependent and are therefore interpreted as a signature of the cluster states. Thus, for this cluster, we evidently observe not only ballistic emission of electrons from the substrate through the cluster but also emission from the two highest-lying cluster states.

When a cluster with 2.3 ± 0.6 nm diameter was deposited on the W tip two peaks were again resolved. During this deposition, two well-separated clusters were observed on the apex of the field emission tip. The two-peaked structure observed for both clusters are similar as shown in Figure 2. Both peaks are cluster-related states because their position depends on the applied electric field. The data shows that the peak at lower energy is larger than the one nearer the Fermi level, a result indicative of a partially filled upper energy shell.

As cluster size increases, the discrete states should become more closely spaced until their separation is smaller than the energy resolution of our apparatus. This behavior is observed in the spectrum obtained for a 3.2 ± 0.8 nm diameter cluster where only one broad peak was observed. This peak is broader than the W field emission energy distribution from the substrate. It is not clear what mechanism is responsible for this broadening, but it is likely a signature of electron emission from many closely spaced cluster states that can not be resolved by the energy analyzer used in this study. The disappearance of structure at

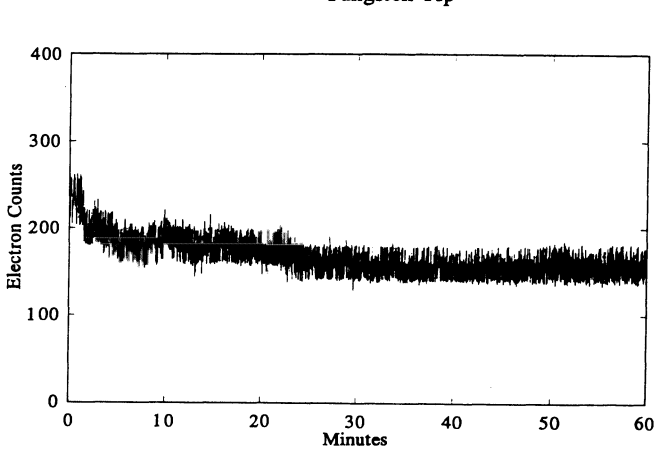

Figure 4: A typical plot of electron counts vs. time for field-emitted electrons from a tungsten tip after desorption of the Au cluster.

the $\sim$ 3 nm cluster size is in good qualitative agreement with model calculations presented elsewhere.[10,11,13]

Finally, a representative energy spectrum is shown from a clean tungsten tip. This spectrum was obtained after a supported cluster was thermally desorbed from the tip. A fit to this data using the standard theory of field emission[14,15] locates the Fermi level of the substrate and provides a convenient reference curve for intercomparison of the cluster emission spectra.

4. Structural Stability

The structural stability of a supported cluster in the nanometer size range is a question that is still under considerable debate. It has been established from computer simulations that a nanometer-size cluster has many structural configurations that are closely separated in energy from the true ground state. These calculations predict structures that deviate from the cluster shape given by the classical Winterbottom criterion[16] which dictates that minimization of the surface free-energy determines the final cluster shape.

In contrast to these theoretical calculations which attempt to predict a well-defined structural state for a nanometer-size cluster, other investigations have postulated the presence of a new state, often referred to as the 'quasi-molten' state, as the equilibrium state for a small nanometer-size cluster.[17–20] However, the high-resolution transmission electron microscope (TEM) studies of this proposed cluster state requires electron-beam irradiation of the clusters, producing effects by the high-energy incident electron beam which are difficult to characterize. Despite arguments to the contrary, concerns regarding the role of the incident electron beam in producing the observed 'quasi-molten' state have not been

conclusively eliminated.

As discussed in the previous section, we have performed a number of experiments utilizing electron emission from a nanometer-size cluster supported on the apex of a sharp field emission tip. While it is not possible to achieve the spatial resolution necessary to determine structural changes directly from field emission microscopy, fluctuations in the field emission current do provide information about this important question. For instance, it is well established that fluctuations in the field emission current from a sharp tip can give useful information about the diffusion of intentionally adsorbed gaseous species.[21–23] We take advantage of this technique to study the stability of a nanometer-size object to determine the inherent stability of a supported nanometer-size cluster. By following this approach, we can obtain results without resorting to the bombardment of the supported cluster by a flux of energetic electrons.

A priori, any instability in the cluster structure should cause abrupt changes in the total field emission current. This follows because of the exponential dependence of the emission current on the local value of both the work function and the applied electric field. Field emission can therefore serve as a very sensitive monitor to structural changes in cluster shape and/or orientation on a substrate. It is important to realize that because of the small radius of curvature of the cluster with respect to the field emission tip, electrons emitted from one cluster only can be directed through the probe-hole of our energy analyzer, thereby permitting a study of the structural stability of a single supported cluster.

The experimental procedures are similar to those described earlier. The major modification occurs in the way data is acquired. The experiment was performed by first depositing a Au cluster on the W tip from the cluster beam. Subsequent TEM images of a carbon grid exposed to the same cluster beam showed a size-distribution that was characterized by a nominal diameter of 2.6 ± 0.8 nm. After deposition, the electrons emitted from the supported cluster were directed into the probe hole of the energy analyzer. After measuring the energy distribution of the electrons from the supported cluster, the bias voltage on the fourth plate of the retardation section of the energy analyzer was fixed at a value that maximized the electron count rate. This procedure minimized the effect of any small drifts in bias voltage that may have occurred during the course of data acquisition.

A computer was programmed to accumulate the number of electrons emitted from the cluster in time intervals of 0.5 seconds. Due to the large amount of data, an IBM 386 25MHz lap-top computer with 4Mb RAM was used as an auxiliary computer to store the experimental data. The zero of time was set by adjusting the total field emission current from the cluster to approximately 2 nA for a brief period of time followed by a return to its nominal value of $\sim$0.5 nA.

In Figure 3, the field emission current striking the electron multiplier from the nominal 2.6 nm gold cluster during a time span of three hours is presented. At the beginning, the rate of electron emission per 0.5 second time interval is maintained at $\sim$110 electrons. After $\sim$ 12 minutes, the emission rate jumps to $\sim$ 160 electrons per half second and remains stable for about 4 minutes. A discontinuity of emission rate occurs between these two stages. Similar discontinuities can be observed during the first two hours of field emission and seem to occur less frequently as the experiment progresses. Besides the discrete levels observed in this spectrum, the emission rate was found to decrease in a somewhat continuous way

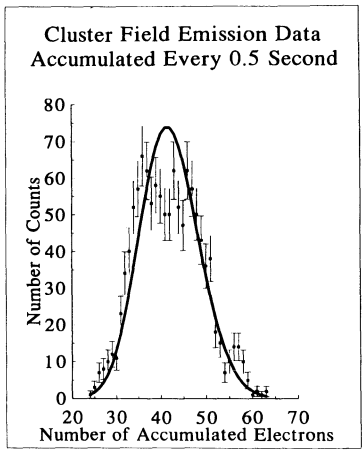

Figure 5: The experimental distribution in count rate during the last 1200 $\frac{1}{2}$-second time intervals for field emission from the Au cluster shown in Fig. 3. The solid curve is the best least-squares fit to a Poisson distribution with mean value of 42.

on one occasion (see Figure 3). For example, the emission rate of field-emitted electrons is decreasing continuously from ~150 electrons to ~80 electrons per half second between the ~ 62nd minute and the ~ 85th minute of the data record. On only one occasion did the emission rate drop to zero at ~ 100 minutes after the experiment had begun.

From this data it is evident that abrupt changes are a characteristic of electron emission from a supported cluster in a high electric field. These abrupt changes occur between ~ 5 distinct emission states that have steady electron emission characteristics. Examination of this data also shows that the time dependence of the field-emitted electrons can be classified into a number of well-defined levels. It is likely that each level is associated with a different configuration between the cluster and substrate. The electron emission, when studied in this way, suggests that the cluster sequentially visits the same five configurations during the three hour period of data acquisition.

A possible explanation which might account for the abrupt changes in the electron emission rate is related to sudden contamination by gas atoms in the ultra-high vacuum (UHV) environment. In order to eliminate this possibility, the cluster was thermally desorbed from the tip apex and an electron emission stability experiment was performed on electrons emitted from a small region of the W tip alone. The results of this experiment are shown in Figure 4, and demonstrate that the emission rate is quite stable with time. No abrupt change in the emission rate is observed and the time dependence of the emission current is consistent with a gradual increase in the tip's work function due to slow contamination by residual gas in the UHV chamber. On the basis of this data, contamination and diffusion effects can be ruled out as a possible explanation of the data shown in Figure 3.

Probable explanations for the instabilities observed in this experiment can be suggested.

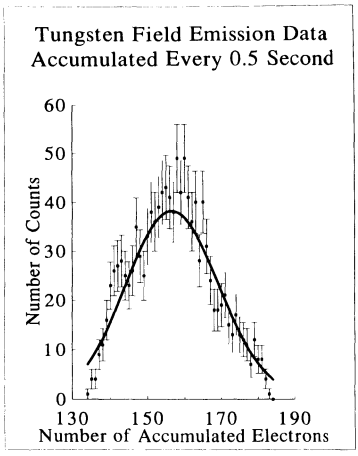

Figure 6: The experimental distribution in count rate during the last 1200 $\frac{1}{2}$-second time intervals for field emission from the W tip shown in Fig. 4. The solid curve is the best least-squares fit to a Poisson distribution with mean value of 157.

For instance, electron tunneling resonance effects are known to influence field emission from clusters.[10] These effects determine the current enhancement factor for cluster field emission and are strongly dependent on the coupling between the cluster and substrate. As a result, the field emission rate will vary, accounting for the discontinuities in Figure 3. The resonance tunneling enhancement factor can also be changed by rotating the cluster. One mechanism that can be discounted is a diffusion of the cluster across the substrate. This would be readily observed due to the high spatial resolution of the field emission microscope.

5. Statistical Analysis of Emission Rate

Further insight into each emission state can be gained by further analyzing the data from one emission state using Poisson statistics. These statistics describe the probability $P(x, \mu)$ of observing x events separated in time by a mean value τ over a time interval t. This distribution, which describes the fluctuation in the count rate for a process in which emission occurs at random intervals, is given by

$$P(x, \mu) = \frac{\mu^x}{x!} e^{-\mu} \tag{1}$$

where $\mu = t/\tau$ is the average number of events observed in the time interval t. It is useful to compare our experimental data from the individual cluster to the predictions based on Poisson statistics.

Typical results of this comparison are shown in Figure 5 for emission from the Au cluster and in Figure 6 for emission from the W tip. The solid lines in these Figures are the

least-squares fit to the count rate distribution based on Poisson statistics. It is difficult to determine the quality of these fits to the experimental data by eye. Therefore, we use the reduced χ^2 test[24] to check the agreement between the experimental distributions and the Poisson fits. The results are given in Table 1 and clearly indicate that while the likelihood of fitting the Poisson distribution to the tungsten field emission data is better than 20%, the two cases of electron emission analyzed from the cluster are fit with a likelihood of less than 0.5%.

Table 1: Table comparing the experimental data to a fitted Poisson distribution using reduced χ^2 analysis. (a) The first 1415 samples of the count rate for field emission from the Au cluster, (b) the last 1200 samples of the count rate for field emission from the Au cluster, (c) the last 1200 samples of the count rate for field emission from the W tip after the cluster was thermally desorbed, (d) the same as in (b), but assuming two closely spaced emission channels (hence two mean values) characterize electron emission from a supported cluster.

	Number of Samples	Bins	Mean Value	Reduced χ^2	Probabilities
(a)	1415	61	107	2.0	less than 0.5%
(b)	1200	40	42	3.0	less than 0.5%
(c)	1200	50	157	1.15	~21%
(d)	1200	40	38,46	1.4	~5%

Improvements in the fit of the cluster data occurs if the mean value of the Poisson distribution is split into two well defined values. Using the *ad-hoc* approach that emission from one cluster state is actually fluctuating between two closely-spaced levels, a least squares fit shows that a combined Poisson fit to the data acquires a 5% significance level (see Table 1(d)). This result suggests that the emitted current from the cluster is fluctuating between two different emission channels at a rate comparable to the sampling time of 0.5 seconds employed in these preliminary studies. By further exploiting this technique, non-obtrusive information about the stability of nanometer-size objects supported on substrates will be possible.

6. Summary and Conclusions

Experiments that measure the properties of individual nanometer-size clusters of atoms have been described. By combining the Multiple Expansion Cluster Source and field emission techniques, the distribution in energy of electrons emitted from single Au clusters has been studied as a function of cluster size. This data provides evidence that the quantized cluster states survive the deposition process and can now be studied in a systematic way

at room temperature.

We also summarize the evidence for the structural stability of a supported cluster obtained by studying the electron emission current from a supported nanometer-size cluster as a function of time. The data are interesting because they were taken without the need for irradiation by a high-energy flux of incident electrons produced by a TEM electron gun. Abrupt changes in the electron emission current suggest that a change in cluster shape or orientation on a substrate occurs as a function of time. It is found that the electron emission level revisits values previously measured, indicating that changes in electron current are due to structural fluctuations between well-defined cluster-substrate configurations.

Acknowledgements

This work was partially supported by the U.S. Department of Energy under grant DE-FG02-88ER45162 and by the National Science Foundation under grant ECS-9117691. M.E. Lin is thankful to the David Ross Foundation at Purdue University for partial support during this study.

References

[1] T. Castro, R. Reifenberger, E. Choi, and R.P. Andres, Surf. Sci. **234**, 43 (1990).

[2] T. Castro, R. Reifenberger, E. Choi, and R.P. Andres, Phys. Rev. B **42**, 8548 (1990).

[3] T. Castro, E. Choi, Y.Z. Li, R.P. Andres, and R. Reifenberger, Proc. Mat. Res. Soc. **206**, 159 (1991).

[4] Seung Bin Park, PhD thesis, Purdue University, 1988.

[5] E. Choi and R.P Andres, in *Physics and Chemistry of Small Clusters*, edited by P. Jena, B.K. Rao, and S.N. Khanna, page 61, Plenum Press, New York, 1987.

[6] T. Castro, Y.Z. Li, R. Reifenberger, E. Choi, S.B. Park, and R.P. Andres, J. Vac. Sci. Technol. **A7**, 2845 (1989).

[7] D.L. Haavig and R. Reifenberger, Surf. Sci. **151**, 128 (1985).

[8] Y. Gao, R. Reifenberger, and R.M. Kramer, J. Phys. E: Sci. Instrum. **18**, 381 (1985)

[9] M.E. Lin, R.P. Andres, and R. Reifenberger, Phys. Rev. Lett. **67**, 477 (1991).

[10] M.E. Lin, R. Reifenberger, and R.P. Andres, Phys. Rev. B , (submitted for publication) (1992).

[11] M.E. Lin, R. Reifenberger, A. Ramachandra, and R.P. Andres, Phys. Rev. B , (submitted for publication) (1992).

[12] Y. Kuk, M.F. Jarrold, P.J. Silverman, J.E. Bower, and W.L. Brown, Phys. Rev. **B39**, 11168 (1989).

[13] M.E. Lin, A. Ramachandra, R. Reifenberger, and R.P. Andres, Clusters to Crystals Conference (Richmond VA; Oct. 1991) , (submitted for publication) (1992).

[14] J.W. Gadzuk and E.W. Plummer, Rev. Mod. Phys. **43**, 487 (1973).

[15] A. Modinos, *Field, Thermionic and Secondary Electron Emission Spectroscopy*, Plenum Press, New York, 1984.

[16] W.L. Winterbottom, Acta Metallurgica **15**, 303 (1967).

[17] P.M. Ajayan and L.D. Marks, Phys. Rev. Lett. **60**, 585 (1988).

[18] P.R. Couchman and C.L. Ryan, Philos. Mag. **37**, 369 (1978).

[19] M. Hasegawa, K. Hoshino, and M. Watabe, J. Phys. **F10**, 619 (1980).

[20] J.P. Borel, Surf. Sci. **106**, 1 (1980).

[21] C. Dharmadhikari and R. Gomer, Surf. Sci. **143**, 223 (1984).

[22] R. DiFoggio and R. Gomer, Phys. Rev. **B25**, 3490 (1982).

[23] R. Gomer, Appl. Phys. **A39**, 1 (1986).

[24] P.R. Bevington, *Data Reduction and Error Analysis for the Physical Sciences*, McGraw-Hill, New York, 1969.

ON THE ENERGY DISSIPATION IN FIELD EMISSION AND TUNNELING MICROSCOPY

J. XU[1], R. MÖLLER[1], K. LÄUGER[1], K. DRANSFELD[1] and C. C. WILLIAMS[2]
[1] *Fakultät für Physik, Univ. Konstanz, D-7750 Konstanz, Germany*
[2] *Dept. of Physics, Univ. of Utah, Salt Lake City, Utah 84112, USA*

ABSTRACT In this paper we are discussing first the energy delivered to a monoatomic tip in the field emission process. Strong phonon excitation is expected for an emission current exceeding 1 nA.

Secondly we are reporting in detail first experiments in air on the heat generation due to the tunneling of electrons in a scanning tunneling microscope (STM). Using a small thermocouple mounted on the substrate of a STM the thermal power deposited in the sample was measured with high resolution as a function of the bias voltage and its polarity. For small but constant tunneling currents we found a heating of the sample increasing linearly with the applied bias voltage, and being nearly independent of its polarity. Thus the energy deposition in tip and sample are equal and directly proportional to the electric energy fed into the tunneling gap. But for high tunneling currents, large bias voltages and close tunneling distances there is more power to be dissipated in the emitting than in the receiving electrode which is not expected theoretically. Our results are compared with a theoretical estimate based on the free electron model for the electrode materials and tunneling across a planar vacuum gap. The discrepancy between our observations and the theoretical expectations may be partially explained by the strong thermal coupling between tip and sample due to adsorbed films reducing the temperature differences between both electrodes.

For the process of field emission as well as for tunneling between closely spaced electrodes our analysis of the experimental data indicates that at high currents more energy is deposited in the emitting electrode than expected theoretically.

1. Introduction

If electrons are tunneling from a sharp metallic tip to a flat metallic electrode or other conducting substrate two different cases have to be distinguished: For a large separation d between tip and substrate (much larger than the deBroglie-wavelength λ_B) the electronic transport across the gap can only proceed in the presence of high fields via field emission. For close tip-sample separation (d ~ λ_B), however, as realized in scanning tunneling microscopy, electrons can tunnel directly across the tunneling gap even if only small voltages are applied between tip and substrate.- This paper is concerned with the local energy dissipation for the two tunneling processes mentioned above and is organized as follows: The second short section analyses the problem of energy deposition in field emission and the third part describes in detail new experiments on the energy deposition in a tunneling microscope.

V.T. Binh et al. (eds.),
Nanosources and Manipulation of Atoms Under High Fields and Temperatures: Applications, 89–100.
© 1993 *Kluwer Academic Publishers. Printed in the Netherlands.*

2. Energy Dissipation in the Process of Field Emission

In the case of *field emission* from a tip it is well known that in the high current regime resistive heating often limits the thermal stability of the tip [1]. Furthermore an energy exchange process (the Nottingham-effect) which is directly related to the tunneling process may not only lead to heating but also to cooling during the emission process, depending on the experimental circumstances, as first described by Nottingham [2].

For the Nottingham effect it is of primary importance whether the average energy $<E>$ of the emitted electrons is lower or higher than the Fermi energy E_F [3]. If the emitted electrons leave the tip with an energy below the Fermi energy (at which energy the electrons are supplied to the tip by the external circuit) the energy difference (E_F - $<E>$) is dissipated at the tip. Vice versa, if the energy of the field-emitted electrons exceeds the Fermi energy - which can occur at elevated tip temperatures - the tip may cool down during the emission process [4]. Using macroscopic (not monoatomic) tips the Nottingham effect has been experimentally studied both for normal metals [5, 6] and for superconductors [7], but its verification has not been easy. At high current densities the resistive heating alone usually leads to high tip temperatures.

For macroscopic tips, having a radius of curvature above 100 nm, the surface area effectively contributing to the field emission current has a diameter of more than 20 Å [8]. In contrast, if monoatomic tips (or "nanotips") are used, which can be fabricated now [9], nearly all electrons are emitted from the single topmost atom of the tip.

Recently Binh et al. [10] have measured for the first time with a high energy resolution (of 0.01 eV) the energy of field emitted electrons, using not only macroscopic but also monoatomic tungsten tips formed on a W<111> single crystal [10]. For *macroscopic* tips (radius of curvature about 100 nm) the energy of the emitted electrons showed the well known [11] strong and somewhat asymmetric peak with a sharp drop to high energies just above the Fermi energy, with a slower decrease at the low energy side and a total halfwidth of about 0.25 eV, exactly as expected theoretically for the field emission of the free metal electrons tunneling through the nearly triangular potential barrier shaped by the external field.

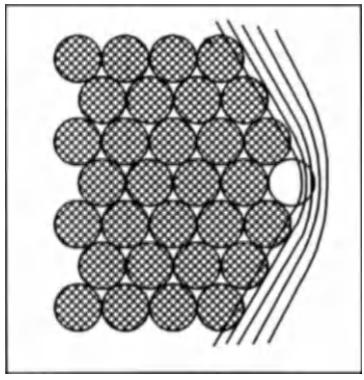

Fig. 1. Schematic representation of a monoatomic tip in the presence of an applied electric field. The equipotential lines penetrate more deeply into the topmost atom (white), where also the electric field is highest.

But the energy of electrons emitted from *monoatomic* tungsten tips showed a very different and quite unexpected spectrum. The origin of this different behavior may be the relatively

strong field penetration and the relatively high field to which the topmost atom of a monoatomic tip is exposed as schematically indicated in fig. 1. In addition to the maximum near E_F the energy spectrum for a monoatomic tip shows a second peak almost 2 eV below the Fermi energy E_F. The exact position and magnitude of both - almost equally strong - peaks depends on the applied field, but the average energy $<E>$ of the emitted electrons is now more than 1 eV below the Fermi energy. Since the electrons are supplied to the tip from the external circuit with the energy E_F and since they are emitted from the tip with the considerably lower energy $<E>$, the energy difference $(E_F - <E>)$ must be deposited at the tip for each emitted electron. At a total field emission current of 1 nA (corresponding to about 10^{10} electrons/s), energy is liberated in the tip at a rate of $10^{10} \cdot (E_F - <E>) \approx 2$ nW. If this surplus energy is not used elsewhere (for example for photon- or plasmon-emission) it will be converted into thermal phonons and finally into heat. For the vibrational frequency of a tungsten atom of about 10^{13} Hz the corresponding phonon energy is 0.05 eV. The available surplus energy liberated during the emission of each electron $(E_F - <E>) \sim 1$ eV is sufficient for the generation of 20 phonons, and a field emission current of 1 nA thus leads to the creation of $2 \cdot 10^{11}$ phonons per second. From the observed linewidth of optical Raman lines [12], the lifetimes of high frequency phonons in most materials - including metals - can be estimated to be of the order 10^{-11} s. For lifetimes of this order a serious overpopulation of the phonon levels must be expected if the field emission current exceeds 1 nA. In fact, the interesting anomalies observed by Binh et al. [10] for high voltages and high field emission currents may be caused by strong phonon generation. This could also contribute to the very strong deviation of the current-voltage relationship from the standard Fowler-Nordheim theory, as has been found experimentally for field emission from monoatomic tips [13].

Little is known at present about the nature of the phonons which are excited, but the topmost atom of the tip is expected to play a major role, since its motion would modulate the field emission current most effectively. The volume of the tip, in which the phonon generation occurs, is probably limited by the electronic mean free path in tungsten ($\leq$ 100 Å). Thus in monoatomic tips the field emission at high emission currents is expected to lead to strong excitation of phonons near the apex of the tip in contrast to the behavior of macroscopic tips.

3. Energy Dissipation in Tunneling Microscopy

3.1 INTRODUCTORY REMARKS

In scanning tunneling microscopy (STM), when a small voltage U (usually below 1 V) is applied and electrons are tunneling (tunneling current I) from the tip to a conducting substrate (or vice versa), it is of great interest to know, where the power $P = I \cdot U$, which is supplied by the external power source, is deposited, only in the substrate or in the tip or in both. Unfortunately there are very few experimental data available to clarify this rather basic question. In order to investigate this problem it is necessary to use microscopic thermometers.

The first thermal measurements with high local resolution were carried out by R. Dahlberg [14]. Using sharp glass needles onto which two different metals were evaporated from opposite sides he was able to prepare an extremely fine thermocouple at the apex of the tip. Combining a similar design with the technology of a scanning tunneling microscope (STM) Williams and Wickramasinghe [15] developed a scanning thermal profiler with a lateral resolution of better than 100 nm and a sensitivity of about 1 mK at room temperature.

Using tip and sample of different materials and thus with different thermoelectric coefficients

the tunneling gap of the STM itself can act as a microscopic thermocouple. Weaver et al. [16] used this technique to measure the lateral variation of a temperature difference across a sample with high resolution. More recently Williams and Wickramasinghe [17] were even able to measure the local variation of the thermoelectric coefficient of a crystalline sample on an atomic scale.

Shklyarevskii et al.[18] observed surprisingly a strong thermoelectric voltage at a point contact made of two identical gold electrodes in the presence of a temperature gradient. This very interesting discovery they explained by the suppression of the phonon drag contribution to the thermoelectric voltage only in the point contact but not in the external circuit.

Stovneng and Lipavsky [19] finally estimated theoretically the thermoelectric voltage between two metallic electrodes, which are kept at different temperatures at a distance small enough to allow electronic tunneling between them.

In all experiments mentioned above external heating has been applied to the tunneling contact. Subject of this section is an experimental investigation of the heat created internally by the tunneling electrons. In our experiments described here the energy dissipated by the tunneling electrons is measured by a small thermocouple mounted on the substrate directly underneath the tip of the STM. For the analysis of our results we adopted the theoretical procedure described by Simmons [20].

3.2 EXPERIMENTAL PROCEDURE

The experiment has been performed in air by using a standard STM [21] which allowed a precise positioning of the tunneling tip above the center of a small "thermocross" mounted on

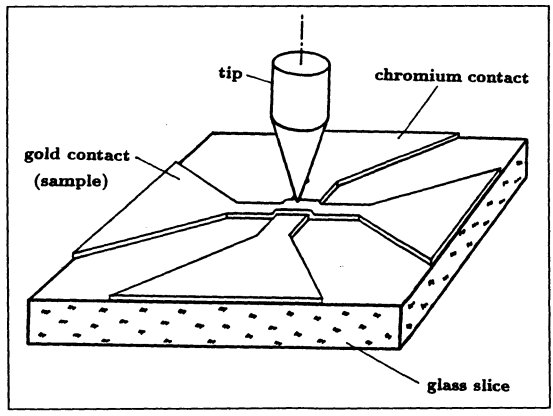

Fig. 2 View of the thermoelectric cross made up by two crossed films of chromium (or (Ag90/Cu10)) and of gold on a glass slide (dimensions: 15 x 12.5 x 0.13 mm). Both films have a thickness of 150 nm, a width of 7 μm and a total length of 200 μm. The tip material was in general also gold.

a glass slide. A schematic drawing of the thermocross is shown in fig. 2. It was produced by sequentially evaporating first a film of chromium (or of Ag90/Cu10) onto the glass slice and covering it later on by a gold film of the shape shown in fig. 2. The feedback loop of the STM adjusts the distance between tip and gold film (sample) in such a way that the actual tunneling current equals a preset value which has a dc- and a modulating ac-component. We have used modulation frequencies between 35 and 150 Hz, well below the thermal relaxation rate of the thermocross (125 kHz) and also below the cut-off frequency of the feedback loop. Thus the position of the tip could be adjusted fast enough to reach the modulated preset

value of the tunneling current. The dc. current ranged between 60 and 1500 nA and was typically modulated from almost zero to twice the dc. value.

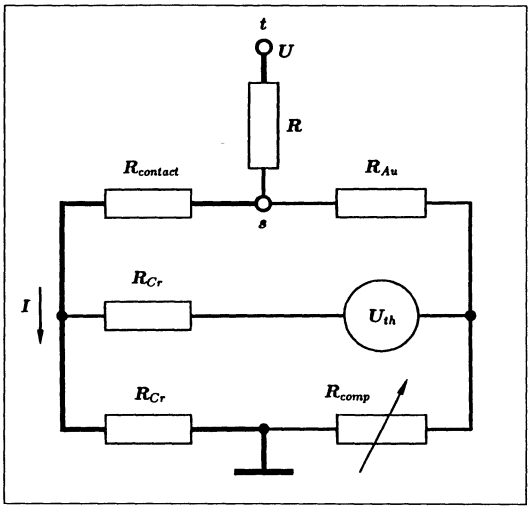

Fig. 3 The electrical bridge circuit which was used to cancel the ohmic voltage between the chromium- and gold-film of the thermocross shown in fig. 2 in the presence of the ac-tunneling current. U is the bias voltage, R the tunneling resistance and U_{th} the thermoelectric voltage.

The electric circuit to detect the thermoelectric signal U_{th} is shown in fig. 3. The modulated tunneling current I flows through the gold/chromium junction symbolized by $R_{contact}$ and along one leg of the chromium electrode to the ground. The ohmic voltage drop in our contact which might have interfered with the thermoelectric voltage of the contact, can be compensated to zero by a variable resistance of R_{comp} which allows part of the tunnel current to flow along the gold film to the ground. R_{comp} was adjusted such that no ohmic signal occurred between the two metals of the thermocross. This adjustment was performed at almost zero bias where no thermoelectric signal was expected. The thermoelectric voltage was measured by a preamplifier connected to the other sides of the chromium and the gold electrode, respectively. The thermovoltage is amplified by a low noise differential amplifier with a very high common mode rejection ratio (of about 150 dB). Connected to the thermocouple and the microscope the spectral density of the voltage noise was about 6nV/√Hz in the frequency range of interest. The output of the preamplifier is connected to a lock-in-amplifier to detect selectively the thermoelectric signal which is correlated to the modulation of the tunneling current.

3.3 EXPERIMENTAL RESULTS

Fig. 4 shows the thermoelectric voltage at the chromium/gold thermocross as a function of the applied bias voltage. Each curve represents an average over 20 sweeps during some tens of seconds. The modulation amplitude of the tunneling current has been varied between 100 and 1500 nA. Since the average tunneling current was kept constant for each voltage, the gap distance varied accordingly (becoming very small for low bias). The voltage range between -100 mV and +100 mV has been excluded to avoid too low tunneling resistances and damage to the sample.

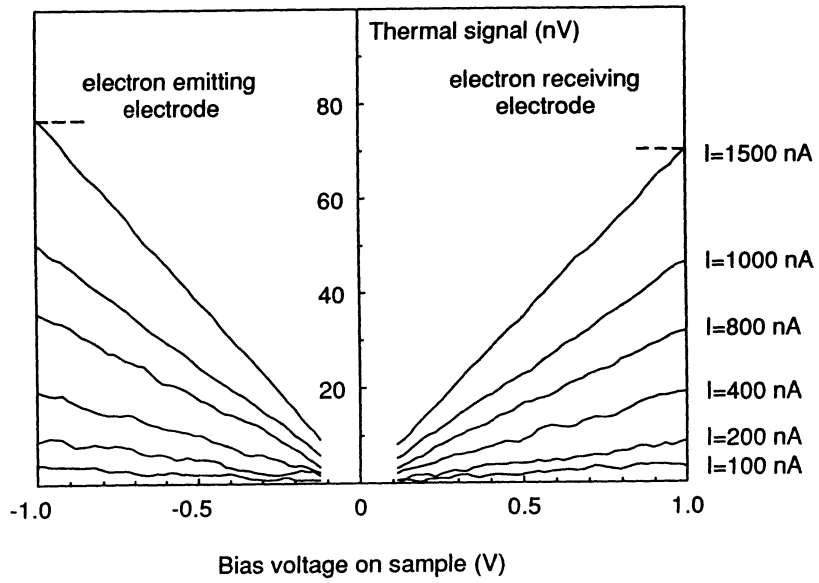

Fig. 4 *The measured thermoelectric voltage of the thermocross as a function of the applied bias voltage for both directions of the bias voltage. For each curve the average tunneling current is constant. The sensitivity of the thermocross was 10 μV/K.*

As can be seen from fig. 4 the thermoelectric voltage is to a first approximation proportional to the applied bias voltage and for low tunneling currents nearly independent of the polarity of the bias. Only at the highest currents (above 1000 nA), more heat seems to be deposited in the thermocross when it acts as an *emitter* of electrons (see left side) and less when it *receives* the same electronic current (right side).

To verify the data the experiment was repeated with another thermocouple made up by a (Ag90/Cu19)/gold contact instead of the chromium/Au junction. The sensitivity was smaller (2.5 μV/K instead of 10 μV/K), but the basic results remained unchanged. The signal also decreased as expected if the tip was moved laterally along the gold stripe some ten microns from the center of the thermocouple. Both tests show that there is no significant contribution to the measured signal by capacitive coupling etc. Since the experiment requires fairly high tunneling currents compared to standard STM practice, we tested that the surface is not modified by the strong tunneling current, especially at low bias voltages. We have recorded topographic images of the gold surface have been recorded switching at subsequent line scans back and forth between extreme conditions such as I = 800 nA and I = 15 nA (both at the same bias voltage of U = 20 mV). The sequential topographic images showed no differences.

Another effect which should be mentioned and which might, in principle, influence our measurements is the Peltier heating or cooling by the tunneling current flowing through the

thermocross. The Peltier heating or cooling is given by the product of thermopower of the thermocross, absolute temperature and tunneling current. However, for our maximum currents the corresponding temperature change would be smaller than 1 mK which is less than our lowest detectable signal. Furthermore it should depend only on the sign but not on the absolute value of the bias voltage in contrast to the observed heating which increases linearly with the voltage U for both polarities of U.

3.4 DISCUSSION

The energy diagram for the electronic tunneling process between the two identical gold electrodes is shown in fig. 5. Since the negative bias is applied to the left electrode the electrons are tunneling to the right. In general, not only electrons having the Fermi energy E_F

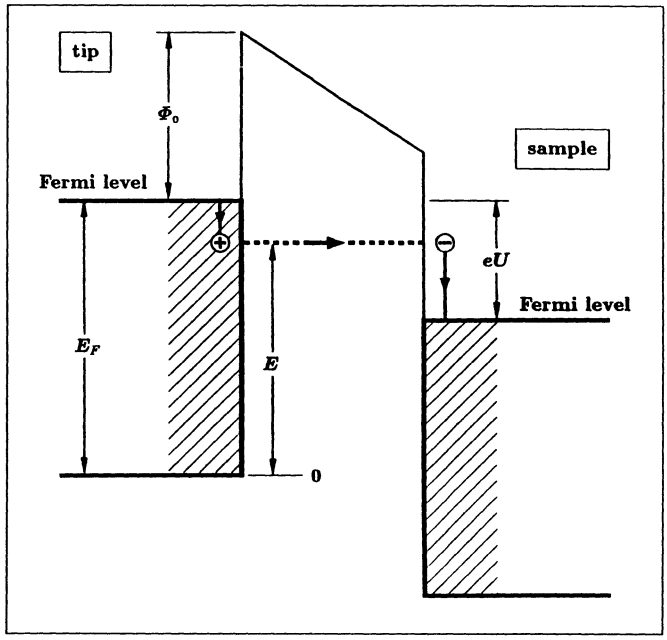

Fig. 5 Energy diagram for electrons tunneling from a gold tip (left) across an energy barrier to a gold substrate (right) for an applied bias voltage U. Φ_0 is the workfunction of Au and E < E_F is the energy of the tunneling electron.

are able to tunnel. Also electrons of lower energy E < E_F have a smaller but finite probability to tunnel across the gap. In this case the total energy eU supplied externally is - after the tunnelling - redistributed between both electrodes in the following way. At the left (emitting) electrode the hole - created by the departure of the electron - is filled from above and thereby the energy (E_F - E) is dissipated as heat there. At the right (receiving) electrode the remaining kinetic energy eU -(E_F - E) of the electron is deposited. The sum of both energies is just e·U.

To evaluate according to this model the partition of the total energy deposited between both electrodes in a more quantitative way one has to integrate the product [electronic energy]· [tunneling probability] over the relevant electronic energies. The theoretical procedure which we have followed has been described by Simmons [20]. The details of our calculation will be published separately. Here we will only discuss the result of this analysis: Fig. 6 shows the calculated ratio P_s/P_{1V} between the energy P_s deposited at the sample (emitting electrode in

this case) and the total energy P_{1V} (at U = 1 V) as a function of applied bias voltage. For positive values of U the sample is the electron receiving electrode while for negative values of U the sample becomes the electron emitting electrode, and with respect to fig 5 P_s becomes equal to P_t, which is the power deposited at the emitting tip. In accordance with our experimental situation (constant mean current, unknown tunneling distance d) P_s has been

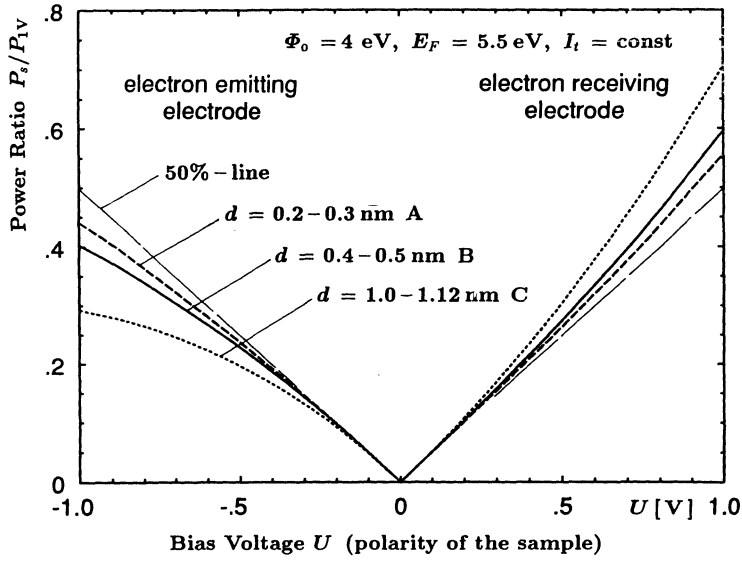

Fig. 6 *The power deposited at the substrate P_s divided by the total Power P_{1V} (at U = 1 V) as a function of the applied bias voltage for three ranges of tunneling distances related to three constant tunneling currents as calculated for the model of fig. 5 following the computational procedure of Simmons [20]. More energy is deposited in the receiving electrode rather than in the emitting electrode. This behaviour becomes especially pronounced at the higher bias voltages and the larger tunneling distances d.*

calculated for three values of the tunneling current (related to d = 0.2, 0.4 and 1.0 nm at U = 0.1 V). In order to keep the current constant in the whole voltage range the distance must be varied in accordance with the change of the bias voltage. The resulting ranges for d for the curves A,B and C are 0.2 - 0.3 nm, 0.4 - 0.5 nm and 1.0 - 1.1 nm respectively. Our calculations were based on a Fermi energy of 5.5 eV and a work function of Φ_0 = 4 eV for gold and a rectangular potential well. Following calculations by N.Lang [22] the absolute distance between tunneling tip and sample can be estimated from the tunneling resistance for the given parameters of our experiment. This leads to an absolute distance of 5 Å for a bias voltage of 0.1 eV and a tunneling current of 500 nA, corresponding to curve B in fig. 6.

As can be seen from a comparison between the left and right curves (in fig. 6, at negative and positive bias, respectively) the power deposited at the emitting electrode P_t should always be lower than 50% of the total power, in contrast to the power P_s (= P_{1V} - P_t) dissipated at the receiving electrode (positive bias) which is expected to always exceed 50% This difference

becomes more pronounced at high bias voltages and small tunneling distances as shown in fig. 6, and is a consequence of the standard assumption that electrons of higher energies contribute more strongly to the tunneling current. Clearly, our calculation shows a *nonlinear* dependence of both powers P_t and P_s on the bias voltage. Only for a small bias the relationship becomes linear, when the same power is dissipated on both electrodes.

As pointed out by Flores et al. [23] in principle two mechanisms contribute to the energy dissipation of the tunneling electrons. For lower energies the electrons can penetrate into the receiving electrode for a depth according to the mean free path which is typically several tens of nanometers. For higher energies the excitation of cascades of electron hole pairs becomes important forcing the electrons to depose their energy into a very thin surface region having a depth of only about 0.5 nm. This effect influences only the volume where the energy is dissipated but not the total energy deposited there.

In contrast to the theoretical expectations shown in fig. 6 the experimental data (fig. 4) show a strictly linear dependence of the deposited powers on the bias voltage. With the exception of the high current results ($I_t \geq 1000$ nA, to be discussed later) our data show symmetry with respect to the polarity: The same power is deposited in the emitting and in the receiving electrode. To explain this discrepancy an important experimental condition has to be considered: Since the experiments described here have been performed in air a strong thermal coupling between tip and sample by a thin film of adsorbed vapors (for example of water) cannot be excluded. Such a strong thermal coupling between tip and sample would lead to an effective elimination of the asymmetry between negative and positive bias or between the energy deposited at the tip and the sample due to the nearly complete exchange of heat between tip and sample.

To clarify if the energy is deposited asymmetrically it would be highly desirable to perform the experiments under ultrahigh vacuum (UHV) conditions: In the absence of adsorbed vapor films the disturbing thermal coupling between tip and sample would be substantially reduced: In perfect vacuum the remaining mechanisms of heat transfer across the gap, for example by the tunneling electron [24] or by electromagnetic coupling [25, 26] are considerably smaller.

If one compares the experimental curves of fig. 4 with the theoretical expectations (fig. 6) there is surprising disagreement *for high tunneling currents* ($I > 1000$ nA). The experimental curves of fig. 4 (upper curves, left and right) indicate that - for the highest currents and the highest bias voltages - more power is deposited in the emitting electrode than in the receiving electrode. This is in fundamental contradiction with the theoretical expectation of fig. 6 which predicts, in contrast, that the highest power should always be dissipated in the receiving electrode. This discrepancy, which only occurs at high currents, high bias voltages and at close tunneling distances, remains puzzling. It cannot be explained by the standard theory of tunneling in the free electron model nor by a thermal coupling between tip and sample. In fact, without the presently existing thermal coupling (due to adsorbed films) the discrepancy between observation and theory would be even greater. This is one more motivation to repeat our experiments in ultra high vacuum.

This discrepancy between our observations and the the theoretical expectations can neither be explained by the assumption that - due to the smaller radius of curvature of the tip relative to the substrate - the gap distance and thus the thermal resistance between tip and substrate may depend on the polarity of the bias. This effect if detectable would not act in a direction to explain our observations.

Finally, it is interesting to note that both in the case of field emission discussed in section 2 and in the case of tunneling microscopy treated in this section the experimental evidence indicates that at high currents more energy is dissipated in the emitting electrode than one can account for by the classical theory of tunneling. The electrons are leaving the emitting electrode with less energy than theoretically expected.

4. Conclusion

In this paper we have discussed first the energy delivered to a monoatomic tip in the field emission process. From an analysis of recent experimental data on monoatomic tips which clearly show that the field emitted electrons leave the tip with a surprisingly low average energy we conclude that strong phonon excitation is expected to occur for an emission current exceeding 1 nA.

In the second part of this paper we discussed the heat which is generated in the electrodes of a scanning tunneling microscope due to electronic tunneling. We presented first experiments in air with a resolution of 10 nW. The experimental data reveal that at low tunneling currents the thermal energy deposited in the emitting and receiving electrodes are equal and proportional to the electric bias voltage applied between the electrodes. The heating effects in both electrodes are in this case independent of the polarity of tunneling current and bias voltage. No support is seen from our data for the theoretical expectation that the receiving electrode should be heated stronger than the emitting electrode. At high tunneling currents the reverse seems to be true: Our high current data indicate that it is the emitting electrode which is heated strongest. Since the experiments have so far been performed in air there is probably a strong thermal coupling between tip and substrate in our experiments due to the presence of adsorbed vapors. This, however, only partially acounts for the discrepancy between our observations and the theoretical analysis presented above. It seems highly desirable to perform the same experiments under ultrahigh vacuum conditions to prevent the strong thermal contact between both electrodes.

In conclusion, it is interesting that both for field emission and for STM- tunneling there seems to be more power deposited in the emitting electrode than a simple theoretical treatment of the tunneling process can account for. We have proposed here that a new process of phonon emission at the emitting electrode may be responsible for the extra energy deposition there. Before discussing the possible physical mechanisms of phonon generation at the emitting tip, it seems at present more important to repeat our experiments under UHV-conditions

5. Acknowledgements

We greatly appreciate the experimental help and advice we received from Ch. Baur and B. Koslowski. This work has been partially supported by the Deutsche Forschungsgemeinschaft (SFB 306).

References

[1] W. W. Dolan, W. P. Dyke and J. K. Trolan; Phys. Rev. **91**, 1054 (1953)

[2] W. B. Nottingham; Phys. Rev. **59**, 907 (1941)

[3] see for example : N. M. Miskowsky, S. H. Park, J. He and P. H. Cutler; in print (1992)

[4] I. Engle and P. H. Cutler, Surf. Sci. **8**, 288 (1967)

[5] M. Drechsler; Z. Naturforsch. **18a**, 1376 (1963)

[6] L. W. Swanson, L. C. Crouser and F. M. Charbonnier; Phys. Rev. **151**, 327 (1966)

[7] H. Bergeret, A. Septier and M. Drechsler; Phys. Rev. **B31**, 149 (1985)

[8] R. Gomer, "Field Emission and Field Ionisation", Harvard Monographs in Applied Science 9, Cambridge, USA (1961)

[9] see for example: H. W. Fink; Physica Scripta **38**, 260 (1988) and Phys. Rev. Lett. **67**, 1543 (1991)

V. T. Binh and N. García; J. Phys. I, **1**, 605 (1991) and Ultramicroscopy, in print (1992)

[10] V. T. Binh, S. T. Purcell, N. García and J. Doglioni; in print (1992)

[11] C. E. Kuyatt and E. W. Plummer; Rev. Sci. Instru., **43**, 108 (1972)

[12] see for example: H. Kuzmany: "Festkörperspektroskopie", Springer-Verlag, (1989), p. 155

[13] P. H. Cutler, J. He, N. M. Miskovsky and T. E. Sullivan; in print (1992)

[14] R. Dahlberg; Z. Naturforsch. **10a**, 953 (1955)

[15] C. C. Williams and H. K. Wickramasinghe; Appl.Phys.Lett. **49**, 1587 (1986).

[16] J. M. R.Weaver, L. M. Walpita, and H. K. Wickramasinghe; Nature **342**, 783 (1989).

[17] C. C. Williams and H. K. Wickramasinghe; Nature, **344**, 317 (1990).

[18] O. I. Shklyarevskii, A. G. M. Jansen, J. G. H.Hermsen and P. Wyder; Phys.Rev.Letters, **57**, 1374 (1986)

[19] J. A. Stovneng and P. Lipavsky; Phys.Rev. **B42**, 9214 (1990).

[20] J. G. Simmons; J. Appl. Phys. **34**, 1793 (1963)

[21] for further details see: R. Möller, A. Esslinger and M. Rauscher; J. Vac. Sci. Technol. **A8**, 434 (1990)

[22] N. D. Lang; Phys. Rev. **B36**, 8173 (1987)

[23] F. Flores, P. M. Echenique, and R. H. Ritchie; Phys.Rev. **B34**, 2899 (1986).

[24] M. Kohler; Ann. d. Physik, **38**, 542 (1940)

[25] D. Polder and M. Van Hove; Phys.Rev. **B4**, 3303 (1971).

[26] K. Dransfeld and J. Xu; J. Microscopy, **152**, 35 (1988)

MINIATURIZED ELECTRON MICROSCOPE

U. STAUFER
Institute of Physics, University of Basel,
Klingelbergstrasse 82,
4056 Basel (Switzerland)
L.P. MURAY
National Nanofabrication Facility at Cornell,
Cornell University Knight Laboratory,
Ithaca, NY 14853-5403 (USA)
D.P. KERN and T.H.P. CHANG
IBM Research Division,
T.J. Watson Research Center, P.O. Box 218,
Yorktown Heights, NY 10598 (USA)

ABSTRACT. Useful probes for conducting experiments in the low nanometer and atomic scale range are either ultra sharp tips of scanning proximity probe microscopes e.g. in the STM or AFM, or highly focused particle beams. Electron- or ion-beams are very attractive in view of their flexibility, the working distance and the relatively high writing speed in lithographic applications.

The invention of point-sources and the development of micro-lenses now offer a new approach to ultra fine particle beam formation without the need of high particle energies. Because of the small size of a point source, it needs not to be demagnified. In addition, the reduced aberrations of a micro-lens system allow high brightness to be achieved. Thus, even at low voltages, small beam diameters with high beam currents can be obtained.

1. Introduction

Experiments on surface examination and modification with resolution in the low nanometer to atomic scale range have to deal with the same challenge: the probing "tool" has to be ultra sharp. There are several approaches to solve this problem. One possibility is to make use of three dimensionally confined proximity effects, such as the tunneling electron current from a sharp tungsten tip, e.g. in the scanning tunneling microscope (STM). In other techniques particle beams are applied. These beams can either be used for direct probing if focused by a suitable lens system, e.g. in the scanning electron microscope (SEM). Alternatively, in a recently introduced projection electron microscope (PEM) [1], coherent electrons, field emitted from a point source, are used to generate a high resolution interferogram of the sample. In a STM like set-up, the tunneling tip is replaced by a single-atom

V.T. Binh et al. (eds.),
Nanosources and Manipulation of Atoms Under High Fields and Temperatures: Applications, 101–110.
© 1993 *Kluwer Academic Publishers.*

tip, which serves as an electron point-source, and the sample acts simultaneously as anode. This approach to electron microscopy circumvents the problems arising from aberrations of any beam forming system. However, the PEM has the drawback that the source must be operated in close proximity to the sample in order to get a high magnification. Therefore, the risk of ruining the source by inadvertent contact with the sample always exists.

In this article we report about a new method of generating highly focused low energy particle beams, which combines some of the advantages of a point-source, namely the high brightness and coherence, with the flexibility of a lens formed probe. Though the article deals explicitly only with the generation of an electron probe, an extension to ion and proton beams respectively is implied and in most cases is straight forward.

Forming an image by means of free electrons implies, that the paths of all electrons passing through one point of the left side, the object space, of the optical system will meet again in exactly one point at the right side or image space. It is known, that electric and magnetic fields which have rotational symmetry with respect to an axis, say the z-axis of a coordinate system, can be used to form such an optical system [2]. However, the electron trajectories fulfill the requirements mentioned above only in a first order approximation. This approximation is also called Gaussian approximation. It applies only to paraxial electron paths, which have a smooth slope and are in proximity to the axis of symmetry. Such an electron optical system can be characterized by the Gaussian focal length. Any deviation from the paraxial approximation by the real trajectories is considered as a geometrical aberration of the optical system. Also variations in the electron energy or instabilities in the fields will move the actual focal plane away from its Gaussian position, and, as in light optics, this is referred to as chromatic aberration. Compared to light optics, particle optics suffers from large aberrations, and, in addition, the aberration coefficients of different round lenses all have the same sign. Therefore, aberrations cannot be compensated by a combination of different types of lenses.

1.1 MOTIVATION FOR MINIATURIZING PARTICLE LENSES

Micro-miniaturization of electron and ion optical systems offers an opportunity to minimize the problems mentioned above. Electron trajectories and thus parameters such as beam diameter and aberration disks scale directly with the dimensions of the electrode and magnet structures when certain rules about electron energy, electrode potentials, and magnetic field strengths are satisfied. Therefore, the aberrations of a microminiaturized lens system can be significantly reduced. This is especially interesting if the microlenses are combined with a point-source. In such a device, exceptionally high values of beam brightness and coherence at low energy levels will be achievable. Further attractive features of a micro column are:

First, its compactness is appealing for many new applications such as parallel processing in electron beam lithography, testing and inspection, or, in general, for any application where space is limited.

Second, the small volume of the source together with the greatly reduced bore diameters of the lenses make the microcolumn well suited for environmental-SEM. In this special version of electron microscopy, only the source is kept at ultra high vacuum conditions, whereas the pressure in the specimen chamber can be relatively high. This enables, for example, the *in vivo* investigation of biological material.

Third, a significantly reduced column length offers better immunity to external interferences.

Forth, microcolumns can be mass-produced with microfabrication techniques. This will eventually reduce production costs.

1.2 BASIC LAYOUT OF THE MICROCOLUMN

A first version of a microminiaturized scanning electron microscope based on field emission source [3-5] and electrostatic microlenses has been realized. A cross-section of this microcolumn is shown in Fig. 3, and its electron optical performance will be discussed in some detail in the next paragraph. The principle components are described as follows: The STM feedback mechanism is used for precise x, y, and z alignment of the field emission tip relative to a dual electrode immersion microlens. Together, these components form the electron source of the microcolumn. One of the main advantages of this STM aligned field emission (SAFE) source is, that the STM feedback loop can be used to improve emission stability. Also, the tip can be prepared away from the lenses, thus allowing freedom for the selection of tip materials and tip preparation techniques, including the use of single atom tips [6] for optimum performance. In order to deflect the beam, an eight pole scanner/stigmator was placed between the microsource and the einzel lens. The last element in the SAFE microcolumn is the probe forming einzel lens. For convenience in column fabrication, the limiting aperture has been incorporated into the last lens electrode.

Another STM based microsource with magnetic focussing has also been introduced [7] and was recently realized [8].

2. Electron Optical Considerations

The overall performance of a microprobe system can be evaluated by separately characterizing the source and the probe forming lens first. The properties of the microsource are analyzed by replacing the emitter by a virtual source d_0. The dual electrode accelerator structure performs as an imaging lens to form an intermediate image of the source [9]. The intermediate image, which might be again virtual, has a diameter d_1 and represents the effective source size of the microsource. It can be expressed as:

$$d_1 = M_1\sqrt{d_0^2 + d_d^2 + d_{so}^2 + d_{co}^2} \ , \tag{1}$$

where M_1 is the magnification of the mircosource and d_0 the virtual source size. $d_d(= 1.5/\alpha_0\sqrt{V_1})$ is the diameter (in nm) of the diffraction disk with V_1 being the voltage (in V) of the first electrode and α_0 being the beam semiconvergent angle at the tip (see also Fig. 1). $d_{so}(= 0.5C_{so}\alpha_0^3)$ is the spherical aberration disk with a coefficient C_{so} referred to the object space. $d_{co}(= C_{co}\alpha_0\Delta V/V_1)$ is the chromatic aberration disk also referred to the object space with ΔV being the energy spread of the electron beam. The final spot d_2 after the probe forming lens can be expressed as:

$$d_2 = \sqrt{M_2 d_1^2 + d_{s2}^2 + d_{c2}^2} \ , \tag{2}$$

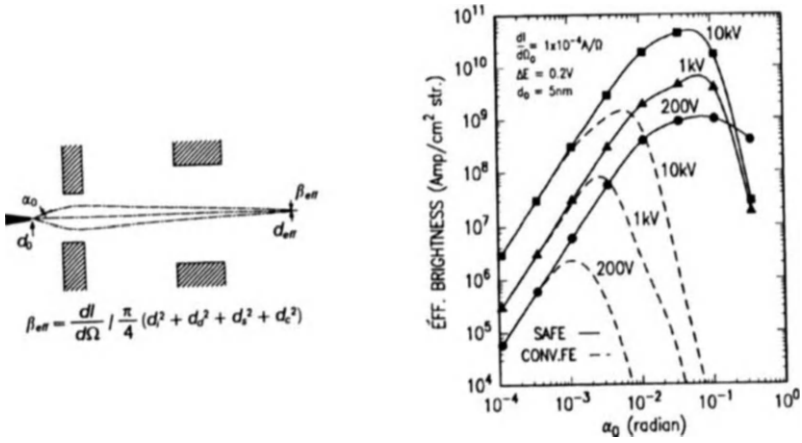

Figure 1: *The effective brightness of a selectively scaled microsource and a conventional field emission source at three potentials. (Taken from [10].)*

where M_2 is the magnification of the lens. $d_{s2}(= 0.5C_{s2}\alpha_2^3)$ and $d_{c2}(= C_{c2}\alpha_2\Delta V/V_2)$ are the spherical and chromatic aberration disks, respectively, of this lens with C_{s2} and C_{c2} being its spherical and chromatic aberration coefficients referred to the image space and V_2 being the final beam potential. Substituting d_1 in Eq. (2) by Eq. (1) and replacing α_2 by:

$$\alpha_2 = \frac{\alpha_1}{M_2} = \frac{\alpha_0}{M_1 M_2}\sqrt{\frac{V_1}{V_2}} \quad , \tag{3}$$

an expression relating d_2 to the source can then be established. In this expression, the only parameters that can be varied are α_0 and M_2. Since for small α_0 the beam current I_2 is related to α_0 by:

$$I_2 = \pi\alpha_0^2 \frac{dI}{d\Omega_0} \quad , \tag{4}$$

where $dI/d\Omega_0$ is the angular emission density of the tip, one can therefore relate d_2 to I_2 with M_2 being the variable. An optimum M_2 value can be found for each I_2 value to give a minimum for the probe diameter d_2.

2.1 SELECTIVE SCALING

In the conventional scaling approach for a lens, all dimensions are uniformly reduced by a fixed factor. However, this will increase the electric fields by roughly the inverse value of the scaling factor. The field can easily exceed the voltage breakdown threshold rendering the scaled structure impractical. In the selective scaling approach [11], one applies judiciously different scaling factors to different parts of the lens to maintain the aberration reduction of the fully scaled case, while allowing a wide range of potentials to be applied.

The following aberration coefficient values for a selectively scaled 1 keV microsource have emerged from a third order aberration analysis:

TABLE 1. *Spherical and chromatic aberration coefficients of a microsource (a) compared to a conventional system (b).*

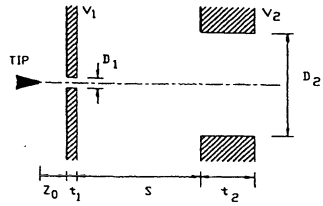

	V_1	V_2	D_1, t_1, z_0	s
(a)	100 V	1kV	$\simeq$ 1 μm	100 μm
(b)	3 kV	1kV	$\simeq$ 1-3 mm	3 mm

	D_2	C_{so}	C_{co}
(a)	100 μm	3.5 μm	3.7 μm
(b)	1.5 mm	70 mm	20 mm

Using these aberration coefficients the effective brightness β_{eff} of the microsource can be computed. In Fig. 1, β_{eff} is plotted against the emission half-cone angle α_0, which is defined by the limiting aperture. At low values of α_0, diffraction dominates the performance yielding a relatively low effective brightness for both the conventional and the microsource. As α_0 increases, so does the brightness initially but it eventually begins to decline when the effects of the other aberrations start to exert themselves. The peak effective brightness corresponds to the condition that the effective source size is at a minimum.

Performance of einzel lenses has been extensively discussed in literature [12]. Based on a given working distance, various configurations for a miniaturized version have been evaluated [11]. The final design of the einzel lens is of a planar-electrode type, involving a careful trade-off between spherical and chromatic aberration.

The detailed analysis of the two components of the microcolumn can be combined to give an assessment of the system performance. In Fig. 2 the calculated beam current for three different working distances W is depicted as function of the beam diameter. It can be seen that the optical performance of the miniaturized column exceeds or approximately equals that of conventional systems at currents that are 2 to 3 orders of magnitude higher

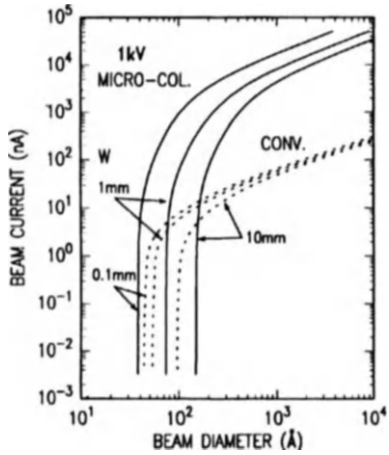

Figure 2: *Performance of a microprobe system compared to a conventional field emission system. The calculated beam current for three different working distances W is depicted as function of the beam diameter. (Taken from [10].)*

for the range of potentials and working distances studied.

3. Microcolumn Fabrication

3.1 TIP PREPARATION

Many different recipes for field emitter preparation are known in literature [13-17]. Based on this knowledge, a technique for producing tips, which meet the special demands for microcolumn operation, was developed [18]. W< 111 > single crystal wire was spot welded to a tungsten filament. The filament wire has an overall length of about 6 mm, a diameter of 0.127 mm, and is bent to a hairpin shape with an angle of about 15°. This hairpin is spot welded to two thicker tungsten rods, which are brazed into a tubular ceramic base. The base has a diameter of three millimeters. The length of the whole assembly is approximately 14 mm. After electrochemically etching the wire to a sharp point and mounting the assembly into the UHV-system, a current of roughly 1.5 A is passed through the filament. By this, the filament and the tip will be outgased for about 20 minutes at 900 K. Afterwards, the tip is flash annealed in an electric field. In this final processing step the tip is reformed to a "build up" shape: the {211} planes are enlarged and the on-axis (111) plane shrinks to an atomic trimer. In future, these tips might also be replaced by single-atom [6] or protrusion tips [17].

3.2 LENS FABRICATION

The material of choice for the lens electrodes was highly boron-doped silicon membranes. These membranes provide a strong mechanical base, high conductivity, and compatibility with ultra-high resolution fabrication techniques. The membranes were also not prone to surface diffusion and "whisker" growth as observed in some metal films.

The membrane size was 1 mm on a side and 1-2 μm thick. On the first electrode, using electron beam lithography and reactive ion etching, 1 μm diameter holes were delineated in a 3×3 array with center-to-center spacing of 4 μm [19]. The array was used to assist in alignment and for redundancy in case one of the holes gets destroyed. The second and third electrode consisted of similarly prepared 100 μm holes. The fifth electrode, forming simultaneously the final lens element and the limiting aperture, was patterned with a single 5 μm hole. The fourth electrode, the center electrode of the einzel lens, was made out of a commercially available 2-3 μm thick silicon (100) wafer. In addition to the holes, registration marks for column alignment were patterned on each electrode except on the final one.

The octupole scanner/stigmator was machined from aluminum to a disk of 2 mm thickness and a diameter of 15 mm. Eight 0.5 mm Kapton coated Cu wires with polished end faces were inserted into the disk to serve as deflection electrodes. Spacing between the electrodes was 2 mm, corresponding to a calculated 4 μm square deflection field at the sample at $\pm$10 V.

The lenses were assembled by placing a 100 μm quartz spacer with a 2 mm hole between facing membranes. Alignment of the electrodes and the octupole scanner was achieved

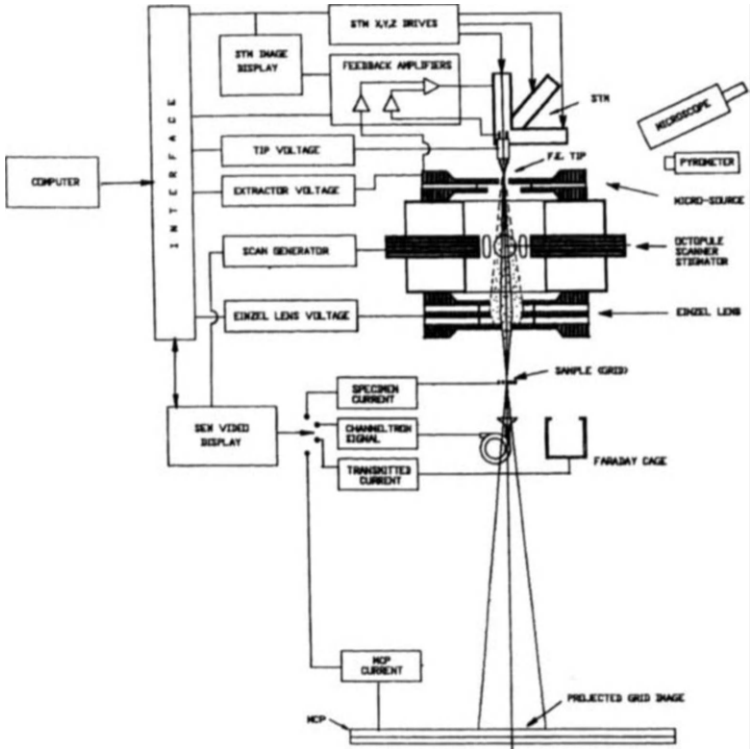

Figure 3: *Schematic drawing of the experimental set-up for testing the SAFE-microcolumn and cross-sectional view of the prototype microcolumn. (Taken from [20])*

under an optical microscope. The electrodes were bonded to the quartz spacer by means of an UHV-compatible epoxy and the lenses were attached to the octupole with Be-Cu springs and secured by a small amount of the same UHV epoxy. The total length of the lens system adds up to 2.5 mm, measured from the first electrode of the source to the final electrode of the einzel lens. Electrical contacts were provided by the Be-Cu springs and by an additional thin wire bonded to the center electrode of the einzel lens.

3.3 EXPERIMENTAL SET UP

A schematic drawing of the whole experimental set up is shown in Fig. 3. The complete lens system was mounted onto the sample stage of an UHV-STM, and the filament assembly was attached to the STM piezo scanner. The base pressure of the UHV system was usually around 2×10^{-10} torr. The test sample, a two-dimensional aluminum grid with 3 μm pitch and 1×1 μm^2 square holes, was mounted to a small sample stage, which itself was attached to the lens assembly. Outside the UHV chamber, a pyrometer was positioned to measure the tip temperature during its annealing procedure. In an STEM-like mode of operation, the

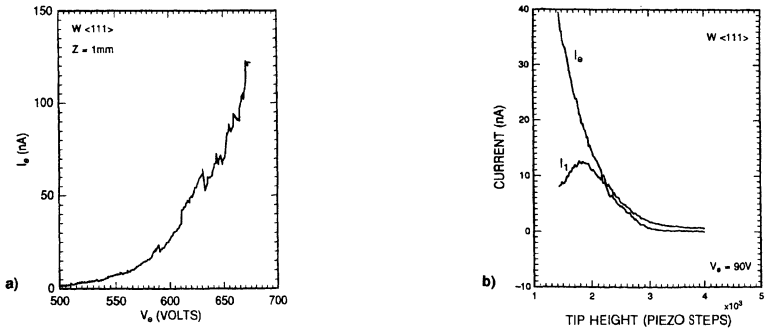

Figure 4: *Emission characteristic of a tip in the microsource. For details see text. (Taken from [20].)*

transmitted current as function of the beam deflection was measured with a channeltron, providing a low noise amplification of up to 10^5. The high gain of the channeltron allowed picoamp level images to be viewed at rates up to 4 frames per second.

4. Experimental Evaluation of the Microcolumn

The following procedure was used to align the field emission tip to the lens system. A rough positioning of the tip was performed using a long working distance optical microscope and alignment marks. Next, a negative potential was applied to the tip until field emission was achieved. Then the tip was scanned over a 10 μm field while digitally recording the transmission efficiency, which is given by one minus the total emission current divided by the current collected on the first electrode. Analogous to an STM image, a map of the electron transmission could be obtained. The resolution of this image was dependent of the height z_0 and the emission angle of the tip. Repeated reductions in z_0 and field emission scans eventually aligned the emitter precisely over the center of the hole.

4.1 SOURCE CHARACTERISTICS

The source performance was measured in terms of the emission characteristics of the tip and the focussing properties of the immersion lens [19]. In Fig. 4 the emission characteristics of a tip at a distance of 1 mm from the first electrode is shown. A typical Fowler-Nordheim behavior is observed and from the corresponding Fowler-Nordheim plot an effective tip radius of 24 nm is estimated. Due to field enhancement, the extraction voltage dropped when the tip was lowered to the surface. This behavior was only observed at small tip to first electrode distances and became more pronounced as the gap decreases. The resulting I versus z dependence can be used for stabilizing the emission current by the STM-type feedback loop. A typical total emission current I_e versus distance curve which defines the feedback characteristics is shown in Fig. 4b. The second curve of Fig. 4b shows the behaviour of current I_1, collected at the first lens electrode, as function of tip to electrode

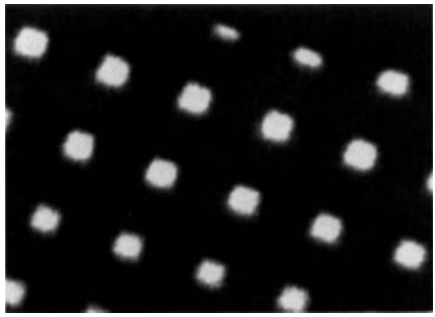

Figure 5: *Scanning image of the sample grid, generated by transmitted electrons. The center to center distance between two holes is 3 μm.*

separation. From these two curves, the transmission efficiency can be calculated. Values as high as 90 % have been observed.

4.2 SCANNING MICROSCOPY

In Fig. 5 a preliminary scanning transmission image formed by the microcolumn is shown. It is one of the first few results showing the operation of a complete microcolumn [20]. It was acquired without any correction for astigmatism. The image was generated using a channeltron to collect the electrons which have been transmitted through the sample grid. For focusing, the lens needed to be operated at about 400 V. Taking a single scan line from a similar picture, the beam diameter was estimated to be less than 200 nm at full-width-half-maximum. The beam current was between 10 - 20 pA for a total emission current of 0.5 μA. Several qualitative features are evident from the first few pictures. The large scan range, about 100 μm at $\pm$150 V is much grater than the limiting aperture. It is expected that, as the scan voltage is increased, more of the off-axis beam is utilized. This will increase the distortion in the image, which was, in fact, observed. The particular tip used in this experiment showed some instabilities in the emission current which were noticeable in the intensity variations along the scan lines. Sometimes, shadow or "ghost" images where observable next to the actual 1 μm squares. These were generated by secondary columns which are formed by the off-axis 1 μm holes of the 3$\times$3-array in the first electrode. The position of the images shifted as the tip position was moved, which supports this interpretation. By positioning the tip closer to the first electrode, less electrons could reach these off-axis holes and the effect is expected to fade out. Alternatively, the extraneous holes could be eliminated.

5. Summary

A short review on the approaches and performance of miniaturized electron microscopes has been presented. For a microcolumn based on field emission point-sources and microlenses,

theoretical analyses predict a 2-3 orders of magnitude improved brightness, compared to a conventional system. We have designed a prototype 1 keV electron microcolumn measuring 2.5 mm in length, which has been built using microfabrication technique. The performance of the microscope is currently under study. Preliminary experimental results have shown, that the beam diameter is less than 200 nm. Considerable improvement is expected with further refinement of the system.

Acknowledgements

We wish to acknowledge E. Bassous, K. Chan, H.-W. Fink, M. Hatzakis, M. McCord, F. Morgan, and S. Rishton for their contributions to this project. U. St. also acknowledges financial support by the "Wolfermann-Nägelin" Foundation.

References

1. H.-W. Fink, H. Schmid, H.J. Kreuzer, and A. Wierzbicki, Phys. Rev. Lett. **67**, 1543 (1991).
2. See any text book on particle optics (e.g.: J. Grosser, *Einführung in die Teilchenoptik*, Teubener, Stuttgart 1983.)
3. D.W. Tuggle, J.Z. Lin, and L.W. Swanson, J. of Microscopy **140**, 293 (1985)
4. J. Orloff and L.W. Swanson, J. Appl.Phys **50**, 2494 (1979).
5. J.C. Wiesner and T. E. Everhart, J. Appl. Phys. **44**, 2140 (1973).
6. H.-W. Fink, W. Stocker, and H. Stocker J. Vac. Sci. Technol. **B8**, 1323 (1990).
7. L.S. Hordon, and R.F.W. Pease, J. Vac. Sci. Technol. **B8**, 1686 (1990).
8. B.D. Terris, and D. Rugar, Proc. of 50th EMSA Meeting 1992.
9. D. Kern, D. Kurz, and R. Speidel, Optik **52**, 61 (1978).
10. T.H.P. Chang, D.P. Kern, M.A. McCord, L.P. Muray, J.Vac.Sci.Technol. **B9**, 438 (1991).
11. T.H.P. Chang, D.P. Kern, and L.P. Muray, J. Vac. Sci. Technol. **B8**, 1698 (1990).
12. P.W. Hawkes, and E. Kasper, *Principles of Electron Optics*, Academic, New York 1989.
13. L.W. Swanson, and L.C. Crouser, Phys. Rev. **163**, 622 (1967).
14. P.C. Bettler, and F.M. Charbonnier, Phys. Rev. **119**, 85 (1960).
15. A.P. Janssen, and J.P. Jones, J. Phys. D **4**, 118 (1971).
16. L.H. Veneklassen, and B.M. Siegel, J. Appl. Phys. **43** 1600 (1972).
17. Vu Thien Binh, J. Microsc. **152**, 355 (1988).
18. U. Staufer, L.P. Muray, D.P. Kern, and T.H.P. Chang, J. Vac. Sci. Technol. **B9**, 2962 (1991).
19. L.P. Muray, U. Staufer, D.P. Kern, and T.H.P. Chang, J. Vac. Sci. Technol. **B9**, 2955 (1991).
20. L.P. Muray, U. Staufer, D.P. Kern, and T.H.P. Chang, to be published in J. Vac. Sci. Technol. Nov/Dec (1992).

DIRECT OBSERVATION OF THE MOTION OF INDIVIDUAL SURFACE ATOMS ON A PICOSECOND TIMESCALE

HARRY HEINZELMANN [a], GARY M. MCCLELLAND,
and FUMIYA WATANABE
IBM Research Division
Almaden Research Center
San Jose, CA 95120-6099 USA

[a]present address: Institute of Physics, University of Basel, Klingelbergstrasse 82, CH-4056 Basel, Switzerland

ABSTRACT. A new instrument, the femtosecond field emission camera (FFEC), has been developed which is capable of following the motion of individual surface atoms in real time at 100 fs resolution. On a field emitting tip, the motion of surface atoms modulates the electron tunneling barrier and thus the intensity of the field emission. In the FFEC, the time dependence of field emission is measured by tightly focussing the field emitted electrons into a beam which is electrostatically swept across a detection screen, as in a streak camera. The motion of single Cs adatoms on an oxidized W(111) tip has been recorded at a time resolution of 2 ps.

The dynamics of atoms and molecules on surfaces determine the rates of adsorption, desorption, diffusion and chemical reactions. The time scale of atomic motion, determined by the vibrational frequency (10^{12}-10^{14} Hz), is so fast that it is experimentally very difficult to access. The kinetic behavior of matter has long been investigated, but only with the development of subpicosecond pulsed lasers has it been possible to temporally resolve atomic motion [1, 2]. Those experiments use a pump-probe scheme: an ensemble of sample molecules is optically pumped at a time t_0 and spectroscopically probed at a well-defined later time t_1. Since the optical interrogation disturbs the sample, in order to get a complete temporal record of atomic motion, the experiment must be repeated many times on identically prepared ensembles of molecules, while scanning the time interval t_1 - t_0. To enable a more direct measurement, we have developed a new field emission method to continuously observe a single atom's dynamics during spontaneous events. A full description of the instrument and observations of Cs atom motion on a clean (non-oxidized) tungsten tip have been described elsewhere [3].

V.T. Binh et al. (eds.),
Nanosources and Manipulation of Atoms Under High Fields and Temperatures: Applications, 111–113.
© 1993 *Kluwer Academic Publishers.*

Field emission (FE) from a sharp tip conveys information about the tunneling barrier penetrated by the emitted electrons. The size and shape of the barrier is influenced by the species and position of the foremost tip atoms. We therefore analyze the temporal behavior of the FE current to observe the motion of the tip atoms. To obtain a sufficiently high emission rate, we use tips described by Fink which emit currents as high as 10 μA from a tip apex of only three atoms [4, 5]. A current of 10 μA corresponds to 63 electrons per picosecond, allowing a temporal resolution of 0.03 ps. (By operating in a pulsed mode, it is likely that this maximum current can be increased by a factor of 3). This scheme is the extension of former FE studies where, on a much slower time scale, fluctuations in the FE current were used to study flipping of a single molecule [6] or diffusion of an ensemble of atoms [7].

In our instrument, which we call the femtosecond field emission camera (FFEC), field emitted electrons are focussed into a narrow beam which is electrostatically swept across a microchannel plate (MCP) electron detector. The FFEC is similar to an optical streak camera, but is not subject to a streak camera's fundamental limit of time resolution. In the FFEC, the electrons are initially accelerated in the very high field at the tip, so that the initial velocity distribution of the electrons causes little loss in time resolution. The design of the focussing optics is adapted from standard designs for electron microscopes [8]. By focussing only in one dimension, and sweeping perpendicular to the focus line, we can achieve one-dimensional spatial resolution on a slightly longer time scale.

Here we describe observations of the motion of an adsorbed Cs atom on an oxidized tungsten tip. A W(111) tip, thermally formed at the corner of three {211} planes [4, 5], is exposed to 30 Langmuir of O_2. The narrowness (5 °) of the field-emitted beam confirms the small size of the emitting area. Because the adsorption of Cs lowers the work function dramatically, the hopping of a single Cs atom between surface sites can be unequivocally identified in a FE image recorded with low current (< 1 nA). An atom is deposited by exposing a 90 K tip to a very low flux of Cs until the appearance of a bright spot signals the landing of the atom. To record atomic motion, the tip is pulsed negatively for a few ns, raising the field emission current to several μA and vibrationally exciting the Cs atom, which may jump to another site. During the pulse the electron beam is electrostatically swept across the MCP. After the pulse, when the Cs atom is at rest, its new position is reflected in the static FE image recorded at low current. In the first three traces of Fig. 1 rapid changes in the FE are observed, indicating the motion of a Cs atom onto a site near the tip apex where FE into the lens is promoted. In the second trace, the rapid rise indicates that the atom has changed sites within the 2 ps separation of the data points. In the final trace, little has happened.

Our measurements are a factor of 10^6 faster than any previous observations of the motion of single atoms [9]. By using higher emission currents, improving detection efficiency, and increasing the beam sweep rate, we should be able to resolve atomic and molecular motion on the vibrational time scale.

This work was partially supported by Office of Naval Research Contract N00014-88-C-0419 and Air Force Office of Scientific Research Contract F49620-89-C-0068. H.H. wants to acknowledge support from the Swiss National Science Foundation and the Treubelfonds, Basel, Switzerland, for fellowships.

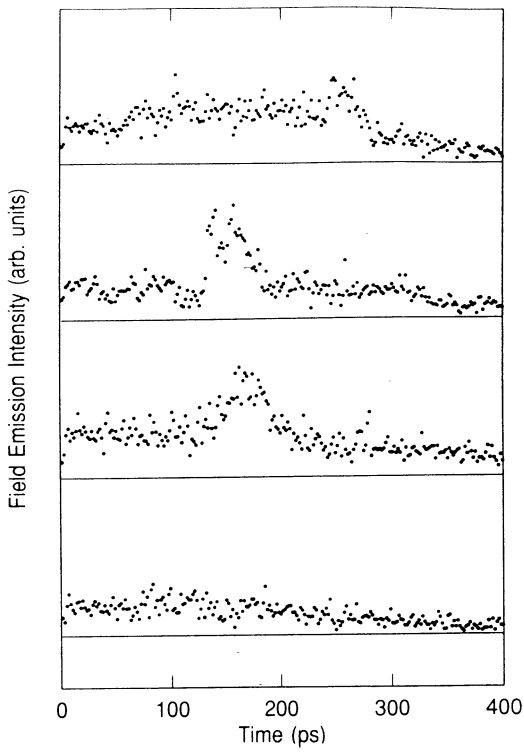

Figure 1. Field emission current intensity from an oxidized W(111) tip on which a single Cs atom is adsorbed at 90K. The intensity fluctuations of the top three traces result from the motion of a Cs adatom. The data points are separated by 2 ps.

References

[1] M. Dantus, H.H.M. Janssen, and A.H. Zewail. *Chem. Phys. Lett.* **181**, 281 (1991).

[2] L. Khundkar and A.H. Zewail. *Ann. Rev. Phys. Chem.* **41**, 15 (1990).

[3] H. Heinzelmann, G.M. McClelland, and F. Watanabe. *Submitted.*

[4] H.-W. Fink. *IBM J. Res. Dev.* **30**, 460 (1986).

[5] H.-W. Fink. *Physica Scripta* **38**, 260 (1988).

[6] Ch. Kleint and K. Möckel. *Surf. Sci.* **40**, 343 (1973).

[7] J.-R. Chen and R. Gomer. *Surf. Sci.* **79**, 413 (1979).

[8] M.M. El Gomati, M. Prutton, and R. Browning. *J. Phys. E* **18**, 32 (1985).

[9] I. Brodie. *Surf. Sci.* **70**, 186 (1978).

SINGLE-ELECTRON MANIPULATION UNDER HIGH-FIELD AT ROOM TEMPERATURE

H.NEJOH [a], S.WATANABE [a], M.NAKAMURA [a] and M.AONO [a,b]
a Aono Atomcarft Project, JRDC, 5-9-9 Tohkohdai, Tsukuba, Ibaraki 300-26 Japan
b RIKEN, 2-1 Hirosawa, Wako, Saitama 351-01 Japan

ABSTRACT. When a liquid crystal (LC) molecule is used as the central electrode of a double-tunnelling junction, single-electron charging can be observed even at room temperature. The experimental i-v curves of these double-tunneling junctions show a Coulomb staircase where the step width varies from step to step. This is because the step width corresponds to the total energy difference between the ionized states and the neutral state of the molecule.

1.INTRODUCTION

Recently a metal droplet on a insulator/metal substrate has been used as the central electrode for building a double tunneling junction by holding the scanning tunneling microscope (STM) tip above the droplet as the counter electrode. [1,2] Also small-area quantum wells (quantum dots) have been used in order to observe single-electron charging effects. [3-5] For such systems it is necessary to decrease the temperature of the junction to 4 Kelvin in order to observe Coulomb blockade, since the associated capacitance is large and the charging energy is relatively small. Hanna et al. and Schonenberger et al. observed equally spaced steps for metal clusters. [6,7] Since both groups observed a uniform step width throughout the bias range, the phenomenon can be understood in terms of the conventional theory of single-electron charging. [8]

We have observed incremental charging of a molecule which acts as the central electrode in a double-tunneling junction at room temperature. [9,10] In previous calculations of this effect, the total energy differences between the ionized states and the neutral state of a molecule are larger than the observed step widths of the Coulomb staircase. Here we report that when the molecular geometry change is included, our calculated results show that the total energy differences agree with the observed steps. In addition, the electric field reduces the total energy difference.

V.T. Binh et al. (eds.),
Nanosources and Manipulation of Atoms Under High Fields and Temperatures: Applications, 115–119.
© 1993 *Kluwer Academic Publishers. Printed in the Netherlands.*

2.EXPERIMENT

In our experiments, the following molecule/substrate combinations were used: 4'-cyano-4-2-alkylbiphenyl (K6 or 2CB), 4'-cyano-4-7-alkylbiphenyl (K21 or 7CB) and 4'-cyano-4-7-alkoxybiphenyl (M21) on Pt(111). A Pt(111) substrate was polished to 0.1 μm roughness and chemically etched using HCl and HNO_3 solution, rinsed by ultra-pure water and dried in air.

A commercial type STM (Nanoscope II) was used to take i-v curves and a PtIr wire was used as a tip. Holding the tip above a molecule so that tip-molecule-substrate makes a double-tunneling junction, the bias voltage was ramped and the tunnel current was measured. The measurements were done in air at ambient pressure.

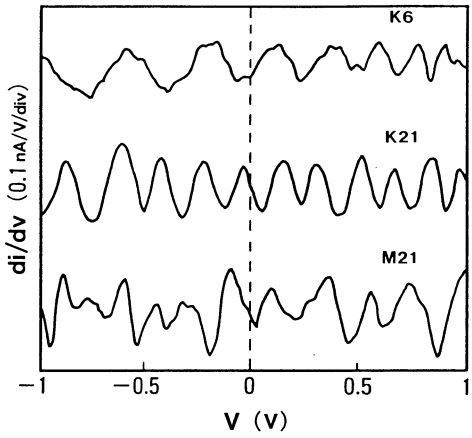

Fig.1 di/dv-v curves of K6,K21 and M21 LC molecules on Pt substrate. All curves show a Coulomb staircase. The larger the molecular size, the narrower the step width. The bias voltage is -1V and set point current 0.2 nA.

Fig.1 shows di/dv-v curves of K6, K21 and M21 LC molecules on Pt substrate measured at room temperature. The Coulomb blockade region corresponds to e/C, where C is the characteristic capacitance of the electrodes. In the Coulomb blockade region at about 200 mV, the calculated electrode capacitance is about 10^{-19}F. This value agrees with the capacitance calculated from the molecular area and the distance between the molecule and the substrate. Since a Coulomb gap of about 200 mV corresponds to 1700 K, single-electron charging effects can be observed even at room temperature. All these show Coulomb staircases and the step width varies from step to step within a molecule and also from LC species to species. From the conventional theory of Coulomb blockade, the step width is inversely proportional to the capacitance and uniform throughout the bias range. But our results show non-equidistant peaks, so that these results cannot be understood from the conventional theory. [8]

Each step should correspond to the electronic state of the molecule at each charging state. Since the central electrode consists of a molecule, the step width corresponds to the total energy difference between the ionized states and the neutral state of a molecule. Then the step widths vary from step to step.

The experimental results show that as more electrons are added to a molecule, subsequent electron entry becomes more energetically favorable. This situation can be understood by the nuclear rearrangement within the molecule due to electrons added.

The LC molecule we used contains two benzene-rings in the molecule. When one electron is added to the molecule it cannot make a double-bond and the bond length of the benzene-ring is not altered much. When two electrons are added they can form a double-bond on the rings in the semi-classical scheme and the bond length is altered. When one electron is subtracted from the ring, one of the existing double bonds is eliminated so that the bond length is also altered. This is shown by calculations in Table 1. Since a benzene-ring has three double-bonds and six electrons are associated to these bonds, six electrons are relatively easily added or subtracted.

Fig.1 shows the alkyl length dependence of the step width. Fig.1 shows that the longer the alkyl length, the smaller the step width. The only difference between these molecules (except M21, where an oxygen atom is located between the biphenyl group and the alkyl group) is the length of the alkyl tail. Since the di/dv curve represents the electronic state of the molecule, each step edge represents the change in the electronic states when electrons are added (subtracted). The number of carbon atoms in the alkyl tails are 2 for K6, 7 for K21 and 7 for M21. The lower the number of carbon atoms in the alkyl tail, the larger the effect of adding (subtracting) electrons. Since the total energy is affected by the nuclear rearrangement in the benzene-ring, the shorter alkyl tail restricts the nuclear rearrangement. This tendency is shown in Fig.1. In other words, the benzene-ring tries to preserve relatively high-symmetry so that the degeneracy is kept. Consequently, the electrons are confined in the same states and feel a large Coulomb repulsion.

TABLE 1 Benzene-ring carbon atoms bond lengths changes. The ratio of bond lengths of the ionized molecule to the neutral molecule (%) are shown. The positive number indicates the bond length increase while the negative number the decrease. The more charging, the more bond expands and vice-versa. Also the shorter the alkyl tail length, the more difficult to rearrange the nuclei of the benzene-ring.

	2CB Charge states				7CB Charge states				M21 Charge states			
Bond	-1	-2	+1	+2	-1	-2	+1	+2	-1	-2	+1	+2
C1-C2	1.6	3.0	2.7	4.0	1.5	3.3	2.3	4.4	1.6	3.3	2.7	5.0
C2-C3	1.4	-0.7	-1.1	-1.8	0.2	-0.6	-0.9	-1.6	0.1	-0.7	-1.4	-2.2
C3-C4	1.1	2.0	2.7	3.6	0.9	2.0	1.9	3.6	1.0	2.1	2.2	4.0
C4-C5	0.2	0.7	0.9	2.7	0.4	0.8	1.5	2.8	0.0	0.4	2.0	3.5
C5-C6	-0.8	-2.3	-1.4	-2.5	-0.8	-2.5	-1.5	-2.8	-0.6	-2.3	-1.5	-2.9
C7-C8	2.0	3.6	1.7	3.2	1.9	3.9	1.7	3.5	1.9	3.8	1.1	3.2
C8-C9	-0.9	-1.4	0.0	-1.0	-0.9	-1.4	-0.1	-0.9	-0.8	-1.3	0.1	-0.7
C9-C10	1.4	2.6	1.2	2.5	2.0	2.8	1.4	2.7	1.4	2.7	0.9	2.3
C10-C11	0.9	1.7	0.9	2.0	0.9	1.7	1.0	1.9	-0.1	1.6	0.7	1.7
C11-C12	-1.9	-2.8	-0.8	-2.0	-1.7	-2.9	-0.7	-2.2	-1.6	-2.9	-0.4	-2.0

The shorter the alkyl tail length, the more difficult it becomes to rearrange the carbon atom nuclei of the benzene-ring (Table 1). Consequently, the symmetry does not change and the total energy remains large. This means that the alkyl tails can allow the benzene-ring nuclear rearrangement when electrons are added (subtracted). The opposite case of this situation is the benzene molecule with no substitutional groups: since it does not have an alkyl tail, it retains its symmetry.

3.CALCULATION

The total energy differences and the energies which are associated with the electric field were calculated. First the geometry was optimized on the potential surface using semi-empirical AM1 method (Table 1). [11,12] Then total energies were calculated by the unrestricted Hartree-Fock (UHF) method using an STO-3G basis set. [13] For simplicity the total energy of only 2CB was calculated. The total energy differences between +2 and +1, +1 and neutral, -1 and neutral, -2 and -1 ionized state are 2.62, 3.72, 3.26 and 9.97 eV respectively. These energy differences are greatly reduced compared to those not geometry optimized. When the geometry of an LC molecule was optimized the geometry changed, especially bond length between the carbon atoms of the benzene rings. This is due to electrons entering and leaving the benzene rings, since the highest occupied molecular orbital (HOMO) and the lowest unoccupied molecular orbital (LUMO) localize on benzene rings.[14] Even if the charge of the molecule is zero, the bond length of the benzene-ring in an LC molecule has changed from that of the original benzene-ring. This is thought to be a substitutional effect: in this case, there is a cyano group and an alkyl group, connected to the benzene-rings. From the viewpoint of symmetry, it might be energetically favorable to lower the symmetry and split the degeneracy in order to lower the total energy. This is Jahn-Teller effect.

TABLE 2. The total energy differences between ionized and neutral states of the molecule without and in an electric field

	Charge	
	+2	-2
No electric field	19.09	15.01
In an electric field	13.75	11.47

The total energy of the molecule in an electric field was calculated (RHF and STO-3G basis set). [15] (Table 2) When i-v curves are taken, the molecule is located in a high electric field (~ 1V/nm=0.001 a.u.). This electric field affects the electronic states and the total energy of the molecule. We have performed calculations to determine the effects of an uniform field applied to the molecule. The molecular geometry was optimized to reveal the electric field effect. Cyanobenzene was used as the molecule for simplicity. Since the LC molecule tilts to the substrate touching the one side of the biphenyl group to the substrate, [14] the electric field direction is defined as the electric field being perpendicular to the substrate plane and the molecule tilts 60 to the substrate. When the molecule is in a field the total energy differences are less than those not in a field. This can be considered as follows: When the plane of the benzene-ring tilts to the electric field direction, the molecule is in a low symmetry state. When the electric field is applied to the charged molecule, electrons move along the electric field and this decreases the total energy (energetically favorable). Although the calculated total energy differences are larger than the measured one, they decrease further by considering the interaction between the molecule and the substrate.[16]

Next, when the number of electrons in a benzene-ring is greater than or less than six, the symmetry of the ring is lowered. Consequently, the total energy of the molecule becomes low compared to an unchanged molecule. This is the reason why the total energy

difference between an ionized state and a neutral state becomes small. In addition, when the symmetry is lowered, the degeneracy of the molecule is split and the additional entering electrons can occupy the split levels with lower repulsion so that the correlation effects prevail. This is the reason why many electrons can exist within a molecule even when there is Coulomb repulsion.

Up to this point, they have studied molecular geometries only from the view point of chemical reactions. The i-v curve reflects the changing geometry over a very short time period (~10^{12}/sec). The solid surface geometry phase transition can occur with the addition of energy of the order of a few meV. Compared to the solid surface, a molecule has more degrees of freedom and the geometry can change with the addition of even 200 meV. Our i-v curve detected the geometry change of molecule.

In summary, we have shown that the nuclei of benzene-ring rearrangement plays an important role to lower the total energy differences between an ionized states and a neutral state. Also the electric field affects the total energies. This is the reason why a molecule contain large excess electrons in it and this enables the small Coulomb staircase using LC molecules. The resonance energies associated with tunneling cannot be written as the sum of single-particle confinement energies and constant Coulomb charging energies.The resonance energies depend strongly on quantum mechanical many-body effects in the molecule. [17]

Acknowledgement

The authors thank A.Koide for allowing us to use the electron density calculation program developed by him. We also thank D.V.Averin, K.K.Likharev, V.J.Goldman, M.Dupuis, E.Snyder, F.Grey and M.Tsukada for useful discussions.

References

[1] van Bentum,P.J.M., Smokers,R.T. and van Kempen,H., (1988) Phys.Rev.Lett. 60,2543
[2] Wilkins,R.,Ben-Jacob,E. and Jaklevic,R.C., (1989) Phys.Rev.Lett.63, 801
[3] Bo Su, Goldman,V.J. and Cunningham,J.E., (1992) Science, 255, 313
[4] Silsbee,R.H. and Ashoori,R.C., (1990) Phys.Rev.Lett. 64,1991
[5]Averin,D.V., Korotkov,A.N. and Likharev,K.K., (1991) Phys.Rev. B. 44, 6199
[6] Hanna,A.E. and Tinkham,M., (1991) Phys.Rev.B. 44, 5919
[7] Schonenberger,C.,van Houten,H. and Donhersloot,H.C., submitted to Phy.Rev.Lett.
[8] Averin,D.V. and Likharev,K.K., (1991) Chp. 6, in V.M.Agranovich and A.A.Maradudin (eds.), Mesoscopic Phenomena in Solids,North-Holland
[9] Nejoh,H., (1991) Nature,353, 640
[10] Nejoh,H. and Aono,M., (1992) Mod.Phys.Lett.6, 187
[11] Dewar,M.J.S. and Storch,D.M., (1985) J.Am.Chem.Soc. 107, 3898
[12] Dewar,M.J.S.,Zoebisch,E.G.,Healy,E.F. and Stewart,J.J.P., (1985) ibid. 107, 3902
[13] Frisch,M.J. et.al., (1988) Gaussian88, Gaussian, Inc., Pittsburgh, PA
[14] Smith,D.P.E., Hober,J.K.H., Binnig,G. and Nejoh,H., (1990) Nature 344, 641
[15] Dupuis, M., A.Farazdel,A, Karna,S.P., and Maluendes (1990) 'HONDO-8' in Clementi, E. (eds.) , Modern Techniques in Computational Chemistry, ESCOM Science, Leiden, pp.277
[16] Nejoh,H.,(1992) Phys.Rev.Lett. submitted
[17] Johnson,N.F. and Payne,M.C., (1991) Phys.Rev.Lett. 67, 1157

FOCUSED ION BEAMS AND THEIR APPLICATIONS IN MICROFABRICATION

P D PREWETT
CENTRAL MICROSTRUCTURE FACILITY
RUTHERFORD APPLETON LABORATORY
CHILTON, DIDCOT
OXFORDSHIRE OX11 OQX
UNITED KINGDOM

ABSTRACT. Focused ion beams present a unique tool for microfabrication by micromachining and deposition. Liquid metal ion sources provide a low emittance quasi point source capable of being focused to spots of a few tens of nanometres using electric lenses. Preliminary models for machining and deposition processes have been developed but more work is required. The technology is already being applied in a number of important applications including mask and reticle repair and "chip surgery".

1. INTRODUCTION

The use of electron beams in microfabrication is widespread, particularly in the microelectronics industry. For example, commercial electron beam gaussian spot machines are routinely used to manufacture chromium on quartz photomasks and reticles used in optical lithography of integrated circuit patterns [1]. These electron beam microfabrication systems are also used for direct write processes in which substrates such as semiconductor wafers are patterned through e-beam exposure of charge sensitive resist layers. Electron beam lithography of this kind is capable of producing nanometre scale structures and is the principal fabrication technology for R&D into low dimensional structures and devices.

The use of focused ion beam (FIB) systems for microfabrication is by no means as widespread as that of e-beam systems, but awareness of the technology is growing rapidly. Several applications have emerged for which FIB methods offer the only solution. These are principally in the area of repair or rework of artefacts fabricated using more conventional techniques. For example, the repair of photomasks and reticles is increasingly carried out using FIB methods, as is the repair or modification of integrated circuits themselves.

The development of FIB microfabrication systems relies upon the availability of ion sources capable of being focused to the small probe diameters required for microfabrication. This need has been met by the

V.T. Binh et al. (eds.),
Nanosources and Manipulation of Atoms Under High Fields and Temperatures: Applications, 121–137.
© 1993 *Kluwer Academic Publishers.*

liquid metal ion source (LMIS), initially developed for space thruster applications.

2. ION PROBE FORMATION

Prior to the development of the LMIS, submicron ion probes made use of gas phase duoplasmatron sources. For example, Drummond and Long [2] developed an FIB system for materials analysis providing a submicron beam of 20 keV Ar^+ ions with a current density close to 1 A/cm^2. It was another 10 years before the LMIS became firmly established as the preferred source for FIB systems, giving rise to the improved probes which have enabled the adaptation of FIB technology to microfabrication applications.

The LMIS relies upon field emission of ions from a tiny protrusion formed under the influence of a high electric field. This liquid emitter is often supported at the apex of a solid needle which is itself blunt in field emission terms, being typically paraboloidal in shape with critical dimensions ~10μm. The precise mechanism of emission from the field-sharpened liquid emitter was the subject of some debate in the early 1980's, but there is strong evidence to support a mechanism of field evaporation (see for example the discussion in Prewett et al [3]). Thus, ion emission involves "evaporation" of ions over a field-reduced barrier of height Q, giving an ion emission current

$$i = eNfe^{-Q/kT} \tag{1}$$

where $f = 10^{13} s^{-1}$, e is the electronic charge, k is the Boltzmann constant and T the absolute temperature of the liquid emitter. The number of sites N is calculated by assuming a roughly hemispherical emitting feature in which the atoms are densely packed. The potential barrier Q is reduced under the action of an electric field F to

$$Q = H + I - W - (e^3F/4\pi\epsilon_o)^{\frac{1}{2}} \tag{2}$$

where H is the heat of evaporation, I the atomic ionization potential for singly charged ions and W is the work function of the liquid surface.

The electric field in equation (2) may be estimated by assuming a balance between electric and surface tension forces on the liquid emitter, so that

$$\frac{1}{2}\epsilon_o F^2 = S/r_a \tag{3}$$

where S is the surface tension and r the apex radius of the liquid emitter.

This simple model predicts the curves shown in Fig.1 relating the temperature of the emitter to its size. Fig.1 has been calculated for a gallium LMIS, which is the most commonly used source in FIB microfabrication systems.

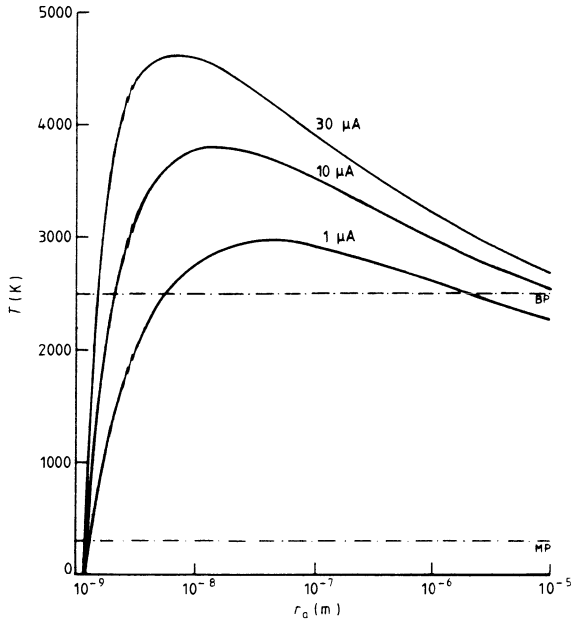

Figure 1. Temperature vs liquid emitter size for Ga^+ LMIS, assuming field evaporation (ref.3).

There is no evidence for heating of LMIS emitters beyond the liquid melting point (29°C for Ga) so that, from Fig.1, an emitting feature no more than a few nm in size is predicted. The basic model of Prewett et al is capable of considerable refinement. For example, it makes the simple assumption that the liquid emitter is a cone capped with a hemisphere. There is no doubt that LMIS emitters approximate to the classic Taylor Cone shape consistent with balanced electric and surface tension stresses [4]. The cone is, however, not terminated by a simple hemisphere, but is thought to support a cusp or jet protrusion [5]. On the basis of this more realistic model, Kingham and Swanson [6] have confirmed a mechanism of field evaporation from a lqiuid emitter measuring ~lnm at its apex.

Ion emission from a stable feature of this size would truly represent a point source. Unfortunately, in practise, it seems probable that the nanometre scale emitter is mobile, causing the effective source to be ten or more times larger, due to a time averaged "blurring" effect. Even so, the LMIS is a much closer approximation to a genuine point source than any other readily available. Using it, ultimate

probes of 10nm or so are possible through the employment of electric lenses of unity magnification.

The emittance and brightness of a source are recognized figures of merit. The transverse emittances of any beam are defined as the areas occupied by the beam in transverse phase space (x,y,p_x,p_y), thus

$$\epsilon_x = \int\int dx\ dp_x \tag{4}$$

$$\epsilon_y = \int\int dy\ dp_y \tag{5}$$

According to Liouville's Theorem, the transverse emittances are, in the absence of acceleration, conserved quantities.

Introducing the particle trajectories $x' = dx/dz$ and $y' = dy/dz$,

$$\begin{aligned} p_x &= p_z\ dx/dz \\ p_y &= p_z\ dy/dz \end{aligned} \tag{6}$$

where

$$p_z = (2ME)^{\frac{1}{2}} \tag{7}$$

is the momentum component in the beam direction z and E its longitudinal kinetic energy. Then

$$\begin{aligned} \epsilon_x &= \sqrt{E} \int\int dx\ dx' \\ \epsilon_y &= \sqrt{E} \int\int dy\ dy' \end{aligned} \tag{8}$$

Integration in the (x,x') and (y,y') planes is in each case performed over the contour containing the fraction of the beam considered. In a focusing system, this is determined by the apertures which select the ions being focused into the final probe. A source of low emittance as defined by equations (8) will possess a high brightness B where

$$B \sim I/(\epsilon_x\ \epsilon_y) \tag{9}$$

so that

$$B \cdot E \propto I/(\int\int dx\ dx' \int\int dy\ dy') \tag{10}$$

The brightness is a figure of merit for the source relating to the current provided from unit area into unit solid angle.

There is very little reported work on the emittance properties of LMIS. Alton and Read [7] have however performed some emittance measurements on a gallium LMIS from which they calculate a brightness figure close to experimentally observed values.

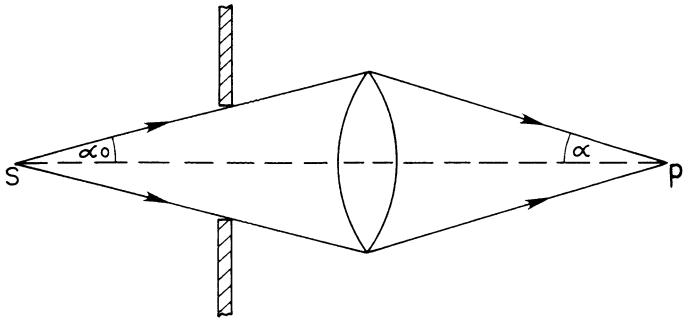

Figure 2. Schematic showing probe formation by single lens.

For most practical FIB systems employing LMIS, the beam brightness is not the most useful figure of merit. Consider the formation of an ion probe P by electrostatic lens action from a point source S as shown in Fig.2. (This is a highly simplified situation in which the lens action of the extraction system has been ignored.) The final probe diameter will be made up of three components, viz.

a) Geometrical

The magnification of an electric lens is

$$M = (\alpha_o/\alpha)\ (V_o/V_i)^{\frac{1}{2}} \qquad (11)$$

where eV_o and eV_i are the ion energies in object and image space respectively for a singly charged particle.

The geometrical contribution to final probe size is

$$d_g = Md_o \qquad (12)$$

where d_o is the gaussian diameter of the source. (This is of the order of a few nanometres as discussed earlier).

b) Chromatic Aberration

Ion trajectories will vary with energy giving rise to a chromatic dispersion in the lens. As in light optics, a disc of least confusion may be defined with diameter

$$d_c = \alpha(\Delta E/E)C_c \qquad (13)$$

where ΔE is the energy spread on the beam of energy E and C_c is the chromatic aberration coefficient of the lens referred to the image side. ΔE is usually taken to be the fullwidth half-maximum value.

c) Spherical Aberration

Spherical aberration effects will be noticeable for larger apertures and therefore larger acceptance angles. The corresponding disc of least confusion has diameter

$$d_s = \tfrac{1}{2}\alpha^3 C_s \qquad (14)$$

where C_s is again referred to the image side.

The final probe diameter formed by the lens action is calculated by adding the areas due to these three effects together to give

$$d = (d_g^2 + d_c^2 + d_s^2)^{\frac{1}{2}} \qquad (15)$$

The probe current I is calculated from the source angular intensity $dI/d\Omega$ as

$$I = \pi\alpha_o^2 \, dI/d\Omega \qquad (16)$$

so that, from (15)

$$d = [(Md_o)^2 + aI + bI^3]^{\frac{1}{2}} \qquad (17)$$

From equation (17) the three principal regimes of operation for typical FIB ion optical systems are apparent.

i) Spherical aberration dominates when large apertures are employed, giving relatively large current and probe size related by

$$d \sim I^{3/2} \qquad (18)$$

ii) Chromatic aberration largely determines probe characteristics for the most useful range of currents and probe sizes for which intermediate apertures are employed and

$$d \sim I^{1/2} \qquad (19)$$

iii) Geometric limits determine the ultimate probe size achieved when the smallest apertures are used, giving

$$d = Md_o \tag{20}$$

The brightness of the source only becomes important in this last regime. In the most useful chromatic aberration dominated regime, we have

$$d = I^{\frac{1}{2}} (\Delta E/E) C_c/(\pi M^2 \, dI/d\Omega)^{\frac{1}{2}} \tag{21}$$

from which the current density in the probe is

$$J = 4 [M^2(E/C_c)^2] [(dI/d\Omega)/(\Delta E)^2] \tag{22}$$

Thus, the current density in the probe depends upon two terms, the first of which is determined by lens properties alone. The second term depends solely upon the quality of the source and represents a useful figure of merit for an LMIS. It is normally referred to as the chromatic weighted angular intensity

$$\Phi = (dI/d\Omega)/(\Delta E)^2 \tag{23}$$

Though the angular intensity $dI/d\Omega$ of of LMIS increases with source emission current, the effect of the energy spread ΔE is dominant. Since this increases with source current, normally according to the relationship $\Delta E \sim I_s^{2/3}$ [8], it is desirable to operate the source at low emission currents. It can be shown that a source current of approximately $2\mu A$ is optimum to maximise Φ [9]

Most advanced FIB systems use at least two electric lenses to achieve flexibility and high ultimate resolution. For example, the MicroTrim commercial system used at Rutherford Appleton Laboratory [10] has an ion focusing column comprising two lenses as shown schematically in Fig.3. The beam deflection electrodes are located upstream from the final probe-forming objective lens in order to minimize chromatic aberration effects. This FIB50 column is capable of producing beams as small as 50nm in diameter with current densities being typically several A cm^{-2}.

Recently, probes approaching 10nm have been obtained using similar systems [11]. Care must be taken to allow for the shape of the beam which may not be a simple gaussian [12]. Nevertheless, FIB probes are capable of use for microfabrication at resolution levels which might genuinely be described as nanotechology.

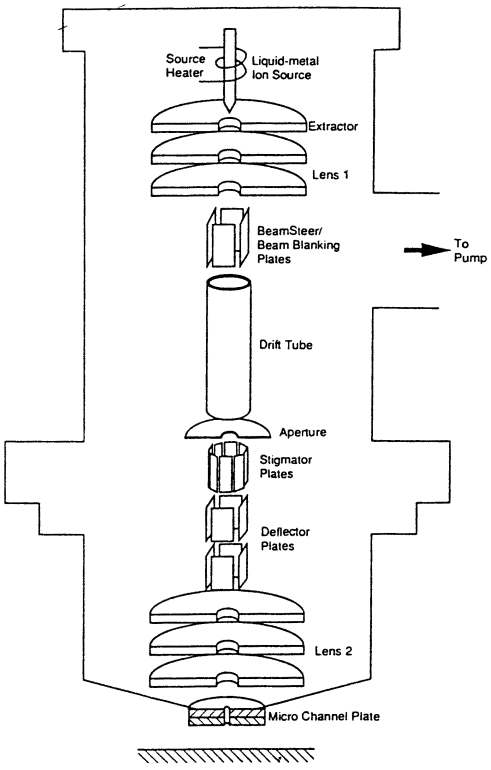

Figure 3. Schematic of FIB50 ion optical column [10].

3. MICROFABRICATION PROCESSES

Microfabrication using FIB technology relies upon three processes viz: material removal by micromachining, material deposition and ion implantation. All three processes are capable of use in the submicron to nanometre range. Ion implantation for applications such as graded gate profiles in semiconductor FET structures normally requires energies of 100 keV or more. FIB columns for this application use magnetic or Wien (ExB) mass filters to separate implantation species from the beams produced by alloy LMIS [13]. There are, however, a wide range of applications for which the simple processes of micromaching and deposition at energies up to 50 keV are sufficient.

3.1 Micromachining

FIB machining has several advantages over the alternatives such as laser removal. As a cold process, FIB removal does not result in the thermal

damage which is a particular shortcoming of laser and e-beam methods.

The rate of etching depends upon the sputter yield Y(E) which depends upon the beam energy, reaching a broad maximum for most materials in the 50-60 keV range.

$$dz/dt = (YM/A\rho)(I/e) \qquad (24)$$

where M is the atomic mass of the target of density ρ. A is the area over which the probe is scanned. FIB machining is inherently slow and is primarily of interest only where high resolution is a critical requirement.

This is illustrated by Fig.4 which shows estimated times for micromachining of silicon to a depth of 1.5μm using typical FIB probes. This shows the usefulness of FIB for micron scale artefacts which can be produced in a few seconds using high resolution beams (<100nA). Artefacts of 10μm or more would require many minutes to produce using high resolution probes and increased in beam sizes must be used to achieve acceptable machining times. Where artefacts are produced in membranes, as in micromechanical sensor applications, trepanning might be used to reduce working times for larger features, as indicated in Fig.4.

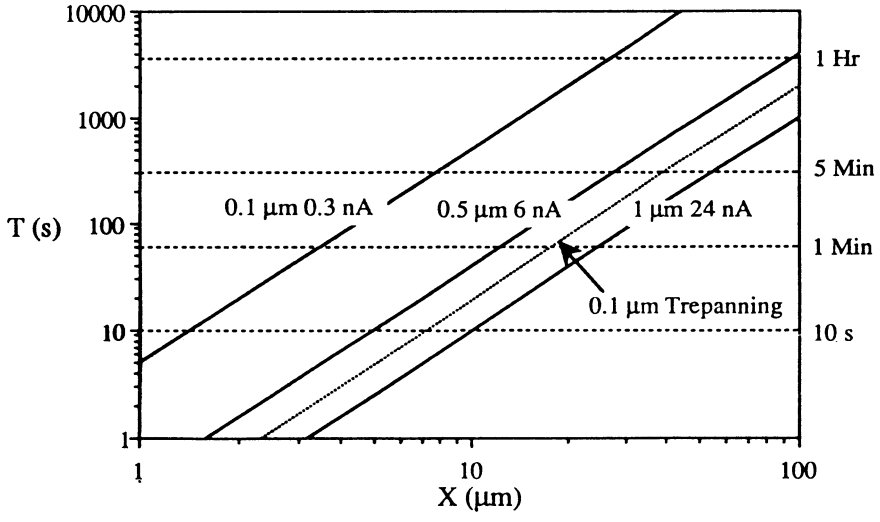

Figure 4. Typical micromachining time vs feature size.
A yield of Y=5 atoms/ion is assumed. Machining is to a depth of 1.5μm.

An alternative method of producing faster machining rates is the use of chemical enhacement. For example, Cl_2 gas dispensers have been used to increase FIB machining of aluminium using Ga^+ beams. In this case, a four fold increase in removal rates has been achieved [14]. Care must be taken to optimise the gas delivery nozzle since excessive coverage of the target surface with Cl_2 molecules will inhibit removal of surface atoms, even to the extent of reducing it below the physical sputter rate.

3.2 FIB Deposition

FIB deposition (FIBD) of material requires the delivery to the surface of a precursor gas which is decomposed by the ion beam to produce a deposit. After decomposition, volatile molecular fragments must leave the surface. Hydrocarbon precursors are used to produce carbon patch deposits for applications such as photomask repair [15]. Other commonly used systems are gold from dimethyl-gold-hexafluoroacetylacetonate [16] and tungsten from tungsten hexacarbonyl. The latter system has been used at RAL for a variety of applications, including integrated circuit modifications.

A principal requirement of any precursor gas is that the adsorbed or chemisorbed molecules should bind adequately to the surface under ion bombardment. Thus the surface binding energy must exceed the decomposition energy if the precursor is not to be sputtered away by the incoming ion beam.

The important hydrocarbon systems have been studied by Vasile and Harriott [17]. They have shown that hydrocarbon precursors should possess an aromatic ring with an unsaturated side group which effects good surface bonding (eg. Styrene C_8H_8 which has an unsaturated vinyl side group).

The growth rate of films deposited by FIBD depends upon the relative effects of precursor decomposition by ion impact and sputter removal of the deposit and adsorbate. Neglecting the latter, a simple model predicts film growth of the form [18]

$$z(t) = \frac{M}{\rho}\frac{J}{e}(\sigma k \Gamma \alpha - Y)\left[\frac{t}{\beta} + \frac{\sigma J k \alpha}{e\beta^2}\left(\frac{N_o \beta}{\Gamma \alpha} - 1\right)\right](1 - e^{-\beta t}) \qquad (25)$$

where N_o m^{-2} is the initial surface coverage of molecules at t=0, Γ is the flux of precursor molecules, α their sticking probability and k is the number of film atoms produced per ion induced decomposition process of cross section σ.

The process is governed by the characteristic frequency β, where

$$\beta = \frac{\sigma J}{e} + \frac{1}{\tau} + \frac{\Gamma \alpha}{N_s} \qquad (26)$$

where N_s m^{-2} is the surface density of sites for precursor adsorption

and t is the mean molecular dwell time on the surface.

Three limiting cases are apparent from this simple, incomplete model.

i) Short Dwell Times ($\beta \simeq 1/\tau$)

Molecules leave the surface rapidly and deposition is poor, because an unsuitable precursor has been selected.

ii) Large Ion Flux ($\beta \simeq \sigma J/e$)

There is an excess of ions and deposition rate is limited by the availability of precursor molecules. This regime is usually dominant for high probe currents and small scanned areas.

iii) Large Molecular Flux ($\beta \simeq \Gamma\alpha/N_s$)

This regime is dominant for larger deposits for which the ion probe current is spread over a relatively large area, which reduces the effective ion flux. The number of molecules arriving per second is correspondingly increased due to the larger collection area, assuming constant pressure of precursor from the nozzle dispenser.

Film growth rates under type (ii) conditions are approximately constant with area, while under a type (iii) regime, growth rates decrease with area. Approximate patch times vs area for carbon deposition using the MicroTrim system are given in Fig.5, showing behaviour corresponding to regime (ii) for smaller patch areas, changing to type (iii) behaviour for larger areas.

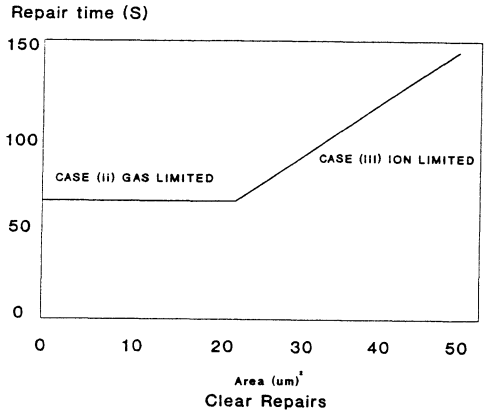

Figure 5. Carbon patch time vs area for MicroTrim, showing type (ii) (precursor limited) and type (iii) (ion limited) behaviour.

Scan control is vital to successful deposition. Most deposits are formed using a pixel-by-pixel method in which the beam dwells for a time t_p at each pixel. If each pixel is visited on n successive occasions, the total exposure time per pixel is

$$t_E = nt_p \tag{27}$$

It is essential that, at the end of each of the n scans, a delay is employed during which the beam is blanked. This is required to allow sufficient time for recoverage with precursor molecules. Unless this delay is incorporated, each scan after the first will remove material and not deposit. This delay is called the loop time t_L and extends the effective patch time to

$$T = N_p t_E + (n-1)t_L \tag{28}$$

where N_p is the number of pixels employed.

4. APPLICATIONS

4.1 Photomask Repair

The repair of chromium on quartz or glass photomasks and reticles by FIB methods is one of the first applications to be exploited. Opaque defects are removed by micromachining and carbon deposition is used to patch clear defects.

One of the principal shortcomings of the process is the so called gallium stain which accompanies opaque defect removal. Thus, removal of a chrome defect is always accompanied by implantation into the quartz or glass substrate of the energetic gallium ions (typically 20-40 keV). This implanted gallium produces a stain which is particularly severe for the ultra violet wavelengths used on advanced optical stepper lithography systems.

The implanted gallium extends for some 20 or 30nm into the substrate with a model profile given by [19].

$$\frac{n(x)}{(\rho/YM)} = [1/(1+\mathrm{erf}(R/\sigma\sqrt{2}))][\mathrm{erf}(R-x)/\sigma\sqrt{2})+\mathrm{erf}((X+x-R)/\sigma\sqrt{2})] \tag{29}$$

The mean projected range is $R \simeq 15$nm and standard deviation $\sigma \simeq 6$nm.

The stain effect due to this implanted zone can be seen in Fig.6. At longer wavelengths, the stain reduces transmission by only 20%, but in the deep u.v., an 80% loss of transmission occurs. The stain can be removed using commercial plasma etch processes. The results of three such processes are indicated in Fig.6, showing stains reduced to 40% and 10%, employing processes 1 and 2 respectively. Process 3 effects complete stain removal at all wavelengths.

Repair of clear defects in photomasks utilizes carbon patch deposition as described earlier.

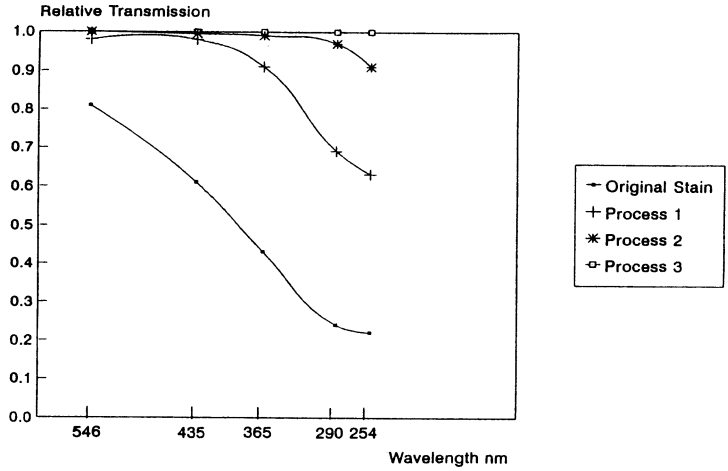

Figure 6. Gallium stain effect in photomasks for different wavelengths. Stain removal by plasma process showing restoration to 100% transmission.

4.2 Xray Mask Repair

The repair of Xray masks requires deposition of high Z Xray absorbing material such as gold or tungsten. Tungsten deposition from $W(CO)_6$ precursor has been used successfully for this purpose [20].

The thickness of the absorber layers (typically in excess of 1μm) requires the repair of high aspect ratio structures by both removal and deposition (see Ref.[20] for further details).

4.3 IC Repair

Tungsten deposition is also used to repair or rework integrated circuits. This is ideally done at the wafer stage, but, frequently, defects are not discovered until the chip has been finally packaged. One such repair exercise involving a complex gate array chip with three layers of metallization and 4μm critical dimensions has been carried out recently at RAL, using the MicroTrim FIB system [21].

Modification to all three layers of metallization were carried out as shown schematically in Fig.7.

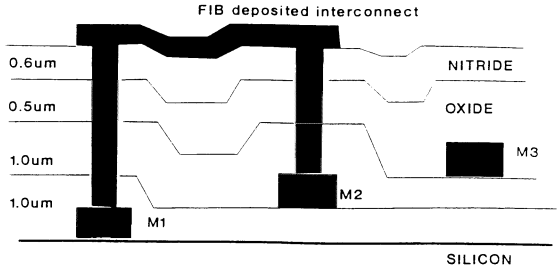

Figure 7. Schematic showing cross section of FIB "chip surgery" repair to prototype ic with three metal layers.

Following identification of the defective area using scanning ion microscopy, the repair processes were defined using the machine's software functions. High aspect ratio vias 1μmx1μm in section were machined to access the first and second layers of metal, buried 3.1μm and 2.1μm below the surface of the chip and separated by oxide insulating layers. The end point for this hole-drilling process was determined by monitoring the ion induced secondary electron signal, which increased dramatically as the buried metal layers were exposed by the ion beam. The two vias were then plugged using tungsten deposition and capped with connection pads measuring 2μmx2μm. The buried gates were then shorted out by connecting these plugged vias by means of a tungsten link deposited across the surface of the chip. Finally, a defective gate in the top metal layer was disconnected by FIB machining. The effects of this FIB surgical procedure can be seen in Fig.8.

The above procedure was successful in restoring the prototype ic to full functionality.

5. CONCLUSIONS

Focused ion beams offer a unique capability for microfabrication to nanometric tolerances. The production of highly focused beams from liquid metal ion sources by electric lenses is normally dominated by chromatic aberration effects. Probes as small as a few tens of nanometres are rapidly beoming commonplace.

Some work has been done using FIB techniques to produce low dimensional structures and devices employing nanometre scale artefacts but the most rapid growth has been in microfabrication areas such as mask repair and chip surgery. Some initial modelling of machining and deposition processes has been undertaken, but more fundamental work is desirable to underpin the rapidly developing application areas.

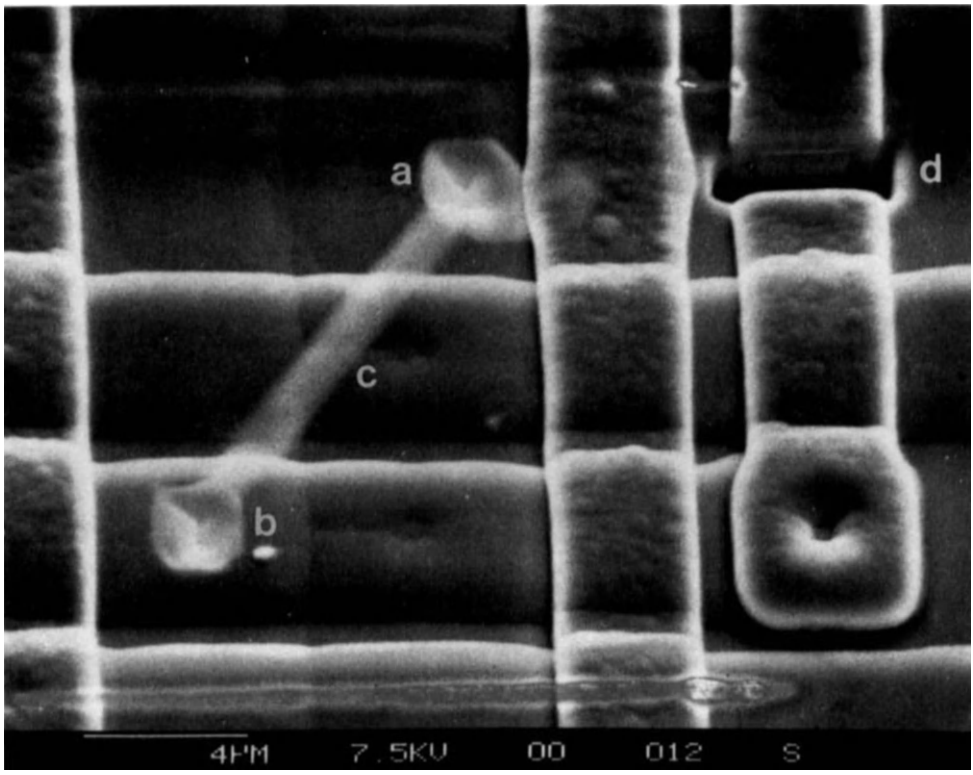

Figure 8. SEM photograph showing FIB "chip surgery" repair to prototype integrated circuit

a,b tungsten-plugged vias to buried metal tracks M1 and M2
c tungsten link deposit shorting M1 and M2
d cut through track M3

6. ACKNOWLEDGEMENTS

This paper has made use of a recent book written jointly by the author and Dr G L R Mair [9].

The contribution of colleagues at RAL is gratefully acknowledged, notably that of J G Watson, G W Brown and G S Turner. The Head of the Central Microstructure Facility at RAL, Professor R A Lawes, is thanked for his continuing role in the strategic development of FIB technology.

7. REFERENCES

1. Lawes, R. A., Appl.Surface Sci. 36 (1989) 485

2. Drummond, I. V. and Long, J. V. P., Int. Conf. Ion Sources (1969) 459, INST Saclay, Paris, France

3. Prewett, P. D., Mair, G. L. R. and Thompson, S.P., J.Phys. D 15 (1982) 1339

4. Taylor, G. I., Proc. R.Soc. A280 (1964) 383

5. Mair, G. L. R., J.Phys. D 17 (1984) 2323

6. Kingham, D. R. and Swanson, L. W.
   a. Appl.Phys. A34 (1984) 123
   b. Appl.Phys. A41 (1986) 157

7. Alton, G. D. and Read, P. M.
   a. J.Phys. D. 22 (1989) 1029
   b. J.Appl.Phys. 66 (1989) 1020

8. Knauer, W.
   a. Optik 54 (1979) 211
   b. Optik 59 (1981) 335

9. Prewett, P. D. and Mair, G. L. R., "Focused Ion Beams from Liquid Metal Ion Sources" Ch.III p.112.
   Research Studies Press, Taunton, 1991

10. MicroTrim ™, Oxford Plasma Technology Ltd., Yatton, Bristol U.K.

11. Kubena, R. L., Stratton, F. P., Ward, J. W., Atkinson, G. M. and Joyce, R. J. J.Vac.Sci.Technol. B7 (1989) 1798

12. Ward, J. W., Kubena, R. L. and Utlaut, M. W. J.Vac.Sci.Technol. B6 (1988) 2090

13. Cleaver, J. R. A., Heard, P. J. and Ahmed, H.
    Microcircuit Engineering 83 eds. H. Ahmed, J R A Cleaver and G A C Jones (1983) 135, Academic Press, London

14. a. Ochiai, Y. Gamo, K. and Namba, S.
       Jpn. J.Appl.Phys. 23 (1984) L400
       J.Vac.Sci.Technol. B3 (1985) 67
    b. Ochiai, Y., Shihoyama, K., Masuyama, A., Gamo, K., Shiokawa, T., Toyoda, K. and Namba, S.
       Jpn. J.Appl.Phys.24 (1985) L169
    c. Ochiai, Y., Shihoyama, K., Toyoda, K., Masuyama, A., Gamo, K. and Namba, S., Jpn.J.Appl.Phys. 25 (1986) L526

15. Heard, P. J., Prewett, P. D. and Lawes, R. A. Microelectronic Eng. 6 (1987) 597

16. Shedd, G. M., Lezec, H., Dubner, A. D. and Melngailis, J. Appl.Phys.Lett. 49 (1986) 1584

17. Vasile, M. J. and Harriott, L. R., J.Vac.Sci.Technol. B7 (1988) 1954

18. Heard, P. J. and Prewett, P. D., Microelectronic Eng. 11 (1990) 421

19. Prewett, P. D. and Heard, P. J., J. Phys D. 20 (1987) 1207

20. Prewett, P. D., Gentili, M., Maggiora, R., Mastriogiacomo, L., Watson, J. G., Turner, G. S., Brown, G. W., Plumb, D., Leonard, Q. and Cerrina, F., Microelectronic Eng. 17 (1992) 249

21. Prewett, P. D., McGeary, M. L., Watson, J. G., Brown, G. W., Turner, G. S., Loader, I. M. and Heard, P. J. Microelectronic Eng 17 (1992) 423

MINIATURIZED LIQUID METAL ION SOURCES (MILMIS)

J. MITTERAUER
Institut für Allgemeine Elektrotechnik und
Elektronik, Technische Universität Wien
Gusshausstrasse 27-29
1040 Wien
Austria

ABSTRACT. Introductory remarks are given on ion sources which are typical spin-offs of space technology, and basic features of liquid metal ion sources (LMIS) are outlined. A special by-product of field emission electric space propulsion by a liquid metal ion thruster is the slit emitter, which may be qualified as a semiminiaturized LMIS.

The state-of-the-art technology of field emitter arrays common in Vacuum Microelectronics is presented in view of the fabrication of miniaturized integrated liquid metal ion sources (MILMIS). The possibility of operation of these devices even in the field emission mode as miniaturized liquid metal electron sources (MILMES) is discussed.

Finally, an outlook is given on prospective applications of MILMIS and MILMES, including micromachining and microelectronic device technology (e.g., focused ion beam techniques), space technology (e.g., ion thrusters with integrated neutralizers), and pulsed power technology (e.g., high power switching and ion beam sources for inertial confinement fusion).

1. INTRODUCTION

In the early 1960s, one of the electric space propulsion activities of the National Aeronautics and Space Agency (NASA) resulted in the construction of an electron bombardment ion thruster with mercury as the propellant /1/ and thus commenced the development of large-size ion beam source technology. Some of the earlier designs were a modest 5-cm model, but the advent of new materials led to the construction of ion sources with typical beam diameters of 30cm and greater.

With the expansion of the semiconductor industry and the demand for high-density devices, it soon became apparent

V.T. Binh et al. (eds.),
Nanosources and Manipulation of Atoms Under High Fields and Temperatures: Applications, 139–164.
© 1993 *Kluwer Academic Publishers.*

that to process and produce high-yield micron and submicron device geometries, it was essential to convert from traditional chemical wet etching to dry etching techniques. It even became apparent that there were numerous industrial applications for large-area ion beam processing; in particular, those associated with device fabrication in the computer memory integrated circuit and optoelectronic industries and the fabrication of optical coatings.

As a typical spin-off product of space technology, the development of broad-beam gas ion sources continued, and they can now be supplied within multi-ion source systems integrated for both ion beam deposition and etching functions.

When the European Space Agency (ESA) started its own development program on electric space propulsion in 1968, the first activities were devoted to the exploration of a colloid thruster, and the idea of using linear emitter geometries instead of capillary or annular-shaped electrodes was advanced. This development was also based on experiments on the emission of cesium ions from capillary tubes /2/. The linear emitter geometries appeared to be suited to obtain high levels of ion emission, which finally resulted in the construction of a-slit type, field emission, liquid metal ion thruster with cesium as the propellant /3/. Homogeneous, high-current ion emission from a micron-sized slit has been demonstrated successfully, allowing the occurrence of a linear series of equally spaced emitting sites /4/, /5/,/11/.

Even being a spin-off product of space technology, this type of semiminiaturized liquid metal ion source (LMIS) represents an ultimate development in precision mechanics, demonstrated by actual numerical values of about 10^{-4}m for both the emitter slit width and the round-off radius of the emitter slit edges. Nevertheless, due to the rather large interelectrode spacing of about 10^{-3}m, the operating voltage of the device is above 10^{4}V for an emission current of 5×10^{-3}A.

On the other side, applying microfabrication technologies similar to that used to construct field emitter arrays common in vacuum microelectronics at the Stanford Research Institute (SRI) micro-field ionizers of the shape of miniature volcanos have been developed for mass spectroscopy of gas samples /6/. This volcano ionizer has been further miniaturized into a microvolcano structure having a volcano orifice with a diameter of about 1×10^{-4}m and an integrated counter electrode with an aperture diameter of about 1.5×10^{-4}m /7/. Furthermore, the microvolcano can be fabricated in arrays with packing densities of the order of 10^{4}cm^{-2}. This is a very recent development, but preliminary results have shown that gaseous ions can be formed with the microvolcano with applied voltages of less than 10^{2}V. Clearly, a

logical extension of the ionization of gas samples with these ion sources is the use of liquid sample material, especially liquid metals /8/.

Combining these two technologies, the construction of miniaturized liquid metal ion sources with integrated counter electrodes (MILMIS) is obvious. Technical concepts which have been developed in vacuum microelectronics offer the possibility of integrated gating electrodes and ion optics. Single MILMIS for focused ion beam (FIB) applications may be fabricated, as well as linear or two-dimensional arrays of MILMIS, generating a ribbon ion beam (RIB) or a broad-area ion beam (BIB), respectively.

2. LIQUID METAL ION SOURCES

In a liquid metal ion source (LMIS) the ions being expelled are not created by electron bombardment of a gas or of a metal vapor, but they are created directly from the surface of a liquid metal exposed to vacuum by means of a high electric field resulting from suitable voltages applied to an emitting electrode geometry. When the surface of a liquid metal is subjected to a high electric field, it is distorted into a cone or a series of cones which protrude more and more from the surface with increasing field strength. With increasing applied voltage, the radius of curvature at the apex of these cones becomes smaller and smaller, and therefore the local electric field at the tip becomes larger and larger.

When the field reaches values of the order of $10^{9} Vm^{-1}$, atoms of the metal tip are ionized either by field evaporation or field ionization. With the proper electric polarity, the free electrons are rejected into the bulk of the liquid metal, while the ions are accelerated and expelled from the emitter by the same electric field which has ionized them. The charged particles leaving the liquid metal surface as an ion beam are replenished by the hydrodynamical flow of the liquid metal. The liquid metal more or less is converted directly into an ion beam without the transitional vapor phase which is common in the technology of other ion sources; therefore ionization operates with high power efficiency.

The ionization process is accompanied by a faint luminous glow surrounding the apex region of the cone; the brightness of this glow increases with growing emission current.

Because the radius of curvature at the apex of such a cone is of the order of $10^{-7} m$ or less, for interelectrode spacings of some $10^{-3} m$ applied voltages of some $10^{3} V$ are sufficient to obtain the required high electric fields. A rough criterion for onset of ion emission is given by the

assumption that electrostatic forces and surface tension forces are in balance. The equilibrium shape of an electrified fluid is well known as the "Taylor cone". However, it is now widely accepted that an operating LMIS does not have the accurate shape of a Taylor-cone but rather looks like a cusp at the apex of a cone.

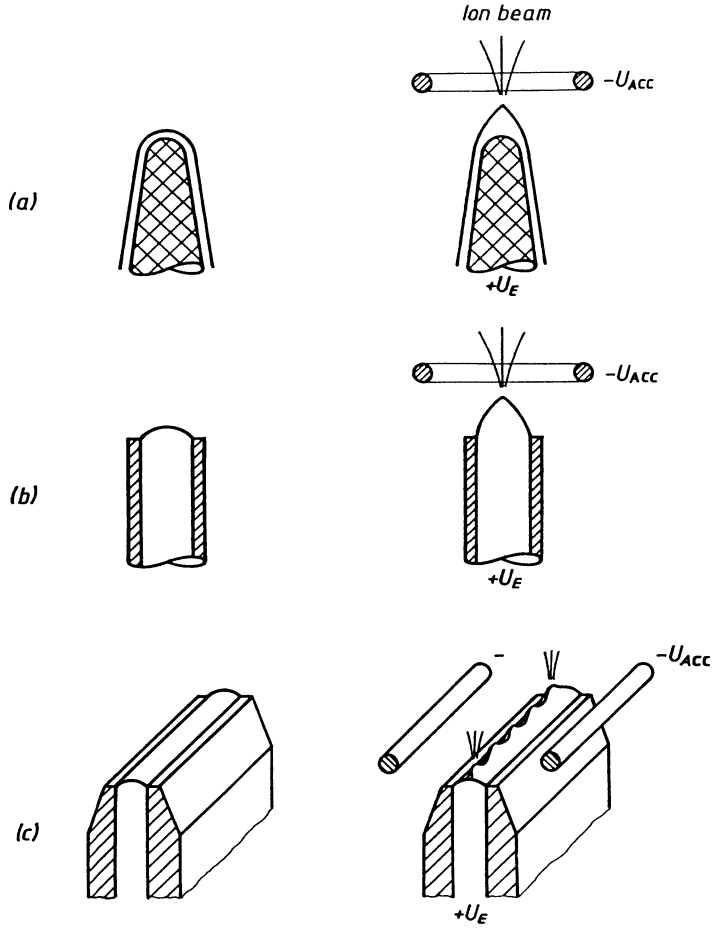

Fig.1: Schematic diagram of different types of liquid metal ion sources: (a) pin or needle type; (b) tube or capillary type; (c) elongated slit type
Left side: shape of liquid metal tip without electric field
Right side: distortion of the liquid metal tip by an electric field due to a positive emitter potential $+U_E$ and a negative accelerator potential $-U_{Acc}$ versus common ground.

Stable and exceedingly bright ion emission with a rather low energy spread from an extremely small apex region of the liquid metal cone characterizes the ion beam and result in some unique applications which never may be met by other ion sources. Single- site ion emission with currents up to several 10^{-6}A may be obtained with a source brightness in excess of $10^{7}Acm^{-2}sr^{-1}$.

For a multiplicity of scientific and technical applications especially devoted to microelectronics technology and surface analysis, LMIS of the needle type and sometimes of the capillary type have been used with a variety of pure metals (e.g., Ag,Au,Bi,Cd,Cs,Ga,Hg,In,K,Li,Na,Pb,Sn,Tl); for nonmetals (e.g., As,B,Be,Ge,Si) or excessively volatile metals, binary or ternary alloy combinations have been used to obtain ion currents from otherwise unaccessible species.

Furthermore, the emission of microdroplets makes LMIS the brightest charged droplet source known, and makes this device very attractive for focused droplet beam experiments /34/.

In LMIS, ion beams can be created from liquid metal wetted needles (or arrays of needles) or from capillaries into which the liquid metal is allowed to flow. In the case of the slit emitter, the capillary is elongated to a long slit of nearly rectangular cross section, allowing therefore the occurrence of a series of emitting cones, each of them contributing to the ion beam. These different types of ion beam emitters are outlined schematically in Fig.1.

3. SEMIMINIATURIZED LIQUID METAL ION SOURCES: THE SLIT EMITTER

3.1. Emitter Geometry

At the European Space Research and Technology Centre (ESTEC), the slit emitter progressively has been developed and evolved from a single-pin emitter through linear arrays of stacked needles to the emitter module /3/. Due to the micron-sized dimensions of both the emitter slit width and the resulting emission site spacing, the slit emitter may be regarded as a semiminiaturized LMIS.

The slit emitter module in principle consists of two symmetrical, highly polished metal plates of the shape depicted in Fig.2. In one or both of the emitter halves there is milled a recess to be used as a reservoir of the liquid metal supplied to the emitter module either by an open funnel or a feeding capillary tube. On certain regions of one of the inside faces (i.e., on the circumference of the reservoir, but without the area adjacent to the emitter edge), there is sputter deposited a layer of nickel with a thickness of the order of 10^{-6}m. When the two halves are

tightly clamped together, they are separated by the thickness of this layer, thus forming a narrow slit of width w and depth d through which the liquid metal can flow and be transported to the edges of the slit by the action of capillary forces. Until now, a number of emitter modules with slit lengths of 1,3,5, and 8 cm have been produced. The material used for the emitter fabrication is stainless steel and, more recently, Inconel which has shown better wetting characteristics for cesium.

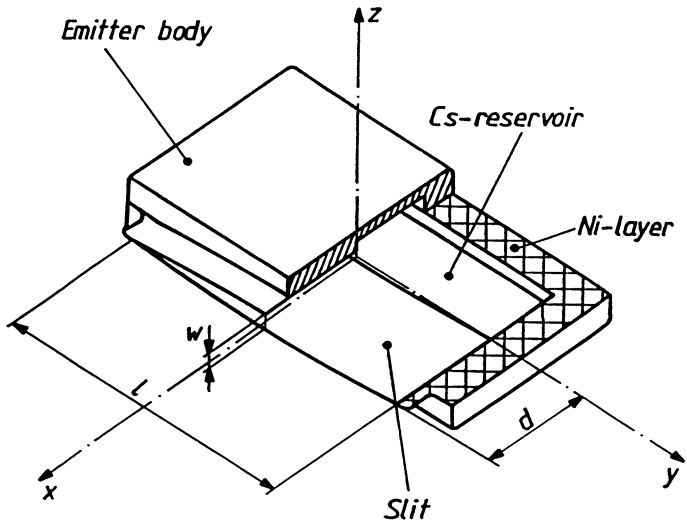

Fig.2: Slit-emitter module showing the principal dimensions of the slit:
l=slit length; d=slit depth; w=slit width.

Although in principle every liquid metal or alloy may be used in LMIS, the slit emitter generally has been operated with Cs which is the most successful liquid metal evaluated for field emission electric space propulsion due to its characteristics of high atomic mass, low ionization potential, good wetting properties, and low melting point. On the other side, due to the extremely high chemical reactivity, the use of Cs requires thorough outgassing of the emitter as well as Cs supply at ultra-high vacuum conditions.

The electrode configuration widely used to create the proper electric field at the emitter slit edge region is

shown in Fig.3. A plane accelerator electrode with an aperture of width 2b is mounted in a distance a of the emitter slit edge. Emitter and accelerator potential in order to create the electric field necessary to produce and accelerate the ion beam. Typical data for the emitter-accelerator geometry according Fig.3 are as follows: a=6x 10^{-4}m, 2b=4x10^{-3}m, d=5x10^{-3}m, w=1.2x10^{-4}m.

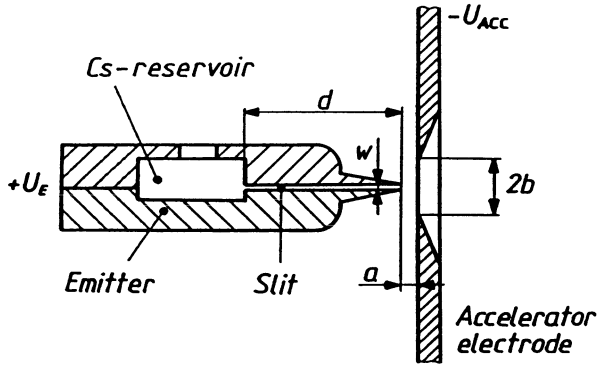

Fig.3: Sectional view of the emitter-accelerator electrode configuration:
a=emitter-accelerator spacing; 2b=accelerator aperture; d=emitter slit depth; w=emitter slit width.

3.2. Emission Site Distribution

If the emitter is filled with liquid metal and the surfaces of the slit until the slit edges are uniformly wetted by the latter, a homogeneous linear liquid tip of semi-cylindrical shape is assumed to exist at the slit edges at onset conditions. The sectional view of this emitter region is schematically outlined in Fig.4, which also shows different idealized assumptions on the equilibrium shape of the liquid tip, the tip radius r_e being dependent on both the emitter slit width w and the radius of curvature r_E of the emitter slit edges, which are both of the order of 10^{-4}m. Enhancing the electric field, the linear liquid tip is distorted. Due to electrohydrodynamic effects, equidistant-spaced emitting sites are originating along the extension of the emitter slit, each of them contributing to the ion beam. The existence of a matrix arrangement of wavelike instabilities on electrically stressed surfaces of fluids

is a well known phenomenon /9/. The linear disposition of emitting features observed on slit emitters previously /10/ and being verified for a rather large number (about 1200) of equidistant distributed emission sites /4/,/5/,/11/ is obviously closely related to these surface instabilities.

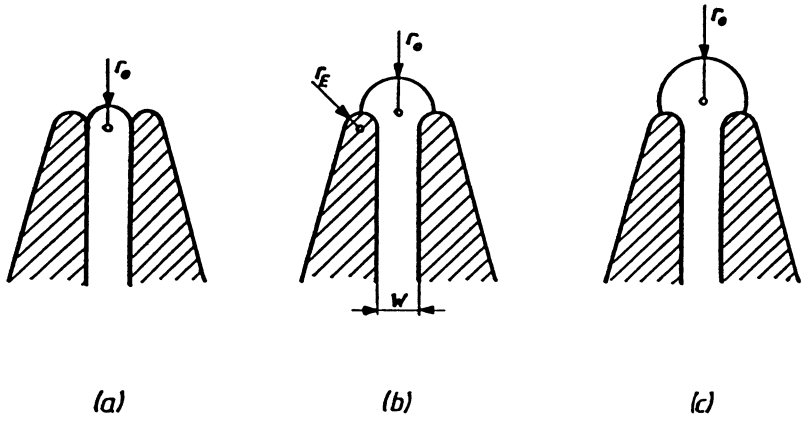

Fig.4: Sectional view of the linear liquid metal tip at the orifice of a slit emitter at onset conditions ($E=E_o$) showing schematically different idealized assumptions on the radius of curvature r_o:
(a) $r_o=w/2$; (b) $r_o=(w+2r_E)/2$; (c) $r_o=2w$.

The mathematical treatment of this problem has been discussed in some detail /4/,/10/, considering on the one hand the development of travelling disturbances in the form of surface waves, and on the other the effect of standing-wave perturbations with no time variations. Among this se-cond group, the analysis of a cylindrical case seems to be of special relevance to the slit emitter, where it is as-sumed that the initial shape of the linear liquid metal tip just before emission onset is of semicylindrical geometry.

Neglecting gravity, the initial preperturbation equilibrium condition is given by:

$$\varepsilon_o E_o^2/2 = \sigma/r_o \qquad (1)$$

where E_o is the initially uniform electric field at the surface of the liquid cylinder, σ is the surface tension of the liquid metal, and r_o is the radius of curvature of the linear liquid metal tip.

Standing wave perturbations of the liquid metal occur, which result in a normal axially symmetrical varicose mode with a wavelength of

$$\lambda = \pi r_o \qquad (2)$$

The initial equilibrium condition (1) therefore may be written:

$$\lambda = 2\pi\sigma/\varepsilon_o E_o^2 \qquad (3)$$

According to Fig.4, different theoretical assumptions on the value of the mean radius of curvature r_o of the liquid Cs surface at onset can be made. Within the limiting values $w/2 < r_o < 2w$, the relation $r_o=(w+2r_E)/2$ seems to be of special importance as the radius of curvature r_E of the emitter slit edges is introduced into the calculation.

Within these theoretical figures, the case $r_o = w/2$ seems to be most unlikely for an emitter slit edge properly wetted, as it results from the homogeneous distribution of emitting sites actually being observed. Furthermore until now there exist no conclusive experimental evidence that the radius r_E only does affect the onset voltage; on the other side, the influence of the slit width w on the onset voltage is well known /3/,/11/.

Results of actual measurements /4/,/5/,/11/ of the emission site spacing λ of slit emitters with slit widths w of 1.2×10^{-4}m and 1.5×10^{-4}m are listed in Table 1; the values of the tip radius r_o resulting from (2) are indicated there.

Table 1: Emission site spacing of slit emitters

w	λ	r_o
1.2×10^{-4}m	7.5×10^{-4}m	2.4×10^{-4}m
1.2×10^{-4}m	8.3×10^{-4}m	2.7×10^{-4}m
1.5×10^{-4}m	10.0×10^{-4}m	3.2×10^{-4}m

Analyzing these results, the value $r_o = 2.4\times10^{-4}$m corresponds exactly to the case $r_o = 2w$ which is shown in Fig.4(c); the larger values of r_o are quite consistent with states of increasing wetting outside the emitter slit orifice that occur after prolonged firing of the emitter. Nevertheless, one always has to bear in mind that this model is based on a standing wave theory of surface insta-

bilities and applies for onset conditions only, neglecting hydrodynamic flow effects always present for an operating emitter. After onset, the actual shape of the emission sites is assumed to be a series of cone- or cusp-shaped features protruding from the wave crests of the varicose mode.

4. MINIATURIZATION OF LMIS

4.1. State-of-the-Art Technology

The slit emitter represents an ultimate development in precision mechanics; this is corroborated by the micron-sized dimensions of the emitter slit width w and the round-off radius r_E of the emitter slit edges (Fig.4). For example, machining of the latter by lapping is limited by the grain structure of the material (stainless steel, Inconel) of the two emitter halves. Furthermore, it is a serious problem to maintain the uniformity of the emitter slit width over a length of several centimeters.

Nevertheless, compared with former constructions, the slit emitter is a semiminiaturized LMIS due to its emitter slit width of about 10^{-4}m, which results in an micron-scaled emission site spacing as it is outlined in Table 1.

However, complete miniaturization of a LMIS requires the reduction of all dimensions to a micrometer scale too. Generally, the principal types of LMIS outlined in Fig.1 are capable of miniaturization. In any case, the crucial problem is the development of fabrication methods which allow to produce such micron-sized structures of metals and insulators. Therefore, methods adopted from semiconductor microelectronics technology as well as from vacuum microelectronics shall improve this situation.

More than ten years ago, using unique electron beam processing and farication techniques, it was demonstrated that individual metal field emitter array (FEA) elements and arrays of these elements could be fabricated with dimensions as small as any solid state device /12/. More recently, using standard microelectronic processing techniques, it was shown that it is possible to fabricate FEA's from single crystal silicon wafers /13/. In the meantime, vacuum microelectronics has become a rapidly growing new field of science and technology, and FEA's have proven to be the most important and powerful electron source in this field /14/.

Within the development of different microtechnologies to fabricate FEA, production methods performed at the Stanford Research Institute (SRI) /15/ are of outstanding importance, since these approaches directly resulted in the fabrication of microvolcano field ionizers /7/,/8/.

The Spindt cathode structure shown in Fig.5 consists of a conductor-insulator-conductor sandwich, holes in the top conductor (gate film), undercut cavities in the insulator layer, and metal cones within the cavities. Field emission from the tips of the cones is obtained when the tips are driven to a negative voltage with respect to the gate electrode. Because of the field enhancement of the tip and the close spacing between the rim of the hole in the gate film and the tip, voltages as low as 50V to 100V can produce large field emission currents. In addition, dense arrays of the tips can be operated without interaction, because the gate film that surrounds each cone prevents reduction of the electric field that would otherwise result from mutual shielding between the tips.

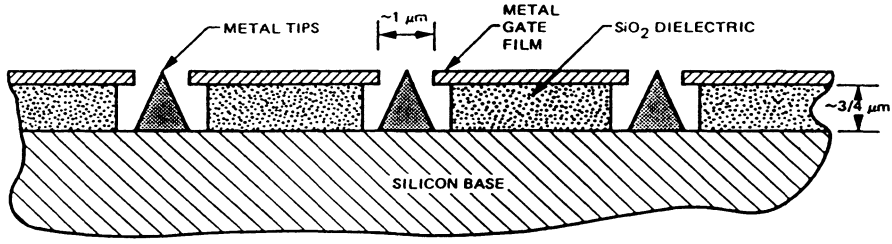

Fig.5: Schematic of a thin-film field emission cathode array (Spindt cathode) /15/.

The field emission cathode array configuration also reduces the problem of ion bombardement of the tips from other high volt-age electrodes, because the tips are well shielded electrostatically by the gate film. Thus most ions formed between the gate film and an external acceleration electrode are directed toward the gate film, rather than toward the tips. In this case of a MILMIS, the analogous feature would apply for secondary electrons released by ion impact, preventing the excessive heating of the liquid metal tips.

The Spindt cathode is fabricated with a combination of thin- film deposition processes and microfabrication techniques similar to those used in the integrated circuit industry. A silicon substrate that has been oxidized to a thickness of about 7.5×10^{-7}m of SiO_2 is coated with a 2.5×10^{-7}m thick film of molybdenum in which an array of holes of about 1×10^{-6}m in diameter is micromachined using electron beam lithography. Holes are then etched through the SiO_2 to the Si-substrate, using the Mo-film as an etch

mask. Finally, Mo cones are formed in the cavities by metal deposition, with their bases at the Si-substrate and their tips in the plane of the gate electrode.

State-of-the-art Spindt cathode FEA's are now fabricated in several sizes from single tips to arrays of 125.000 tips, and with packing densities of up to $1.5 \times 10^7 cm^{-2}$ on a silicon substrate. The hole patterns are printed simultaneously over the entire substrate; thus, in principle, it is possible to print full arrays over at least a 1cm diameter area by this technique.

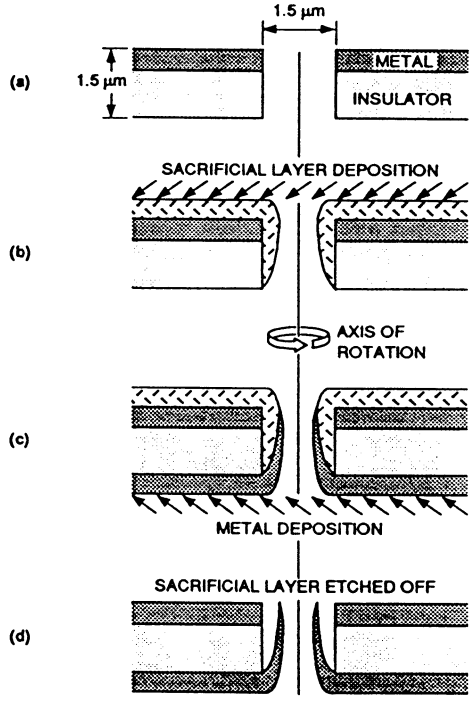

Fig. 6: Fabrication procedure of a microvolcano field ionizer /8/.

At SRI, the Spindt cathode technology has been adapted to fabricate microvolcano field ionizers by a replica method /8/. The challenge was to find a way to fabricate a micron-size emitter cone with a hole through it within a cavity about 1.5×10^{-4}m in diameter and about 1.5×10^{-4}m deep. The procedure to accomplish this task is shown in Fig.6. A metal-coated oxide membrane about 1.5×10^{-4}m thick

is formed aver a 10^{-4}-m-square area. An array of holes about 1.5×10^{-6}m in diameter spaced on 10^{-5}m centers is etched through the membrane using electron-beam lithography and anisotropic etching techniques, producing a structure in which each hole is as shown in Fig.6(a). The holes are then partially closed by angle evaporation of a selectively etchable sacrificial material onto the membrane from the counter-electrod screen side, as shown in Fig.6(b). The microvolcano-forming material is then angle evaporated from the opposite side with a metal that is insoluble in etchants used for removing the sacrificial layer, as shown in Fig.6(c). Finally, the sacrificial layer is removed by wet etching, leaving hollow cones centered in the cavities, as shown in Fig.6(d).

In Fig.7, there is outlined the cross section of such a microvolcano field ionizer, showing the metal-insulator-metal sandwich structure with an undercut cylindrical cavity in the oxide layer and containing a metal microvolcano with an extremely sharp rim, surrounded by the gate electrode with an aperture diameter of about 1.5×10^{-6}m.

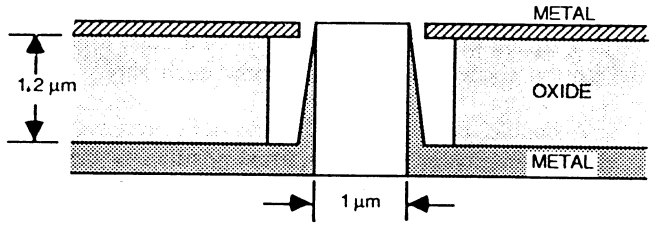

Fig.7: Cross section of a microvolcano field ionizer /8/.

The microvolcano has been fabricated in arrays with packing densities of about 10^{6}cm^{-2}, corresponding to a center-to-center-spacing of 1×10^{-5}m; preliminary results have shown that gaseous ions can be formed with applied voltages of less than 100V.

Microvolcanos have been used successfully as ion sources for quadrupole mass spectrometers and Wien-filter spectrometers as nonfragmenting field ionizers for hydrocarbon and biological gas samples. However, there are other possibilities, the most interesting which is the idea of adapting the technology to LMIS /8/.

4.2. Forthcoming Concepts

If one compares the electrode geometries of the slit emitter (Fig.4) and of the microvolcano (Fig.7), the striking parallelism is evident. Although the accelerator dimensions, the interelectrode spacing and the emitter body extensions are of a macroscopic scale between 10^{-3}m to 10^{-2}m, it is obvious to transform the semiminiaturized slit-emitter-LMIS to a completely miniaturized and integrated LMIS, thus utilizing the acronym MILMIS in its original sense.

The technology of FEA's and microvolcanos allows in principle even the fabrication of miniaturized, lateral-extended, wedge-shaped cathodes and slit emitters with cross sections corresponding to those shown in Figs.5 and 7, respectively. If one adds a proper liquid metal reservoir to such an elongated microvolcano, the device represents a fully miniaturized and integrated slit emitter module, with much lower operating voltages to be anticipated than that of the original model.

However, heating of the whole device above the melting temperature of the liquid metal has to be performed by miniaturized and integrated heater elements. Conforming technologies recently have been developed for vacuum microelectronic applications, resulting in either thermionic integrated circuits which operate at 800°C /16/ or in fine heating elements operating at about 1000°C /17/. In any case, high temperature resistant materials (e.g. Mo,W,Ti, Pt,Al_2O_3) only were used which are compatible with the fabrication technology of FEA's and microvolcanos.

An important requirement is the selection of a proper combination of both the emitter electrode material and the intended liquid metal which allows capillary feeding to the the emitter slit orifice. The emitter material has to be wetted easily by the liquid metal and the material properties of the latter have to be sufficent to make the liquid metal flow easily within a micron-sized capillary and to allow a meniscus to ocurr with a radius r_m at the slit orifice.

Furthermore, one has to prevent any overflow or creeping of the liquid metal over the sharp edges of the emitter slit in order to avoid spurious emission or even shorting toward the accelerator electrode. As the technology developed at SRI allows the use of two different metals in the fabrication process of microvolcanos, the outer slopes of the wedges may be made of a material which is even not or only very poor wettable by the liquid metal. Similar considerations apply to the negative accelerator or gate electrode in order to prevent flashover and arcing by field electron emission from liquid metal which possibly may accumulate on the accelerator due to microdroplets or neutral vapor emission from the slit.

Combining the basic schemes of LMIS shown in Fig.1 and the state-of-the-art fabrication technologies, in principle MILMIS may be produced in a large variety, e.g., single-site microvolcanos and linear or two-dimensional arrays of microvolcanos as well as slit emitters or parallel arrays of slit emitters. Furthermore, it appears feasible to convert the Spindt cathode shown in Fig.5 into a single tip or a tip array of MILMIS of the pin or needle type. In this case, one has to provide for a liquid metal supply by wetting the metal cones only, covering the latter with a thin liquid metal film.

Finally, even a substrate with an array of cones or wedges covered by a liquid metal film and opposed to a planar counterelectrode is of considerable interest, as such a device complies with a recent theoretical study on large-area LMIS /18/. In this case, the originally planar liqid metal surface, which is thought to be distorted into a sharply peaked structure by hydrodynamically driven instabilities, will be superseded by the array structure covered with liquid metal with the apices of the cones or wedges as preferential emission sites.

In conclusion, the term "miniaturized" in the acronym MILMIS applies mainly to the size and lateral extension of single ion emitting sites; the latter even may be combined to large-area emitter arrays, which consequently are defined as large-area MILMIS.

5. MINIATURIZED LIQUID METAL ELECTRON SOURCES (MILMES)

5.1. Film-emission cathodes

A concept similar to that described above /18/ formerly has been applied to electron emission from liquid mercury pool cathodes, inserting a solid metal anchor wetted by Hg /19/, /20/. High current density field emission emanating from an intrinsically microstructured solid substrate of molybdenum with an area of about 0.2cm^2 covered by a thin Hg-film ("film cathode") and capable of supplying pulsed current of more than 10^4A has been demonstrated /21/,/22/.

In Fig.8 there are shown image-converter microphotographs of the flat circular cathode surface of 6mmm diameter at different consecutive surface states with exposure times of 10^{-3}s; the optical resolution is about 10^{-3}m. The open-shutter microphotograph Fig.8(a) shows the cathode in its original surface state; the structure is characterized by macroscopic condensed Hg-droplets and radial wedges and grooves on the Mo-substrate. The short-time microphotographs Fig.8(b)-(d) were obtained at the current maximum of 10^4A of a pulsed arc discharge; the current waveform is a damped oscillation with a frequency of about 3MHz.

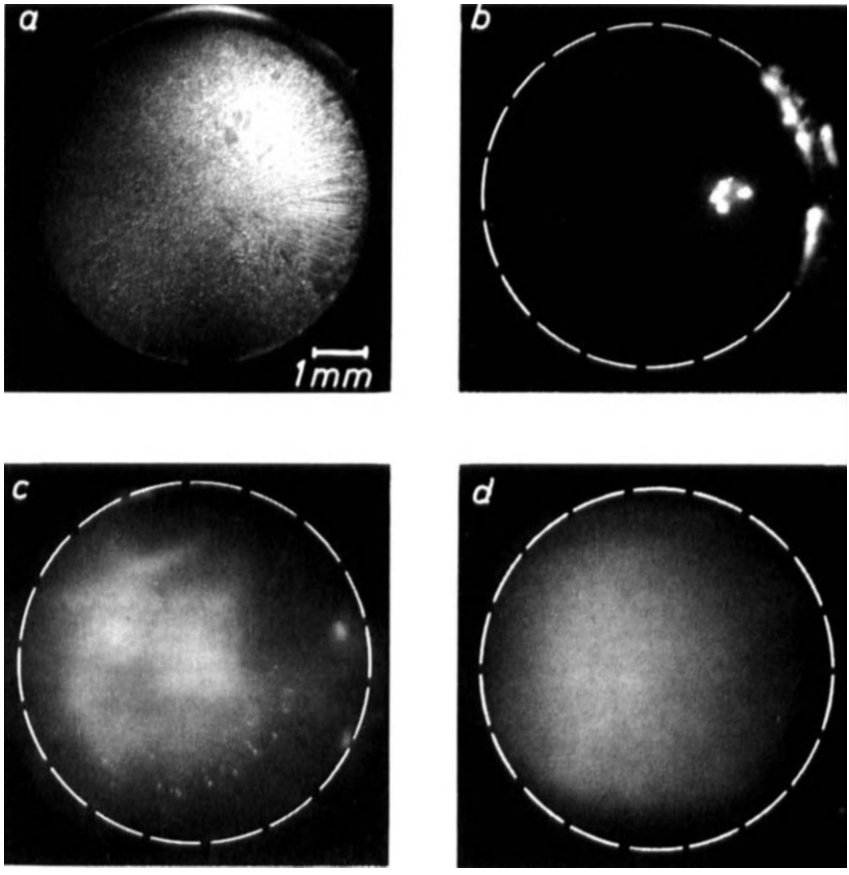

Fig.8: Image-converter microphotographs of a mercury film-cathode, showing different emission modes at a current of 10^4A. The exposure time is 10^{-8}s for the pictures (b)-(d).
(a) original state of the cathode surface; (b) patch emission mode; (c) tracks of radial spread of the emission on the surface in an intermediate state between patch- and film-emission mode; (d) film-emission mode.

In Fig.8(b) distinct luminous features like plasma flares and cathode spots are visible; the latter are called macro-spots and the emission mode characterized by these macro-spots is called "patch-emission mode". By a careful adjust-ment of the cathode temperature and the ambient Hg-vapour

Field electron emission from a regenerative liquid metal emitter is considered as successive explosive electron emission due to thermal runaway like vacuum arcing /23/. A physical model describing the cathode spot of a vacuum arc by successive explosive field emission from microscopic protrusions ("Dynamic field emission") formerly has been proposed by Mitterauer /27/. In the meantime, this model was developed considerably, presently allowing the computer simulation of transient field electron emission in vacuum arc cathode spots /28/.

Field electron emission from large-area liquid metal electron sources (LMES) comparable to those mentioned before /18/ is of great importance, e.g. for specific applications in pulsed power technology /26/. Therefore, technological concepts on the fabrication of large-area MILMIS even are appropriate for high current density miniaturized liquid metal electron sources (MILMES).

6. APPLICATIONS AND OUTLOOK

6.1. Microelectronic Technology

The flexibility and effectiveness of ions in modifying the properties of solids make them attractive tools for microfabrication in the broad sense of two-dimensional patterning. The energy or the momentum of the ions or the ions themselves can serve to alter a material at or near its surface. The three approaches to submicron ion pattern formation that are currently in active use or under investigation are scanning focused ion beam (FIB) techniques, broad ion beam (BIB) or masked ion beam (MIB) techniques and finally ion projection techniques /29/.

It is now more than ten years since the earliest use of LMIS to produce high-intensity, submicron, focused ion beams. Since then, there has been a considerable growth in the field, with FIB-systems being developed for use in surface analysis and microfabrication /30/. It was originally thought that the patterning of resist layers by scanning focused ion beam lithography (FIBL) might ultimately supplant electron beam lithography for the manufacture of microcircuits having densely packed submicron features. Since this is a serial process, typical current densities in the focused spot of the order are presently of $1 A cm^{-2}$, and even at dose requirements as low as 10^{13} ions cm^{-2}, this approach of patterning has a throughput too small to be of interest for direct writing of high-resolution patterns on full wafer fields. An interesting alternative yet is offered by the application of multiple beam machines /8/. Multiple electron and ion beam machines have been developed at SRI in the last decade, these using multiple-focused elec

pressure, transition from the patch-emission mode to a phenomenological new emission mode may be obtained. This transition occurs after evaporation of all visible macroscopic mercury droplets from the cathode surface. The overall picture of emission then is characterized by a homogeneous luminous film of nearly uniform brightness covering the cathode surface; this emission mode therefore has been called "film-emission mode" /19/,/20/.

In Fig.8(c), besides the puzzling coexistence of both the distinct modes of patch- and film-emission, the most striking details are highly luminous lines of almost equal length, which obviously are coincident withh the radial wedges visible in Fig.8(a). Finally,in Fig.8(d) there are shown the typical features of the fully developed film-emission mode.

The cathode surface state seems to be the most decisive parameter for the occurrence of the different emission modes. The essential condition for film-emission is assumed to arise from a "dynamic equilibrium" between the evaporation and condensation of Hg-atoms on the Mo-cathode surface. Condensation of Hg on Mo involves, in the first phase, heterogeneous nucleation; the rate of this process depends largely on minute imperfections and irregularities of the substrate. Therefore it may be assumed that this dynamic equilibrium implies both condensation of micron-sized Hg-droplets at favoured sites of the microstructure of the cathode surface, as well as evaporation of these droplets by the thermal effects of field emission from these microspots; that is, the dynamic equilibrium is maintained by the emission process itself. Obviously, size and life-time of the microspots is beyond the resolution involved in this experiment, which are about 10^{-5}m, and 10^{-5}s, respectively.

5.2. Liquid metal electron sources

According the polarity of the field-generating voltage, liquid metal field-effect sources may operate either in the field ionization (FI) and field emission (FE) mode /23/-/25/. On the one hand, continous electron emission has been observed from single-site needle emitters covered with Cs in a current range up to 1.5×10^{-4}A with applied voltages of 1.5kV to 2.5kV only /24/,/25/. The general type of current-voltage characteristic is similar to the case of the FI-mode; yet the onset of emission is shifted toward much lower voltages for identical emitter geometries.

On the other hand, pulsed electron emission has been reported for single site capillary emitters filled with Ga-In alloys at peak currents between 50A and 250A, at an applied voltage of 10kV to 12kV; repetitive current pulses with a rise time of 2ns and pulse duration from 3ns to 5ns were observed for this free-running self-pulsed mode /23/, /26/.

tron and ion beams that are deflected and blanked in synchrony, and used to lithograph or etch a whole wafer instead of a single chip. Such machines can reduce the processing times for a wafer and thus increase the throughput. In addition, the use of focused ion beam implantation (FIBI) for direct doping of microelectronic circuits has been made possible by the development of alloy LMIS and focusing columns incorporating ion mass-to-charge filters. While FIB systems for FIBL and FIBI are becoming increasingly sophisticated /31/, the largest growth of interest during recent years has been in sytems for perhaps the simplest FIB process of all, namely, micromachining by ion sputtering (FIBM). Systems combining FIBM and focused ion beam deposition (FIBD) are increasingly used for repair of masks used in microcircuit fabrication, and for the repair of part processed and finished microcircuits /32/,/33/.

As pointed out previously, LMIS can produce charged droplets and clusters which can be focused and scanned by electric lens and deflector systems /34/; focused droplet beam deposition (FDBD) even has been used for microcircuit repair /32/.

Low-energy ions could also be used in direct deposition if their energies were below about 100eV, so that deposition dominates sputtering /29/. Just so, the ion energy in FIB's sometimes is too high in instances where very thin MBE-grown layers must be patterned /31/. Since the extraction voltage for normal LMIS is around 10kV, this limitation can only be overcome by using a retarding electrode in the final stage of the ion optical column so that the beam is decelerated.

An alternative low-energy ion beam fabrication and deposition technique has very recently been developed, using a LMIS in a point-to-plane configuration similar to a scanning tunneling microscope (STM) system /35/,/36/. Such a device, operating in the proximity focusing mode, relies upon the low running voltage required for a LMIS when the working distance is very small. Low voltage (about 10V) and low current (as low as 10^{-9}A) operation for Ga can be maintained, provided the tip-to-plane spacings of less than 10^{-7}m can be maintained.

All these applications of FIB's in microelectronics and micromachining as well as in surface analysis (e.g., scanning secondary ion mass spectroscopy (SIMS) and scanning ion microscopy) have been performed with normal LMIS of the needle and sometimes of the capillary type.

However, in principle these conventional LMIS can be replaced by single-site MILMIS, offering therefore the advantage of a much smaller overall size and a lowered voltage requirement. The latter especially would be useful for applications where low ion energies are desirable; e.g., low-energy fabrication and deposition as mentioned before. On the other hand, the miniaturized overall size of MILMIS

is most useful in the STM applications, as it allows easily the integration of the source to the piezoelectric actuator system. Furthermore, MILMIS technology easily can fulfill the demands on extremely sharp needle emitters necessary for low voltage and low current LMIS.

6.2. Space Technology

Although not being related to microelectronics and micromachining, an even fascinating field of applications is offered for array-type MILMIS. On the one hand, considering the original purpose of the slit emitter, large area arrays of parallel, linear slit- type MILMIS could replace the parallel stacking of liquid metal ion thrusters necessary for enhanced thrust requirements /3/. Furthermore, arrays of slits or microvolcanos fed with the same liquid metal but operating in the field electron emission mode can be integrated to these thruster arrays. These MILMES then provide for the electron current which always is necessary to neutralize the ion beam in order to prevent spacecraft charging due to the expulsion of positive charged mass only.

Until now, neutralization of the Cs ion beam emanating from a slit emitter thruster has been antizipated by means of a plasma bridge neutralizer, which even is supplied with Cs. Generally, the concept of MILMIS thruster arrays with integrated neutralizers offers the advantage of both reduced mass and complexity, which is of outstanding importance in space technology.

Ion thruster operation in space modifies the charge state of a spacecraft, changing the spacecraft surface potential with respect to the distant plasma. Even the emission of a neutralized ion beam in energetic environment in sunlight can cause equilibrium potentials of the spacecraft of some 10^2V negative, with variations in potential across the spacecraft surface of comparable magnitude /37/. The latter result in surface arc discharge and related damage on spacecraft dielectrics, and even on spacecraft electronic equipment /38/. Large negative potentials about 10^2V to 10^3V also occur in eclipse. Thruster operation under such conditions raises the mainframe potential to near zero, and discharges the differential potentials on the dielectric spacecraft surface.

Although not yet being planned as an ion thruster, such a MILMIS-MILMES lightweight spacecraft charge neutralizer can provide considerable mass savings compared to noble gas (Xe) hollow cathode plasma bridge neutralizers antizipated nowadays. The liquid metal used for this purpose does not have to be Cs; if a liquid metal which is not harmful for the spacecraft and the solar panels is used, contaminations which possibly may occur with Cs are prevented.

6.3. Pulsed Power Technology

Many developing technologies, such as electromagnetic acceleration, directed energy conversion, and controlled nuclear fusion research involve the use of pulsed-power technology. This technology normally incorporates capacitive storage of electrical energy that is rapidly delivered to a load by means of fast switches such as spark gaps and pseudo-spark switches. There is, however, considerable interest in the use of inductive energy storage primarily because of the order-of-magnitude improvement in stored energy density. One key problem limiting the development of an inductive energy storage system is the lack of a fast, reliable repetitive opening switch. A number of techniques are being investigated for the development of such switches, e.g., electron beam controlled discharge devices and plasma erosion opening switches.

A recent study is focused on the application of LMIS-technology to the problem of fast, repetitive switching, i.e., a vacuum triode with a cathode formed by liquid metal electron sources (LMES) /26/, considering even the free-running self-pulsed mode of a single site LMES with a peak current up to 250A /23/. The liquid metal field emitter has several appealing features for fast repetitive switch application. It can deliver very large peak currents in a pulsed mode and is self-healing, since the emitting tip is resupplied by the liquid metal. It can supply its own positive ions for space charge neutralisation; it can be shut off very rapidly and its emission is highly repeatable for a given geometry.

However, a single-site emitter would not yield a useful pulsed power switch; otherwise, the peak current required could be achieved by an array of LMES, thus striking the concept of MILMES outlined previously. For such an array to work, all the liquid tips have to undergo explosive emission nearly simultaneously because of the shorting effect of a tip explosion. Due to the seemingly inherent feature of minimum time jitter of the onset of explosive emission, simultaneous triggering of such an array appears feasible. Another alternative would be a much larger array such that there would be enough tips exploding at any given time to switch the required current load. Thus the multipoint array would not require individual tips to be controlled, but rather would depend on the random pulsing of a large number of tips.

Clearly, all technologies mentioned initially for the fabrication of MILMIS may be appropriate to realize such a MILMES-array-switch. The ability of a microstructured solid surface covered with a thin liquid metal (Hg) film ("film cathode") to supply pulsed currents of more than 10^4A at an average current density of about $5 \times 10^4 Acm^{-2}$ has been proven

previously /21/,/22/.

A prospective field of pulsed-power technology is inertial confinement fusion (ICF), driven by ligth ion beams (LIB). For example, ICF-experiments with a beam energy of 30MeV on the Particle Beam Fusion Accelerator (PBFA II) at Sandia National Laboratories will require the use of high intensity ($5x10^{3}Acm^{-2}$), high-purity beams of singly ionized lithium (Li) ions /39/. One approach which is being tested to produce such beams is the use of field-enhanced Li ion sources. The anode of such a source is of stainless steel which has a porous, fritted surface structure characterized by protrusions approximately $10^{-4}m$ high separated by $1.5x10^{-4}m$ and having a tip diameter of about $1x10^{-5}m$. This structure is covered with a solid dielectric coating of lithium nitrate ($LiNO_3$) or lithium fluoride (LiF), the thickness of this film is between $1-5x10^{-4}m$. With average anode-cathode gap fields of $2x10^{8}Vm^{-1}$ applied to the anode surface for approximately 20ns, ion beams with Li^{+}-fractions exceeding 70% were successfully produced.

Previously a theoretical approach has even been performed toward the realization of an electrohydrodynamically driven large- area LMIS for the PBFA II experiment, consisting of a planar liquid Li layer on a flat, unstructured surface /18/. Ion production is assumed to occur of the apices of the disturbed surface structure caused by unstable growth of surface waves in a high electric field.

Just intermediate between these experimental and theoretical approaches toward an effective Li-LMIS, the concept of MILMIS can be established. If one enhances the number of emitting sites present in the PBFA II experiment by means of a two-dimensional array of tips or microvolcanos, it seems feasible to approach the current density requirement of $5x10^{3}$ Acm^{-2} /39/ with an emission current of $10^{-4}A$ per emitter and with an array spacing of $1.5x10^{-4}m$. This corresponds to an emitter density of $5x10^{7}cm^{-2}$, which is just above the present state-of-the-art technology. For comparison, according to the theoretical model /18/, the wavelength of the electrohydrodynamic instability at an onset field of $10^{9}Vm^{-1}$ is about $5x10^{-7}m$, corresponding to an emission site density of $5x10^{8}cm^{-2}$ and an emitter current of $10^{-8}A$.

Finally, as the liquid metal under consideration (Li) is an alkali metal like Cs, most of the physical and technological experience obtained in slit emitter experiments for space propulsion (e.g./5/,/11/,/25/) may be transferred to the challenging problem of high current density MILMIS for nuclear fusion research.

References

/1/ Kaufman, H.R. (1961) 'An ion rocket with an electron-bombardment ion source', NASA Tech.Note D-885.

/2/ Mahoney, J.F. et al. (1969) 'Electrohydrodynamic ion source', J.Appl.Phys. 40, 5101-5106.

/3/ Bartoli, C., von Rohden, H., Thompson S.P., and Blommers, J. (1984) 'A liquid caesium field ion source for space propulsion', J.Phys.D:Appl.Phys. 17, 2473-2483.

/4/ Mitterauer, J. (1987) 'Field Emission Electric Propulsion: Emission site distribution of slit emitters', IEEE Trans.Plasma Sci., PS-15, 593-598.

/5/ Mitterauer, J. (1989) 'Field Emission Electric Propulsion: Mass and optical spectroscopy of beam components', Final Report on ESTEC-Contract 6545/85.

/6/ Aberth, W. and Spindt, C.A. (1976) 'Characteristics of a volcano field ion quadrupole mass spectrometer', Int.J.Mass Spectrom.Ion Phys., 25, 183-198.

/7/ Spindt, C.A. (1988) 'An efficient low-voltage field ion source', presented at the 1st Int.Vacuum Microelectronics Conf., Williamsburg, VA, USA, June 13-15, 1988.

/8/ Spindt, C.A. (1992) 'Microfabricated field emission and field ionization sources', Surf.Sci., 266, 145-154.

/9/ Taylor, G.I. and McEwan, A.D. (1965) 'The stability of a horizontal fluid interface in a vertical electric field', J.Fluid Mech., 22, 1.

/10/ Aitken, K.L. and Prewett, P.D. (1983) 'Field Emission Electric Propulsion: Basic investigations of the ion emitting region', Final Report on ESTEC-Contract 4462/80, 1983; see also: ESA Report Reference: ESA CR(P) 2078.

/11/ Mitterauer, J. (1986) 'Field Emission Electric Propulsion: Spectroscopic investigations on slit emitters', Final Report on ESTEC-Contract 5051/82, 1986; see also ESA Report Reference: ESA CR(P) 2330.

/12/ Spindt, C.A., Brodie, I., Humphrey L. and Westerberg, E.R. (1976) 'Physical properties of thin-film field

emission cathodes with molybdenum cones', J.Appl. Phys., 47, 5248-5263.

/13/ Gray, H.F. and Campisi, G.J. (1987) 'Microfabrication of field emission devices for vacuum integrated circuits using orientation dependent etching', Proc. Mat.Res.Soc., 76, 67-72.

/14/ Turner, R.E. (ed.) (1989) 'Vacuum Microelectronics 89' (Proc.2nd Int.Conf.on Vacuum Microelectronics, Bath, UK, July 24-26, 1989), Inst.of Physics, Bristol and New York.

/15/ Spindt, C.A., Holland, C.E. and Stowell, R.D. (1986) 'Field emission array development', presented at the 33rd Int.Field Emission Symposium, Berlin, FRG, July 7-11, 1986.

/16/ Wilde, D.K. (1988) 'Thermionic integrated circuits: A status report', presented at the 1st Int.Vacuum Microelectronics Conference, Williamsburg, VA, USA, June 13-15, 1988.

/17/ Hoshinouchi, S. et al. (1989) 'Fabrication of fine heating elements for microelectronics', Proc. 2nd Int.Conf.on Vacuum Microelectronics, (Bath, UK), R.E.Turner, (ed.), pp.13-16.

/18/ Pregenzer, A.L. (1991) 'High-frequency parametric excitation of electrohydrodynamic instabilities: Applications to large-area ion sources', J.Appl.Phys., 58, 4509-4551.

/19/ Bertele, H.von (1958) 'A new phenomenon of electron emission from thin mercury films', Nature, 182, 1148-1149.

/20/ Gabor, D. and Vithayathil, J. (1962) 'The Bertele Arc' Nature, 189, 821-822.

/21/ Mitterauer, J. (1973) 'The surface dependence of different emission modes on mercury arc film cathodes', J.Phys.D:Appl.Phys., 6, L91-L93.

/22/ Mitterauer, J. (1973) 'Experimental evidence of different emission modes on mercury film cathodes of pulsed high current arcs', Proc.11th Int.Conf. Phenomena in Ionized Gases, (Prague, CSFR), 1973, 71.

/23/ Swanson, L.W. and Schwind, G.A. (1978) 'Electron emission from a liquid metal', J.Appl.Phys., 49, 5655-5662.

/24/ Mitterauer, J. (1981) 'Radiation emission from a liquid caesium field electron and field ion source', Proc.28th Int.Field Emission Symposium, (Portland, OR), L.Swanson and A.Bell, (eds.), 89-91.

/25/ Mitterauer, J. (1981) 'Spectroscopic investigations of a field emission generated radiative zone; Mass spectroscopic measurements', Final Report on ESTEC-Contract 2734/76; see also: ESA Report Reference: ESA CR(P)1589

/26/ Coggiola M.J. and Young, S.E. (1988) 'Characteristics of a pulsed, liquid-metal field emission source for use in fast high-current switches', SPIE-Space Structures, Power and Power Conditioning, 871, 165-172.

/27/ Mitterauer, J. (1972) 'Dynamic Field Emission (DF-Emission): A new model of cathode phenomena in cold cathode arcs', Proc.2nd Int.Conf. Gas Discharges (London, UK), 215-217.

/28/ Mitterauer J. and Till, P. (1987) 'Computer simulation of the dynymics of plasma-surface interaction in vacuum arc cathode spots', IEEE Trans.Plasma Sci.,PS-15, 488-501.

/29/ Brown, W.L. (1989) 'Recent progress in ion beam lithography', Microelectronic Engineering, Amsterdam, North Holland, 9, 269-276.

/30/ Prewett, P.D. (1989) 'Focused ion beams in microfabrication', Colloque de Physique, C8/179-190.

/31/ Ahmed, H. (1989) 'In-situ processing of semiconductors by combining MBE, lithography, pattern transfer, implantation and annealing', Microelectronic Engineering Amsterdam, North Holland, 9, 313-320.

/32/ Sudraud, P., Ben Assayag, G. and Bon, M. (1987) 'Focused ion beam repair in microelectronics', Microelectronic Engineering, Amsterdam, North Holland, 6, 538-595.

/33/ Clampitt, R., Watkins, R. and Whitaker, J. (1987) 'Custom IC repairs using focused ion beams', Microelectronic Engineering, Amsterdam, North Holland, 6, 605-610.

/34/ Ben Assayag, G., Sudraud, P., Alaoui F. and Swanson, L.W. (1987) 'Metal droplet beam microelectronics technology: Production, focusing and deposition', Microelectronic Engineering, Amsterdam, North Holland, 349-354.

/35/ Bell, A.E., Rao, K. and Swanson, L.W. (1988) 'Scanning tunneling microscope liquid-metal ion source for micro fabrication', J.Vac.Sci.Technol., B6, 306-310.

/36/ Komuro, M., Kitamura, O. and Okayama, S. (1989) 'Ion beam fabrication using piezo-actuator and liquid metal source', Microelectronic Engineering, Amsterdam, North Holland, 9, 285-288.

/37/ Olsen, R.C. (1981) 'Modification of spacecraft potentials by plasma emission', J.Spacecr.Rockets, 18, 462-469.

/38/ Balmain, K.G. (1986) 'Surface arc discharge and discharge damage on spacecraft dielectrics', Proc.12th Int.Symposium on Discharges and Electrical Insulation in Vacuum (Shoresh, Israel), R.Boxman, (ed)., 134-138.

/39/ Stinnett, R.W. et.al. (1988) 'Field-enhanced lithium ion sources for PBFA II', Proc.13th Int.Symposium on Discharges and Electrical Insulation in Vacuum, (Paris, France), J.M.Buzzi and A.Septier (eds.), 1, 34-36.

INTEGRATED MICROTIPS: APPLICATION TO FLAT DISPLAYS

R. BAPTIST
LETI-CEA TECHNOLOGIES AVANCEES
DOPT/SCMM CENG, 85 X, 38041 GRENOBLE CEDEX

ABSTRACT . Field-emitter arrays with 10^4 tips/mm^2 packing densities are currently fabricated for flat displays at LETI. For this application the main characteristics needed are:
- moderate current densities,
- low driving voltages,
- moderate pulse recurrence frequency,
- long and short range uniformity over large areas,
- absence of shorts and bright points (or tolerance to shorts),
- resistance to degraded vacuum environments,
- long life times.

We will first briefly present the example of the LETI display and then will try to show why these cathodes are so well suited for this type of application.

1. Preamble

As an introduction, we will refer to two papers on microtips fluorescent displays which were recently published by our group [1,2]. In these papers, thin Cathode-Ray Tubes (CRT) with a large matrix array of microscopic electron guns (microtips) were described. Their electrical and luminous characteristics were presented and compared to those of well-known Liquid Crystal Displays. Here we will especially focus our attention on the electron emission phenomenon and on the technological requirements of such an application. In the second part of this paper, we will present some results obtained on small cathode areas in order to improve the screen performances and to extend the application field of these cathodes.

2. Introduction: the Microtip Fluorescent Display

The microtip fluorescent display is a thin-cathode ray tube with two main features:
- it contains a large matrix array of micro-guns or "microtips" that emit electrons by field effect,
- it has a screen covered with a low voltage phosphor, which emits light when struck by electrons (low voltage cathodoluminescence - few hundreds volts).

V.T. Binh et al. (eds.),
Nanosources and Manipulation of Atoms Under High Fields and Temperatures: Applications, 165–176.
© 1993 *Kluwer Academic Publishers.*

2.1. DESCRIPTION OF THE DEVICE

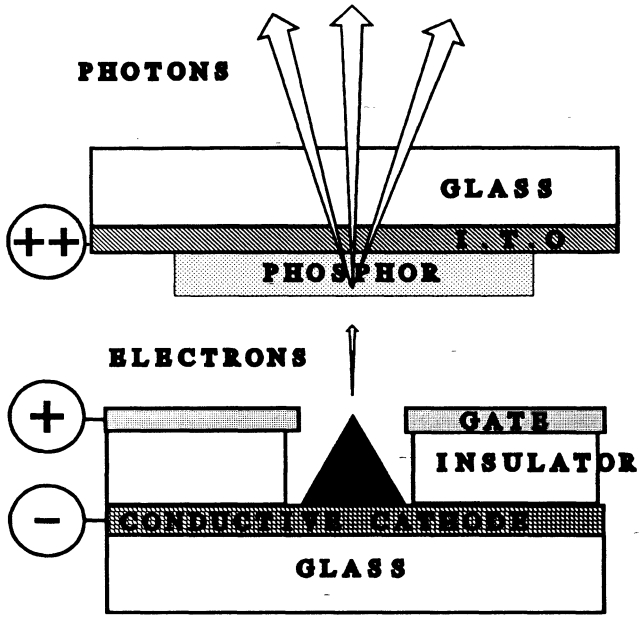

Figure 1. Operation principle of a microtip fluorescent display.

The operation principle is shown on figure 1. Electrons are extracted from microtips by applying a voltage less than 100 V between the gate and the cathode conductors. These electrons are accelerated by an electric field towards the anode, which is biased at a higher potential than the gate. The electrons excite the phosphor, which emits light by cathodoluminescence. The light is observed from the opposite side through the anode substrate. This operation principle is the same as that of conventional cathode-ray tube but unlike CRT, the number of electron guns is greatly increased (some millions), the distance between the cathode and the screen is greatly reduced (some hundred microns) and there is no need of a deflection system, as proximity ensures focusing.

The cathode (back-plate of the device) is shown in figure 2. It consists of a crossed network of metallic electrodes separated by an insulating layer 1 μm thick. A pixel is defined by the intersection of cathode columns and gate lines. Because the tip density is high (10^4 to 10^5 tips per mm^2) each pixel contains enough tips to provide a high degree of redundancy. For a 6" diagonal monochrome display having 256 lines*256 columns, the dot size is 0.12 mm^2 .

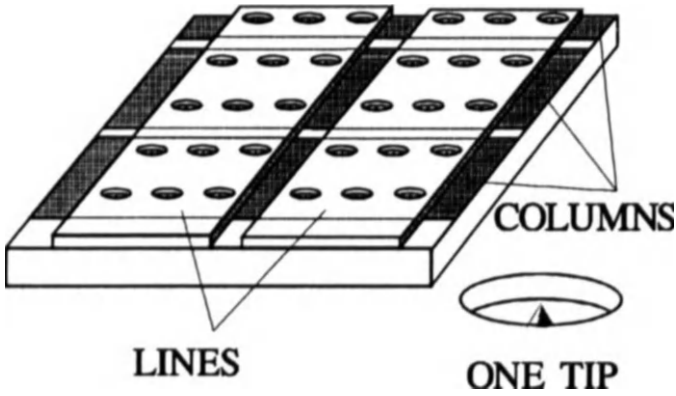

Figure 2. Matrix array of the microtip fluorescent display cathode. Each line-column crossing includes a great number of tips (approximately 1000 tips per pixel in the 6" monochrome display and not 6 as represented on the figure).

Figure 3 shows a side view of the device. The anode-cathode spacing is only 0.2 mm, so that the entire panel is only 2 or 3 mm thick. This gap is maintained by glass balls, which play the role of spacers. An exhaust tube allows one to achieve pressures below 10^{-7} mbar in the cell.

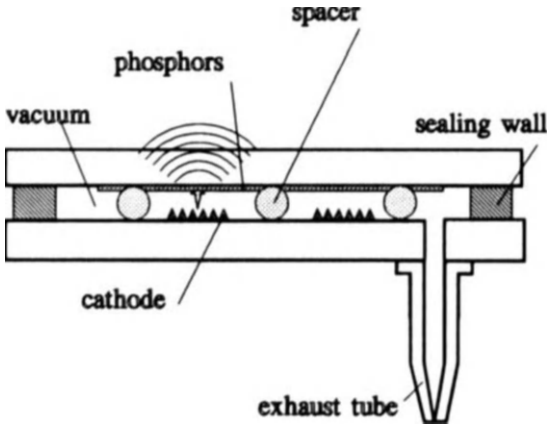

Figure 3. Side view of the display.

2.2. CATHODE REQUIREMENTS FOR A FLAT PANEL APPLICATION

For flat panel application, the cathode must:
- have a fast response time,
- have an uniform electronic emission on the whole surface,

- supply a sufficient current to achieve a suitable brightness at low voltage operation,
- be free from shorts between tips and gate.

All these requirements are fulfilled thanks to:

- the field effect itself, which is fast when the product of the tip-gate capacitance by the tip access resistance is low,(see § 3.) below)
- the averaging effect due to a great number of tips per pixel together with a resistive layer acting as a current limiting circuit, (see § 3.1.) below)
- the use of a high number of microscopic emitters (overall sizes < 1.5 μm diameter) per pixel allowing to supply a current density of 1 mA/mm^2 with a driving voltage lower than 100 V,
- the use of the resistive layer, which in case of a short between a tip and the gate limits the current flowing through the tip without incidence on the driving voltage.

2.3. ADDRESSING MODE

We will not go into the details of all driving schemes which have been tested for monochrome or full-colour displays, the readers should refer to references [1], [2] and [3] for a more detailed description. Instead, we will rather use the simple case of a monochrome display without grey scale. The scheme of addressing is a "one line-at-a-time" addressing which is represented on figure 4.

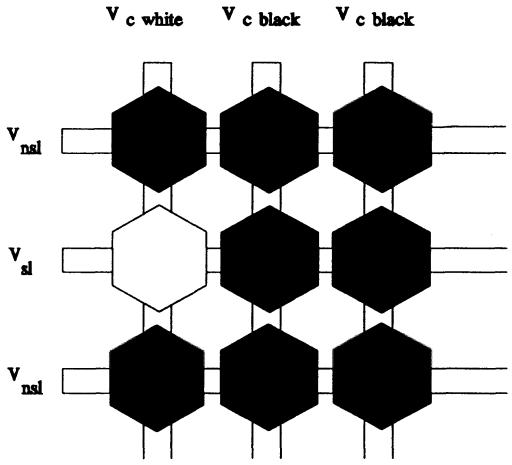

Figure 4. Addressing mode for a monochrome display without grey scale.

When a line is selected (during 64 μs), its potential is chosen to be V_{sl} = 50 V. During the same time, selected columns are raised to $V_{c\ white}$ = - 30 V , whereas other columns remain at $V_{c\ black}$ = 0 V. If the voltage difference between the gate and a column is +80 V, electrons are emitted by the corresponding cathode; these electrons are then attracted by the anode which is positively biased to 400 V. If the voltage difference is only 50 V (V_{sl} - $V_{c\ black}$) the emission current is negligible because of the shape of the field emission current-voltage characteristics curve (see § 3. below). After 64 μs, a new line is selected and new signals are again supplied to the desired columns. A picture is then displayed in ~ 16 ms

(256*64 μs), a time similar to the TV frame time (note that the phosphor response time is ~1μs).

2.4. LIFE TIME

The high reliability of field emission from microtips in ultrahigh-vacuum and even under special moderate pressures has already been demonstrated by C. A. Spindt [4]. However, in a flat panel with static vacuum conditions, the emission current and the luminance stability of the display depend critically on the phosphor material and on the outgasing/baking conditions. For molybdenum tips and ZnO:Zn phosphor, a life time over 20,000 hours has already been demonstrated.

3. Miscelaneous Results with small Cathodes

Cathodes having different geometries are currently produced by LETI for various applications such as electron interferometry, ionisation sources or electron sources for laser pumping [5]. Other cathodes are also produced for studying the field emission effect itself. For example, LETI produces mono-tip cathodes, cathodes with knife edge shaped emitters, cathodes with meshed structures [6], or cathodes with integrated focalisation electrodes. In general, as our applications require "low" but otherwise stable, homogeneous current densities and high reliability, our cathodes normally incorporate a resistive sheet placed below the base of each emitter tip. The effect of this in line resistance will be briefly described before presenting results obtained with different cathodes.

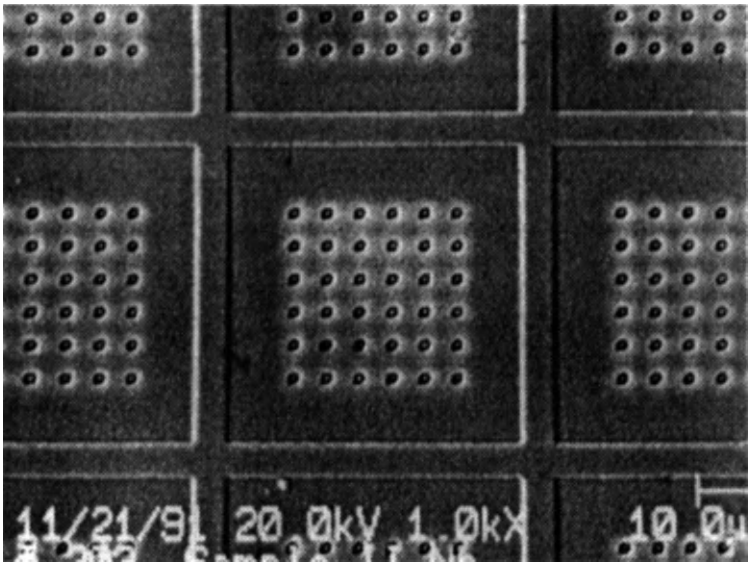

Photo 1. μ-Auger analysis of a cathode with a meshed structure (see reference [6]).

3.1. THE RESISTIVE SHEET.

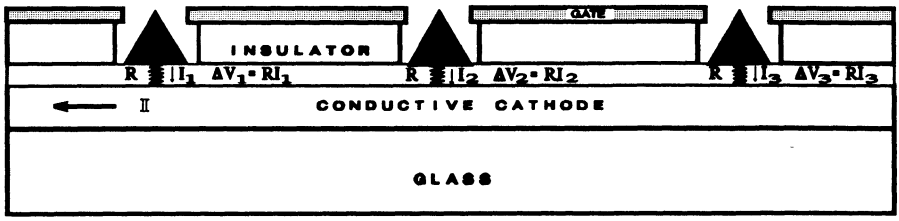

a)

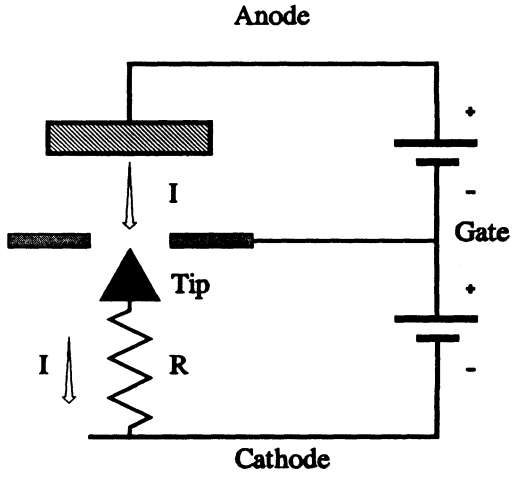

b)

Figure 5. a) Voltage drop induced by a resistor in line with a tip,
b) Electric circuit used for one tip (for example tip1).

Figure 5 presents a) the basic structure of a cathode with three tips which incorporates a resistive sheet below each tip, b) the associated power supplies in a triode configuration. We suppose that each tip would have in absence of the resistive sheet the respective I-V characteristic curves as represented on figure 6. The analysis of the electrical circuit of figure 5 b) illustrates the principle of the current regulation.

By applying Kirchoff's law to the closed loop formed by the cathode and its supply voltage, and by using the Fowler-Nordheim expression for the emitted current, we can write the values of the voltage drops across each resistor.

$$V_{gate}-V_{cath.} = (V_{gate}-V_{tip})+(V_{tip}-V_{cath.})$$

$$(Vtip\text{-}Vcath.) = R * I$$
$$I = a\,(Vgate - Vtip)^2 * \exp(-\,b/(Vgate - Vtip))$$

From this, we deduce the value of the real voltage applied at the apex of each tip. A graphical representation of this has been drawn on figure 6 by using the load line, which represents the value of the possible current flowing through the resistor (co-ordinates of this line are 0, V_{GC}/R and V_{GC}, 0).

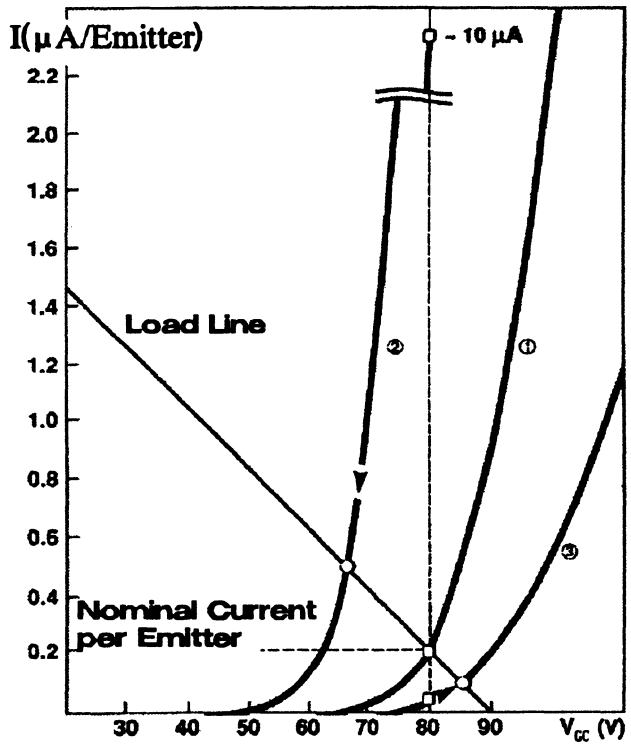

Figure 6. I(V) characteristics for three different tips.

The intersection of the characteristic curve with the load line gives the **effective** current flowing through each tip and each respective resistor. For a given V_{GC} value (voltage "physically" applied to the cathode), different voltage drops across the resistances are obtained depending on the "response" of each tip. For example, in the case of figure 6, a V_{GC} value of 90 V is applied, a voltage drop of 10 V occurs for tip1, 23 V for tip2 and ~ 4 V for tip3.

For the flat panel application, this resistive sheet ensures that very high current of some tips will be avoided and that an "averaging" effect will be created. Typical values for the access resistance are a few tens megohms.

3.2. RESULTS WITH A MONOTIP

If we consider the emission current of one tip, we observe that its amplitude fluctuates between discrete values as a function of time. We have measured the value of this current every second during 15 days for two different tips. The first tip (niobium) was without resistive sheet, the second one (molybdenum) with a resistive sheet. The collected data are represented as an histogram of the relative frequencies found for each value of the current. They are shown respectively in figure 7 a) and 7 b) (these measurements define the probability density function for the emitted current).

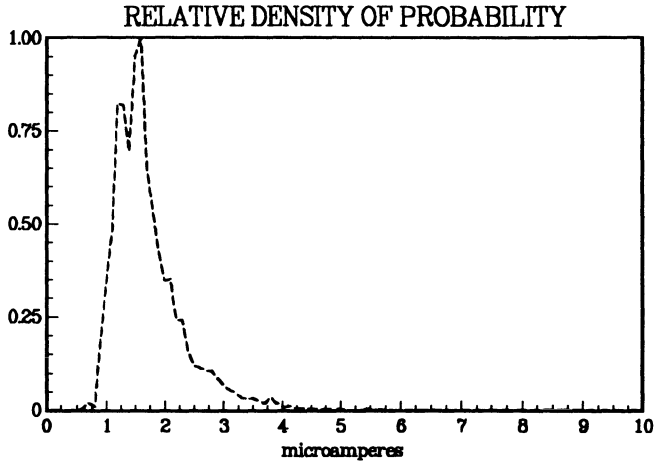

a)

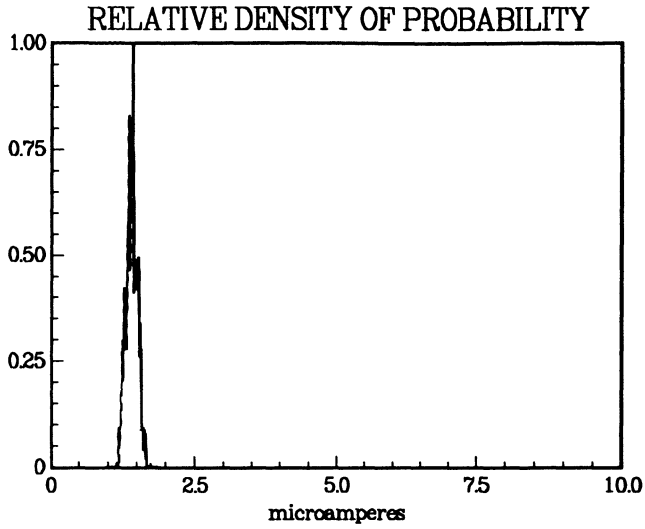

b)

Figure 7. Relative density of probability of the emission current for a tip without resistive layer (a) and with a resistive layer (b); (V_{GC}=85 V).

A comparison of the two curves illustrates the progresses obtained in stabilising "artificially" the emission current through the use of a resistive layer. Moreover with the present molybdenum tips, the emitted current can remain rigorously constant for periods extending up to half an hour.

From the preceding example, it is clear that an I(V) curve is very difficult to measure using a single tip like the first one, whereas it is easier to do it for the second one. Such a characteristic is shown in figure 8 a) together with the associated Fowler-Nordheim curve (b). The Fowler-Nordheim curve presents two portions which are almost linear: at low voltage (high 1/V) the behavior is characteristic of field emission whereas at high voltage (low 1/V) it is characteristic of a saturation due to the access resistance(~ 25 megohms).

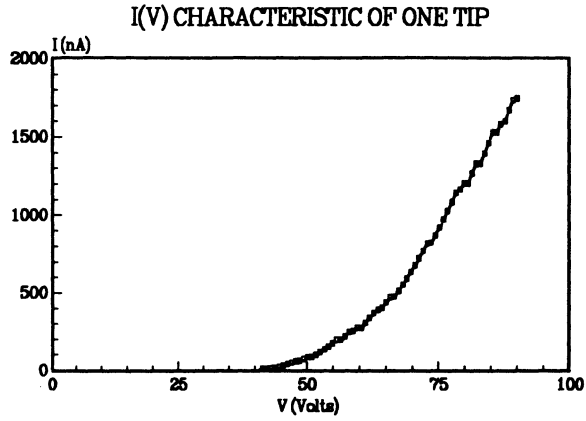

a)

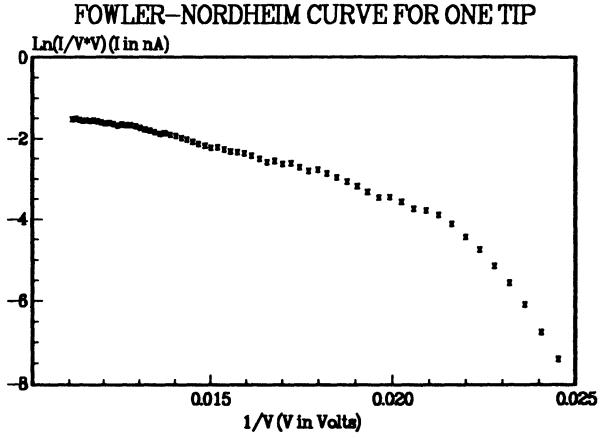

b)

Figure 8. a) I(V) characteristic curve for a mono-tip with resistive sheet,
b) Fowler-Nordheim curve of the preceding characteristic.

3.3. RESULTS WITH LARGER CATHODES

Cathodes with larger emitting surfaces have been fabricated in order to test their performances. For example with a circular cathode (diameter 5mm) having 200,000 tips, mounted in a particular circuit taking into account the space charge effect, it was possible to extract, during a long period, pulses of 2 μs duration (rise time less than 1 μs) with a pulse spacing of 10 μs and a peak current of 65 mA. However, care had to be taken that positive ions do not travel from the anode (biased to 1000 V) towards the tips.

3.4. RESULTS WITH KNIFE EDGE SHAPED CATHODES

Cathodes with such a profile have been also tested (photo 2).

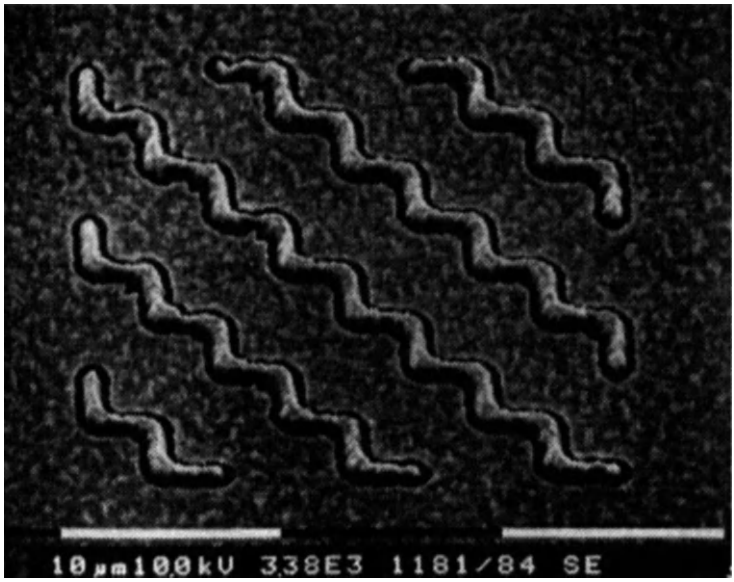

Photo 2. Knife edge shaped cathodes.

The comparison with tip cathodes performances is not obviouse because the size of the emitting surface is not well known. However, for "knife edges" with the largest possible density and a zigzag form (during the parting layer (Ni) evaporation process, the metal must not penetrate into the holes [1]), we have found that the I(V) characteristics were somewhat lower than for the tips. The difference is within a factor of two.

4. Conclusion

Field emitter cathodes covering areas from some square microns to a square decimetre have been fabricated and tested in various environments. The low voltage operation of the cathode in microtips fluorescent displays make them attractive because their lifetime is greatly increased in comparison with the one obtained in high current density applications.

Presently, the integration of microtips on large sizes (14"diagonal displays) can be anticipated, although the photolithography process for the micro-holes production and the tips evaporation process has to be improved.

Acknowledgements: I wish to acknowledge numerous fruitful interactions with the "ECRANS FLUORESCENTS A MICROPOINTES" group.

References:

[1] Baptist, R. (1991) 'Ecrans fluorescents à micropointes' , L'Onde Electrique, Vol. 71, n°6, 36-42.

[2] Vaudaine, P. and Meyer, R. (1991) ' "Microtips" fluorescent displays' , International Electron Devices Meeting , Washington, DC, December 8-11, 1991,197-200.

[3] Chubun, N.N. et . al. (1991) 'Field-emission array cathodes for a flat-panel display' ,4th International Vacuum Microelectronics Conference, August 22-24, 1991, Nagahama, Japan, 60-61.

[4] Spindt, C.A. et. al.(1991) 'Field emitter arrays for vacuum microelectronics' , IEEE Transactions on Electron Devices, Vol 38, n°10, 2355-2363.

[5] Molva, E. et. al. (1992) 'Microgun pumped semiconductor lasers: application to CdTe-CdMnTe' , 7th Trieste Semiconductor Symposium - Wide Band Gap Semiconductors, June 8-12, 1992, Trieste, Italy.

[6] Meyer, R. (1991) 'Recent developments on "Microtips" display at LETI', 4th International Vacuum Microelectronics Conference, August 22-24, 1991, Nagahama, Japan, 6-9.

FIELD-INDUCED TRANSFER OF AN ELECTROPOSITIVE ATOM BETWEEN TWO CLOSELY SPACED ELECTRODES

N. D. Lang
IBM Research Division
Thomas J. Watson Research Center
Yorktown Heights, New York 10598

ABSTRACT. The transfer of an adsorbed atom from one electrode to another in close proximity, with a potential difference between the electrodes, is analyzed theoretically. We focus particularly on the case of a sodium atom.

There have recently been several experiments in which an atom is transferred between tip and sample in the scanning tunneling microscope (STM) under the influence of an applied bias of several volts. [1-3] This process has been analyzed previously [4] for the case of the transfer of a Si atom using a model consisting of two planar metallic electrodes, represented using the jellium model [5], with a single atom in the region between them. Here we consider the case of a sodium atom, which can be expected to be broadly representative of the behavior of alkalis and other electropositive atoms. [6]

Our solution proceeds in the same way as for the Si case. First, within the framework of the density-functional formalism, we find the single-particle wave functions and self-consistent density distribution for the pair of bare metallic electrodes, assuming them for simplicity to be identical ($r_s = 2$ jellium model), in the presence of the bias voltage. We next use the method of Lang and Williams [7] to find the wave functions and density distribution for the total system consisting of the two electrodes plus the Na atom. From the density distribution, we can determine immediately the electrostatic force on the nucleus of the atom.

V.T. Binh et al. (eds.),
Nanosources and Manipulation of Atoms Under High Fields and Temperatures: Applications, 177–183.
© 1993 *All Rights Reserved.*

We use an electrode spacing of 12 bohrs. The polarization of all core orbitals on the Na atom is included in order to obtain an accurate value for the total electrostatic force F on the nucleus. It is also convenient to define an energy for discussion purposes as [8]

$$E(z) = -\int_{z_0}^{z} dz' F(z') ,$$

where z is the coordinate along the surface normal and z_0 is arbitrary.

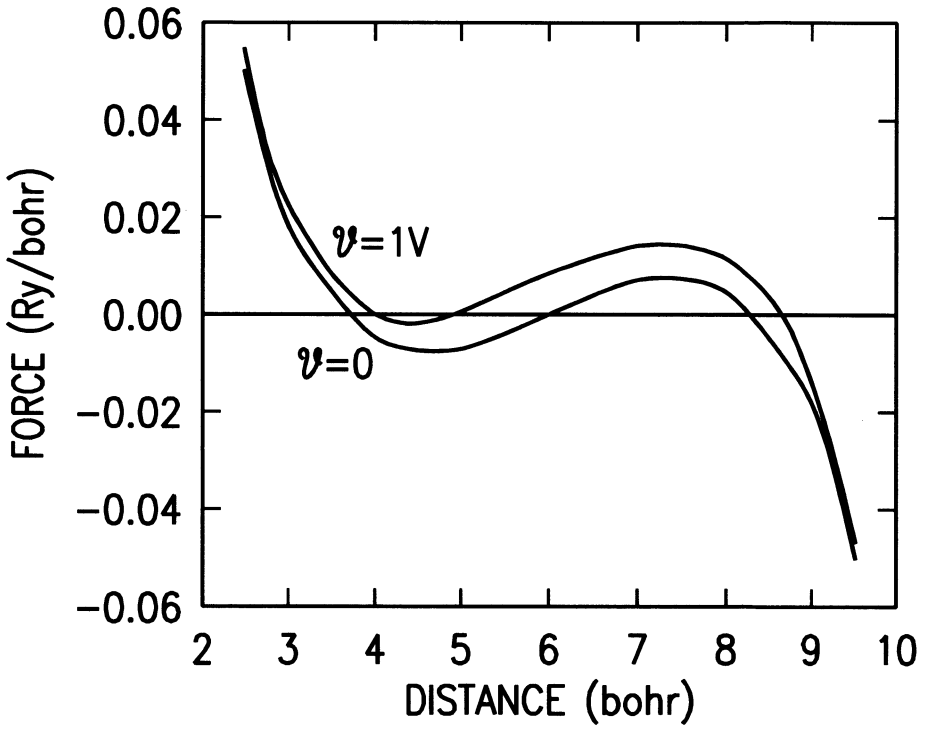

Figure 1. Electrostatic force on nucleus of Na atom placed between two bare jellium-model electrodes ($r_s = 2$), as a function of distance of atom from left electrode. Electrode separation held fixed at 12 bohrs. Positive force moves atom to the right. (1 Ry = 13.6 eV.)

The results for F(z) are shown in Fig. 1 for two values of the bias $\mathcal{V}$: 0 and 1 V, with the left electrode taken positive. Each force curve crosses the horizontal axis in three places. These crossings, i.e. the z values for which F(z)=0, correspond to minima or maxima in the corresponding E(z) curve obtained using the above equation. For each force curve, the center crossing point corresponds to a maximum in E(z), and the other two crossing points correspond to minima.

Consider first just the $\mathcal{V}$=0 curve in Fig. 1. Since the two electrodes are identical, this curve is antisymmetric about the midpoint between the electrodes. The energy curve E(z) derived from this force curve using the above equation, a symmetric double-well potential, is shown in Fig. 2.

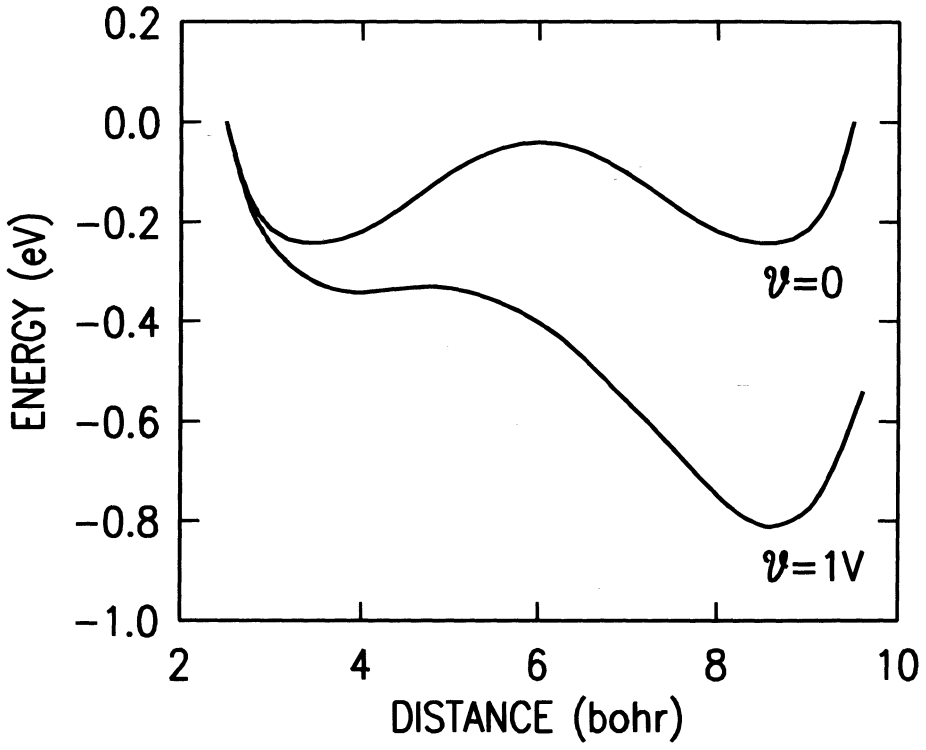

Figure 2. Energy for Na atom between two electrodes considered in Fig. 1, as a function of distance of atom from left electrode, for bias values $\mathcal{V}$ of 0 and 1 V. Electrode separation held fixed at 12 bohrs. Zero of energy is taken to be value at atom distance of 2.5 bohrs (i.e. z_0 in equation in text defining energy is set at this distance).

Returning to Fig. 1, we note that the value of the energy barrier to transferring the atom from the left to the right electrode for a particular bias is given by (the magnitude of) the integral of the corresponding force curve between its left and center F=0 points, with an analogous statement for transfer from right to left. That is, for each curve in Fig. 1, the area under the curve between crossing points gives the activation barrier. We see immediately from this figure that raising the bias $\mathscr{V}$ to 1 V decreases the barrier for transfer from the left electrode nearly to zero. This is clearly evident in the $\mathscr{V}=1$ V curve shown in Fig. 2; this same curve shows that the barrier to transferring a Na atom in the opposite direction is ~0.5 eV. Thus our model predicts a net transfer of Na atoms from the positive to the negative electrode. [9,10] This is the same direction of transfer as observed for Si by Lyo and Avouris. [2]

We note also at this point that the direction of atom transfer in the experiment of Eigler *et al.* [1] for Xe is opposite to that found in the experiment of Lyo and Avouris [2] for Si, i.e. Xe is transferred off of a surface when it has negative polarity. Cerdá *et al.* [11] and Walkup *et al.* [12] have suggested that for the Xe case, where there is negligible charge transfer to or from the atom, the atom transfer has a rather different explanation from that discussed here.

Now the field midway between the electrodes when the bias is 1 V is ~0.2 V/Å. [13] This is not such a large field on the scale of atomic quantities, and so we would expect that for the atom in this region, the net force on it would be $\sim \mathscr{E} q_0$, where q_0 is the net charge on the atom for zero bias, and $\mathscr{E}$ is the electrostatic field (in the absence of the atom). We neglect image effects here, because the image force will vanish for the atom midway between the electrodes at zero bias (by symmetry), and the small field just mentioned will induce only a small dipole moment on the atom; this in turn will not create much asymmetry in the image distributions between left and right electrodes. The value shown in Fig. 1 for the force when the atom is midway between the electrodes, with $\mathscr{V}=1$ V, corresponds to $q_0 \sim 1$ (in units of the magnitude of the electron charge $|e|$). We cannot conclude from this that the alkali is completely ionized, since the form for the force just noted represents an oversimplification of the quantum-mechanical calculation involved here [14], but it nonetheless suggests that there is a significant charge transfer from the atom to the metal. [15]

The net charge on the atom is a quantity that is difficult to define precisely, although several reasonable definitions are possible. To further our discussion, it is convenient to discuss the charge on an atom near just a single surface, in terms of the dependence of the dipole moment on distance. This has been computed in Ref. [7]

for a number of different atoms. One measure of the charge on the atom is the rate of change of this dipole moment with distance, which yields a value of ~0.4 | e | for Na. For our two-electrode problem, this measure is less useful, because the slope of the dipole-moment curve vanishes by symmetry for the atom midway between the electrodes. However the value for the charge should not be too different from what it is in the single-electrode case.

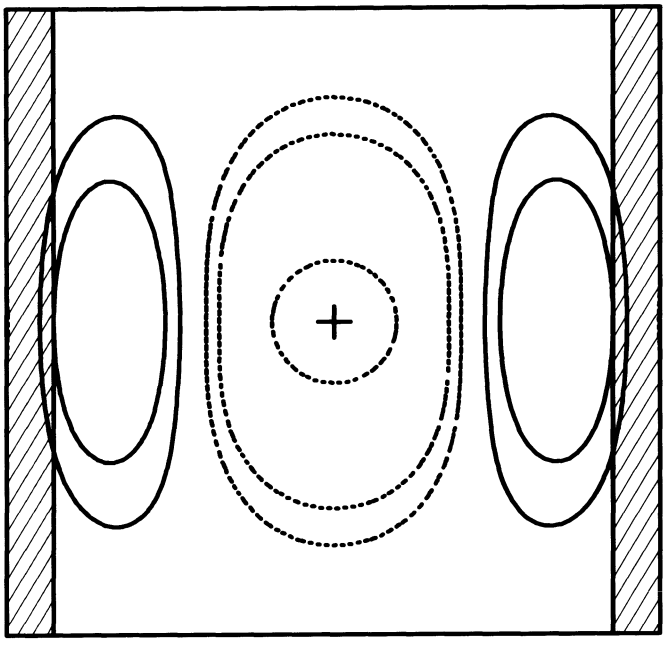

Figure 3. Contour map of electron number density for Na atom placed midway between two jellium-model electrodes minus electron number density of free atom. Positive backgrounds of two electrodes (shaded areas) are separated by 12 bohrs; bias $\mathscr{V}$ is zero. Solid contours are positive (i.e. an electron excess) and broken contours are negative, with values shown ± 0.0006 and ± 0.0003 electrons/bohr^3. Contours in immediate vicinity of nucleus have been deleted for clarity.

A map of the electron number density for a Na atom midway between the two electrodes at zero bias, minus the electron number density of the free atom, is shown in Fig. 3. The charge depletion within the largest dotted contour at the center of the map is ~0.3 | e | , but the actual amount of charge that should be thought of as being transferred away from the atom is larger. The charge transferred to the metal electrodes can be expected to be distributed about the image plane of each electrode.

The image plane here is about 1½ bohrs in front of the positive background edge [16], which is roughly where the solid contours in front of each electrode are centered, suggesting that these represent the transferred charge. These contours are however still within the region of the Na 3s orbital, and so the charge, that should be thought of as being transferred out of the 3s orbital and onto the electrodes (as evidenced by the 3s component of the state-density resonance [15] moving up through the Fermi level), does not in fact go very far spatially. This has the effect of obscuring part of the depletion of the charge in the 3s orbital. It also means that the core-level eigenvalues are not shifted substantially from their free-atom values, and so this measure of charge transfer, which had been useful in the study of Si, which has an appreciably more compact valence orbital than Na, is much less useful here. The point for our present discussion is simply that the effective charge on the Na atom, in the absence of an electric field, should be thought of as being substantial (and positive), and that the interaction of this with the applied field is the driving force behind the atom transfer.

References

1. D. M. Eigler, C. P. Lutz, and W. E. Rudge, Nature **352**, 600 (1991).
2. I.-W. Lyo and Ph. Avouris, Science **253**, 173 (1991); Ph. Avouris and I.-W. Lyo, Appl. Surf. Sci. (to be published).
3. H. J. Mamin, P. H. Guethner, and D. Rugar, Phys. Rev. Lett. **65**, 2418 (1990).
4. N. D. Lang, Phys. Rev. B **45**, 13599 (1992).
5. See e.g. N. D. Lang, in *Solid State Physics*, eds. F. Seitz, D. Turnbull, and H. Ehrenreich, Vol. 28, p. 225 (Academic Press, New York, 1973).
6. No experimental data are currently available for the transfer of alkalis between tip and sample in the STM. Results for field-induced diffusion of Cs along a sample surface in the STM are given by L. J. Whitman, J. A. Stroscio, R. A. Dragoset, and R. J. Celotta, Science **251**, 1206 (1991).
7. N. D. Lang and A. R. Williams, Phys. Rev. B **18**, 616 (1978).
8. The Hellmann-Feynman theorem allows us to define a total energy for the system in terms of the electrostatic force on the nucleus. This theorem is discussed in, for example, J. I. Musher, Amer. J. Phys. **34**, 267 (1966); S. T. Epstein, *The Variation Method in Quantum Chemistry* (Academic Press, New York, 1974), p. 107.

9. The transfer rate at a given temperature of course depends on the exact value of the activation barrier, which as seen in Ref. [4] can depend sensitively on the electrode spacing. In the absence of experimental data on Na transfer, we have simply chosen a reasonable spacing value at which to do our calculation.

10. Note also that the heat of adsorption of Na on a single jellium surface was calculated in Ref. [7] to be 0.9 eV. Calculated values for Na on Al(111) are found to be ~½ eV larger than this by J. Neugebauer and M. Scheffler, Phys. Rev. B (to be published), while adsorption energies of Na on transition metals are considerably larger: G. Rangelov and L. Surnev, Surf. Sci. **185**, 457 (1987).

11. J. R. Cerdá, F. Flores, P. L. de Andres, and P. M. Echenique, to be published.

12. R. E. Walkup, D. M. Newns, and Ph. Avouris, to be published.

13. The desorption field values in a field desorption experiment for Na on tungsten surfaces were found to be ~½ V/Å by C. J. Todd and T. N. Rhodin, Surf. Sci. **42**, 109 (1974). Fields for atom transfer are typically smaller than those for field desorption, as seen in Refs. [2] and [4].

14. We have also done a frozen-core calculation (with 1s, 2s, and 2p orbitals frozen). An expression for the force in such a case is given by R. Yu, D. Singh, and H. Krakauer, Phys. Rev. B **43**, 6411 (1991). The elimination of core-polarization effects in this way changes the calculated force (and hence the implied q_0 value) by less than 10%.

15. See N. D. Lang, "Theory of Alkali Adsorption on Metal Surfaces," in *Physics and Chemistry of Alkali Metal Adsorption*, eds. H. P. Bonzel, A. M. Bradshaw, and G. Ertl (Elsevier, Amsterdam, 1989), pp. 11-24, for a discussion of the degree of ionization of alkali atoms adsorbed on metal surfaces. See also M. Scheffler, Ch. Droste, A. Fleszar, F. Máca, G. Wachutka, and G. Barzel, Physica B **172**, 143 (1991); G. Pacchioni and P. S. Bagus, Surf. Sci. **269/270**, 669 (1992).

16. N. D. Lang and W. Kohn, Phys. Rev. B **7**, 3541 (1973).

MOLECULAR DYNAMICS SIMULATIONS OF METAL SURFACES: SURFACE MELTING AND NON-MELTING, AND TIP-SURFACE INTERACTIONS

F. ERCOLESSI [a,1], O. TOMAGNINI [b], S. IARLORI [b], E. TOSATTI [a]

[a] *SISSA*
Via Beirut 4
I-34014 Trieste
Italy

[b] *IBM ECSEC*
Viale Oceano Pacifico 171/173
I-00144 Roma
Italy

ABSTRACT. Molecular dynamics simulations have been used in order to gain some insight into two problems of interest to this workshop.

The first concerns surface melting, well known to occur on several open fcc metal surfaces such as Pb(110) and Al(110), but not on the well-packed (111) surfaces which remain crystalline up to melting. This (111) stability is not observed on rare-gas crystals, where all orientations appear to melt, and must therefore be related to the nature of atomic interactions at a metal surface. Non-melting of (111) faces is at the origin of many interesting phenomena observed on small metallic particles, such as overheating when only (111) faces are present and presence of sharp edges on crystal shapes, leading to collapse of isolated monoatomic steps on a (111) surface close to melting.

The second problem concerns tip-surface interactions in STM/AFM experiments. While a large amount of experimental data has been collected, the microscopic aspects involved when a tip approaches a substrate and comes possibly into contact with it, are still largely unexplored. We have used a model system consisting of a gold tip on a Pb(110) surface to study tip-induced deformations, contact formation with local heating, adhesion, and total force acting on the tip, as a function of distance and of temperature up to the surface melting regime.

1 Introduction

A traditional role of computer simulation is to act as a "bridge" between theory and experiments. This is particularly true for the latest development in surface physics. The information on structure and dynamics at the microscopic level that can be obtained by atomistic simulations can now be directly compared with the outcome of experiments involving probes with atomic resolution, such as high-resolution electron microscopy (HREM), ion scattering and atomic force microscopy (AFM). Thus, theoretical models can be tested "on the field".

Such comparisons are quite a challenge for the computational physicist. It is often the case that a typical length scale in a surface physics problem is of the order of many tens or even hundreds of Ångstroms. This is the case in particular when the problem involves long-periodicity reconstructions, or stepped surfaces, or liquid films (such as in surface melting),

[1]Present address: Materials Research Laboratory, University of Illinois at Urbana-Champaign, 104 South Goodwin Avenue, Urbana, IL 61801, USA. Electronic mail: ercolessi@uimrl7.mrl.uiuc.edu

V.T. Binh et al. (eds.),
Nanosources and Manipulation of Atoms Under High Fields and Temperatures: Applications, 185–205.
© 1993 *Kluwer Academic Publishers.*

or a tip scanning a surface, or any type of surface critical phenomenon. A large surface length translates into a number of atoms N required for a realistic description of the order of many thousands. Moreover, finite temperature studies of such systems are often quite demanding in terms of the times needed to achieve thermal equilibrium, typically of the order of the nanosecond.

Nowadays, computer simulations in condensed matter physics can be classified in two broad categories:

1. first-principles simulations, where the electronic degrees of freedom are explicitly considered and atoms move under the action of forces obtained by solving—usually by approximate methods—the Schrödinger equation for the electrons for each position of the nuclei, within a Born-Oppenheimer framework, and

2. classical simulations, where forces are obtained by a classical potential which is function only of the atomic coordinates. The effects of the electrons (which manifest themselves in many different ways, such as in metallic bonding, covalent bonding, etc.) are simply modelled by the potential. Potentials are usually constructed empirically, by means of fitting procedures, and the construction of a realistic potential for a given material is far from trivial.

While the first-principles approach is certainly more satisfying and accurate, the computational effort is larger by many orders of magnitude. So, while *ab initio* simulations are moving at present from $N \sim 100$ to $N \sim 1000$ by use of the most powerful parallel machines, with typical simulation times of the order of picoseconds, classical simulations can be done for systems with N in the 10^4–10^6 range and simulation times of the order of nanoseconds.

For this reason, many problems in surface physics of the kind mentioned above can be attacked at present only by classical simulations based on empirical potentials. The two studies discussed below, on surface melting and tip-surface interactions at finite temperature, are typical examples of cases where classical molecular dynamics appears as the only possible route to follow at present.

We present in section 2 a short overview on the potentials we used for the metallic interactions, and on the simulation method. Work to be presented subsequently deals with a) surface melting, and b) tip-surface interaction in STM/AFM.

Surface melting has been one major research area in surface physics in the last few years. Section 3 shows how simulation accounts for the simultaneous presence of melting and non-melting surface orientations on the same material. We also present some intriguing consequences of this fact on equilibrium crystal shapes at high temperature.

The recent advent of the scanning tunneling microscope (STM) and of the atomic force microscope (AFM) has raised a number of challenging theoretical problems, related to what happens *microscopically* when two bodies are brought into close contact. In section 4, we present our computer simulation results for an Au tip (simulated by approximately 500 atoms attached to a rigid support) approaching a Pb(110) surface. Our focus is on studying at an atomic level the deformation and adhesion phenomena occurring in the short-distance regime as a function of the tip-sample distance and of temperature. In particular, we discuss jump to contact at room temperature, and when the substrate is

in the surface melting regime, which has been the subject of very recent experimental observations.

Conclusions are presented in section 5.

2 Potentials and Method

2.1 POTENTIALS FOR METALS

Descriptions of solids based on pairwise potentials, historically very popular, have long been known to work rather badly, or not at all, for materials such as metal and semiconductors [1]. This is particularly true when surfaces are considered, since at a surface the atomic environment is quite different from the bulk. The distribution of the electronic charge around atoms at the surface can cause interactions between surface atoms to be very different from those between bulk atoms. This, in turns, often leads to interesting surface phenomena such as relaxations, reconstructions, anomalous vibrational properties, which cannot usually be accounted for by the two-body potential models.

Research on empirical potentials carried out in the last decade has, however, led to new families of potentials including many-atom terms which enable them to overcome the most important failures of pairwise potentials. In particular, the situation appears to be rather satisfactory for the case of noble metals, where realistic modelling can be achieved by adding to the usual pairwise term a coordination-dependent term with a nonlinear dependency of the energy upon coordination. This is the idea behind the "glue" [2], the "embedded-atom-method" Hamiltonians [3] and other similar schemes [1, 4, 5]. In most of these schemes, the total potential energy is written as

$$V = \frac{1}{2} \sum_{\substack{i,j=1 \\ (j \neq i)}}^{N} \phi(r_{ij}) + \sum_{i=1}^{N} U(n_i) \tag{1}$$

where n_i is a superposition of some fictitious "atomic charge densities" $\rho(r_{ij})$:

$$n_i = \sum_{\substack{j=1 \\ (j \neq i)}}^{N} \rho(r_{ij}). \tag{2}$$

One major advantage of this formulation is that it is still strictly based on pair distances r_{ij}, and is therefore very well suited for computer simulations. In fact, when using efficient algorithms, the range of the functions is often a more important factor than the increased complexity of the potential in determining computing speed. The expression (1) is invariant under the two transformations

$$\rho(r) \rightarrow C\rho(r) \quad , \quad U(n) \rightarrow U(n/C) \tag{3}$$

and

$$\phi(r) \rightarrow \phi(r) + 2\lambda\rho(r) \quad , \quad U(n) \rightarrow U(n) - \lambda n \tag{4}$$

for any choice of $C > 0$ and real λ. Additional constraints which may remove this kind of "gauge" freedom can be arbitrarily imposed without any change in the physics [2].

The three functions $\phi(r)$, $U(n)$ and $\rho(r)$ appearing in this potential may be obtained by fitting to properties of the material such as cohesive energy, lattice spacing, elastic constants and vibrational frequencies, etc. The various existent implementations are however widely different, even for the same material, reflecting different choices in the fitting process and different goals (see, e.g., [6]). In the "glue" parametrization, which we developed independently in Trieste in the 80's [7] and which we use in our studies of Au [2] and Pb [8], priority was given in obtaining the correct surface structure and energetics, essential for a correct description of all the major reconstructions of gold [6, 9], as well as the *absence* of reconstruction in lead, and the correct melting point and thermal expansion. It is obvious that an accurate modelling of the crucial defect and surface properties is very important for a realistic description of the high temperature surface phenomena discussed in this paper. On the other hand, modelling of other properties such as bulk elastic constants and phonons is not as accurate as in other parametrizations. These parametrizations however do not give rise to the Au(100) and Au(111) reconstructions [9] and yield values for surface energies much lower than the experimental ones [3].

In the AFM-like system described in section 4, a gold tip comes into contact with a Pb surface. Therefore, to carry out this study it is necessary to extend our scheme in order to be able to treat interactions between atoms of two different species A and B. We choose to define the Hamiltonian for a mixed system in the form

$$V = \frac{1}{2} \sum_{\substack{i,j=1 \\ (j \neq i)}}^{N} \phi_{S(i)S(j)}(r_{ij}) + \sum_{i=1}^{N} U_{S(i)}(n_i / C_{S(i)}) \tag{5}$$

with

$$n_i = \sum_{\substack{j=1 \\ (j \neq i)}}^{N} C_{S(j)} \rho_{S(j)}(r_{ij}) \tag{6}$$

where $S(i)$ represents the specie of atom i, that is, $S(i) = A$ or $S(i) = B$. The functions ϕ_{AA}, ϕ_{BB}, U_A, U_B, ρ_A and ρ_B are taken from the Hamiltonians for the pure elements. The new quantities are $\phi_{AB}(r)$ and the two weights C_A and C_B used to construct the effective "coordination" n_i.

The pair interaction between atoms of different species is taken as

$$\phi_{AB}(r) = \frac{1}{2} \left[\frac{\rho_B(r)}{\rho_A(r)} \phi_{AA}(r) + \frac{\rho_A(r)}{\rho_B(r)} \phi_{BB}(r) \right] \tag{7}$$

As pointed out in ref. [10], this particular choice guarantees invariance of the Hamiltonian under transformations of the type (4). Since the potentials for the single element Hamiltonians are determined to within such transformations, requiring the invariance to be retained in the mixed system is very desirable for consistency reasons.

The weights C_A and C_B appearing in eqs. (5) and (6) can still be chosen without altering the single element potentials, due to the invariance (3). Their absolute scale is totally arbitrary. Instead, their ratio C_A/C_B controls the physics, and in particular it does have

an effect on the AB alloy properties. In our case, we have fixed C_A/C_B by fitting to the lattice spacing of the Au_2Pb alloy, which has a crystal structure with cubic symmetry, and of $AuPb_2$, which has a tetragonal structure. Our choice, $C_{Au} \simeq 1.045$ and $C_{Pb} \simeq 0.957$, yields $a = 8.038$ Å (vs. $a_{exp} = 7.927$ Å [11]) for Au_2Pb, and $a = 7.325$ Å, $c = 5.766$ Å (vs. $a_{exp} = 7.325$ Å, $c_{exp} = 5.655$ Å [11]) for $AuPb_2$.

The above extension of the potentials for pure elements to mixed systems is certainly one of the simplest one can conceive. Nonetheless it has proved to be a quite satisfactory solution for our purposes.

2.2 METHOD

In the molecular dynamics calculations presented below, atoms are arranged in a slab geometry. Periodic boundary conditions are used in the (x, y) directions parallel to the surface. One side of the slab is the free surface under investigation, with the chosen orientation. On the opposite side of the slab, a few atomic layers are kept frozen in bulklike lattice positions to mimic a semi-infinite bulk. The in-plane lattice parameter of the slab is continuously adjusted as the temperature T changes, consistently with the bulk thermal expansion curve as obtained from independent bulk simulations with the interaction potential in use.

We have used a molecular dynamics (MD) program carefully written to avoid unnecessary involvement of interparticle distances much larger than the potential cutoff. It uses a partition of the simulation box into cells combined with a neighbour list, such that the execution time scales linearly with N. Moreover, force evaluation has been coded so as to take advantage of vectorization. The majority of the results presented here were obtained on a IBM 3090/600E with Vector Facility, where the performance with the Au potential presented in 2.1 is about 70 CPU seconds per thousand of time steps and per thousand of particles.

In a typical calculation, several quantities are monitored. For surface melting studies, it is particularly useful to have z-resolved densities of the number of particles, potential energy, in-plane orientational order, mean square displacement (MSD). The MSD as a function of time is one of the most useful indicators to separate regions with solid-like and regions with liquid-like behaviour: the former exhibit saturation of MSD, while the latter display a continuous growth, indicating diffusion. Maps of atom positions and trajectory plots are also very valuable tools.

3 Surface Melting and Non-Melting

Many recent experiments have shown that most surfaces of metals and of other systems undergo surface melting [12]. That is, a liquid-like film of microscopic size appears at a crystal-vapour surface well below the bulk melting point T_m, and its thickness ℓ grows as a function of temperature. In a genuine surface melting case, $\ell(T)$ diverges as T approaches T_m.

The presence of surface melting on most surfaces will prevent superheating of solid crystals above T_m. While the first order character of melting would suggest the possibility to overheat a solid, just as it is possible to supercool a liquid, in practice this cannot usually be

done. In fact, when surface melting occurs, a "liquid seed" is always present at the surface of the material, ready to propagate into the bulk as soon as T_m is reached. Experiments where surface melting is avoided by coating the surface with a similar material with a higher melting point confirm this picture [16].

Another very important feature is that surface melting is anisotropic, that is, it depends on the surface orientation exposed. There are metals exhibiting surfaces which are known *not* to melt. This is the case for the close-packed (111) surfaces of Pb [17], Al [18], Cu [19], Au [20]. In these systems, the more open (110) surfaces, as well as many other orientations, melt.

We have undertaken a study of the surface melting behaviour of Au(111) and Au(110). This study was motivated by the desire to understand better the nature of surface melting, or non-melting, in metals, and the choice of gold was favoured by the presence of the reliable model potential described in 2.1, which appears to be one of the few available models for metals yielding correct surface energetics (surface energy, liquid surface tension) as well as the correct melting temperature, all crucial for a realistic description of the surface melting behaviour.

3.1 DETERMINATION OF THE MELTING POINT

Before a detailed presentation and discussion of our surface simulations results, there is an important technical point that should be addressed: how to determine the bulk phase diagram, and the melting temperature T_m for a solid described by a given potential ? Studying surface melting implies dealing with temperatures that differ from T_m by amounts of the order of 1% or even less. Therefore, we must be able to estimate T_m with at least this level of precision.

The näive method of setting up a "bulk" system in the computer—where periodic boundary conditions are present in all directions so that there are no free surfaces—and heating it up until the crystal structure is destroyed, cannot be used for this purpose. The lack of any surfaces makes it practically impossible for the liquid phase to nucleate in a small cell, and in a short time. In fact, in such a simulation the crystal usually breaks off when its "mechanical instability point" T_i is reached. At this temperature the crystal becomes unstable because, for instance, one of the Born stability criteria for the elastic constants [25] fails, or for some other reason. But this usually happens far above T_m (by at least 20–30%). Inserting a point defect like a vacancy may help in decreasing the amount of overheating, since it is easier for the liquid to form a seed around the vacancy where some diffusion is possible, but does not eliminate it.

In fact, the melting point is by definition the temperature at which the solid and liquid phase have the same free energy, and therefore *both* phases must be taken into consideration for a precise determination of T_m. While methods based on explicit free energy evaluation have been devised and successfully applied [26], we have found convenient and reliable to set up a system where both the solid and the liquid phase are physically present in the same sample, and find the conditions under which the two phases coexist.

In particular, we artificially construct a ring-like sample where the lower half is crystalline and the upper half has liquid-like disorder. Periodic boundary conditions are used in all directions, so that there are two planar solid-liquid interfaces (one of which near the MD

box boundary). This system is then equilibrated by means of long MD runs in proximity of the melting point. Runs are performed at a constant total energy, chosen to lie between the solid and the liquid internal energy at T_m (whose difference is the latent heat of melting). In this way, the system is forced to separate into two phases, with the energy controlling their relative amount by the lever rule. A small correction takes into account the presence of the interfacial free energy associated with the two solid-liquid interfaces present in the system. By definition, T_m can be then measured as the temperature that the system reaches at thermal equilibrium without either phase wanting to expand. Typical runs of the order of 10^5 time steps ($\sim$ 1 ns) yield a temperature resolution of about 0.2%.

The remaining problem with this method is that there is a slight dependence on the resulting T_m on the lateral (x, y) and vertical (total length of the ring) size, as well as on the orientation of the interfaces. Such dependencies cause changes of T_m which are of the order of 2–3%. This is small, but large enough to be unacceptable for a precise determination of the growth law of the liquid layer.

Of course, the conceptually correct way of obtaining the "true" bulk T_m would be finite-size scaling, where T_m would cease also to depend on orientation in the thermodynamic limit. However, this does not solve the problem of what T_m to choose for a given finite sample. The best way we have found to deal with this unfortunate situation is, for each surface sample under investigation, to "calibrate" its melting temperature on a two-phase bulk system *with the same size and orientation.* By this method, for example, T_m has been estimated to be 1327 ± 3K for the Au(110) sample discussed in the next subsection, and 1357 ± 5K for the Au(111) sample discussed in subsection 3.3. We stress that the difference between these two values of T_m is strictly a size effect. Yet, use of the former value for the (110) surface simulations, and of the latter for the (111) surface simulations, effectively allows for a very efficient cancellation of these size problems in the resulting description. We also notice that both values are quite close to the experimental value for Au, 1336K. This is not surprising, since T_m was among the quantities fitted in constructing the potential (although the method used in the fitting, based on the approximate relation $T_m \sim T_i/1.2$, was far less accurate than the one discussed here).

3.2 A CASE OF MELTING: Au(110)

As discussed above, surface melting is commonly observed on ordinary (110) fcc metal surfaces such as those of Pb and Al. The case of Au is particular, however, since Au(110) reconstructs with a (1×2) periodicity (for references, see e.g. [6]). The reconstruction is well characterized to be of the "missing row" type, where every other $\langle 1\bar{1}0 \rangle$ row is missing from the topmost layer, resulting in a succession of slanted microfacets forming a zig-zag profile. The orientation of these microfacets is of the (111) type. Moreover, this reconstruction is known to disappear (that is, a (1×1) diffraction pattern is recovered) with a continuous transition at a temperature of about 650–700K [32]. Above this temperature, the surface is believed to be in a disordered state similar to a lattice gas. These features make the case of Au(110) somewhat different than that of simple, non-reconstructing surfaces like Pb(110) [33] and Al(110) (surface melting of the latter has already been simulated in the literature [34]).

For Au(110), we have used a slab geometry as described in 2.2, with 32 layers of which

3 kept frozen, and 280 atoms per layer, for a total of 8820 particles. Several temperatures were investigated, with typical equilibration times of the order of 1 ns. The details of the calculation have been reported in [31].

As expected, the original (1×2) missing row structure disappears well below the melting point, leaving place to a disordered but still crystallike structure around 850K. A true thermal equilibration in this region probably requires much longer times than those attainable by simulation, so that no attempts were made to investigate the details of the $(1 \times 2) \rightarrow (1 \times 1)$ transition. Surface melting roughly begins around 1000K ($\sim 0.75 T_m$), where the two topmost layers together gradually become fluid. The liquid thickness increases with increasing T.

Figure 1 shows a snapshot of the slab and its density profile at 1315K. The melting point for this system (see 3.1) was estimated to be $T_m = 1327 \pm 3$K. Note the different periodicity of the density oscillations near the liquid-vapour interface, compared with the spacing between (110) layers.

Figure 2 shows that the growth of the liquid layer is compatible with $\ell(T) = \frac{1}{2}\xi \ln[T_o/(T_m - T_o)]$, as expected for a system controlled by short-range forces [12, 21]. The optimal parameters, $\xi = 4.6 \pm 0.4$ Å and $T_o = 795 \pm 300$K [22], turn out to be in very good agreement with very recent experimental observations [23] giving $\xi^{exp} = 3.9 \pm 0.2$ Å and $T_o^{exp} = 639.7$K, confirming the validity of our overall description.

In a real system, electromagnetic dispersion forces are known to give rise to a crossover to a power law growth $\ell \sim (T_m - T)^{-1/3}$ very close to T_m. On Pb(110) such a crossover has been observed to occur about 0.3K below T_m [24]. The strength of dispersion forces can be obtained from the dielectric functions of the solid and of the liquid [35]. A calculation for Au led to an estimate of about 0.5K below T_m for the crossover point of Au(110) [31]. Therefore, our simulation results, based on strictly short-range forces, are expected to be valid up to a liquid film thickness $\ell \sim 15$ Å, where crossover is expected as indicated on fig. 2.

Ongoing simulation work for Pb(110) [29] also displays presence of surface melting, with

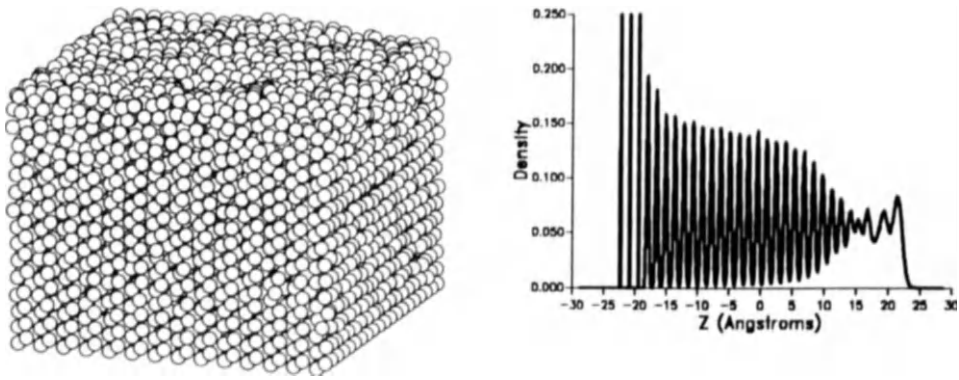

Figure 1:
Left: snapshot of the atomic positions of the Au(110) slab at $T = 1315$K. Right: density profile, as a function of the normal coordinate z, at the same temperature.

a growth law in close agreement with the experimental data. Interaction of Pb(110) in the surface melting regime with an AFM tip will be discussed in 4.3.

3.3 A CASE OF NON-MELTING: Au(111)

We have chosen Au(111) as a case of a well-packed metal surface. For the investigation of its surface melting behaviour, we have set up a slab system with 40 layers of 56 particles each. The two bottom layers were frozen in bulklike positions. The details of the calculation have been reported in [30].

We note that our Au potential favours reconstruction for this surface. The reconstruction is characterized by a slight in-plane contraction of the topmost layer, implying a higher density than for the non-reconstructed surface [6] and in agreement with experimental observations. Therefore, a reconstructed structure was used as a starting point for this investigation. Due to the relatively small size of the cell, the amount of packing obtained is somewhat too large; however, the resulting surface energy is still lower than in the non-reconstructed case. A non-reconstructed starting structure was also tried.

After locating the melting temperature, we found it impossible to obtain stable configurations where the surface is covered by a liquid film. While it is possible to artificially stabilize a partially melted configuration by means of constant energy runs, where the solid-liquid (SL) interface is practically locked in place by the impossibility to take or release the latent heat necessary for its motion without a large change in the temperature, such stabilization is not possible in constant temperature runs (which in this context are certainly closer to

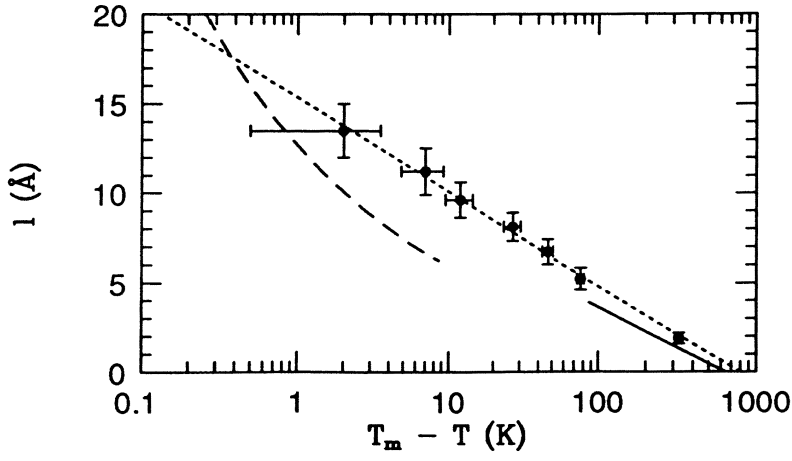

Figure 2:
Growth of the liquid layer thickness ℓ as a function of $T_m - T$ (on a logarithmic scale) for Au(110). The points are the results of our MD simulations. Error bars reflect fluctuations on runs with lengths up to 0.5 ns. The dotted line is the fit described in the text. The continuous line is the experimental fit of Hoss *et al.* [23] from measurements up to 1250K. The dashed line is the contribution of long-range forces (not present in our simulation) as estimated in [31].

reality). In this case, we have found that the SL interface moves steadily, leading either to complete crystallization up to the surface layer, or to complete melting (except for the layers very close to the rigid substrate), depending on the sign of $T - T_m$. Therefore, we concluded [30] that Au(111) using this model is a non-melting surface.

An even more striking proof of the absence of surface melting in the (111) surface simulation is that it appears to be possible to overheat the solid slab up to $\sim$ 150K above T_m. This would certainly be not possible if the system were prone to surface disorder close to T_m. Experimental reports of similar amounts of overheating for Pb(111) have been made very recently [44]. A simulation study of Pb(111) recently performed by our group also yielded a non-melting behaviour [47].

It is interesting to note that, while most metals appear to have at least one non-melting surface orientation, rare gases or models based on the Lennard-Jones potential exhibit melting on all the surfaces including (111) [13, 14, 15]. Chernov and Mikheev [36] suggested, on phenomenological grounds, that layering in the liquid film induced by the crystal may generate effective interactions between the two interfaces.

In fact, in metals there are also density oscillations induced by the liquid-vapour interface into the bulk liquid, which might play a crucial role in inhibiting melting of close-packed orientations. Such surface-induced layering effects in liquid metals are clearly visible both by simulation (see fig. 1, and ref. [37] for the surface of liquid gold) and experimentally [38], while they are absent on Lennard-Jones surfaces [27]. They arise from the tendency of surface atoms to achieve a higher coordination, generating a density peak at the surface which then acts as a perturbation for the underlying liquid. Moreover, in the surface melting regime the liquid film is also perturbed, on its other side, by the underlying crystal, with a periodicity which is orientation dependent. The combined response of the liquid film to these two perturbations coming from opposite sides may end up in an effective repulsive or attractive interactions between the two interfaces, resulting respectively in melting or non-melting. Calculations using a simple model and non-equilibrium MD simulations confirm the validity of this picture in understanding melting for (110) and non-melting for (111) fcc metal surfaces [28].

3.4 EFFECTS OF NON-MELTING ON VICINALS AND ON THE CRYSTAL SHAPE

The equilibrium shape of Pb crystals has been studied quite extensively by microscopy methods [39]. Upon heating, edges separating the low-index facets become rounded, as expected when roughening sets in and allow steps to proliferate freely [40]. Recent experiments [41, 42] have however shown a curious reappearance of sharp edges in the equilibrium crystal shape of Pb crystals around (111) facets about 20K below the melting point. Similar observations have also been made for Cu [19] and Au [20]. Clearly, this phenomenon is to be connected with surface melting and non-melting, since that is about the temperature where melting appears on most orientations [12, 17], with the exclusion of Pb(111) which remains crystalline up to bulk melting and even beyond [43, 44].

In an interesting paper [45], Nozières sketched an explanation of the presence of sharp edges at high temperature by considering the total interfacial free energy $\gamma(\theta)$ as a function of the tilting angle θ with respect to the (111) plane. The curve for a crystalline, stepped surface and that for a surface covered by a thin melted layer (where γ includes both the

solid-liquid and the liquid-vapour interfaces) must exhibit a crossing at some angle. In fact, the former must be lower at $\theta = 0$, since the flat surface is known to be stable in the crystalline state, while the latter must be lower far away from (111), where surface melting is known to occur. Therefore, there is a first-order phase transition as the angle is increased, and a consequence of this, easily seen by means of a conventional Maxwell-type construction (called in this case the Herring construction [40]) is that there must exist a whole angular region, from $\theta = \theta_{\min}$ to some critical angle θ_c, where the system undergoes phase separation. This has two intimately related consequences:

1. Vicinal surfaces whose mean tilt angle lies in this region are not stable (in neither the crystalline stepped phase or the surface melted phase), and facet into a flat (or nearly flat if $\theta_{\min} \neq 0$) crystalline surface, plus a melted surface tilted to $\theta = \theta_c$;

2. Sharp edges must occur on the crystal shape.

G. Bilalbegović *et al.* have carried out extensive MD studies, using the same methods outlined in section 2, for vicinals of Au(111) [46] and Pb(111) [47]. The aim of these simulations was to check the possible occurrence of the condition 1. above. Figure 3 shows how a regular stepped structure [in this case, a Pb(423) surface, vicinal of Pb(111)] transforms into a faceted structure close to the melting point. The structure on the right, obtained after about 1 ns of equilibration at $T = 0.97\,T_m$ (with $T_m = 618 \pm 4$K for our system, determined with the methods discussed in subsection 3.1), is constituted by a flat region with a (111) orientation and very limited surface diffusion, and a tilted region exhibiting a "drop" with liquid-like diffusion.

4 Tip-Surface Interactions

The advent of STM [48] and AFM [49] has opened the way to a large number of experimental investigations of surface structures with atomic resolution. Other contributions in this volume offer an excellent account of the present state of the art and of the many problems still unsolved.

Figure 3:
Atomic trajectories, from MD simulations of Pb(423) and taken on a time window of $\sim$ 15 ps, at $T = 0.26\,T_m$ (left) and $T = 0.97\,T_m$ (right). The stepped structure on the left, stable at lower temperatures, transforms into the structure on the right, where phase separation is apparent, close to T_m (from ref. [47]).

The operation of an AFM system is influenced by a number of different physical aspects related to the interaction [50] between two real bodies. For this reason, a full, comprehensive theory is missing, and many experimental findings are still waiting to be fully understood. While problems associated with tunneling phenomena can of course be addressed only by theoretical methods including a quantum treatment of the electrons, classical molecular dynamics can be of help in understanding issues related to structural properties, such as adhesion, indentation [51], induced deformations, effect of the tip geometry, differences in behaviour between different materials. In this sense, MD can be considered as a theoretical tool quite complementary to electronic structure calculations.

Contact between the tip and the surface is essential for the operation of microscopes since, in order to be able to obtain a map of the surface with atomic resolution, the tip must be operated close enough to the surface to experience short-range forces in a region of microscopic size. As pointed out by Goodman and Garcia [52] as well as by one of us [53], in fact, long-range van der Waals (vdW) attractive forces are expected to be able to resolve only structures whose size is of the order of the tip radius. On the other hand, one must be careful not to operate the system in conditions that may lead to sample damage. Even if the tip still experiences an overall attractive force, such force might be the difference between attractive vdW forces, shown to be rather large [52, 53] but exerted on practically all the atoms of the tip, and a large repulsive force in the small contact region which is applied only on a few atoms. If excessive, these forces may damage the sample in the contact region.

Interaction of tips with surfaces at very high temperature is another very interesting issue. In a recent STM experiment [54], Frenken *et al.* observe that formation of a "neck" between Pb(110) and a W tip is unavoidable when the temperature is brought into the surface melting regime ($T >\sim 0.75\,T_m$). In fact, the surface jumps to make contact with the tip when their distance is still large enough that the tunneling current is too small to be measured. At that point, the feedback mechanism of the microscope automatically starts to retract the tip until the neck breaks. This happens at a typical length of 2500 Å. This behaviour is probably due to the combination of the high surface mobility which makes mass transport possible, as suggested in [54].

We present below some preliminary results of a simulation study currently under way aimed at understanding better the contact phenomena between tip and surface in the regime of small separations (a few Ångstroms), and their temperature dependence. Phenomena range from mutually induced deformations in the approach phase to the rather dramatic formation of a neck when tip and sample come into contact at lower distances. Contact is accompanied by diffusion phenomena, particularly relevant at high temperature.

Plans for the near future include an investigation of the effect of vdW forces, that will probably give rise to considerable effects in the surface melting behaviour [53], horizontal scanning of the tip on the substrate, studies of different materials.

4.1 METHOD

We have studied a system constituted by an Au tip approaching a Pb(110) surface. Our simulation setup follows the scheme described in section 2. The Pb(110) slab is constituted by 16 layers with 280 atoms per layer, for a total of 4480 atoms. The four bottom layers (1120 atoms) are kept fixed in bulk-like positions. The lateral size of the slab is about

70 Å, both along $\langle 1\bar{1}0 \rangle$ and $\langle 001 \rangle$. The tip is constituted by 505 fully mobile Au atoms, arranged in a crystalline geometry. Its axis is along $\langle 100 \rangle$, and the tip is cut as to form an inverted pyramid with (111)-like surfaces left exposed. The vertex of the pyramid is a single atom. The tip is attached to a support constituted by 660 fixed Au atoms arranged in three Au(100) layers. The lateral size of this support is large enough to appear of infinite extension to the atoms of the tip.

The system as it appears after equilibration at room temperature is shown in figure 4. During equilibration, the tip vertex atom collapsed into the hollow site, giving rise to a tip with an initial contact area approximately square and of the order of 40 $Å^2$. The collapse of the vertex atom is obviously connected with the tendency of gold to achieve a high degree of surface packing [6].

The distance D between tip and surface is varied by displacing the rigid layers to which the tip is attached. We define $D = H - H_0$, where H is the distance between the rigid layers of the substrate and of the tip support, and H_0 is a constant distance such that when tip and surface are well separated (non interacting), D represents the actual distance between them. The actual distance is defined as that between the peak in the density profile along z corresponding to the first layer of the surface, and the peak due to the atoms at the extremity of the tip. This calibration is done at each temperature in a preliminary run. During our simulation, the force exerted on the tip is measured on the fixed atoms

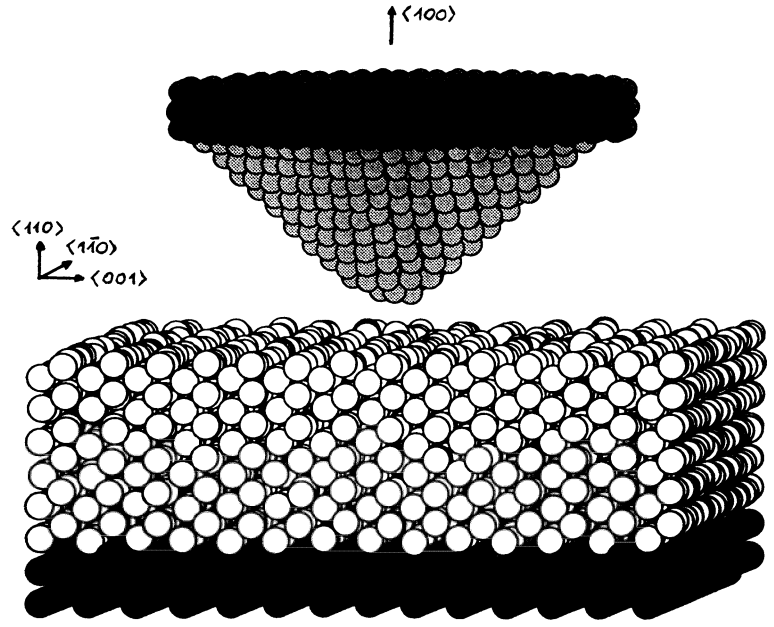

Figure 4:
Surface-tip system under investigation. The tip is made of Au atoms and interacts with a Pb(110) surface. Mobile Pb atoms are white, mobile Au atoms are light grey, all fixed atoms are dark grey.

constituting the tip support.

In-plane periodic boundary conditions are always present. The tip must therefore be thought as replicated in neighbouring MD cells. As a consequence, the deformation pattern becomes less realistic as one moves towards the cell boundary, where horizontal displacements of atoms will not occur since they are roughly equidistant from two tips.

Most simulations have been performed at constant energy (microcanonical ensemble). The release of the adhesion energy and of wetting energy (Pb atoms tend to cover the surface of the Au tip) leads to an initially large local heating, and after equilibration ($\sim$ 0.1 ns) to an increase of the temperature of the tip, which however is typically contained within reasonable limits (less than $\sim$ 100K).

4.2 RESULTS AT ROOM TEMPERATURE

We have performed a series of MD runs at $T = 300$K where the tip-surface distance D is decreased until contact occurs. In each run D is decreased by 0.3 Å and the time evolution is then followed for 0.28 ns (40000 time steps). To reduce the effect of transient phenomena related to the change of D, measurements are taken only on the second half (0.14 ns) of each run.

Interaction between the two systems is found to start at $D = 5.6$ Å. Figure 5 shows the various stages of neck formation at this distance.

Fig. 5a shows that, before contact is made, some Pb atoms jump from the surface to the tip. Reverse jumps of Au atoms do not occur. We believe that the driving force for these events is that it is energetically favourable for an Au surface to be wetted by Pb atoms, since the surface energy of Pb is about 40% that of Au [55], and the Au-Pb interface energy is probably not large enough to compensate the difference. The Pb surface appears bulged and somewhat defected near the sites left vacant, while it is well ordered elsewhere.

The initial stage of neck formation is visible in fig. 5b. The contact area is relatively small. More Pb atoms have flowed into the Au tip, and tend to arrange themselves on the edges of the pyramidal tip. Since Pb atoms are bigger (the lattice constant is about 20% larger than that of Au), the edge positions probably minimize strains on the Au lattice and are, therefore, energetically favoured. The trajectory plot in fig. 5b shows a considerable amount of elastic deformation of the tip, with internal atoms pulled more towards the surface than external atoms, and the diffusive motion of Pb atoms at the Pb surface and across the tip surface. Some atomic jumps can also be seen in the second layer, and between the first and the second layer of Pb(110). As a consequence of the migration of Pb atoms, this run shows a slight temperature difference between tip and surface, with the former about 15K warmer than the latter.

In fig. 5c the system has been further equilibrated for 0.28 ns at the same distance. More Pb atoms have climbed the tip, for a total of 12 Pb atoms adsorbed on the tip facets. The lateral size of the neck is slightly increased. Here, the tip is about 60K warmer than the substrate. This correspond to a total kinetic energy increase of the tip $\Delta E \sim 4$ eV. In the hypothesis that this energy comes from partial wetting of the Au surface with Pb, one can approximately write (neglecting the Au-Pb interface energy) $\Delta E \sim (\gamma_{Au} - \gamma_{Pb})A$, where γ are the surface energies and A is the wetted area, obtaining $A \sim 70$ Å^2. This corresponds to an area of about 6 Å^2 per atom, which is reasonable considering that atoms sit on edges.

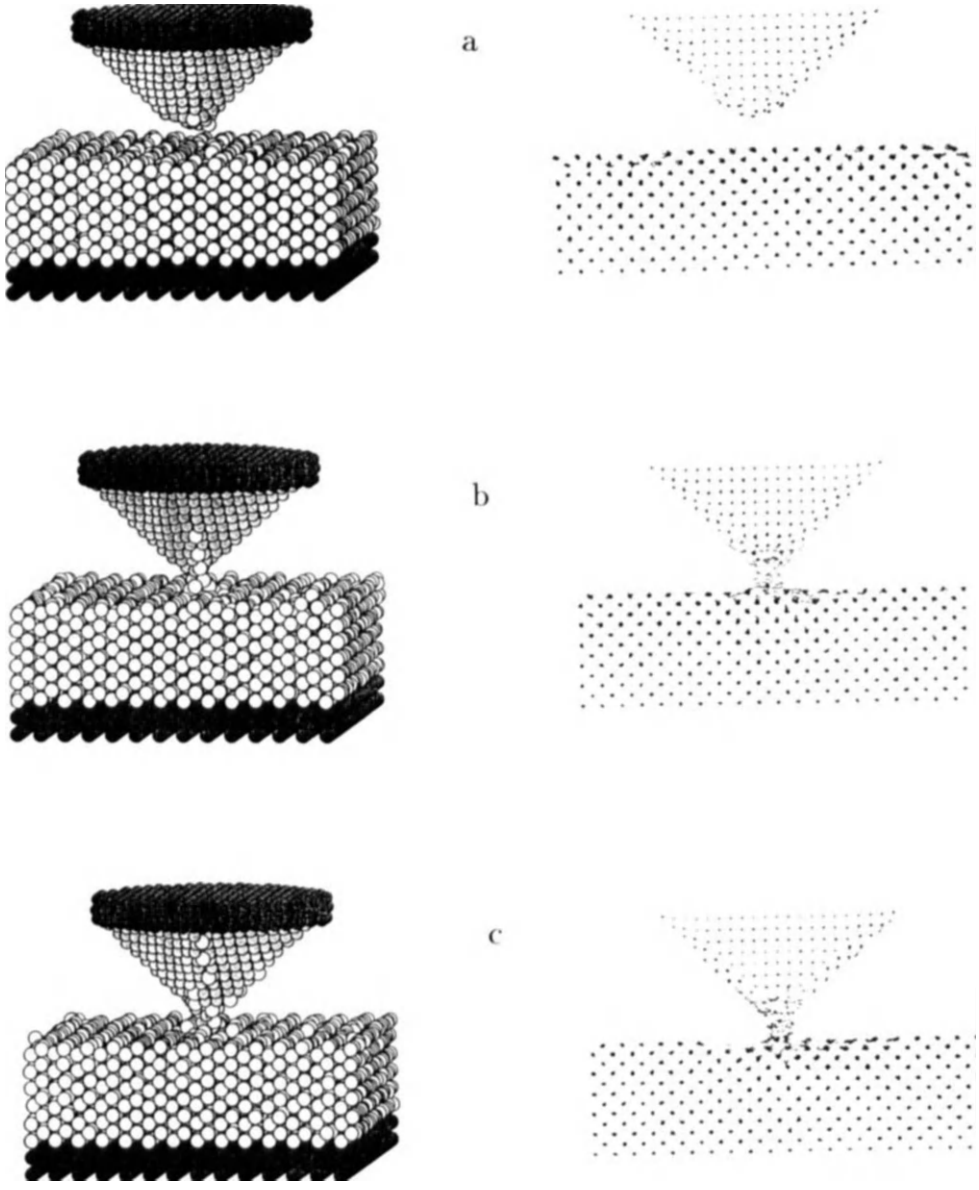

Figure 5:
Instantaneous atomic configurations and trajectories at $T = 300$K, before contact (a), when the neck begins to form (b), and after further equilibration (c). Colours are as in fig. 4. All the three runs are done at $D = 5.6$ Å, and their length is 0.28 ns. Trajectories include only atoms within a slice with a thickness of 7 Å parallel to the page, and are taken over a time of 0.14 ns.

We expect that the diffusive phenomena described above could be somewhat less dramatic if the approaching tip is already wetted by an external layer of Pb atoms. We hope to be able to address this question soon.

The force transmitted by the tip to the rigid layers which support it during the approach phase is plotted in fig. 6. It can be seen that it is always attractive in the region investigated and that the force gradient is approximately constant for $D < 5\,\text{Å}$. The intensity of the force is of the same order of magnitude of that obtained experimentally by Dürig and Züger [56].

4.3 RESULTS IN THE SURFACE MELTING REGIME

The same procedure described in 4.2 has been repeated for a temperature of 600K. This is slightly below the melting temperature of Pb using our model potential ($T_m = 618 \pm 3\,\text{K}$, obtained with the method described in 3.1). At this temperature, Pb(110) is in the surface melting regime [29], with a liquid thickness of 4 ± 1 layers. The dynamics of neck formation is shown in fig. 7.

As already mentioned, vdW forces are not present in our simulation, so that tip and surface are independent until their distance is small. In particular, the interaction range of our Au-Pb potential is $R_c = 5.5\,\text{Å}$. Therefore, one cannot expect the two bodies to interact at distances significantly greater than R_c. However, due to thermal fluctuations, interactions can begin at nominal distances D slightly larger than R_c. When interactions occur, they quickly lead to jump into contact by an avalanche process. In our runs this occurred at $D = 7.4\,\text{Å}$.

Fig. 7a shows the system immediately before contact. Surface melting of the substrate is clearly shown by the large diffusivity.

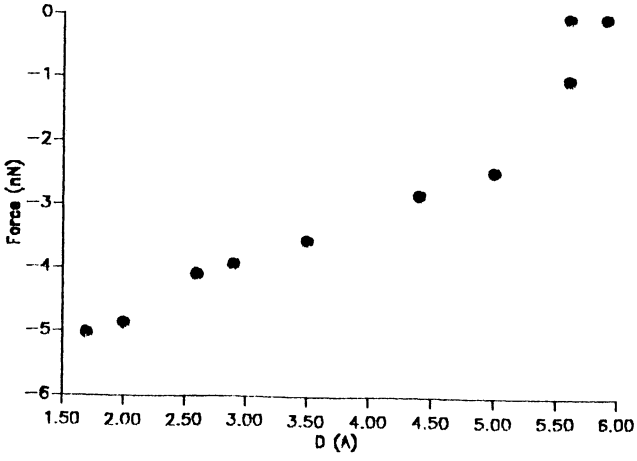

Figure 6:
Force transmitted by the tip to the support as a function of the nominal tip-surface distance D, as the tip is brought closer to the surface. Jump into contact occurs at $D = 5.6\,\text{Å}$. The force becomes increasingly attractive as D is decreased.

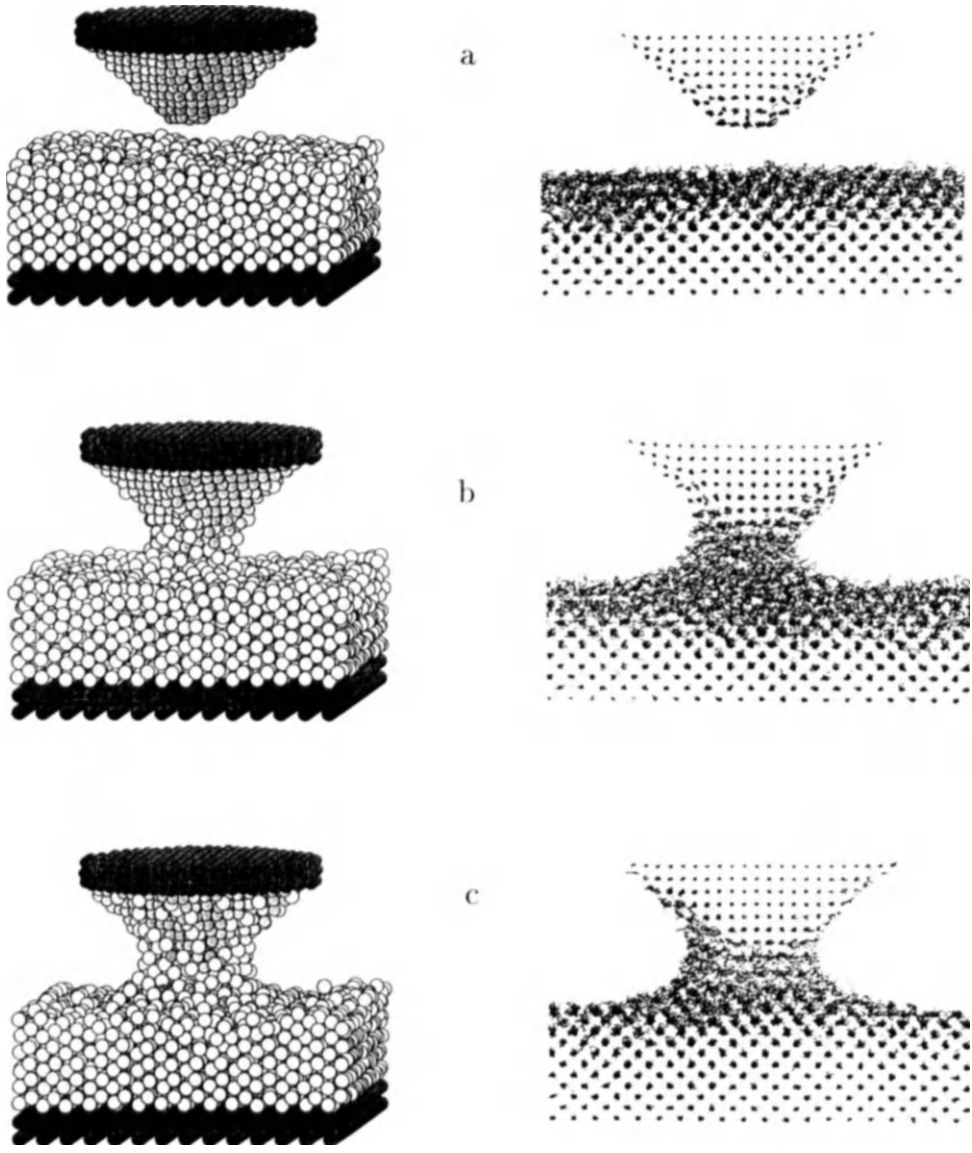

Figure 7:
Instantaneous atomic configurations and trajectories at $T = 600$K, before contact (a), when the neck begins to form (b), and after further equilibration (c). Colours are as in fig. 4. The nominal tip-surface distance is $D = 7.4$ Å in (a), and $D = 7.1$ Å in the other two runs. The length of the runs is 0.28 ns, except that in (b) whose length is 0.07 ns [it is quickly evolving towards a state similar to (c)]. Trajectories include only atoms within a slice with a thickness of 7 Å parallel to the page, and are taken over a time of 0.035 ns.

Decreasing further D to 7.1 Å caused jump into contact to occur. Fig. 7b shows the initial stage of neck formation immediately following the jump. A relatively large contact area of $\sim 250\,\text{Å}^2$ is formed within a very short time of the order of 0.05 ns, favoured by diffusion of Pb atoms belonging to the liquid film.

The system after 0.28 ns of equilibration is represented in fig. 7c. The contact area is further increased to $\sim 400\,\text{Å}^2$. As clearly seen, the extremity of the tip is entirely surrounded by liquid. Pb atoms flow massively in the liquid film, reach the contact area and then move upwards to wet the tip. As already discussed, the associated energy transfer acts to increase the temperature of the tip, and therefore to decrease that of the surface in our constant energy simulation. In fig. 7c, the substrate has $T \sim 550$K, causing partial recrystallization. This would not occur in presence of an external heat bath. In this case, as Pb atoms leave the surface to cover the tip, surface melting would probably proceed towards the bulk in order to keep the liquid thickness roughly constant. In such a situation, pulling the tip outwards would be likely to drag a liquid wire behind it, with a continuous supply of atoms made possible by the motion of the solid-liquid interface into the bulk. This would explain the experimental observations of Frenken *et al.*. We are presently working at it.

Of course, vdW forces are very likely to increase the tip-surface distance at which jump to contact occurs. We have already shown in a preliminary calculation reported in [53], where the tip was modelled by a sphere, that the presence of long-range interactions causes an outwards bulging of the surface towards the tip, eventually leading to adhesion, when the distance is still relatively large. Detailed studies including vdW forces are in progress, with a view of investigating these questions.

5 Conclusions

This paper presented an overview of surface physics research we have been carrying on using classical simulation techniques. In the two problems discussed here, surface melting and tip-surface interactions, simulation has proven to be a very effective tool for a better understanding of several structural, dynamical and thermodynamical aspects.

Simulations confirm the occurrence of surface melting on Au(110) and its absence on Au(111), as experimentally observed in Au as well as in other fcc metals, and in contrast with the Lennard-Jones system and rare gases.

MD simulation appears to be a rather useful tool to investigate the mechanical aspects concerned with the operation of an AFM microscope. We have presented here some first results, and there is certainly room for further developments in this area, including extension to new systems and materials (often involving development of new, reliable potentials), inclusion of long-range forces, effects of different tip geometries, and so on.

Acknowledgements

We are deeply indebted to G. Bilalbegović, P. Carnevali, X. J. Chen and C. K. Ong who have collaborated with us on some of the projects described in this review.

References

[1] See, e.g., *Many-Atom Interactions in Solids*, ed. by R. M. Nieminen, M. J. Puska and M. J. Manninen (Springer, Berlin, 1990).

[2] F. Ercolessi, M. Parrinello and E. Tosatti, *Philos. Mag. A* **58**, 213 (1988).

[3] M. S. Daw and M. I. Baskes, *Phys. Rev. B* **29**, 6443 (1984); S. M. Foiles, M. I. Baskes and M. S. Daw, *Phys. Rev. B* **33**, 7983 (1986); Erratum, *Phys. Rev. B* **37**, 10378 (1988).

[4] M. W. Finnis and J. E. Sinclair, *Phil. Mag. A* **50**, 45 (1984); Erratum, *Phil. Mag. A* **53**, 161 (1986).

[5] K. W. Jacobsen, J. K. Nørskov and M. J. Puska, *Phys. Rev. B* **35**, 7423 (1987).

[6] E. Tosatti and F. Ercolessi, *Modern Phys. Lett. B* **5**, 413 (1991).

[7] F. Ercolessi, Thesis, University of Trieste (1983); Ph. D. Thesis, SISSA, Trieste (1987).

[8] C. K. Ong, F. Ercolessi and E. Tosatti, unpublished.

[9] M. I. Haftel, *Mater. Res. Soc. Symp. Proc.* **238**, 229 (1992).

[10] R. A. Johnson, *Phys. Rev. B* **39**, 12554 (1989).

[11] *Pearson's Handbook of Crystallographic Data for Intermetallic Phases*, Volume 1 (Am. Soc. Metals, Metals Park, 1985).

[12] See, e.g., J. F. van der Veen, B. Pluis and A. W. Denier van der Gon, in *Chemistry and Physics of Solid Surfaces VII*, ed. R. Vanselow and R. F. Howe (Springer, Berlin, 1988), p. 455; J. G. Dash, *Contemp. Phys.* **30**, 89 (1989).

[13] J. Q. Broughton and G. H. Gilmer, *Acta Metall.* **31**, 845 (1983); *J. Chem. Phys.* **79**, 5105, 5119 (1983).

[14] S. Valkealahti and R. M. Nieminen, *Physica Scripta* **36**, 646 (1987).

[15] Y. J. Nikas and C. Ebner, *J. Phys.: Condens. Matter* **1**, 2709 (1989).

[16] J. Daeges, H. Gleiter and J. H. Perepezko, *Physics Letters A* **119**, 79 (1986).

[17] B. Pluis, A. W. Denier van der Gon, J. W. M. Frenken and J. F. van der Veen, *Phys. Rev. Lett.* **59**, 2678 (1987).

[18] A. W. Denier van der Gon, R. J. Smith, J. M. Gay, D. J. O'Connor and J. F. van der Veen, *Surf. Sci.* **227**, 143 (1990).

[19] K. D. Stock, *Surf. Sci.* **91**, 655 (1980).

[20] K. D. Stock and B. Grosser, *J. Cryst. Growth* **50**, 485 (1980).

[21] R. Lipowski and W. Speth, *Phys. Rev. B* **28**, 3983 (1983).

[22] These values are slightly more precise than those published in [31].

[23] A. Hoss, M. Nold, P. von Blanckenhagen and O. Meyer, *Phys. Rev. B* **45**, 8714 (1992).

[24] B. Pluis, T. N. Taylor, D. Frenkel and J. F. van der Veen, *Phys. Rev. B* **40**, 1353 (1989).

[25] M. Born, *J. Chem. Phys.* **7**, 591 (1939).

[26] S. M. Foiles and J. B. Adams, *Phys. Rev. B* **40**, 5909 (1989).

[27] D. L. Heath and J. K. Percus, *J. Stat. Phys.* **49**, 319 (1987); M. J. P. Nijmeijer, A. F. Bakker, C. Bruin and J. H. Sikkenk, *J. Chem. Phys.* **89**, 3789 (1988).

[28] O. Tomagnini *et al.*, in preparation.

[29] H. S. Lim, C. K. Ong, C. P. Toh and F. Ercolessi, in preparation.

[30] P. Carnevali, F. Ercolessi and E. Tosatti, *Phys. Rev. B* **36**, 6701 (1987); *Surf. Sci.* **189/190**, 645 (1987).

[31] F. Ercolessi, S. Iarlori, O. Tomagnini, E. Tosatti and X. J. Chen, *Surf. Sci.* **251/252**, 645 (1991).

[32] For recent theoretical work on this transition and a list of references, see G. Mazzeo, G. Jug, A. C. Levi and E. Tosatti, *Surf. Sci.* **273**, 237 (1992); I. Vilfan and J. Villain, *Surf. Sci.* **257**, 368 (1991).

[33] However, Pavlovska *et al.* [*Europhys. Lett.* **9**, 797 (1989); *Surf. Sci.* **234**, 143 (1990)] have reported the presence of reconstruction on Pb(110). On the other hand, Breuer *et al.* [*Surf. Sci. Lett.* **239**, L493 (1990)] did not find any evidence for extra spots in their diffraction experiment.

[34] P. Stoltze, J. K. Nørskov and U. Landman, *Phys. Rev. Lett.* **61**, 440 (1988); *Surf. Sci.* **220**, L693 (1989).

[35] X. J. Chen, A. C. Levi and E. Tosatti, *Surf. Sci.* **251/252**, 641 (1991); *Nuovo Cimento* **13 D**, 919 (1991).

[36] A. A. Chernov and L. V. Mikheev, *Phys. Rev. Lett.* **60**, 2488 (1988); *Physica A* **157**, 1042 (1989).

[37] S. Iarlori, P. Carnevali, F. Ercolessi and E. Tosatti, *Surf. Sci.* **211/212**, 55 (1989); *Europhys. Lett.* **10**, 329 (1989).

[38] B. N. Thomas, S. W. Barton, F. Novak and S. A. Rice, *J. Chem. Phys.* **86**, 1036 (1987); L. Bosio and M. Oumezine, *J. Chem. Phys.* **80**, 959 (1984).

[39] J. C. Heyraud and J. J. Métois, *Surf. Sci.* **128**, 334 (1983); *Surf. Sci.* **177**, 213 (1986).

[40] M. Wortis, in *Chemistry and Physics of Solid Surfaces VII*, ed. R. Vanselow and R. F. Howe (Springer, Berlin, 1988), p. 367.

[41] A. Pavlovska, K. Faulian and E. Bauer, *Surf. Sci.* **221**, 233 (1989).

[42] J. C. Heyraud, J. J. Métois and J. M. Bermond, *J. Cryst. Growth* **98**, 355 (1989).

[43] J. J. Métois and J. C. Heyraud, *J. Phys. (Paris)* **50**, 3175 (1989).

[44] J. W. Herman and H. E. Elsayed-Ali, *Phys. Rev. Lett.* **68**, 2952 (1992); *Bull. Am. Phys. Soc.* **37**, 58 (1992).

[45] P. Nozières, *J. Phys. (Paris)* **50**, 2541 (1989).

[46] G. Bilalbegović, F. Ercolessi and E. Tosatti, *Surf. Sci. Lett.* **258**, L676 (1991).

[47] G. Bilalbegović, F. Ercolessi and E. Tosatti, *Europhys. Lett.* **17**, 333 (1992).

[48] G. Binnig, H. Rohrer, C. Gerber and E. Weibel, *Phys. Rev. Lett.* **50**, 120 (1983); G. Binnig and H. Rohrer, *Rev. Mod. Phys.* **59**, 615 (1987).

[49] G. Binnig, C. F. Quate and C. Gerber, *Phys. Rev. Lett.* **56**, 930 (1986); D. Rugar and P. Hansma, *Physics Today* **43**, 23 (1990).

[50] For a representation see, e.g., fig. 1 in C. Girard and S. Maghezzi, *Surf. Sci. Lett.* **255**, L571 (1991).

[51] U. Landman, W. D. Luedtke, N. A. Burnham and R. J. Colton, *Science* **248**, 454 (1990); U. Landman and W. D. Luedtke, *J. Vac. Sci. Technol. B* **9**, 414 (1991).

[52] F. O. Goodman and N. Garcia, *Phys. Rev. B* **43**, 4728 (1991).

[53] E. Tosatti, in *Highlights of the Eighties and Future Prospects in Condensed Matter Physics*, ed. by L. Esaki (Plenum, 1991).

[54] J. W. M. Frenken, H. M. van Pinxteren and L. Kuipers, *Surf. Sci.*, to be published.

[55] The potentials we use are fitted on the experimental surface energies [6].

[56] U. Dürig and O. Züger, *Vacuum* **41**, 382 (1990).

ATOMIC MANIPULATION USING FIELD EVAPORATION[§]

N. M. Miskovsky[*], Tien T. Tsong[**] and Ching Ming Wei
Institute of Physics
Academia Sinica
Nankang, Taipei
Taiwan 11529 ROC

ABSTRACT. Field evaporation of positive and negative ions of Au adatoms from a Au(100) surface and Si adatoms from a T4 site above a Si(111) unreconstructed surface are investigated within the charge exchange model. The atomic potentials for gold were determined using the embedded atom method and a method due to H. Gollisch[Surf. Sci. 166,87(1986)]. For Si, the atomic potentials used were the empirical potential due to Tersoff[Phys. Rev. B **37**,6991(1988)] and an environment dependent potential developed by Bolding and Andersen[Phys. Rev. B **41**,10568(1990)]. In the FIM configuration, for both materials, the singly charged positive ion is predicted as the observed species; in the STM configuration, the doubly charged negative ion is the favored ion species since it requires the lowest evaporation field.

1. Introduction

Field Evaporation is the removal of surface atoms in the form of ions under the application of an electric field of a few volts per angstrom to a surface. It is normally considered to be a thermally activated process due to the lowering of the potential barrier with the application of an electric field. This mechanism is the basic physical process in field-ion microscopy (FIM) [1] and has been suggested as an important process for transfer of atoms in the STM configuration [2,3].

Mamin et al.[2] report the creation of mounds of Au atoms in an STM with the application of 600 ns pulses of 3.6 eV. These mounds were deposited only above a threshold field estimated to be less than 1 V/Å. Equivalent mounds were produced for reversed polarity. These authors view the process as field evaporation of either positive or negative ions depending on the sign of the applied field. However, the ion species transferred has not been unequivocally determined.

Lyo and Avouris[3] demonstrated that Si atoms could be reversibly transferred between a Si surface and a W tip. In their experiments they observe only the positive ion species for a tip-sample separation of about 4 Å. Again in their case, the fields are estimated to be less than 1 V/Å. Kobayashi et al.[4] have investigated the transfer of Si in the STM configuration and report the majority ion species is negatively charged Si. In their experiments, the tip-sample separation is large (about 10 Å).

One of the difficulties with the identification of the process as field evaporation is that the fields associated with the evaporation of Au^{+} and Si^{+1} or Si^{2+} range from 3.5 to 4.7

V.T. Binh et al. (eds.),
Nanosources and Manipulation of Atoms Under High Fields and Temperatures: Applications, 207–212.
© 1993 *Kluwer Academic Publishers.*

V/Å [5], whereas the fields estimated in the STM experiments are less than 1 V/Å.

A question that will be addressed in this paper is how the evaporation field changes from the FIM geometry to the STM geometry as well as how it varies with the tip-sample separation. In addition, we will examine what the preferred ion for field evaporation is for the FIM and STM configurations. The two cases considered her are 1) a Au adatom placed in a hollow site on a Au(100) surface and 2) a Si adatom in a T4 site above an unreconstructed Si(111) surface in both the FIM and STM configurations.

The theoretical model to be used for the analysis of the field evaporation process and the calculation of the evaporation fields is the charge exchange model[6]. In the simplest form we view the field evaporation process as a transition form a substrate + adatom (M + A) configuration to a $M^{-n} + A^{+n}$ state. This transition occurs at the intersection point of the atomic curve U_a and the ionic curve U_{ion}. The activation energy for the process (Q) is the value of U_a or U_{ion} at the intersection point.

In section 2, the calculation of the atomic and ionic binding energy curves are presented for Au. The analysis for Si is outlined in section 3. Results and conclusions are given in section 4.

2. Atomic and Ionic Potentials for Au

Two different atomic potentials were used in the analysis for Au. One was calculated using the effective binding potential method(EPBM) due to Gollisch[7], and the other determined by the embedded atom method(EAM) due to Daw et al.[8] and Foiles et al.[9].

Within the EBPM, the effective binding of atom i in a homonuclear system is

$$U_i = b\sum_{j\neq i}^{N} [Q_{ij}(r_{ij})]^{\mu S\lambda} - \left[a\sum_{j\neq i}^{N} [Q_{ij}(r_{ij})]^{\lambda}\right]^{\mu}. \qquad (1)$$

here Q_{ij} is the overlap between two atoms at $\mathbf{r}_i$ and $\mathbf{r}_j$. Gollisch[7] determined Q_{ij} by solving the relativistic Kohn-Sham eq. using the $X\alpha$ approximation and fit it to a sum of exponentials. The explicit functions and the values of the parameters are given in ref. 7.

Within the embedded atom method, the energy of an atom is a functional of the density of the unperturbed host. The total energy of the system is

$$E_{total} = \sum_{i=1}^{N} F_i(\rho_{h,i}) + \frac{1}{2}\sum_{\substack{i,j \\ i\neq j}} \phi_{ij}(r_{ij}), \qquad (2)$$

where ϕ_{ij} is the short ranged repulsive pair potential and $F_i(\rho_{h,i})$ is the energy required to embed atom i into the background host electron density. If the host density is approximated as the sum of atomic densities, the energy becomes a simple function of the positions of the atoms. Values of the parameters and the functions ϕ_{ij} and $F(\rho)$ are taken from ref. 9. The atomic densities used are taken from Mc Lean and Mc Lean[10]. The depths of the well were scaled to 3.5 eV for both potentials.

For a positive ion, the energy is given by

$$U^{+n}{}_{ion} = \sum_{i=1}^{n} I_i - n\phi + U_{rep} - \frac{(ne)^2}{4z} - neFz, \qquad (3)$$

where I_i is the ionization energy, ϕ is the work function, U_{rep} is the repulsive ion-core potential and the last two terms are the image lowering and the field lowering, respectively.

For a negatively charged ion,

$$U^{n-}_{ion}=n\phi-E^{n-}_{aff}+U_{rep}+U_{image}-neFz, \tag{4}$$

where E^{n-}_{aff} is the electron affinity of the -n ion, and U_{image} is the image potential. For Au^- it has a value of +2.31 eV and is estimated to range between 0 and -2 eV for Au^{2-}. This estimate is obtained by assuming the maximum coulomb repulsion between two conduction electrons is $\sim e^2/d$ or about 4.5 eV.

The repulsive pair interaction is taken to be the same as that of the atom. For the FIM configuration the simple image interaction is used; for the STM configuration, the multiple image interaction is used[11].

3. Atomic and Ionic Potentials for Si

Two model potentials, one due to Tersoff[12] (denoted hereafter as TER2) and another developed by Bolding and Andersen[13] (denoted hereafter as BA), are used to calculate the potential energy of the atom-surface interaction. Both authors assume the total potential energy of interaction among a collection of N atoms can be written as a sum of **environment dependent** pair potentials, U_{ij},

$$U=\sum_{1\le i<j\le N} U_{ij} \tag{5}$$

The form of the interatomic potential in the Tersoff model is [12]

$$U_{ij}=f_C(r_{ij})[U_R(r_{ij})+I_{ij}U_A(r_{ij})]. \tag{6}$$

The quantities U_A and U_R are the pairwise attractive and repulsive components of the potential energy, f_C is the cutoff function for the interaction, the I_{ij} is the term which includes the bonding environment effect on the (i,j) bond. The interference effect includes bond order and the directionality of the covalent bonds in addition to many body effects. For the pairwise potentials, Tersoff used two exponential terms in a Morse potential [12].

To ensure that the energy per bond decreases monotonically with increasing coordination and the energy is minimum for the diamond structure, Tersoff used the following form for I_{ij},

$$I_{ij}=\frac{1}{2}\left[(1+a^n\zeta^n_{ij})^{-1/2n}+(1+a^n\zeta^n_{ji})^{-1/2n}\right] \tag{7}$$

The function ζ_{ij} is a function of the environment of atom i, and hence I_{ij} is a function of the (i,j) bond. The parameters in TER2 potential are given in ref. 12. This particular potential was chosen because it gave the most reasonable result for the binding of an adatom at a T4 site on a Si(111) surface. In addition, it is similar in form to the potential obtained by Bolding et al.[13] who conclude that TER2 generally yields better agreement

when used in the calculation of surface properties and clusters.

The function f_C provides a smooth cutoff of the potential which was extended to include next nearest neighbor interactions.

Bolding and Andersen[13] parametrize their potential in the following form,

$$U_{ij}=f_C(r_{ij})[U_R(r_{ij})+I^{\pi}_{ij}U_{\pi}(r_{ij})+I^{\sigma}_{ij}U_{\sigma}(r_{ij})] \tag{8}$$

The attractive potential is made up of sigma and pi contributions that represent covalent bonding derived from putting electrons into these states. The sigma bonding function involves the angles between the bonds and the coordination of bond (i,j). The pi interference function includes the coordination of atom i as well as three, four and five body terms. The explicit functions and values of parameters are given in ref. 13.

For a positive ion in an applied field F,

$$U^{n+}_{ion}=\sum_{i=1}^{n} I_i-n\chi-neFz+U_{rep}+U_{image}-U_{f-p} \tag{9}$$

where χ is the electron affinity,and U_{f-p} is the energy change due to field penetration into the semiconductor. In the calculations presented here, the formalism used is due to Tsong[14].

For negative ion emission,

$$U^{n-}_{ion}=n\chi-E^{n-}_{aff}+U_{rep}+U_{image}-U_{f-p}. \tag{10}$$

For the FIM configuration, the simple classical image interaction is used[14] and for the STM configuration, the multiple image interaction is[15],

$$U_{image}=\frac{(ne)^2}{2}\left(-\frac{\alpha}{2z}-\frac{\alpha}{2(d-z)}-\frac{1}{2}\sum_{n=1}^{\infty}\alpha^{2n+1}\left[\frac{1}{nd+z}+\frac{1}{(n-1)d-z}\right]-\frac{1}{d}\ln(1-\alpha^2)\right) \tag{11}$$

where $\alpha=(\epsilon-1)/(\epsilon+1)$, with $\epsilon=12$ for Si. The electrodes are located at z=0 and z=d.

The value of E^{-}_{aff} is 1.39 eV. The value of E^{2-}_{aff} is taken to range from 0 to -2 eV as was the case for Au.

4. Results and Conclusions

For the FIM configuration, the field necessary to evaporate Au at a rate of one per second at 300 K (with an activation energy of 0.772 eV and E^{2-}_{aff}=0 eV), as Au^+, Au^- and Au^{2-} are found to be 3.2 , 2.0, and 1.4 V/Å, respectively, for the EAM potential and 2.7, 1.4, and 1.2 V/Å when the EBPM potentials are used. If E^{2-}_{aff}=-2 eV, the evaporation increases to 1.8 eV for the EAM and 1.6 eV for the EPBM. Although the calculation predicts the lowest evaporation field for Au^{2-}, when the negative field exceeds 0.6 V/Å, the field emission current is large enough to melt the tip by resistive heating. Thus the preferred ion for observation is Au^+.

In the STM configuration for Au, due to the overlap of the atomic potentials, a double

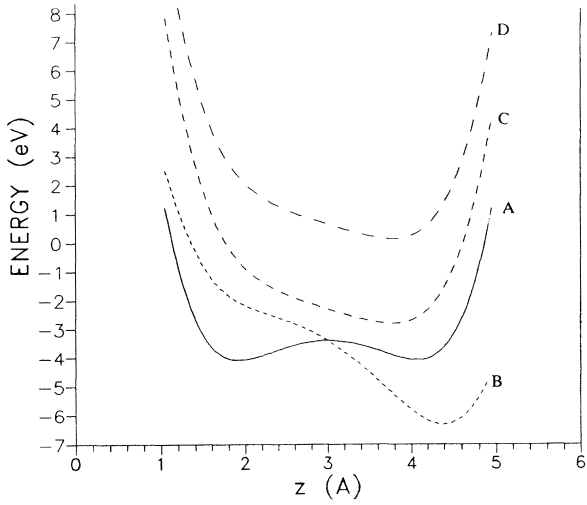

Fig. 1. Atomic and ionic curves for Au (F= 0.9 V/Å, d=6Å) for the EBPM. Curves A-D correspond to Au, Au^{2-}, Au^{-} and Au^{+}, respectively. Q=0.772eV for Au^{2-} with E^{2-}_{aff}=0 eV.

well structure is formed. The barrier height is about 0.772 eV at a spacing of 5.5 Å. The fields required to reduce Q to 0.772 eV for evaporation as Au^{+}, Au^{-} and Au^{2-} are 2.93, 1.73 and 0.90 V/Å for the EPBM, respectively. In the double electrode system as the applied potential is increased, atoms will start to transfer when the field reaches that required for an ion species of the lowest evaporation field (in magnitude) to start field evaporating. This is illustrated in Fig. 1. For z>2.6 Å the favored ion is Au^{2-}.

For the case of Si in the FIM configuration, the well depth for TER2 is 4.18 eV and for BA is 3.85 eV for an adatom interacting with a Si(111) surface in a T4 site. The fields necessary to evaporate Si as Si^{+}, Si^{2+}, Si^{-} and Si^{2-} at a rate of 1 s^{-1} at room temperature are 2.76, 3.28, 2.26, and 1.4 V/Å, respectively, for the TER2 potential and 2.79, 3.30, 2.26, and 1.38 V/Å for the BA potential. The preferred ion for emission is the Si^{+} ion.

In the STM configuration, there is no lowering of the barrier for separations > 6 Å due to the short range covalent bonding. For a separation of 5 Å, the BA potential predicts fields for evaporation at room temperature of Si^{+}, Si^{2+}, Si^{-} and Si^{2-} of 2.65, 3.00, 2.12, and 1.09 V/Å, respectively. Similar numerical results are obtained with TER2. Both potential models predict that in the STM configuration, the preferred ion species is Si^{2-} consistent with the results of Kobayashi et al.[4].

5. References

§ Research supported by the NSC of ROC.
* Visitor from the Dept. of Physics, Penn State Univ., University Park, PA 16802.
** On leave from the same department.
1. T. T. Tsong, **Atom-Probe Field Ion Microscopy**, Cambridge Univ. Press. (1990).

2. H. J. Mamin, P.H. Guethner and D. Rugar, Phys. Rev. Lett. **65**,2418(1990).
3. I. Lyo and P. Avouris, Science **245**,1369(1989).
4. A. Kobayashi, F. Gray, R.S. Williams and M. Aono, private communication.
5. Tien T. Tsong, Phys. Rev. **B44**,13703(1991).
6. R. Gomer and L. W. Swanson , J. Chem. Phys.**38**,1613(1963).
7. H. Gollisch, Surf. Sci.**166**,87(1986);**175**,249(1986).
8. M. S. Daw and M. I. Baskes, Phys. Rev.**B29**,6443(1984).
9. S.M. Foiles, M.I. Baskes and M.S. Daw, Phys Rev.**B33**,7983(1986).
10. A.D. Mc Lean and R.S. Mc Lean, Atomic Data Nucl. Tables **26**,197(1981).
11. G.Binnig, N.Garcia,H.Rorher, J.M.Soler and F. Flores, Phys. Rev.**B30**,4816(1984).
12. J. Tersoff, Phys Rev. **B37**,6991(1988).
13. Barry C. Bolding and Hans C. Andersen, Phys. Rev. **B41**,10568(1990).
14. T.T. Tsong, Surf. Sci. **81**,28(1979).
15. The result was derived by the authors.

WHAT IS UNDERNEATH? MOVING ATOMS AND MOLECULES TO FIND OUT

P. S. WEISS*† and D. M. EIGLER*
*IBM Research Division
Almaden Research Center
650 Harry Road
San Jose, CA 95120
USA

†Department of Chemistry
The Pennsylvania State University
University Park, PA 16802
USA

We have used the scanning tunneling microscope (STM) to move adsorbates such as benzene molecules and Xe clusters in order to determine their initial adsorption site. This has allowed us to image the initiation of the growth of a Xe surface overlayer, and to identify the sites at which this growth begins. This capability has also allowed us not only to examine the binding sites of the adsorbates, but also to learn the effect that these sites have on the STM images.

1. Introduction

Special surface sites such as steps and defects are thought to play an important and often dominant role in surface chemistry and in other surface processes such as diffusion [1]. We have previously shown how Xe atoms at dilute coverage first fill adsorption sites adjacent to steps, then form clusters on the terraces of the Pt{111} surface [2]. Using the STM tip to move the clusters allows subsequent imaging of the substrate sites at which the cluster islands nucleated and grew. In addition, we have shown how the appearance of an adsorbate in an STM image can vary according to binding site [3,4]. While this provides useful information on how electronic structure varies according to chemical environment, it also places constraints on the use of the STM in identifying molecules on surfaces. Moving the adsorbates once again allows examination of the initial binding sites.

2. Experimental

The experiments described here were conducted with an ultrahigh vacuum (UHV) scanning tunneling microscope at 4K. This microscope is equipped with a room temperature ultrahigh vacuum preparation and analysis chamber and a load lock. A schematic of the instrument is shown in Fig. 1. The STM is housed in a UHV chamber which itself is in an

V.T. Binh et al. (eds.),
Nanosources and Manipulation of Atoms Under High Fields and Temperatures: Applications, 213–217.
© 1993 *Kluwer Academic Publishers.*

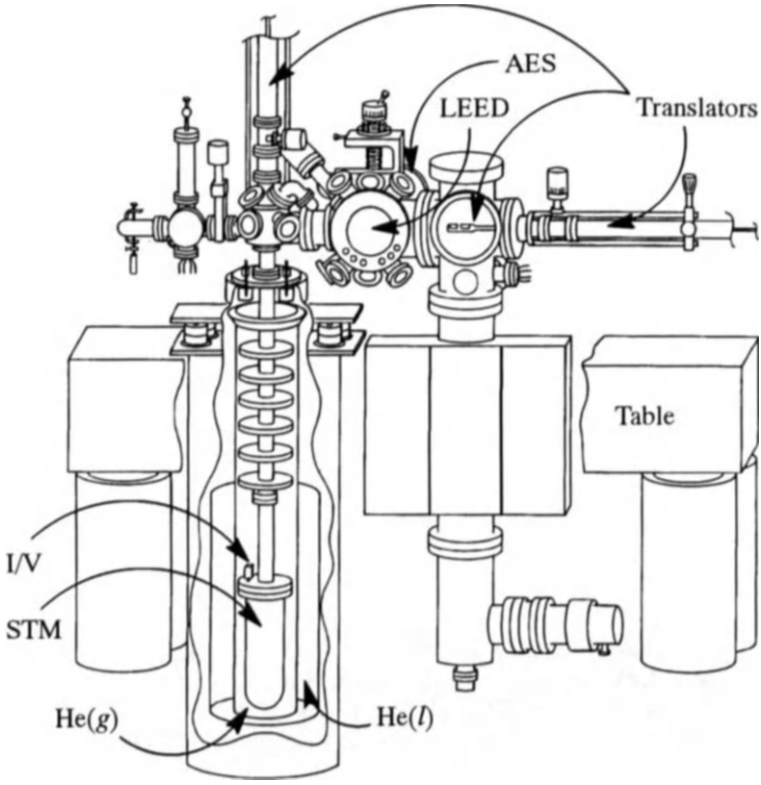

Figure 1. Experimental set up showing the ultrahigh vacuum low temperature scanning tunneling microscope and associated vacuum chambers. The key is as follows: AES – Auger electron spectrometer, He(l) – liquid He dewar, He(g) – exchange gas chamber, I/V – electrometer, LEED – low energy electron diffractometer, STM – low temperature scanning tunneling microscope, Table – custom laser table supporting the instrument, and Translators – vertical and horizontal sample translators.

exchange gas chamber containing *ca.* 1 torr of He gas. The exchange gas chamber is immersed in a liquid He storage dewar with a five day capacity. We have shown using Johnson noise thermometry of the STM tunnel junction that this efficiently cools the STM to the temperature of the liquid He, *i.e.* to T=4.5 ± 0.5K [5]. The STM itself is a modified louse design. The room temperature UHV preparation and analysis chamber is equipped with Auger electron spectroscopy, low energy electron diffraction, mass spectroscopy, ion sputtering, multiple sample transport, and rf induction, electron beam, and resistive heating. Samples are dosed by bleeding gas through sapphire leak valves into the upper room temperature chambers with the crystal in one of the upper room temperature chambers or in the microscope at 4K. Of particular importance here is the stability of the low temperature STM which allows us to turn off the feedback loop controlling the STM tip–sample separation for hours at a time and have the tip remain over the same atomic site during this time.

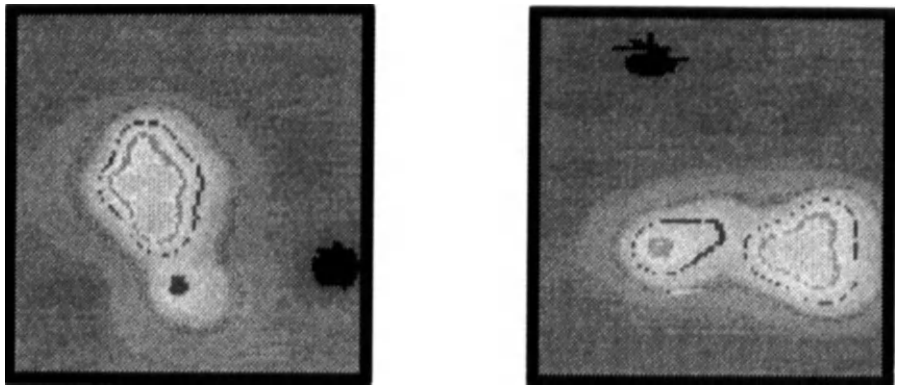

Figure 2. Topographic STM images of a 40Åx40Å area showing a cluster of Xe atoms adsorbed on Pt{111} in their initial adsorption site in the left frame, and after moving the cluster to reveal a defect in the right frame. Both images were recorded with a tip bias of ⁻2 mV and a tunneling current of 5 pA. Two gray levels are highlighted to outline the positions of the five Xe atoms.

3. Results

3.1. MOVING XE CLUSTERS

We have found that Xe atoms preferentially bind at step edges on Pt{111} [2]. After these sites are filled, the Xe atoms nucleate into small islands on the Pt{111} terraces. In order to identify the nucleation sites of these islands, we have moved the Xe islands from their initial adsorption sites [2]. Our procedure for moving the islands was:

1) Positioning the STM tip over the outer perimeter of the island.
2) Turning off the feedback loop.
3) Moving the tip in towards the surface by 2.6Å.
4) Changing the tip bias voltage of the tip to V=$^{+}$0.010V for 10 msec.
5) Returning the bias voltage to its original value (⁻0.002 to ⁻0.010 V).
6) Returning the tip to its original height above the surface.

This procedure resulted in centering the island about the STM tip with approximately 50% efficiency [7]. By repeating this procedure, an island could be moved completely away from its initial adsorption site. An example of this is shown in Fig. 2. In all cases when this was done for the Xe islands on the Pt{111} surface, it was found that a depression of ≤0.1Å in the STM images lay underneath the initial island positions. We have tentatively identified these point defects as surface carbon atoms [2]. The concentration of the point defects tracks the surface C contamination as measured by Auger spectroscopy. Theoretical calculations also indicate that a C atom on this surface would appear as a depression in an STM image [6].

3.2. MOVING BENZENE MOLECULES

Benzene adsorbed on Pt{111} appears to exhibit three different types of images depending upon adsorption site [3]. This result is consistent with theoretical calculations of images of benzene on graphite and MoS_2 [9], and the known variety of binding sites for benzene on

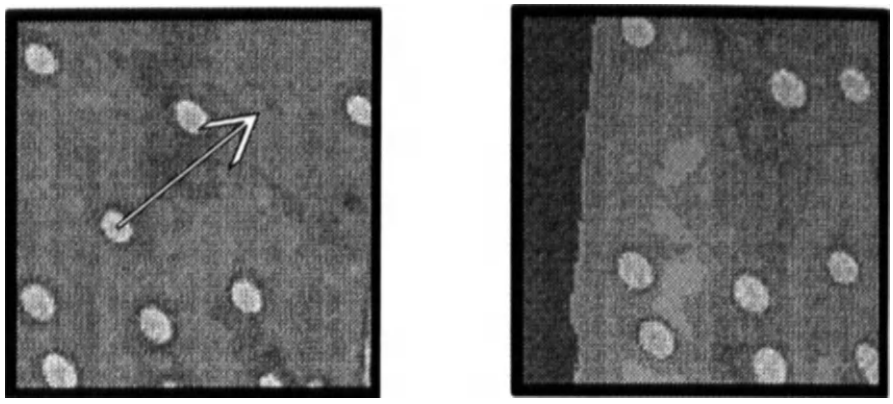

Figure 3. Topographic STM images of a 50Å x 50Å region of Pt{111} which has been covered with 0.001 monolayers of benzene. Both images were recorded with a tip bias of ¯10 mV and a tunneling current of 100 pA. Each bump corresponds to a single benzene molecule. The arrow in the left frame indicates the position of a benzene molecule before and after being moved, as described in the text. The right frame shows the surface after the molecule has been moved. Note that the two images are shifted somewhat laterally.

Pt{111} [10,11]. We have used the STM to move benzene from one of these sites to show that benzene which appears simply as a bump for low bias conditions does not sit at a defect. This is shown in Fig. 3. The left panel shows several benzene molecules as imaged initially. Then, one of the benzene molecules was lifted off the surface using the tip and redeposited back on the surface elsewhere (as shown by the arrow in the left panel). The right panel shows both the final position of the benzene molecule which has been moved and the substrate surface at this molecule's adsorption site. There does not appear to be a defect at this site. This is consistent with our interpretation of the different sites which we believe lead to the different images for benzene on this surface [3]. The procedure that we used to lift and replace the molecule was simply shutting off the feedback loop controlling the STM tip–sample separation, moving the STM tip in towards the surface 2.5Å for 50 msec, then pulling the tip back out and turning the feedback loop on.

While we were able to remove a number of molecules from the surface, this was the only case where we successfully dropped off the molecule afterwards. Still, by attempting to drop off the adsorbate far from the initial adsorption site so as to diminish the possibility of affecting this site, or by imaging with the molecule on the tip, the initial molecular adsorption site can be determined.

4. Conclusions

We have shown how it is both possible and useful to use the scanning tunneling microscope to move adsorbates so as to determine their surface adsorption sites. Knowledge of adsorption sites allows us to understand aspects of film growth and adsorption as well as the STM imaging process itself.

Acknowledgments

The authors would like to thank Norton Lang for helpful discussions, Joe Schlaegel and Les Harlow for help in the construction of the apparatus, and Stephan Stranick for help in preparing the figures. One of us (PSW) would like to acknowledge support from the National Science Foundation, the Office of Naval Research, and the Petroleum Research Fund (administered by the American Chemical Society).

References

[1] *e.g.* G. A. Somorjai, Chemistry in Two Dimensions (Cornell University Press, Ithaca, New York, 1981).
[2] P. S. Weiss and D. M. Eigler, 'Adsorption and Accommodation of Xe on Pt{111},' *Phys. Rev. Lett.* **69**, 2240 (1992).
[3] P. S. Weiss and D. M. Eigler, 'Site Dependence of the Apparent Shape of a Molecule in STM Images: Benzene on Pt{111},' to be published.
[4] J. A. Stroscio and D. M. Eigler, 'Atomic and Molecular Manipulation with the Scanning Tunneling Microscope,' *Science* **254**, 1319 (1991).
[5] P. S. Weiss and D. M. Eigler, unpublished.
[6] N. D. Lang, private communication.
[7] *N.B.* A more efficient procedure was subsequently found for moving single Xe atoms on Pt{111} and Ni{110} [8].
[8] D. M. Eigler and E. K. Schweizer, 'Positioning Single Atoms with a Scanning Tunneling Microscope,' *Nature* **344**, 524 (1990); D. M. Eigler, E. K. Schweizer, C. Lutz, and P. Zeppenfeld, unpublished.
[9] A. J. Fisher and P. E. Blöchl, 'Adsorption and STM Imaging of Benzene on Graphite and MoS_2,' to be published.
[10] C. M. Mate, Ph. D. Thesis, 'A Molecular Surface Science Study of Adsorbates on Surfaces: Importance to Lubrication,' University of California, Berkeley (1986).
[11] A. Wander, G. Held, R. Q. Hwang, G. S. Blackman, M. L. Xu, P. de Andres, M. A. Van Hove, G. A. Somorjai, 'A Diffuse LEED Study of the Adsorption Structure of Disordered Benzene on Pt{111},' *Surface Sci.* **249**, 21 (1991).

LOCAL EXPERIMENTS USING NANOFABRICATED STRUCTURES IN SCANNING TUNNELING MICROSCOPY (STM)

J.K. GIMZEWSKI, R. BERNDT* and R.R. SCHLITTLER
IBM Research Division
Zurich Research Laboratory
8803 Rüschlikon, Switzerland

ABSTRACT: Various experiments in which we fabricate nanostructures and then utilize them for local experiments are described. In the examples presented structures are used as atomic markers to observe temporal changes on Au(110)(1×2) surfaces, as electronic markers on oxidized Ti (0001) facets, and as a local probe for electromagnetic field enhancement and inelastic tunneling on a variety of metal and adsorbate systems. Local optical/uv analysis of structures on Cu(111) surfaces is found to be related to the fabrication technique. We illustrate that the combination of fabrication and manipulation, together with the ability to experiment using a range of physical phenomena on the local scale, can provide a significant contribution to scanning probe microscopies and the development of nanoscale science. In particular the importance of and prospects for obtaining local chemical information are addressed.

1. Introduction

Interest in the use of STM to fabricate and manipulate nanoscopic objects goes back to the early days of STM [1], and the fascination with this topic has endured throughout the past decade [2,3], leading to the manipulation of single atoms [4] and, on a larger scale, to the fabrication of structures approaching primitive devices [5]. In many, but not all, of the experiments the applied bias voltage, tip-surface distances and electrical current flowing play a significant role, yet our understanding of the physics involved is at best phenomenological, which is partially due to the lack of methods suited to characterize local chemical structure [2]. On the other hand, our ability to construct simple structures has become more sophisticated and the images recorded more spectacular.

In this paper we focus on another related aspect of this field of research that perhaps provides additional justification and understanding of surface modification. The role of scanning tunneling microscopy (STM) as a local probe technique [6] puts it at the forefront to investigate various properties of individual objects on the nanometer scale. Hence, the two-fold ability to actually prepare and then investigate chemical or physical properties of nanostructures provides exciting prospects for the future development and understanding of science on the nanometer-scale. A typical sequence of operations for performing such experiments as described in this paper is schematically illustrated in Fig. 1.

*Present address: Université de Lausanne, Institut de Physique Expérimentale, 1015 Lausanne, Switzerland

V.T. Binh et al. (eds.),
Nanosources and Manipulation of Atoms Under High Fields and Temperatures: Applications, 219–228.
© 1993 *All Rights Reserved.*

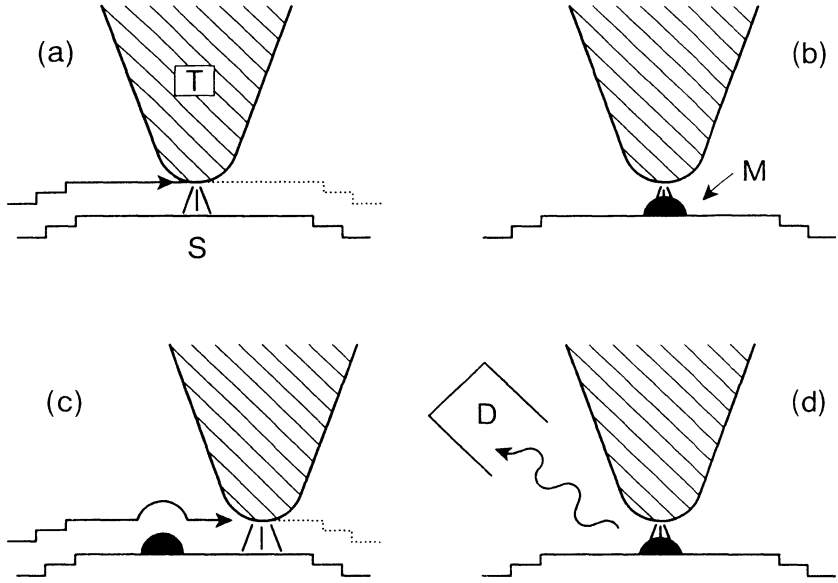

Figure 1. Schematic sequence of operations for performing local experiments on STM-fabricated structures. (a) Tip (T) characterizes topography of surface (S). (b) Preparation of surface modification (M). (c) Inspection of structure. (d) Local experimentation (photon emission).

In the context of this workshop we shall present a variety of experiments conducted in our laboratory in which structures deliberately induced by the STM tip have been used to study local properties of the structures themselves, the surrounding surface or even the tip. Reviews on surface modification can be found in Refs. [2,3]. An enormous variety of novel measurements and approaches have already been attempted, and the possibilities are practically limitless. Here we shall confine the discussion to our own work. Most of the experiments presented are described elsewhere and have been performed under ultra-high-vacuum (UHV) conditions on atomically well-defined surfaces. Details of actual experimental techniques and the instrument can be found in those references.

2. Markers for Surface Diffusion: (Au 110)(1×2) Surfaces

Under observation, structural changes occur in both Au [7,8] and Ag [9] surfaces on a time scale amenable to STM at 300 K. In particular, for the Au(110) surface, which reconstructs into (111) microfacets by removal of alternate rows along [1$\bar{1}$0] resulting in a (1×2) structure, fascinating changes in step structure and antiphase domain boundaries can be observed on the time scale of some 10 minutes. The constantly developing structure of the surface prevents a static frame of reference in the images from being established. By using foreign atoms deposited from the tip that are immobile on the time scale of the study, a convenient sequence of atomic markers can be introduced to provide stable reference points on time-lapse sequences of images. Through our experience in tip sharpening, we found that protrusions that do not

resemble topographic features characteristic of the Au(110)(1×2) surface can be generated by applying short pulses on the tip voltage ($V_t \sim +5$ V). The behavior differs from the effects of mechanical contact or pulses at negative tip polarity and we propose it to be a combination of thermally and/or current flow assisted field desorption of tip material [10]. The chemistry of the structures will be elucidated later.

Figure 2 shows a series of STM images recorded sequentially every 5 minutes [11]. Three protrusions which were deposited from the tip using voltage pulses ($V_t = +5$ V) are visible in the upper left corners. Their relative positions in the form of a triangle, but not the surrounding (1×2) surface structure, are stable over the sequence of images presented although a small thermal drift offsets the images. These markers serve as convenient reference points for evaluating the surface structural changes at the kink sites along [1$\bar{1}$0]. Comparison of the steps in the lower parts of the pictures at sequential time lapse intervals reveals a strong variation in the location of the kink sites from image to image. The markers also serve to evaluate tip structural changes that may influence the observations.

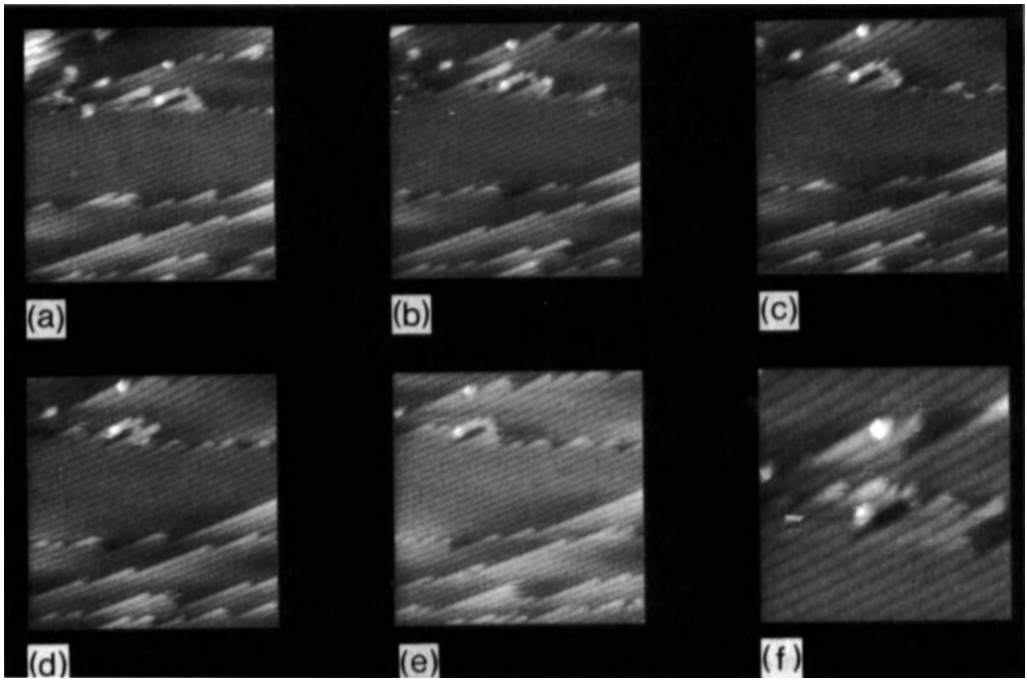

Figure 2. Time series of STM topographs of (1×2) reconstructed Au(110). Area: 300 Å × 300 Å in (a) to (e); 150 Å × 150 Å in (f). $V_t = 0.56$ V and $i_t = 200$ pA. Pictures were recorded every 5 minutes. Three protrusions deposited from the tip are visible in the upper left corners. Their relative positions and the gold surface in their vicinity both appear to be stable, forming a reference, whereas kink sites of the clean gold are in a state of constant motion. From Ref. [11].

Figure 2(f) shows a more detailed image of the region of the reference structure itself. The structures have an apparent diameter of ~8 Å and height of ~2 Å. We did not observe such a single-atom-type defect on other clean areas of the gold surface, which strongly suggests that the protrusions arise from foreign atoms deposited from the tip [7].

As demonstrated this particular form of surface modification can provide a novel function even in conventional surface physics.

3. Electronic Markers: Oxygen Adsorption on Ti(0001) Facets

This section deals with similar modifications on titanium prepared by controlled evaporation of thick films of Ti on silicon, resulting in Ti(0001) facets. The initial stages of oxygen adsorption on these surfaces was characterized using x-ray photoemission and STM [12]. In STM oxygen adsorption results in topographic features that exhibit a pronounced bias dependence. At positive bias voltages small structures of ~20 Å – 50 Å in diameter appear as protrusions ~1-2 Å high, whereas at negative tip voltages they appear as indentations. These oxygen-induced features are shown in Fig. 3 imaged at two different voltages. In addition, using short positive voltage pulses, a line of new structures was deposited; they are indicated by white arrows. This procedure, very similar to that used on the Au(110) surfaces, results in structures that bear a resemblance in apparent lateral and vertical dimensions to those of the Au example. The voltage dependence of the artificial structures, which have dimensions on a similar scale as the oxygen-induced features (at $V_t = -3.6$ V), is much less pronounced. These features appear as protrusions over a variety of tunnel voltages at different polarities, which is indicative of a metallic character. The change in apparent size of the artificial features is dominantly related to the change in the tip-surface distance with the bias voltage at constant current.

In contrast, oxygen-induced features exhibit a marked dependence on bias voltage as shown in Fig. 3, changing from protrusions to depressions with reversed polarity – typical of electronic effects that play an important role in the imaging mechanism. In the framework of Norton Lang's theoretical model for jellium surfaces with various adsorbed atoms [13,14], the larger features imaged at $V_t \sim -3.6$ V should reflect an increase in the unoccupied DOS in the sample, whereas at low or positive bias a decrease in occupied DOS would be expected. With regard to the topic of this paper, the artificial structures act as a means to provide a reference system for identifying the oxygen-induced features to discriminate topographic and electronic contributions of the image, particularly regarding the possible modifications of the tunnel tip. Moreover, the effect of lateral drift between images can be counteracted.

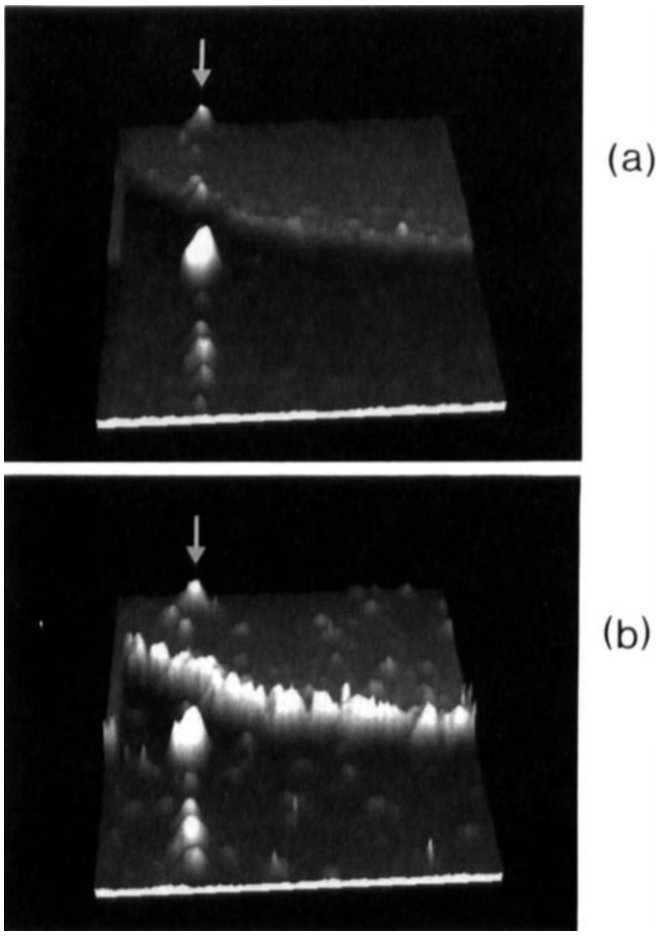

Figure 3. Bias dependence of STM topographs of a 250 Å × 250 Å area of a Ti film that has been exposed to 20 Langmuirs of molecular oxygen. Topographs rendered as pseudo-three-dimensional images are shown for $i_t = 1$ nA and $V_t = -3.5$ V in (a) and $V_t = +3.5$ V in (b). Height scale = 7 Å. A row of protrusions indicated by arrows running down the left-hand side of the image was written with the tip as described in the text.

4. Nanostructures on Cu(111) Surfaces: Local Probe Structures for Electromagnetic Fields and Inelastic Tunneling

In addition to the static electric field that exists between tip and sample, electromagnetic modes localized between tip and sample have also been shown to be important in metals [15].

Schematically shown in Fig. 4 are these tip induced plasmons (TIP), which interact strongly with electrons via inelastic tunneling. They form an additional energy dissipation mechanism which is relevant to a scanning probe geometry, or more

generally, to two small metallic objects in nanometer proximity. At bias voltages of $\gtrsim$1-5 V, spontaneous photon emission in the optical/near-uv region can be detected and used as a local probe of the chemistry of the surface.

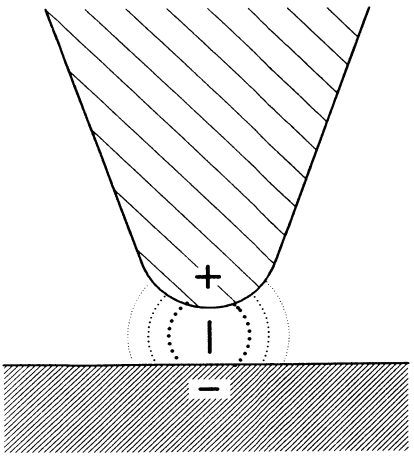

Figure 4. Schematic model of a tip induced plasmon (TIP) mode in the STM configuration. These electromagnetic modes are localized in the tip surface gap region. The + and − indicate the charge density oscillations frozen at a point in time.

The nature of the coupling both of the objects to form these electromagnetic modes is determined by a variety of factors. In particular, the dielectric properties – a chemical characteristic – of the junction materials dominate the radii of curvature [16], and the local density of occupied and unoccupied states of tip and sample [15] – also a chemical property – play a role in local photon emission properties. Given that dielectric properties are characteristic of a given material, a form of chemical mapping is made. This ability provides new and useful information on the nature of nanostructures and can furthermore assist in understanding the mechanism of the modification technique.

Figure 5(a) shows a topograph of Cu(111) crystal imaged in UHV. At the top of the image a series of small structures are clearly resolved. They were created by applying a sequence of short pulses with positive tip polarity ($V_t \sim 5$ V), and they also resemble, in dimension, the structures produced on Au(110) and Ti(0001). Figure 5(b) is an image of the photon signal detected simultaneously while scanning the surface. One can observe that the structures appear as dark patches, however, a few appear as bright patches superimposed on a background of fairly constant emission. For a W tip and Cu surface, the emission characteristics of the tunnel junction have been modelled and measured [15]. The constant background emission is characteristics of such a W-Cu tip-sample combination. In contrast, the lack of emission from the structures in Fig. 5b provides evidence that foreign material was deposited from the tip by the pulsing procedure. The bright feature, on the other hand, is consistent with a copper structure. The photon maps actually provide useful local chemical information on the nature of the surface modifications.

Further development is required to fully explore the capabilities of the technique of photon detection; nevertheless this example illustrates that additional information can be obtained from the photon emission characteristics of surface structures.

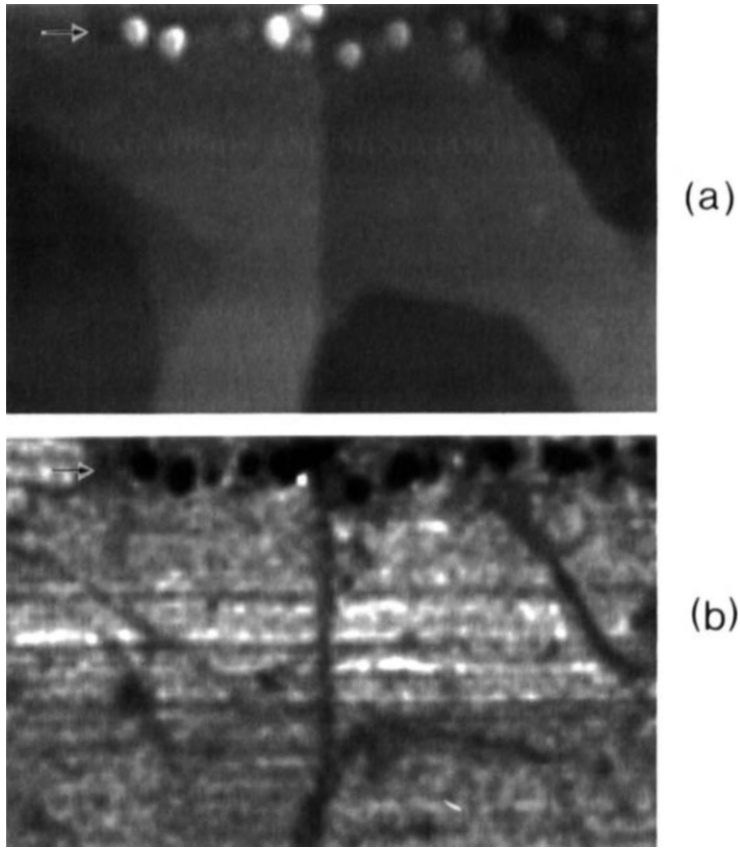

Figure 5. (a) Constant current topography and (b) photon intensity STM images of a Cu(111) surface exhibiting terraces separated by steps and small structures, indicated by arrows, created by a series of electric-field pulses at positive tip polarity. Images recorded simultaneously at $V_t = -3.5$ V, $i_t = 2$ nA. Area = 500 Å × 300 Å. From Ref. [15].

Using a similar procedure with a negatively biased tip tends to produce larger structures; an example is shown in Fig. 6(a). The feature has an apparent diameter of ~250 Å and is ~50 Å high. For structures of such dimensions it should be noted that their actual shape may differ from the imaged topography owing to a folding factor with tip apex geometry. Simultaneous photon mapping (Fig. 6(b)) shows fairly constant light emission for tip positions above the flat portions of the surface, whereas an increase in emission by a factor of ~10 is found when the tip is placed in direct proximity to the protrusion. The emission intensities are consistent with a copper structure whose dimension leads to an increase in the strength of TIP mode photon emission [17]. If this structure were composed of W or contained a significant quantity of O or C, then a significant reduction of photon emission would be expected. In

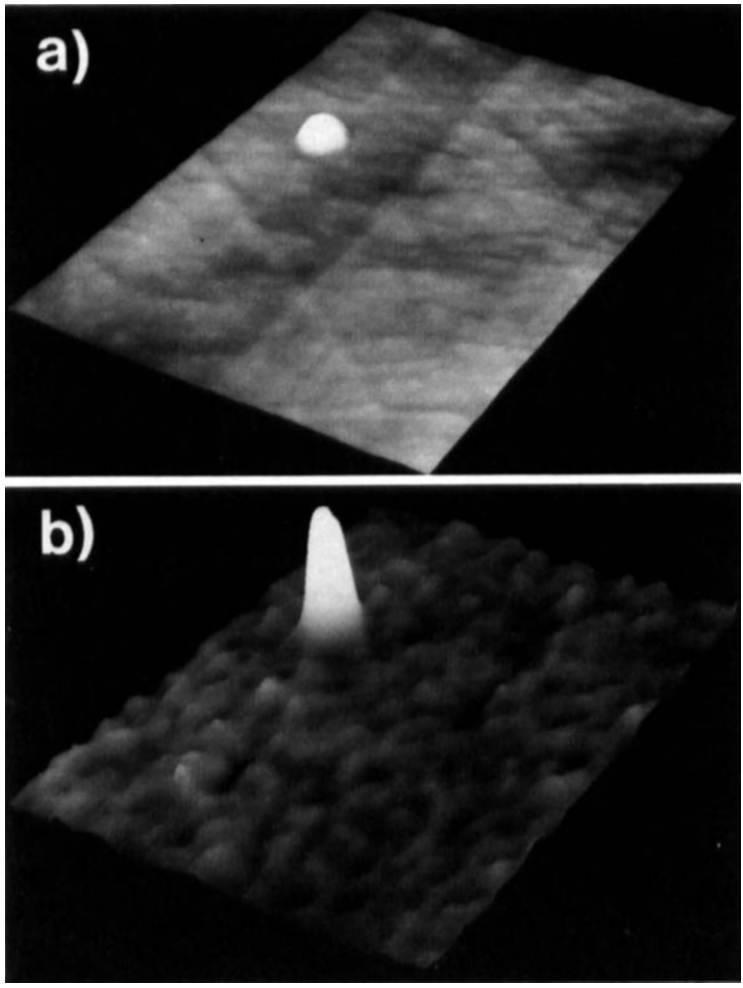

Figure 6. Topograph and photon map measured simultaneously in constant current mode on a 250 × 250 nm area of a Cu(111) surface with $V_t = 2.2$ V and $i_t = 2$ nA. (a) Topographic image. The surface had been modified prior to this measurement by applying short negative voltage pulses to the tip. This resulted in the formation of a protrusion and the creation of a dislocation network. (b) Photon map observed simultaneously. The light intensity data was used for shading with a grey-scale corresponding to 0 to 2000 counts per second. From Ref. [16].

passing, we note that this ability to map out the local electromagnetic enhancement has a relationship to surface enhanced raman scattering (SERS), where local enhancements in the electromagnetic field is thought to be responsible, in whole or part for the SERS enhancement [18]. The ability of our technique to map this effect, in a more general sense, makes it possible to observe the geometric dependence of electromagnetic modes arising from two nanoscopic objects (tip and structure) in close proximity, which thus provide a model system to explore in a controlled manner.

5. Deductions of the Chemical Identity of the Structures Illustrated

The examples outlined in Sections 2-4 present indications of the usefulness of surface modifications for local experiments using STM. In this final section we present deductions based on those studies of the chemical identity of the structures.

First, for Cu(111), Au(110) and Ti(0001) surfaces (using W tips prepared in a similar manner), the structures induced by positive tip pulses produce protrusions of similar lateral and vertical dimensions. The immobile nature of the structures on Au(110)(1×2) surfaces indicates that they are not Au atoms; their dissimilarity in bias-dependent imaging compared to that of O-induced structures suggests they do not contain oxygen (or carbon atoms [19]); reduced photon intensity in photon maps on Cu(111) shows that most (but not all) do not contain copper. Those copper observations are consistent with objects containing W [20]. Additionally, photon spectra of TIP modes are understood to be sensitive to the tip material. The spectra recorded in the above example can be modelled by using the dielectric properties of W for the tip [15]. In contrast, for tips with overlayers of substrate material, photon emission spectra are significantly different (we have observed such spectra by coating the W tip with different tip materials [20]). This additional chemical information is, in our opinion, consistent with a tip apex constructed from W atoms as a source of the deposited material.

For negative tip pulses the structures produced tend to be larger and the photon emission maps on Cu(111) in Fig. 6 are consistent with a Cu-containing structure, implying a thermally assisted process.

6. Concluding Remarks

For a better understanding of the mechanisms involved in surface modification there is a clear need for local chemical information. While *I-V* tunneling spectroscopy and bias-dependent imaging provide some useful information on the metallicity/non-metallicity of the structure, photon emission studies go further in differentiating local deposits of tip material from modifications in the substrate. In the examples presented, the first steps to deduce chemical information on the nature of nanostructures have been attempted. We hope that we have been able to convey the exciting prospects of combining surface modification with local experimentation using the STM, particularly those involving photons.

Acknowledgments

We wish to thank E. Courtens, H. Rohrer and B. Reihl for their support.

References

[1] See Proc. of the STM Workshop in Oberlech, Austria, IBM Europe Institute (1985), published in IBM J. Rev. Develop. 30, (4) and (5) (1986).

[2] Staufer, U. (1992) "Surface Modification with a Scanning Proximity Probe Microscope," in H.J. Güntherodt and R. Wiesendanger (eds.), Scanning Tunneling Microscopy Vol. II, Springer Verlag, Berlin, Heidelberg, in press.

[3] Quate, C.F. (1990) "Manipulation and Modification of Nanometer Scale Objects with the STM," in Proc. NATO Science Forum '90 "Highlights of the Eighties and Future Prospects in Condensed Matter Physics," Biarritz, France, Sept. 16-21, 1990, Plenum Press, (1992) in press.

[4] Eigler, D.M. and Schweizer, E.K. (1990) Nature 344, 524.

[5] Awschalom, D.D., McCord, M.A. and Grinstein, G. (1990) Phys. Rev. Lett. 65, 783.

[6] Rohrer, H. (1990) "Scanning Tunneling Microscopy-Methods and Variations," in R.J. Behm, N. Garcia and H. Rohrer (eds.), Scanning Tunneling Microscopy and Related Methods, Proc. NATO ASI on Basic Concepts and Applications of Scanning Tunneling Microscopy, Erice, Italy, April 17-29, 1989, NATO ASI Series E, Applied Sciences, Vol. 184 Kluwer Academic Publishers, Dordrecht, p. 1.

[7] Gimzewski, J.K., Berndt, R. and Schlittler, R.R. (1992) Phys. Rev. B 45, 6844.

[8] Jaklevic, R.C. and Elie, L. (1988) Phys. Rev. Lett. 60, 120.

[9] Gimzewski, J.K. and Möller, R. (1987) Phys. Rev. B 36, 1284.

[10] Strosio, J.A. and Eigler, D.M. (1991) Science 254, 1319.

[11] Gimzewski, J.K., Berndt, R. and Schlittler, R.R. (1991) Surf. Sci. 247, 327.

[12] Berndt, R., Gimzewski, J.K. and Schlittler, R.R. (1991) in Proc. Int'l Conf. on Scanning Tunneling Microscopy "STM 91," Interlaken, Switzerland, Aug. 12-16, 1991, Ultramicroscopy, in press.

[13] Lang, N.D. (1985) Phys. Rev. Lett. 55, 230.

[14] Lang, N.D. (1986) Phys. Rev. B 34, 5947.

[15] Berndt, R., Gimzewski, J.K. and Johansson, P.J. (1991) Phys. Rev. Lett. 67, 3796.

[16] Berndt, R. and Gimzewski, J.K. (1992) Surf. Sci. 269/270, 556.

[17] Berndt, R., Baratoff, A. and Gimzewski, J.K., in Ref. [6] p. 269, and Persson, B.N.J. and Baratoff, A. (1992) Phys. Rev. Lett. 68, 3324.

[18] See for example, Gimzewski, J.K., Humbert, A., Bednorz, J.G. and Reihl, B (1985) Phys. Rev. Lett. 55, 951, and references therein.

[19] Brune, H., Wintterlin, J., Ertl, G. and Behm, R.J. (1990) Europhys. Lett. 13, 123.

[20] Many different recipes exist for preparing tips. In our case freshly etched W tips were annealed in UHV to ~1300 K, then sputter-cleaned using Ne ions, and run in the field emission mode prior to mounting them in the STM. The procedure and the materials used would indicate that W, O and C are the most likely elements at the tip apex. During tunneling an additional coating with sample material is also possible.

[21] Berndt, R. and Gimzewski, J.K., in preparation, and Berndt, R. and Gimzewski, J.K. (1992) Physica Status Solidi A 131, 31.

QUANTUM ATOM SWITCH: TUNNELING OF Xe ATOMS

J.J. Sáenz and N. García
Dept. Física de la Materia Condensada
Universidad Autónoma de Madrid
Cantoblanco, 28049-Madrid
SPAIN

ABSTRACT. Eigler, Lutz and Rudge have reported a bistable switch that derives its function from the motion of a single Xe atom. It has been shown that this atom can be transfered, in a reversible way, from a scanning tunnelling microscope (STM) tip to a sample by means of a voltage pulse. In this work we show that the atom transfer process can be understood in terms of single atom tunneling process. We present a tunneling model, based in the charge transfer from the metal to the 6s resonance of the Xe atoms, which is able to reproduce the experimental results.

1. Introduction

The most dramatic evidence of the scanning tunnelling microscope's (STM) ability to manipulate individual atoms has been presented recently by Eigler, Lutz and Rudge [1]. They have been able to transfer a single Xe atom back and forth between a STM tungsten tip and a nickel substrate surface by means of a voltage pulse. As the conductance of a tunnel junction depends exponentially on the spacing between electrodes, even a slight rearrangement of the atom lead to a measured change in the STM conductance.

The physical mechanism that causes the motion of the atom in the "atom switch" is not clear. Any candidate mechanism should explain, at least, the qualitative behavior observed in the experiment. This behavior is resumed in the following items:

- The atom switch is only effective in a small window of tip-sample distances such that the junction resistance is between 0.7 and 1.5 MΩ. At smaller separations (resistances) the xenon atom moves spontaneously to the tip without the need to apply a positive voltage pulse. At larger separations the xenon atom sometimes escape from the junction region entirely.
- The motion of the xenon atom is always towards the positively biased electrode.
- The transfer rate of a xenon atom from the surface to the STM tip seems to have a power-law dependence with the current during the applied voltage pulse.
- The device switches between a low conductance state when the atom is on the substrate to a high conductance state when the atom is on the tip.

Several mechanisms for atom transfer, such as ionization or negative-ion formation followed by field evaporation, have been discused. However, none of them can account for all the observed phenomena. It was speculated [1] that heating-assisted electromigration

V.T. Binh et al. (eds.),
Nanosources and Manipulation of Atoms Under High Fields and Temperatures: Applications, 229–237.
© 1993 *Kluwer Academic Publishers.*

[2,3] could be a good candidate. Electromigration is odd in the applied field, and the competition between electron heating and the relaxation of vibrational energy to the lattice could account for the observed transfer rate.

None of the proposed mechanisms include two physical aspects of the problem that must play an important role in the understanding of the switching mechanism. The first aspect is related to the non zero probability of **quantum tunneling** of the atom between tip and sample. The second is related to the **charge transfer** from the metal to the 6s resonance of the Xe atom [4,5]. In this work we propose a switch mechanism which is based mainly on these two physical facts. As we will see, this mechanism is consistent with all the experimental observations.

2. Tunneling of Xe Atoms

2.1. SWITCH WINDOW

Let us first analyze qualitatively the origin of the small window of tip-sample distances

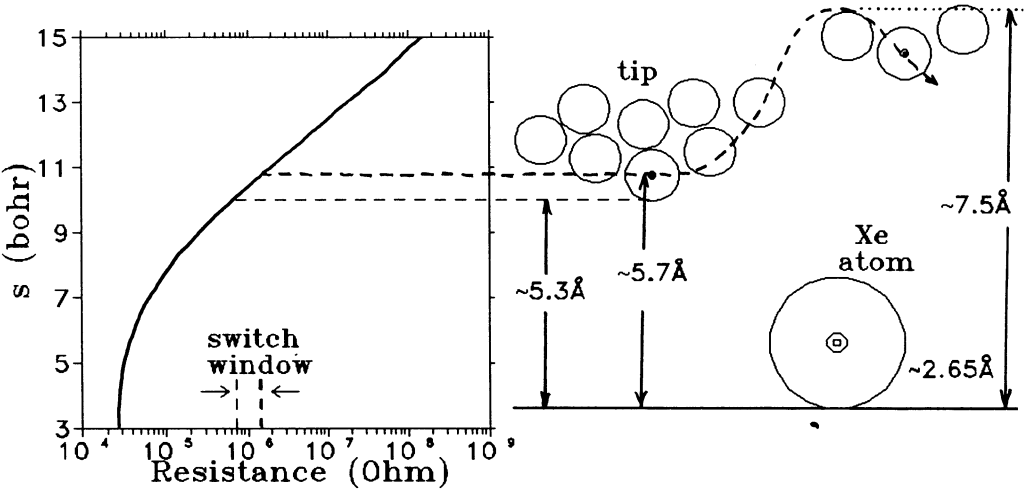

Figure 1: (a) Tip-sample separation, $s(Y = \infty)$, versus resistance (after Lang [6]). (b) Sketch of the tip trajectory across the center of a Xe atom adsorbed on a metal surface. The curves represent the small window of tip-sample distances corresponding to resistances between $R_{min} \approx 0.7$ MΩ and $R_{max} \approx 1.5$ MΩ.

in which the atom switch is effective. Experimental switching occurs for tip-sample resistances, R, between $R_{min} \approx 0.7$ MΩ and $R_{max} \approx 1.5$ MΩ. Let Y be the lateral separation between the tip and the Xe atom and $s(Y)$ the tip-sample distance. Then, from the experimental STM results and atom-on-jellium calculations [5,6], R_{min} and R_{max} correspond to tip-sample distances $s_{min}(Y = \infty) \approx 5.3$ and $s_{max}(Y = \infty) \approx 5.7$ Å (see Figure 1a) . Taking into account the normal tip displacement when the tip is just on top of the Xe atom, we estimate [7] $s_{min}(Y = 0) \approx 7.1$ and $s_{max}(Y = 0) \approx 7.5$ (see Figure 1b). Now, in the switching regime, the tip is left at a fixed position above and ≈ 5 Åto the

side of the Xe atom. Let D be the distance between the tip and sample surfaces at the position of the Xe atom. Although the exact value of D depends on the geometry of the tip surface, it should be of the order of $s(Y = 0)$. Bellow $D = D_{min}$ the Xe atom jumps spontaneously from the sample to the tip even without any applied pulse. On the other hand, for distances larger than D_{max} , the xenon atom, after an applied pulse, instead of jump to the tip, diffuse over the Ni surface indicating that the diffusion barrier on the surface is lower than the barrier towards the tip. It is then possible to have an idea of the order of magnitud of the parameters involved in the atom switch. In the switching range, the xenon atom sees a potential barrier ΔE lower than the diffusion barrier on the surface (typicaly $\Delta E \approx 40$ meV [8]) but large enough to avoid spontaneous jump. On the other hand, the equilibrium distance of xenon above the surface, Z_e, is ≈ 2.65 Å with respect to the surface jellium edge [9]. Then, at tip-sample distances of the order of 7 Å , the Xe atom jumps a distance of the order or smaller than 1.5 Å . Such small barriers and distances strongly suggest the possibility of atom tunnelling between tip and sample.

2.2. TUNNELING MODEL

In order to have a quantitative comparison with the experiments we have developped a theoretical model of the atom switch. As a first step, the model involves an estimation of the interaction potential, $U(Z)$, between the xenon atom and the Ni and W surfaces. At large separation distances, Z, between a Xenon atom and a surface, $U(Z)$ is essentially

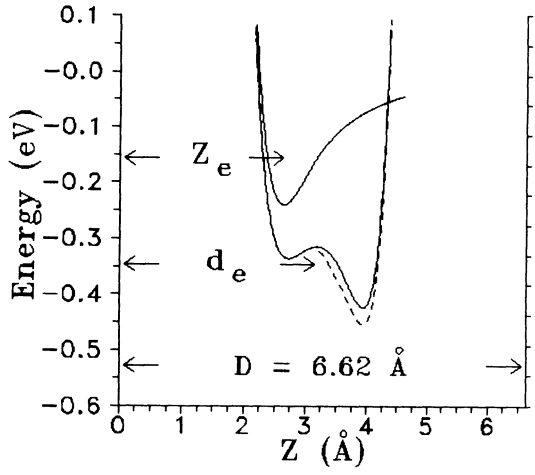

Figure 2: Potential energy diagram for a xenon atom placed between a Ni surface ($Z = 0$) and a W tip ($Z = 6.62$ Å). Distances are referred to the jellium edges. The single well potential represents the Xe-Ni surface interaction in absence of the tip. Z_e is the xenon-surface equilibrium distance. d_e is the effective image plane on the adsorbed atom. The discontinuous line is the potential energy with the tip biased at +0.1V with respect to the surface.

a van der Waals interaction $\approx C(Z - Z_0)^{-3}$, with C being typically of the order of ≈ 3.3 eV Å^3 [10]. Close to the equilibrium position, the interaction is not longer van der Waals. We assume a Morse-like potential with a potential well V_0 taken from the experimental results on the adsortion energy : $V_0\{Xe/Ni\} \approx 0.24$eV [11] and $V_0\{Xe/W\} \approx 0.35$eV

[12]. Assuming that these two different behaviors joint smoothly at the Morse inflexion point, we have

$$U_{Xe/Surface}(Z) = \begin{cases} V_0(e^{-2(Z-Z_e)/b} - 2e^{-(Z-Z_e)/b} & \text{if } (Z - Z_e) < b\ln 2 \\ C(Z - Z_0)^{-3} & \text{otherwise} \end{cases} \quad (1)$$

where Z_e is the equilibrium distance, $Z_0 = -3.8b$ is the van der Waals reference plane, and $b^3 = 0.015C/V_0$ (distances are given in Å and energies in eV). The total interaction potential, U_T, of a xenon atom between the tip and sample surfaces separated at a distance D would then be $U_T(Z) = U_{Xe/Ni}(Z) + U_{Xe/W}(D - Z)$. The resulting double well potential is sketched in Figure 2.

When the xenon atom is, for example, on the Ni surface it has to surmount an energy barrier ΔE in order to jump to the tip (see Figure 2). In Figure 3 we show the energy barrier as a function of the tip-sample distance D. Even in absence of applied voltage, there is a probability of atom transferring per unit time. Assuming a thermal assisted quantum tunneling, a typical transfer rate, τ^{-1}, would be

$$\tau^{-1} \approx \left\{ \sum_{i=0} w_i e^{-E_i/K_BT} T(E_i) \right\} \left\{ \sum_{i=0} e^{-E_i/K_BT} \right\}^{-1} \quad (2)$$

where w_i and E_i are the frecuencies and selfenergies of a xenon atom on the Ni well, $\exp(-E_i/K_BT)$ the occupation probabilities, and $T(E_i)$ the tunnelling probabilities to go through the barrier. We have calculated τ^{-1} within the Wentzel-Kramers-Brillouin-Jeffreys (WKBJ) approximation [13]. The calculated transfer rates of a xenon atom from the Ni surface to the STM tip at zero applied voltage are shown in Figure 3 as a function of the tip-sample distance. As it can be seen, in absence of applied voltage, the xenon atom will be estable on the Ni surface until tip-sample distances, D, at which the transfer rate goes above, let say, $10^{-1}s^{-1}$, i.e. D of the order of 6.6 Å. Below this distance, the Xe atom would *tunnel* espontaneously to the tip. Since the well depth on the tungsten tip is larger than on the Ni surface, the energy of the xenon atom is released rapidly (typically in $\approx 10^{-10}$ seconds) and the atom remains estable on the tip surface. Above ≈ 6.8 Å ΔE is larger than 40 meV, and the xenon atom could diffuse over the surface instead of jump towards the tip. These results are in close agreement with the estimated experimental switch window discussed above. It is remarkable the sensitivity of the transfer rates with the gap distance D : *a small change of* ≈ 0.02 *Å lead to an order of magnitud change in* τ^{-1} !. In Figure 3 we have also plotted the calculated thermal rate, τ_{th}^{-1}, at 4 K without including atom tunneling. It is clear that at 4 K tunneling rates are much higher (about six orders of magnitud) than the thermal rates.

3. Charge transfer

3.1. S-RESONANCE MODEL

We now turn to the intriguing question of the origin of the switch dependence with the sign of the applied voltage pulse. This could be related to the charge transfer from the metal surface to the xenon atom ("s-resonance model" [4]). Because of the 6s resonance, the conduction electrons at the Fermi level protrude further out into the vacuum at an adsorbed Xe atom than over the bare metal [4,5]. This effect leads to a simple physical picture of the charge distribution in the adsorbed atom. First, there is a charge transfer

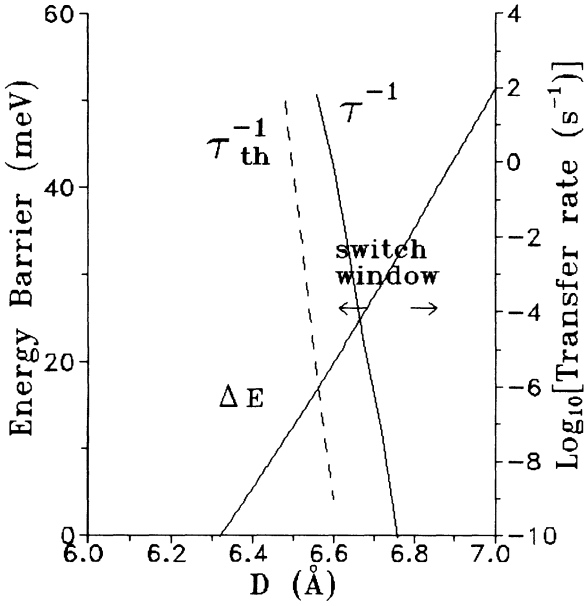

Figure 3: Atom energy barrier, ΔE, as a function of tip-sample separation D (left scale) and calculated transfer rates for atom tunneling and pure thermal excitation (continuous and dotted line respectively; right scale) as a function of the tip-sample distance for zero applied voltage. The adsorbed atom remains stable on the Ni surface for distances larger than $\approx$ 6.6 Å . For distances larger than $\approx$ 6.8 Å the energy barrier becomes larger than the barrier for diffusion over the surface. The estimated theoretical window of distances in which the atom switch is possible is also shown.

(or polarization) of the Xe electrons, close to the metal surface, towards the metal leading to the well known Xe dipole moment. However, this charge is screened to the external field because is closer to the metal surface than the image plane. On the other hand, in the 6s resonance there is some extra *negative* charge comming from the metal at a relatively large distance from the metal surface. Because of this extra charge, when the Xe atom is on the substrate surface, a negative voltage pulse, V, applied to the surface would introduce a perturbation, $\Delta U(Z)$, in the atom potential, leading to a lower barrier and, as a consequence, to lower transfer rates.

3.2. TRANSFER RATES

We can get an idea of the effect of the perturbation on the transfer rates by assuming a simple model. When the tip is over the xenon atom, the applied potential drops between the tip image plane and some effective image plane in the xenon atom at a distance $d_e \approx 3.15$ Å from the jellium edge [14]. It is likely that, because of the screening, the effect of the applied potential on the adsorbed atom is small. However, as we move the xenon atom towards the tip, the screening of the applied potential would be less effective resulting in a net force. As a simple approximation, we will assume a linear perturbation potential between the effective image planes, i.e. between $Z = d_e$ when the atom is on the

surface and $Z = D - d_e$ when it is on the tip,

$$\Delta U(Z) \approx -Q_{eff}V \begin{cases} 0 & \text{if } Z < d_e \\ (Z - d_e)/(D - 2d_e) & \text{if } d_e < Z < D - d_e \\ 1 & \text{if } Z > D - d_e \end{cases} \quad (3)$$

where Q_{eff} is the effective xenon charge and V the applied voltage. We estimated $Q_{eff} \approx 0.1e$ from reference 5 and private communication by N.D. Lang. We have calculated equation 2, for a fixed distance and $T = 4$K, as a function of the applied voltage, for a xenon atom going from the Ni surface to the STM W-tip. In Figure 4 we present our

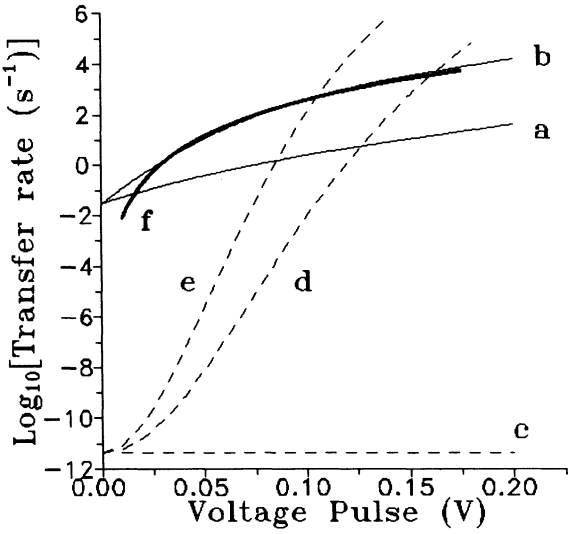

Figure 4: Calculated transfer rate of a xenon atom from the Ni surface to the STM W-tip as a function of the voltage pulse for a distance $D = 6.62$Å. Continuous lines represent the results of our tunneling s-resonace model for two different effective charges $Q_{eff} = 0.1e$ (a) and $0.3e$ (b). Dashed lines are the results assuming an effective atom temperature $T_a = T + CV^2$ based on the thermal-electromigration model of reference [2]. (curve c is for $C = 0$, d for $C = 250$ and e for $C = 500\text{KV}^{-2}$). The power-law fit of the experimental results is also shown (thick line f).

results for $\log(\tau^{-1})$ as a function of the applied pulse, V, for a distance $D = 6.62$ Å (curve a). The transfer rate behavior is related to the tunnelling probability dependence with the applied voltage. For small voltages ($Q_{eff}V$ small), since the barrier height decreases linearly with the applied voltage, the tunneling transfer rates follow an approximatelly exponential-law dependence ($\log\tau^{-1} \propto V$). with the applied voltage. However, as $Q_{eff}V$ increases there is a saturation effect on the transfer rate. This can be seen clearly if we assume larger values of the effective charge as in curve b ($Q_{eff} = 0.3e$). This saturation effect appears as a consequence of the screening of the potential at the effective image plane d_e (see equation 3). Since the equilibrium position of the xenon atom, Z_e, is closer to the substrate surface than d_e, there is a remaining barrier even for larger voltages. This is shown in Figure 2, where we have plotted the potential energy for $Q_{eff}V = 30$meV.

Then, as the voltage increases there is a crossover from exponential to Field-Emission-like behavior ($\log \tau^{-1} \propto 1/V$) [15], similar to the well known crossover from Tunneling to Field Emission in tunnel junctions.

It is interesting to compare this transfer rate behavior, obtained with our "tunneling s-resonance" model, with other possible mechanism. It has been suggested that the responsible of the experimental behavior could be a mechanism similar to the heating-assisted electromigration at low temperatures. Following Ralls et al. [2], this could imply the existence of an effective atom temperature T_a which is different from the overall sample temperature T, and increases with the square of the applied voltage, i.e. $T_a \approx T + C \times V^2$. We have replace T with T_a in equation 2 and calculated the corresponding thermal transfer rates for different values of the constant C. The results for $C = 0$ (no voltage dependence), 250 and 500KV^{-2} are shown in Figure 4 (curves c,d and e). The behavior is quite different than that obtained with our model. These curves are orders of magnitud smaller than the corresponding tunneling s-resonance results and they meet only at temperatures higher than 10K. In Figure 4, the thick line represents the experimental fit with the power-law dependence ($\tau^{-1} \propto V^{4.9}$) proposed by Eigler et al..

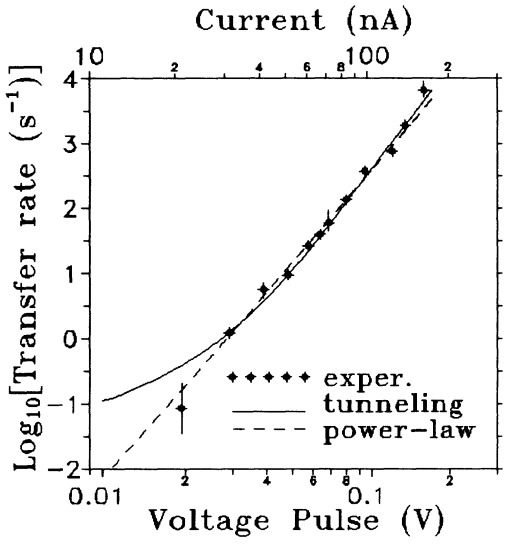

Figure 5: Calculated transfer rate of a xenon atom from the Ni surface to the STM W-tip as a function of the voltage pulse (with $D = 6.62$Å , $Q_{eff} = 0.3e$. The same as curve b in Figure 4). The experimental results obtained by Eigler, Lutz and Rudge [1] as well as their power-law fit ($\tau^{-1} \propto V^{4.9}$) are also shown. A quantum tunneling mechanism is consistent with the experimental behavior.

Although our model is able to reproduce qualitatively all the experimental observations, we could not get quantitative agreement except if we assume $D \approx 6.62$Å and an effective charge, $Q_{eff} \approx 0.3e$. It is not clear whether this large effective charge has a physical origin or it is an overestimation of our model. An increase of the effective charge could arise from different reasons. Lang's calculations of Xe adsorved on a jellium surface [5,9] (leading to $Q_{eff} \approx 0.1e$) do not include tip-induced effects that could modify the

width of the 6s resonance. On the other hand, dynamical screening effects can increase the effective charge as it has been discussed in the analysis of the direct-force contribution in electromigration [3,16]. In Figure 5, we represent our results together with the experimental results [1] corresponding to a fixed resistance $R \approx 0.9$ MΩ. The original fit with a power-law dependence is also shown in Figure 5. As it can be seen, the agreement between our results and the experiments is as good as that obtained with the power-law fit (of unknown physical origin), except for the experimental point (which has the largest error bar) at low voltage, $V \approx 0.02$V. An interesting point is that the negative tip bias, $V \approx -0.02$V (used to control the tip-sample distance) estabilize the xenon atom on the substrate surface. In any case, the nonzero probability of atom tunneling at zero voltage implies that the power-law can not be valid at small voltages. It would then be possible to measure the transfer rates for very small, and even negative, voltages. More experiments in the low voltage region will clarify the situation.

Our model predict an asymmetry of the transfer rates when the atom jumps from the W-tip to the Ni surface. Because of the different adsortion energies, larger voltages are needed to transfer the Xe atom from the tip to the sample. As a consequence, there is a minimun voltage, V_{min}, below which reversible switching is not possible. Within our model, this minimun value is at least of the order of 0.3V. However, for large fields, equation 3 is not a good approximation since it assumes a perfect screening of the field by the xenon atom and a better estimation of the field effect is needed.

4. Conductance states

Experimental results and atom-on-jellium calculations [5] have shown that the charge transfer to the 6s resonance is also the mechanism that explain the corrugation of Xe atoms observed in STM experiments. Although the 6s resonance lies near the vacuum level, its low energy tail spreads bellow the substrate Fermi level leading to some occupation of the resonance. This occupation will vary with the substrate work function [4], ϕ, thereby causing correspondig changes in the resonance occupation (the charge transfer increases as the work function decreases). This dependence with the work function could be the origin of the low and high conductance states in the atom switch. Although we do not know the geometry of the W tip, the work function of a (110) Ni surface ($\approx$ 5eV) is larger than that of most of the W surface orientations ($\approx$ 4.5eV). Then, as observed experimentally, we would expect a switch from a low-conductance state when the Xe atom is on the Ni surface (high ϕ) to a high-conductance state when it is on the W tip (low ϕ).

5. Conclusions

We have shown that the physics of the "atom switch" can be understood in terms of a single atom tunnelling process, while a mechanism similar to the heating-assisted electromigration can not account for the experimental observations. The switch dependence on the sign of the applied pulse is associated to the charge transfer from the metal surface to the adsorbed xenon atom. Under the applied pulse, the atom *tunnel* through the potential barrier existent between the two electrodes. We have presented a simple model which is in good agreement with the available experimental data.

There are several questions that have not been discussed in the original experiments. Because of the tunneling process, there is always a finite probability of atom transfer, even

at zero voltage. The transfer rates must be extremely sensitive to the tip-sample distance (a change of ≈ 0.02 Å would lead to an order of magnitud change in τ^{-1}). On the other hand, we claim that there is a minimun voltage below which the xenon atom can not move reversibly between the W-tip and the Ni surface. These predictions of our model should be observable experimentally.

Acknowledgment

The authors wish to thank H. Rohrer for many useful conversations. We also gratefully acknowledge support from the Universidad Autónoma de Madrid, the CICyT and the EEC Science Program.

References

[1] D.M. Eigler, C.P. Lutz and W.E. Rudge, (1991) Nature 352,600
[2] K.S. Ralls, D.C. Ralph and R.A. Buhrman, (1989) Phys. Rev. B 40,11561
[3] A.H. Verbruggen, (1988) IBM J. Res. Dev. 32, 93
[4] K. Wandelt and B. Gumhalter, (1984) Surface Science 140, 355
[5] D.M. Eigler, P.S. Weiss, E.K. Schweizer and N.D. Lang, (1991) Phys. Rev. Lett 66, 1189
[6] N. D. Lang, (1987) Phys. Rev. B 36, 8173
J.K. Gimzewski and R. Müller, (1987) Phys. Rev. B 36, 1284
[7] Notice that the apparent height of the xenon atom at 20 MΩ is approximately 1.53 Å and increases about 0.1 Å for each 0.5 Å decrease in D (see ref. 5).
[8] R. Gomer, (1983) in "Surface Mobilities on Solid Materials" p217, ed. by Vu Thien Binh (Plenum, New York)
[9] N.D. Lang and A.R. Williams, (1978) Phys Rev. B 18, 616
N.D. Lang, (1985) Phys. Rev. Lett. 55, 230
[10] E. Zaremba and W. Kohn, (1976) Phys. Rev. B 13, 2270
[11] K. Christmann and J.E. Demuth, (1982) Surf. Science 120,291
[12] T. Engel and R. Gomer, (1970) J. Chem. Phys. 52,5572
J.T. Yates and N.E. Erickson, (1974) Surf. Science 64,43
[13] P.M. Morse and H. Feshbach, (1953) "Methods of Theoretical Physics", p1092, (McGraw Hill, New York)
[14] P.A. Serena, J.M. Soler, and N. García, (1986) Phys. Rev. B 34, 6767; From the image plane results of Serena et al. and the decay length of the xenon wave functions we estimated that the effective image plane is placed at ≈ 0.5 Å from the Xe equilibrium distance.
[15] J.J. Sáenz, N. García, Vu Thien Binh and H. de Raedt, (1990) in "Scanning Tunneling Microscopy and Related Methods", p. 409, ed. by R.J. Behm, N. García and H. Rohrer (Kluwer Academic)
[16] R.S. Sorbello, Phys. Rev. B 31, 798 (1985)

THE EIGLER Xe SWITCH: ITS ATOMIC STRUCTURE FROM Xe ENERGY MINIMIZATION AND STM IMAGE CALCULATIONS.

C. JOACHIM[1], X. BOUJU[2] and C. GIRARD[2]

[1]*CEMES*
29, rue J. Marvig
P.O. Box 4347
31055 Toulouse Cedex
France

[2]*Lab. de Physique Moleculaire*
Université de Franche-Comté
La Bouloie
25030 Besançon Cedex
France

ABSTRACT. From the calculation of the Xe potential energy on the Cu(110) surface, on a copper tip apex and of the constant current images of this Xe on Cu(110), atomic structures of the tip apex in the "off" and "on" state (during a scan) and of the "tip apex Xe surface" tunnel junction (before scanning) are proposed.

1. Introduction

In STM experiments, the technique of tip to substrate bias voltage modulation has opened the way of small adsorbate manipulations. In short, for small pulses (i.e. below 0.2 V/Å) adsorbates can be concentrated under the tip [1], for intermediate pulses (i.e. between 0.3 and 0.7 V/Å) chemical reactions can occur under the tip like surface atom desorption or unimolecular reactions [2] and for large pulses, it is the tip apex which begin to emit its atoms [3].

The Eigler Xe switch works in the small pulse regime [4]. In the "off" state, the Xe is adsorbed in a kink of the (110) nickel surface and in the "on" state, "somewhere" in the "tip apex to nickel surface" tunnel junction [1]. The tip to surface electric field triggers the Xe move, up the tip or down the surface. The tunnel current intensity is 7 times higher in the "on" than in the "off" state [4].

From a mechanistic point of view, the complete understanding of a switch requires first the knowledge of the switch structure. After, one can work on the physical phenomena responsible for the switching event and for other important properties like the threshold voltage or the response time. For a switch of sub-nanometer dimension, the atomic structure of the "tip apex to surface tunnel junction" in the "off" and "on" states of the switch must be determined. For this purpose, STM image calculations [5] and structure energy minimizations have to be used. Calculated images are compared to the experimental ones (if possible scan by scan) to reach a good fit, trying different tip structures or compositions [6], different adsorbate positions or conformations in the junction [5]. Energy minimization of the adsorbate position (or conformation) is required to find the good atomic structure of this junction. In STM, such a structure determination will become a general procedure for adsorbate recognition or for surface reconstruction understanding [7]. It is based on the hypothesis of an adiabatic scanning of surface: the atomic structure of each part of the STM

V.T. Binh et al. (eds.),
Nanosources and Manipulation of Atoms Under High Fields and Temperatures: Applications, 239–252.
© 1993 *Kluwer Academic Publishers.*

tunnel junction stays in an equilibrium geometry during a scan. This procedure is applied in the following to determine the atomic structure of the Xe switch.

Instead of a Ni(110) surface, we have chosen to work with a Cu(110) surface because physisorbed rare gas atoms on copper have been well studied and because the Cu(110) surface structural properties are very similar to the Ni(110) ones. Moreover, the finding by calculation of an equivalent switching effect on copper will indicate that an atom switch can be fabricated on other surfaces than the Ni(110) one [5].

In section 2, the "off" state structure of the Xe switch is discussed. The equilibrium position of the Xe in the Cu(110) kink is first calculated. Then, STM images are calculated which lead to two possible structures for the tip apex in the "off" state. In section 3, the structure of the junction in the "on" state is discussed from the calculated tunnel current intensity in the "on" and "off" states. Confirmation of the junction structure found is obtained by calculating the STM image of the Cu(110) kink with a transformed "on" state of the tip apex. A sub-section is devoted to the optimization of the Xe equilibrium position upon scanning in this state.

In the following, the STM images presented were calculated using our STM-ESQC technique [7], with a tip end consisting of a flat Cu(110) basal plane (to mimic a tip terminated by a large curvature radius) with a grown apex made of (110) layers of copper atoms [5]. The parametrization chosen to describe the chemical structure of the Xe switch is based on the extended Huckel Molecular Orbital theory [8]. Calculations of the potential energy of the Xe in the switch were done using the method we have recently developped to obtain the dispersive potential energy of a Xe adsorbed on a metal surface completed by semi-empirical Born-Mayer repulsive terms for short tip to substrate distances [8].

2. The Xe switch structure in the "off" state

On Ni(110), the "off" state is obtained after a 5 Å lateral shift of the apex away from the Xe, setting a 1.5 MΩ resistance for the STM junction at this position [4]. In this case, the experimental distance zo between the apex and the surface was estimated to be 5 Å above the lower terrace and 3.8 Å above the upper one [4]. If we suppose an equivalent switch preparation on the Cu(110) surface, the lateral shift of the apex relative to the Xe must be 5.4 Å instead of 5 Å to match the Cu(110) to Ni(110) lattice difference [5]. To complete the understanding of this "off" state structure, the Xe equilibrium position in the Cu(110) kink and the atomic structure of the tip apex must be determined. This will serve to find the tip to surface distance when the 1.5 MΩ resistance is settled to obtain the "off" state.

2.1. THE Xe EQUILIBRIUM POSITION IN THE Cu(110) KINK

On a flat Cu(110) surface, the Xe equilibrium positions are the surface hollow sites located along the rows [8]. On these sites, the equilibrium distance of the Xe relative to the surface was calculated to be 2.78 Å [8]. The corresponding adsorption energy is in good agreement with the experimental one. This confirms the validity of our parametrization to decribe the Xe physisorption on Cu(110). With this parametrization, we have calculated the Xe equilibrium position on a Cu(110) surface presenting a monoatomic step and a kink along

its edge. The Xe potential energy as a function of the Xe to surface distance is presented in figure 1. Standard atomic distances were chosen for the surface copper lattice and the kink.

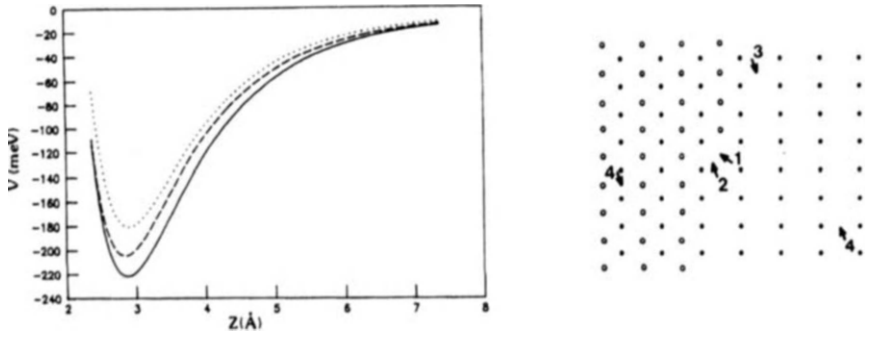

Figure 1. (a) Calculated energy of the Xe as a function of its distance to the Cu(110) surface for the adsorption sites specified in 1b. (b) Atomic structure of the Cu(110) kink studied. Four adsorption sites are labelled: (1) the hollow site next to the kink atomic row, (2) the equilibrium site found for the Xe (——), (3) the stable position sites along the step edge (- - -) and (4) the hollow sites on the flat Cu(110) surface (. . .). (o) is for the monoatomic step Au atoms and (●) for the surface ones.

As on a flat Cu(110) surface, a possible equilibrium position for the Xe on the figure 1b surface is the hollow site next to the last atom of the kink edge [8]. This site is indicated by a circle on figure 1b. But at this position, the Xe is too close to the kink atom compared to the Xe van der Waals radius. Therefore, the Xe is shifted away from this hollow site. It is also attracted by the Cu(110) step edge. This induces a small increase of the Xe altitude: 2.875 Å instead of 2.78 Å. All the copper atoms were frozen to determine this equilibrium position. This is not a drastic approximation since the Xe is very free to move on the surface compared to any Cu atoms on this surface, even the last one on the kink edge.

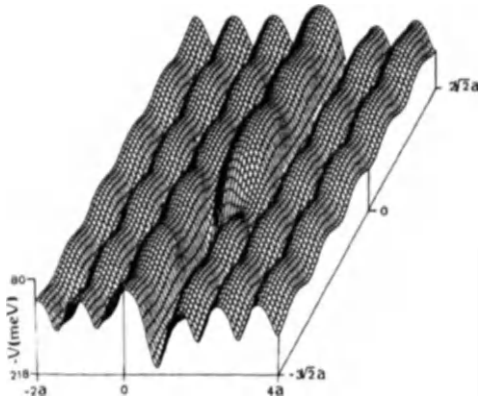

Figure 2. Calculated Xe equilibrium energy map constructed from the Xe equilibrium energy. The scanned area is 21.68 x 12.77 Å2.

The figure 2 presents the Xe equilibrium energy map near the kink. Among the equilibrium sites, it is possible to distinguish all the hollow sites on the Cu(110) upper and lower terraces, the attractive effect of the step edge producing Xe stable positions along this edge and the Xe equilibrium site just at the kink corner.

2.2 STM IMAGES OF THE Xe IN THE Cu(110) KINK

When a tip approaches the Xe stabilized in the kink edge, its apex may destabilize the Xe. On a flat Cu(110) surface, the threshold z_0 distance for destablization was found to be 5.8 Å [8,9]. But for I = 0.5 nA and V = 20 mV, the constant current scans presented in figure 3 shows a z_0 = 8.5 Å when the tip apex is exactly located at the vertical of the Xe. This scan was calculated with three (110) layers of copper atoms in the apex (hereafter the (t_1) apex), with the Xe atom in the equilibrium position calculated in section 2.1. Therefore, an STM image can be recorded at 0.5 nA and 20 mV without disturbing the Xe from its kink site. The other apex structures discussed in the following give the same order of magnitude for z_0. A complete constant current STM image calculated with (t_1) is presented in figure 4 [5]. For this calculation, the Xe was positionned in the hollow site indicated in figure 1b. Compared to the Xe on Ni(110) STM experimental images [4], the Xe apparent bump is well reproduced. Furthermore, the surface corrugation on the upper and the lower terraces is found to be less than 0.07 Å. It was not possible to observe this corrugation on the experimental images [4]. Moreover, the step edge appears too deep compared to the experimental one.

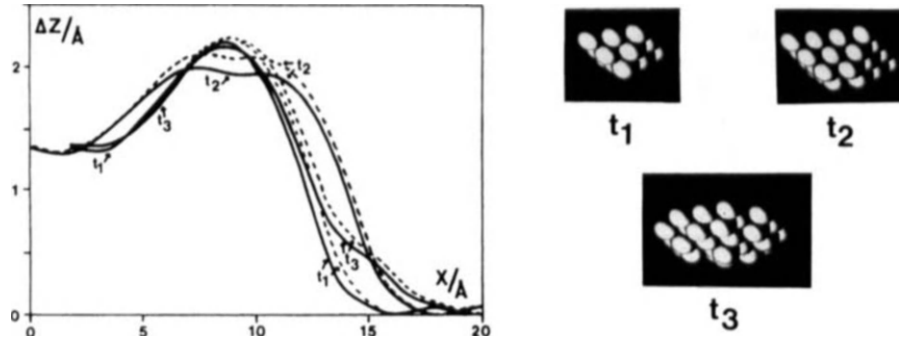

Figure 3. Calculated constant current STM scans on Xe with the (t_1), (t_2) and (t_3) apex structures. I = 0.5 nA and V = 20 mV. Two series of scans are presented: the (——) series for the Xe in its equilibrium position labelled (2) in fig. 1b and the (- - -) series for the Xe in the hollow site labelled (1) in fig. 1b.

2.3. THE TIP APEX STRUCTURE

Secured about the Xe stability upon scanning, the apex structure of the tip in the "off" state can now be determined by a comparison between the calculated and the experimental STM scans for different apex structures. We try the flat apex (t_2) (see figure 3) proposed many times for the interpretation of the Eigler switch [4] and another apex (t_3), equiped with a single end copper atom but with flat lateral facets in view of the Xe adsorption on the apex [5]. Since (t_1) already produces images corresponding well the the Xe on Ni(110)

experimental one (see figure 4), these two apex were chosen to explore other structures as a tentative to obtain a better fit. The corresponding scans were also presented in figure 3.

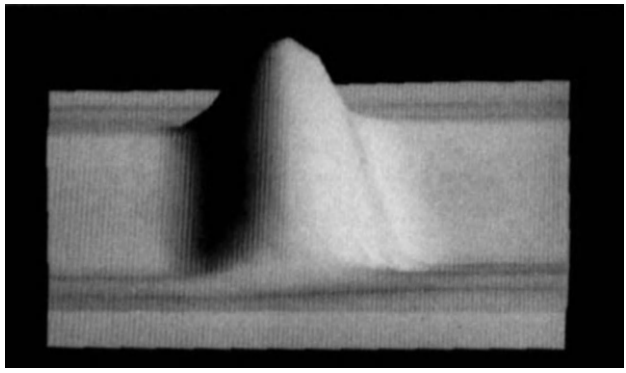

Figure 4. Calculated constant current image of a Xe located in the Cu(110) kink edge obtained with the (t_1) apex specified fig. 3. Scan size: 21.68 x 17.89 $Å^2$, Δz max = 2.202 Å, I = 0.5 nA and V = 20 mV.

Like (t_1), both (t_2) and (t_3) produce scans of the Cu (110) step edge very close to the Ni(110) experimental ones [4]. A difference is the bump height and lateral shape of the Xe. A single atom at the end of the apex is always better for the apparent height than a flat apex end. Therefore, the (t_1) and (t_3) scans look very similar. The only difference is the step edge rendering. The (t_3) apex leads to a small bump at the bottom of the step edge. This is due to the (t_3) large facets which interact with the Xe atom. This open an indirect tunneling channel between the apex facets edge and the Xe when this apex is away from the kink. Therefore, the overall current intensity increases compared to an apex without such facets. As a result, the step edge appears smoother than with (t_1). The (t_2) apex does not reproduce very well the experimental Xe print in the STM image. The calculated bump width is larger than in the experiment [4] and shows up with two bumps instead of one. This is the so-called double tip effect due to the flat end of this apex.

Therefore, for the (110) layered apex tested here, only the (t_1) and (t_3) apex produce scans close to the experimental ones. Apex with a (111) layered structure can also be tested. But as already noticed by Tsukuda and co-workers [10], the corresponding scan will not be too different compared to the (110) ones. Only the absolute value of the tunnel current intensity will change, not the Δz relative variation of the apex to surface distance upon scanning at constant current.

2.4. THE Xe SWITCH STRUCTURE

For the "off" state, two possible apex structures are now known together with the Xe equilibrium position in the kink of the Cu(110) surface. Only the z_0 absolute apex to surface distance in the "off" state is missing. This will be also the distance in the "on" state if there is no apex structural deformation due to the applied bias voltage pulse. The I(z) current -

distance characteristics for the (t_1) and (t_3) apex are presented in figure 5. To calculate these I(z), the apex was positionned 5.4 Å away from the Xe but in the same alignement as already discussed. The "off" state of the switch must be settled for a 1.5 MΩ tunneling resistance between the tip apex and the surface. With V = 20 mV, the correponding "off" current intensity is 13.33 nA. With this intensity, the apex end atom to surface distance evaluated from the I(z) in figure 5 are 4.878 Å for (t_1) and 5.158 Å for (t_3). These distances are lower than the threshold distance for tip induced displacement on Cu(110). In the "off" state, the Xe is not at the vertical of the apex but close to a facet. This makes the facets to surface distance equal to 7.7 Å for (t_1) and 6.4 Å for (t_3). At these distances, the Xe will stay in its kink equilibrium site.

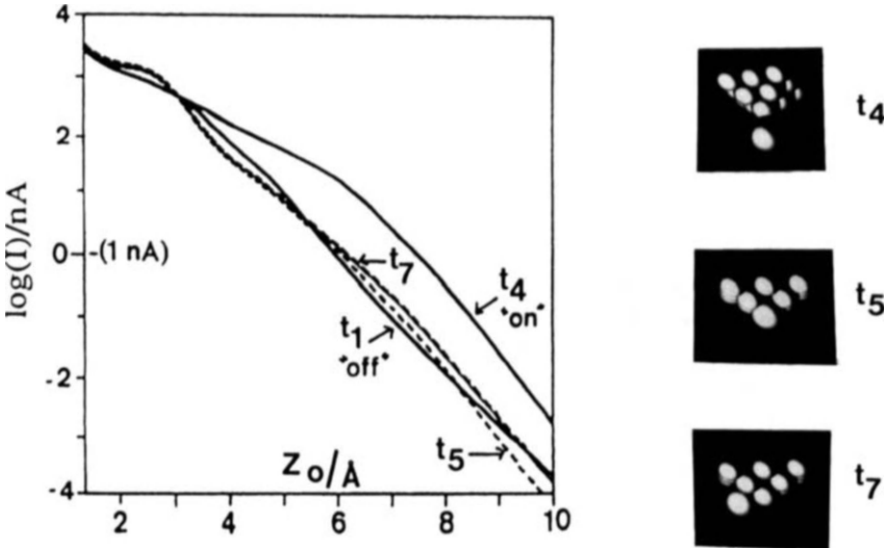

Figure 5. Calculated current - distance I(z) characteristics of the switch for V = 20 mV in the "off" and "on" states for the differents apex structures specified on each I(z). z_0 is the distance between the apex end copper atom and the Cu(110) surface. For the "off" state, the I(z) were calculated with the Xe in the hollow site (1) defined in fig. 1.

This ends the structure determination of the "off" state of the Xe switch. Notice that the distances found are of the same order of magnitude than the one estimated by D. Eigler for the "off" state on Ni(110) [4]. This proves that our STM-ESQC method is not only able to calculate well STM corrugation [6] but also absolute tunnel current intensity [5].

3. The Xe switch structure in the "on" state

The "on" state of the switch is prepared by a 0.8 V positive pulse with the tip held in the same (x,y,z) position than in the "off" state. This pulse can induce two kinds of distorsion in the

structure of the "off" state switch: a deformation of the copper apex structure or/and a change of the Xe position in the junction. The most advertised transformation has been the jump of the metal end atom of the apex "somewhere" (but preferentially on the apex) and the stabilization of the Xe in the hollow site so created [4]. The other solution is base on the fact that the pulse amplitude is too small to deform the tip apex. In this case, the conductance increase in the "on" state must be due to the change of the Xe equilibrium position. The Xe must find ist place in the junction between the apex and the Cu(110) surface. Moreover, this must really be a stable position, since after the positive pulse, the Xe stays at least 5 ms in this position as shown experimentally [4].

To decide between these two transformations, the Xe equilibrium position (if any) in the interface between the apex and the surface must be known together with the I(z) of this interface. We have also to calculate STM images with such a Xe equiped apex to compared with experimental images.

3.1. THE Xe EQUILIBRIUM POSITION ON THE TIP APEX

The equilibrium position of a Xe on (t_1), (t_2) and (t_3) are calculated here using the same parametrization than in section 2.1. Let us insist on the fact that the end bulk structure of each tip considered here is a Cu(110) large basal plane where the apex is grown. When the tip is far from the Cu(110) surface, the only equilibrium positions on (t_1) are at the edge between the basal plane and the first apex layer (figure 6a). There is no equilibrium position on the top end atom of (t_1) such as on the (t_4) structure and only very small minima on the facets, referenced as (t_7) and (t_8). For (t_2), the principal equilibrium position is the hollow site at its top end, leading to an apex referenced as (t_5), with still the attractive effects of the apex to basal plane edge (figure 6b). Finally, for (t_3), there is no equilibrium position on its top end atom such as the (t_6) structure. But due to the large width of its facets, four equilibrium positions exist (figure 6c). The one which will be close to the kink upon a surface approach is referenced as (t_9) and the more distance as (t_{10}). The (t_3) apex was constructed to get such positions.

If now the tip approaches the Cu(110) surface, new equilibrium positions appears in the interface between the apex and the surface depending on the z_o apex to surface distance [8]. For (t_1), we have already characterized these positions: for $z_o > 5.8$ Å, the Xe is stabilized when positionned between the end atom of the apex and the surface like in (t_4). This new equilibrium position does not occur when the tip is far away from the surface (figure 7a). When the apex is lower than 5.8 Å, new lateral equilibrium positions appear which lead to a tunnel junction with an apex structure intermediate between (t_4) and (t_7), (t_8) (figure 7b). For (t_2), the Xe is already stable in its hollow site on the apex end. Approaching (t_2) closer to the surface will re-enforce this stabilization (figure 7c). For (t_3), the same new equilibrium position at the apex top than for (t_1) appears for the same distance range leading to a (t_6) like structure. The only difference is for the equilibrium positions on the facets which gain in stability when the apex end copper atom is very near the surface (figure 7d).

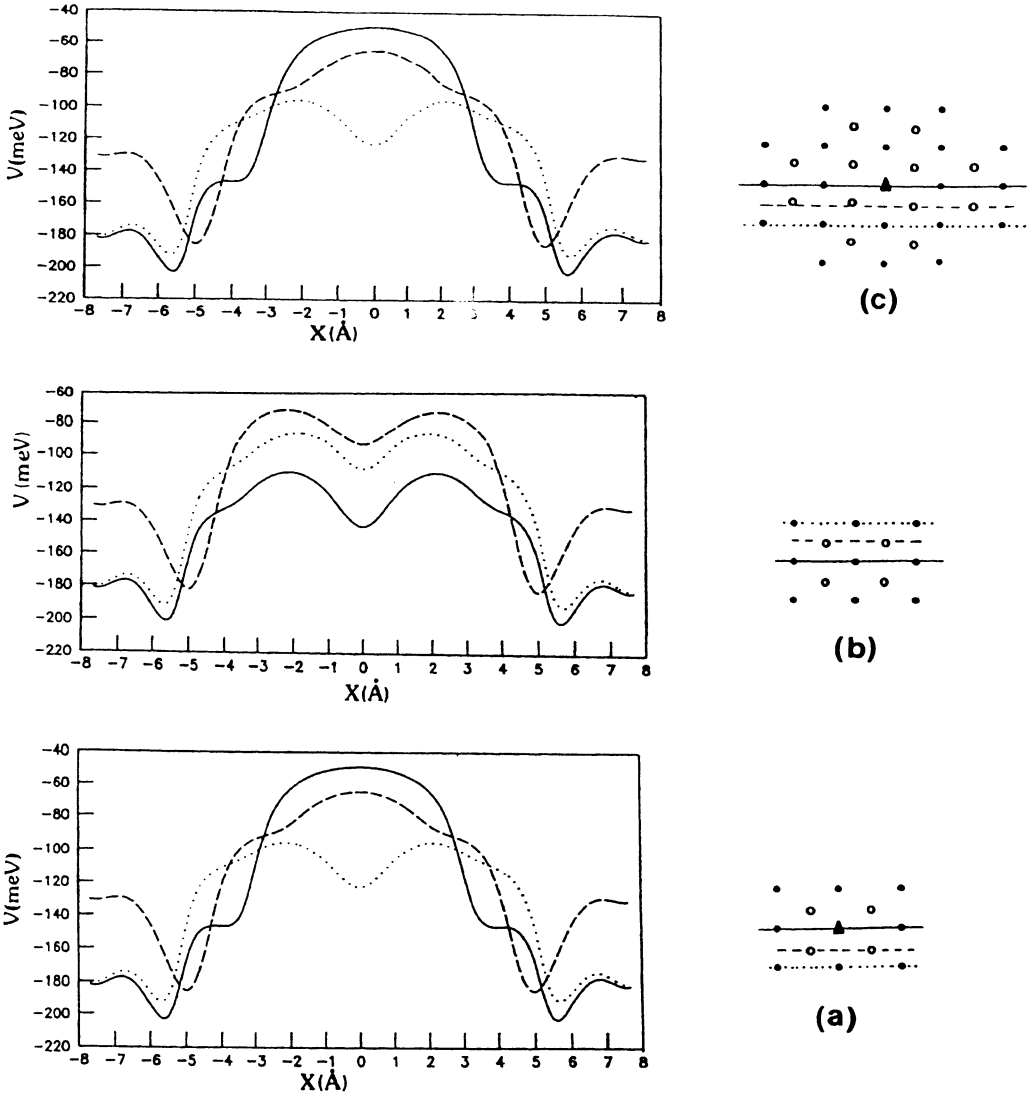

Figure 6. Calculated Xe equilibrium energy scans constructed as in fig. 2 for the tip far from the surface. (a) is for the (t_1), (b) for the (t_2) and (c) for the (t_3) apex. The orientation of each scan is specified for each apex.

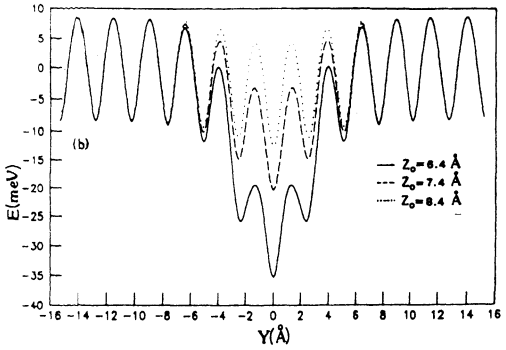

(a)

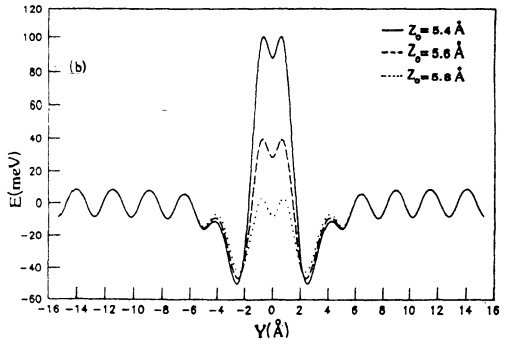

(b)

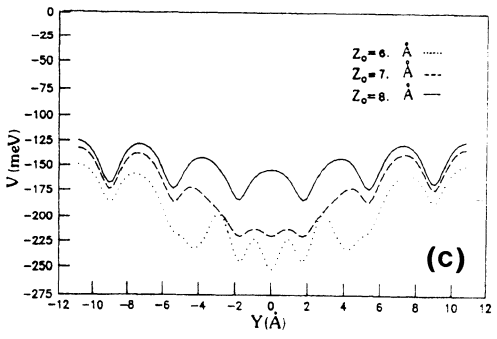

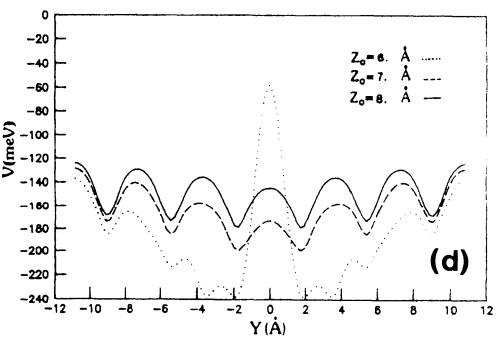

Figure 7. Calculated Xe equilibrium energy scans constructed as in fig. 2 for the tip close to the surface on an hollow site. (a) and (b) are for (t_1), (c) for the (t_2) and (d) for the (t_3) apex. The z_o distance is specified for each Xe scan.

3.2. I(z) FOR SOME Xe POSITIONS IN THE APEX-SURFACE INTERFACE

Since the z_0 tip surface distance is held at the "off" state value, it is easy to find the "on" current intensity of the switch at a 20 mV bias voltage from the "on" state I(z) already presented in figure 5. For (t_1) and (t_3), we have chosen the (t_4) and (t_6) top site positions and the lateral positions (t_7) to (t_{10}). Compared to the "off" I(z), the "on" current is much higher only when the Xe bridges the gap between the apex and the surface. When the Xe takes the available lateral equilibrium positions on (t_1) and (t_3), leading to (t_7), (t_8) and (t_9), (t_{10}), the current intensity is very close to the "off" one for the same z_0.

For (t_2), the "on" state apex structure is (t_5) and the reference "off" state apex is (t_1). The corresponding I(z) are presented in figure 8. Again, it is the Xe which favor the "on" current when brigging the gap between the flat (t_2) apex and the surface. What is interesting in the (t_2) case is that its flat apex is 1.278 Å higher in altitude the end copper atom of (t_1). But still, the Xe 6s orbital is able to very efficiently couple this apex with the surface compared to this copper atom.

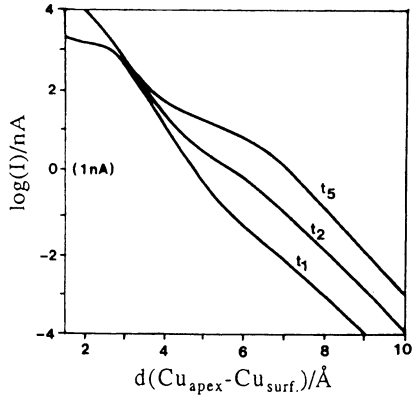

Figure 8. Calculated current-distance I(z) characteristic of the switch at V = 20 mV for the (t_2) and (t_5) apex structures. The (t_1) I(z) is also presented for reference of the "off" state. The same Xe position than in fig. 5 was used.

3.3. THE Xe POSITION BEFORE SCANNING IN THE "ON" STATE OF THE SWITCH

Since a high "on/off" current intensity ratio is obtained by D. Eigler on Ni(110) [4], we must obtain an equivalent ratio on Cu(110) [5]. This means that (t_7), (t_8), (t_9) and (t_{10}) are not the good apex structures since the "on" current obtained is of same order of magnitude than the "off" current using (t_1) and (t_3). Only three structures may play this role: (t_4), (t_5) and (t_6). With (t_5), the Xe is in a very favorable and stable position to connect electrically the apex and the surface as noticed by many authors [4]. But the end flat apex is too far away from the surface because one copper atom is missing on the apex. Therefore, the current intensity in this "on" state is small (figure 8). Moreover, since (t_2) is not a possible apex structure for the "off" state, the "off" current must be taken from (t_1). In this case, the "on" current found with (t_5) is only 4 time higher than the (t_1) "off" current which is not the

experimental result. Notice that in this experiment, the Xe is attached to a tungsten tip. The electronic structure difference may favor a higher "on" intensity for (t_5), but not to the point to win one order of magnitude.

Therefore, only stays (t_4) and (t_6). Without scanning, there is no way to decide between the two. Moreover, the corresponding Xe positions on the (t_4) and (t_6) structures chosen to calculate I(z) are not the equilibrium ones. As shown in section 3.1, with $z_o < 5.5$ Å, these position are lateral to the apex end, less than 2 Å away from the apex end atom for (t_6) and close to 2.0 Å for (t_4). For these intermediate atomic positions in the apex to surface interface, the "on" current can still be 3 times higher than in the "off" state as shown in figure 9 starting with (t_3). We must now check that (t_4) and (t_6) produce STM images comparable to the experimental ones on Ni(110) and chose between the two.

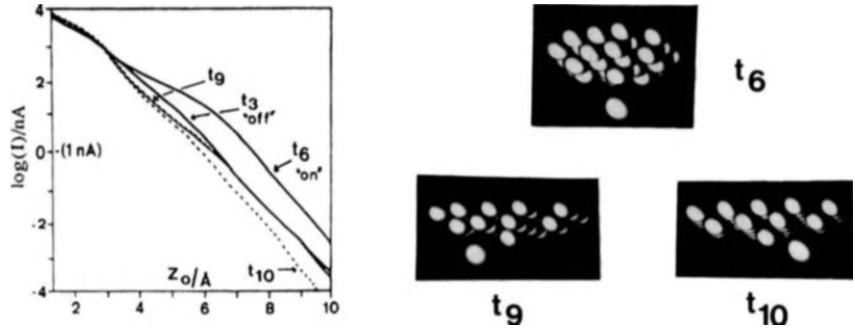

Figure 9. Calculated current - distance I(z) characteristic of the switch for V = 20 mV in the "off" and "on" states for the differents apex structures specified on each I(z). For the "off" state, the I(z) were calculated with the Xe in the hollow site defined in fig. 1.

3.4. STM SCANS ON A Cu(110) STEP EDGE WITH AN APEX EQUIPED WITH A Xe.

After the switching pulse and compared to the images before the pulse, the experimental images on Ni(110) have changed since the Xe is no more in its Ni(110) kink. The apparent corrugation on the upper and lower (110) terraces have also increased. A large bump appears all along the image of the step edge not visible in the image obtained with the "off" state apex structure.

Following the section 3.3 results, one can scan on the Cu(110) step with (t_4), (t_6) and (t_5). But upon scanning, the Xe will not stay on the apex end atom of (t_4) and (t_6) used to calculate the I(z) presented in figure 5 and no more in the intermediate positions discussed in section 3.3. because z_o is 3 Å larger when scanning at 0.5 nA constant current. This is shown in figure 10 which presents the stability of the Xe on the apex surface as a function of the distance of the apex from the step edge.

Therefore, upon scanning, and as soon as the apex has reached the step edge for the first time, the Xe will migrate on the apex facets. The corresponding equilibrium position have been discussed already in section 3.1. They correspond for example to the (t_7), (t_8), (t_9) and

(t_{10}) apex. The scans presented in figure 11 are calculated 5.442 Å away from the kink to avoid edge effects. Since the Xe in (t_5) is in its equilibrium position, the corresponding scan has been calculated too.

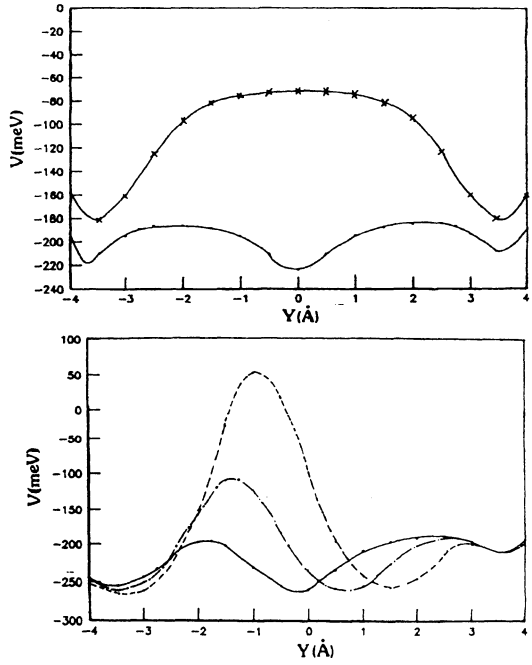

Figure 10. Minimum energy of the Xe for differents tip positions relative to a mono-atomic step on Cu(110) with the Xe atom adsorbed on the (t_1) tip apex. At each position, the Xe is scanned on the apex. The tip positions are (relative to the step edge, x axis parallele to the step and z axis perpendicular to the surface): (a) x_{tip} = 0. 0 Å, yt_{tip} = -10.83 Å and (—x—x—) z_{tip} = 10.276 Å (———), z_{tip} = 6.776 Å; (b) x_{tip} = 0.0 Å, zt_{tip} = 6.776 Å and (———) y_{tip} =-3.61 Å, (— · — · —) y_{tip} = -2.7075 Å, (- - - -) y_{tip} = -1.805 Å.

All these apex lead to an increase of the apparent copper surface corrugation on the upper and on the lower terraces (0.11 Å instead of 0.075 Å). This enhancement is not due to an apex end atom size effect since the van der Waals radius of Xe is larger than the Cu one, but has an electronic origin. When Cu is the end atom, its atomic valence states are close in energy to the surface Fermi level. This good matching across the tunnel gap leads to a large tunnel current and therefore to a large absolute tip to Cu(110) distance, for example 6.5 Å for the (t_1) apex. On the contrary, with a Xe end atom, the Cu(110) surface is probed at the Fermi level by the tail of the Xe 6s virtual resonance [8,14]. In this case, the tip has to come closer to the Cu(110) surface to compensate for the bad energy matching between the surface energy level and this 6s orbital some eV higher in energy. For example, the absolute tip to Cu(110) distance is 5.25 Å in average with the (t_4) apex. This explains the enhancement since in STM the apparent corrugation is better when the tip to substrate distance is smaller.

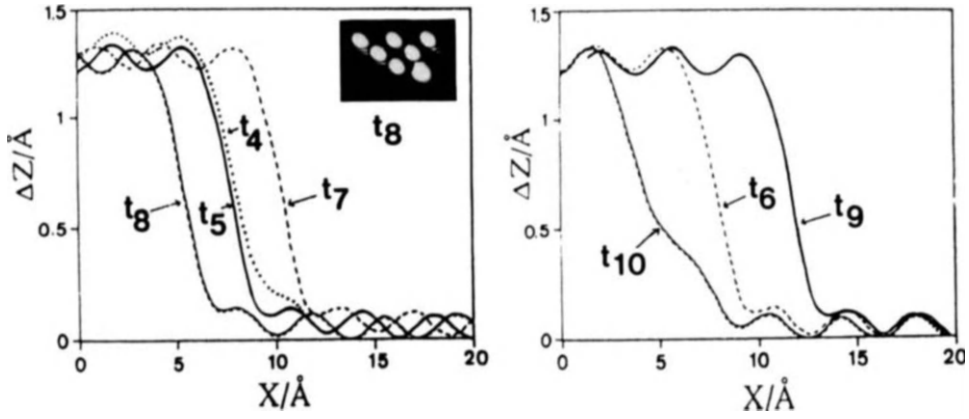

Figure 11. Calculated constant current ligne scans in the "on" state of the switch for the different apex structures specified in the figure. I = 0.5 nA and V = 20 mV.

The step height is also well reproduce. But only (t_{10}) leads to an apparent bump on the step edge image similar to the experimental one on Ni(110): near the step edge, the end apex copper atom in (t_{10}) (which is still there opens a new tunneling channel even if for (t_{10}), the Xe is the probe. This increases the overall tunnel current intensity which means that for a constant current scan, the tip must raise up a little before reaching the step edge. A complete constant current STM image of the kink is presented figure 12 using the (t_{10}) apex.

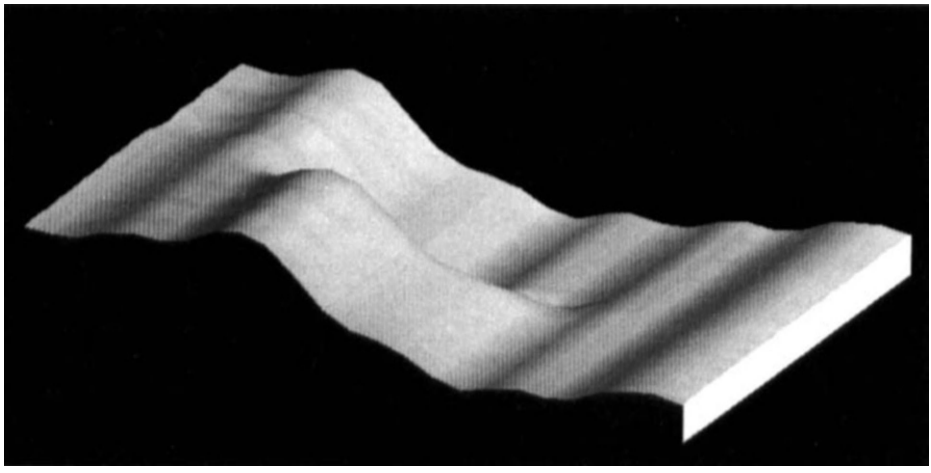

Figure 12. Calculated constant current image of the Cu(110) step with the (t_{10}) apex. Scan size: 21.68 Å x 22.44 Å and Δz_{max} = 1. 408 Å. I = 0.5 nA and V = 20 mV.

4. Conclusion

We believe that the (t_3) apex in the "off" state, the (t_9) one after the pulse and before scanning and the (t_{10}) one during a scan after the switching are reasonnable models for the D. Eigler et al. switch tip apex structures. Calculations of the Xe potential energy with the electric field should confirm this interpretation. Finally, the difference between the tetragonal apex we have used and the trigonal experimental apex are not significative for the scans calculated here.

5. Acknowledgments

We like to thank Fujitsu France for the full support of the computing during this work. Thanks also to P. Sautet for valuable discussions on the Xe electronic structure parametrization.

6. References

[1]: Strocio, J.A. and Eigler, D.M. (1991) Science 254, 1319.

[2]: Garcia, R.G. (1992) Appl. Phys. Lett. 60, 1960.

[3]: Gimzewski, J.K., Berndt, R. and Schlittler, R.R. (1992) Phys. Rev. B 45, 6844.

[4]: Eigler, D.M., Lutz, C.P. and Rudge, W.E. (1991) Nature 352, 600.

[5]: Joachim, C., Sautet, P. and Lagier, P. (1992) submitted to Europhys. Lett..

[6]: Girard, C., Joachim, C., Chavy, C. and Sautet, P. (1992) submitted to Surf. Sci..

[7]: Sautet, P and Joachim, C. (1992) Surf. Sci.271, 387.

[8]: Bouju, X., Joachim, C., Girard, C. and Sautet, P. (1992) submitted to Phys. Rev. B.

[9]: Eigler, D. and Schweizer, E. (1990) Nature 344, 524.

[10]: Tsukuda, M., Kobayashi, K. and Isshiki, N. (1991) Surf. Sci. 242, 12.

FRICTION AND FORCES ON AN ATOMIC SCALE

O. MARTI, J. COLCHERO AND J. MLYNEK
Physics Department
University of Konstanz
D-W-7750 Konstanz
Germany

ABSTRACT. The Scanning Force and Friction Microscope based on the optical lever deflection method measures simultaneously forces normal and parallel to the sample surface with a resolution of down to the atomic scale. Lateral forces on a sub-nanometer scale consist of conservative and dissipative terms. A simple model for the origin of friction on an atomic scale is discussed. Using micro fabricated cantilevers the friction coefficient of silicon nitride tips against a flat mica surface was determined at a range of loads. On a larger scale the material dependency of friction is discussed and it is shown that this property leads to a chemical sensitivity of the Scanning Force and Friction Microscope. The sensitivity to lateral forces can be used to determine adhesion properties of small structures. The Scanning Force and Friction Microscope may be useful for studies of friction and wear inaccessible to classical equipment.

Introduction

The descendants of the Scanning Tunneling Microscope[1] are ideally suited to probe properties of surfaces at nanometer and sub-nanometer scales. Of these the Scanning Force Microscope[2] (SFM) stands out because of its ability to probe conductors[2], non-conductors[3], to work in liquids[4] and to image organic monolayers[5] biological samples[6]. A particularly easy to operate scanning force microscope is based on the optical lever technology[7,8]. The development of combined force and friction microscopes[9,10,11] opens new ways to measure properties of small structures such as clusters.

Theory

The interaction forces between a sharp tip and a sample surface include many different forces. Some of these forces are attractive, some are repulsive and some can have either sign, depending on the exact physical situation. The most prominent repulsive force is the repulsion due to the overlap of electron clouds. This force may be directional or non-directional, depending on the electron states on the surface of the sample and the tip. In any case, it varies very sharply with distance. In high resolution imaging, this repulsive force is responsible for the good spacial resolution.

Always present is also the van-der-Waals force. This force is, in one picture, due to the interaction of induced dipoles. Normally this force is attractive, but using a tip, an intermediate

V.T. Binh et al. (eds.),
Nanosources and Manipulation of Atoms Under High Fields and Temperatures: Applications, 253–269.
© 1993 *Kluwer Academic Publishers.*

medium and a sample that satisfy the relations $n_{Sample} > n_{Intermediate} > n_{Tip}$ or $n_{Sample} < n_{Intermediate} < n_{Tip}$ for ultra-violet frequencies, the van-der-Waals interaction becomes repulsive[12].

Additional forces contribute to the total force. Some of them are properties of the tip and the sample, like magnetic forces or patch charges[13]. Others can be controlled by external means like electrostatic forces. Particular to the operation in air are capillary forces. In electrolytes, ionic layers on the surfaces can affect the magnitude of forces. These forces are known as electrical-double-layer forces.

A careful variation of the relevant parameters in a force microscope experiment can help to determine the importance of the various contributions. Images by Scanning Force Microscopy (SFFM) can only be understood with a theoretical interpretation of the data.

LATERAL FORCES ON AN ATOMIC SCALE

The interaction potential between a sharp tip and a corrugated surface leads to lateral forces influencing both the tip position and the apparent topography. Even completely conservative interactions lead to lateral forces. Assuming an additive potential with no directionality between atoms, we can write the total potential as

$$U(x,y,z) = \sum_{i=1}^{n}\sum_{j=1}^{m} U_{i,j}\left(r_{i,j}(x,y,z)\right) \tag{1}$$

$$\text{with } r_{i,j}(x,y,z) = \sqrt{\left(x + x_i - x_j\right)^2 + \left(y + y_i - y_j\right)^2 + \left(z + z_i - z_j\right)^2}$$

Here the index i denotes atoms in the tip and j atoms in the sample; (x,y,z) is the vector describing the displacement of the tip with respect to the sample surface. For a rigid sample and tip, the normal force in an SFM is given by the derivative of the potential U(x,y,z) with respect to z. Similarly the lateral force along x is given by the derivative with respect to x.

$$F_z(x,y,z) = \frac{\partial}{\partial z}U(x,y,z)\Big|_{x,y=const} = \sum_{i=1}^{n}\sum_{j=1}^{m}\frac{\partial}{\partial r_{i,j}}U_{i,j}\left(r_{i,j}\right)\frac{z}{r_{i,j}} = zA \tag{2}$$

$$F_x(x,y,z) = \frac{\partial}{\partial x}U(x,y,z)\Big|_{y,z=const} = \sum_{i=1}^{n}\sum_{j=1}^{m}\frac{\partial}{\partial r_{i,j}}U_{i,j}\left(r_{i,j}\right)\frac{x}{r_{i,j}} = xA$$

$$\text{with } A = \sum_{i=1}^{n}\sum_{j=1}^{m}\frac{1}{r_{i,j}}\frac{\partial}{\partial r_{i,j}}U_{i,j}\left(r_{i,j}\right)$$

In this model, normal and lateral forces are equivalent. We have, though, neglected an important aspect. Lateral forces are usually measured under the condition of constant normal force and not

for constant y and z. Only for constant forces is the friction coefficient $\gamma = F_{lat}/F_n$ well defined. This means, that for a friction image, we have to evaluate the function

$$\tilde{F}_x(x,y,z) = \frac{\partial}{\partial x} U(x,y,z)\Big|_{y,F_z(x,y,z)=const} \tag{3}$$

The function $\tilde{F}_x(x,y,z)$ is not proportional to the normal force any more. In fact evaluating forces this way, one already obtains the sawtooth like behavior of the lateral force.

The behavior of this analytical model for forces indicates, that lateral forces can not be uniquely attributed to friction. Hence care must be taken in the analysis of lateral force images on an atomic scale.

DISSIPATION MECHANISMS

On the basis of the findings of the previous chapter, we have to introduce dissipation explicitly into the model to obtain the real lateral-force versus position curves as found in the experiments. The question now is what are the relevant mechanisms for dissipation. Many different models have been brought forward over time to explain friction. Still the question of dissipation on an atomic scale is not entirely resolved. Early theories on an atomic level like the independent oscillator model [14] or the Frenkel-Kontorova-model [15] introduce the concept of atoms behaving like damped harmonic oscillators. Provided the interaction potential of such a harmonic oscillator with the opposite surface assumed to be rigid is steep enough, the oscillator will be periodically excited. In the time between the excitations the oscillator looses its heat to the body of the crystals. Besides being asymmetric with respect to the two interacting bodies the model neglects the interaction of the surface atoms with each other. It is not capable of dealing with surfaces with directed bonds.

Some theories on friction forces introduce a dissipative term by simply postulating an asymmetry in the potential[16]. This approach leads to realistic values of the friction force. However the physical mechanisms of the conversion of kinetic or potential energy to heat are hidden.

If a sharp tip moves across a surface the atoms in the tip and the surface will be subject to periodic forces. These forces will cause a local deformation of the tip and the sample. For strong interactions the tip and the sample relax periodically and very fast. The rapid movement of the atoms in the contact region is transmitted to other parts of the crystal in the form of phonons. These phonons distribute the friction energy all over a crystal. Since their life time is limited the phonon energy is effectively transformed to heat.

SIMULATION OF FRICTION FORCES

To better understand the imaging mechanisms in a Scanning Force and Friction Microscope a simple two- dimensional molecular dynamics simulation was run. This simulation was set up in a way that could be handled on a desk-top computer.

A frame of fixed atoms was defined both for the tip and the sample. No distinction was made between the tip and sample atoms. The interaction between the atoms, arranged in a hexagonal pattern, was of the Lennard-Jones type, and hence additive. The atoms, except for the fixed frame, were allowed to relax before the tip starts to move laterally. The tip movement was set to scan

repetitively from 2 atomic positions to the left to 2 atomic positions to the right. The resulting trajectories for the tip atoms are shown in figure 2 and for the sample atoms in figure 3.

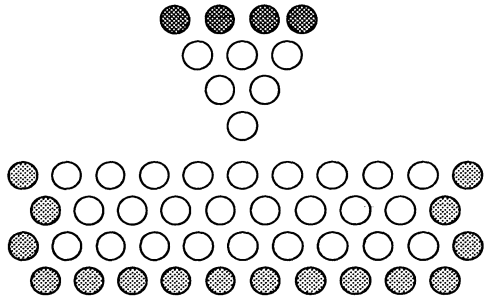

Figure 1: The array of atoms used in the simulation model. Atoms colored light gray are fixed. Atoms colored dark gray are fixed within them, but moved to simulate the scanning of the tip. The position of the white atoms is calculated in the simulation.

The excursions of the tip atoms from their rest position are drawn to scale. From figure 2 it is obvious, that very local deformations of the very end of the tip can not be neglected. This deformation, however, is exaggerated in our model. A true three-dimensional tip would lower the sideways excursions of the apex atom because a stable configuration would provide more than the two binding sites to the rest of the tip.

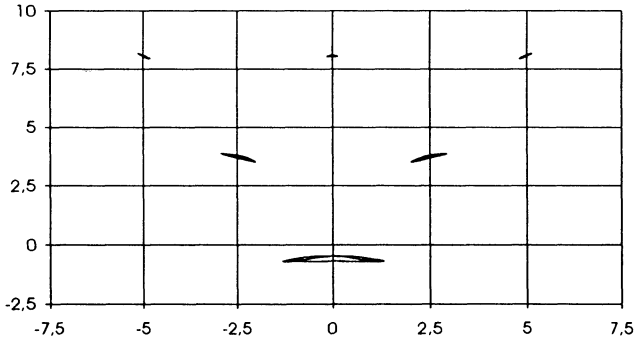

Figure 2. Trajectories of tip atoms while the tip scans a sample surface. The movement of the atoms is to scale.

Deformations occur also at the sample. Figure 3 shows the atoms in the close vicinity of the contact region between tip and sample. The surface atoms at the positions -10 and 10 show only a limited response to the scanning tip because the tip changes direction exactly overhead. Even the atoms at the positions -5 and 5 do not show the complete pattern of the movement when the tip crosses.

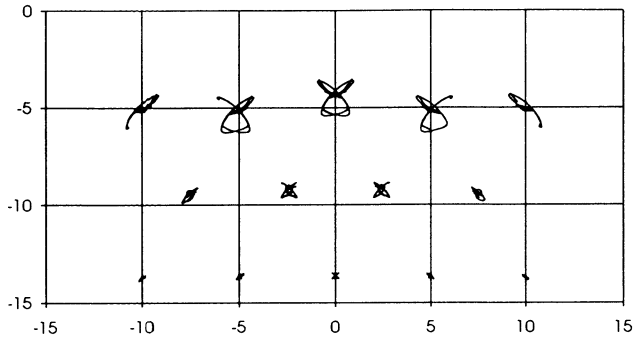

Figure 3. Trajectories of sample atoms while being scanned by the tip in figure 2. The scanning range is from -10 to 10.

The analysis of the motion of the central surface atom shows that it is first attracted by the tip to the upper left, through the lower path, then pushed down to the lower right. It then jumps to the lower left, follows the tip to the upper right and relaxes back to the rest position. The fast movement from the lower right to the lower left is reminiscent of plucking a guitar string. Similarly, the potential energy of the atom is transported all over the crystal by phonons. These phonons interact with other phonons and excitations and eventually with the heat bath surrounding the crystal. In this way energy from the motion of the tip is converted to heat, or in other words, dissipated.

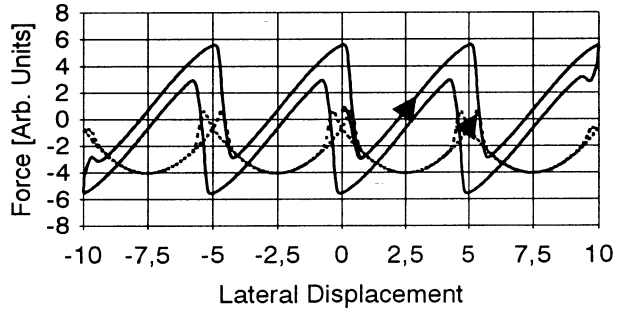

Figure 4. Result of the model calculation. The full lines show the lateral force as a function of position. The broken line denotes the normal force. The arrows indicate the direction of the curve.

Figure 4 shows the lateral (full line) and the normal (broken line) force during the scan in our model system. The lateral force curve encloses an area (force times distance) equivalent to an energy. The hysteresis is, although to a lesser extent, also visible in the normal force curve. The model faithfully reproduces the lateral force curve, as evident from the lateral force measurement in figure 8. Figure 4 also demonstrates, that on an atomic scale, one can not just take the amplitude of the lateral force and call it friction force. The energy dissipation calculated this way

is too big, much larger than the enclosed area in figure 4. A considerable amount of the lateral force is conservative.

Still another problem arises in the interpretation of the friction data with respect to the topography. The shearing of the very end of the tip gives a wrong apparent position for the lateral force. Hence the measurement must be repeated at a range of normal loads and scanning speeds to try to sort out these problems.

INTERACTION WITH SMALL STRUCTURES

The interaction of the force microscope tip with clusters or other small structures can be used to study the adhesion to the substrates. When the tip approaches a cluster or step it is pinned to the step until some lateral force is exceeded. This lateral force on a structure can be increased up to an upper limit after which the structure is detached from the substrate or desintegrated. A sketch of the lateral force is shown in figure 5.

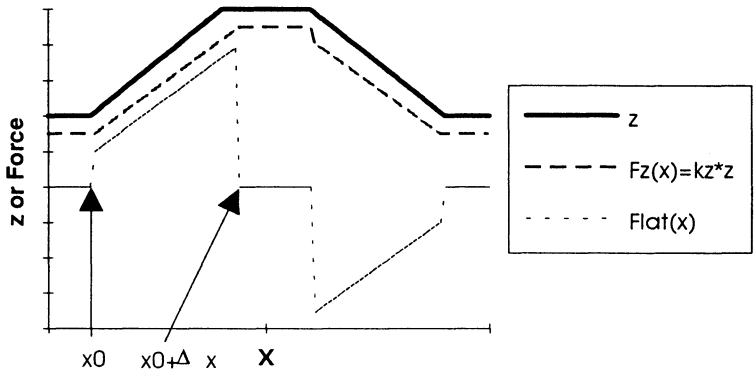

Figure 5. The traces measured by a scanning fortce and friction microscope. Curve "z" is the actual shape of the structure. Curve "Fz(x)=kz*z" is the normal force signal which is not corrected here. Curve "Flat(x)" is the lateral force curve. All curves have been calculated assuming a frictionless contact. The lateral spring constant was 10 time larger than the spring constant for the normal force.

To clarify the effect of the lateral spring constant figure 5 was calculated with a ratio between the lateral spring constant (k_{lat}) and normal spring constant (k_z) of 10 instead of 1000 found in commercial cantilevers. The lateral force will induce a deformation in the structure. This deformation causes a deviation from the lateral force behavior depicted in this figure. Assuming that the dissipation due to friction is small compared with the magnitude of the lateral force when the tip crosses the structure, we can calculate the total enery stored in both the tip and the structure.

$$E_{tot} = -\int_{x_0}^{x_0+\Delta x} F_{lat}\,dx \tag{4}$$

where the two points x_0 and $x_0 + \Delta x$ are marked in figure 5. From this energy the energy stored in the cantilever in the lateral and normal modes must be subtracted.

$$E_{struct} = E_{tot} - \left(\frac{1}{2}\frac{F_{lat}^2(x_0+\Delta x)}{k_{lat}} - \frac{1}{2}\frac{F_{lat}^2(x_0)}{k_{lat}}\right) - \left(\frac{1}{2}\frac{F_z^2(x_0+\Delta x)}{k_z} - \frac{1}{2}\frac{F_z^2(x_0)}{k_z}\right) \tag{5}$$

For structures with a low adhesion this energy must be compared to the adhesion energy in the interface region of the structure to the substrate. A common way to characterize the interface energy is to give an energy per unit area.

$$W = \frac{E_{Adh}}{A} > \frac{E_{struct}}{A} \tag{6}$$

Typical values for W are 1 J/m^2[17]. For strongly bound structures on the other hand, this energy could also mean a disintegration of the structure. Hence E_{struct} must also be compared to the melting energy of the cluster or structure under investigation.

The successful repeated imaging of a structure like a cluster can be used to calculate a lower limit of the adhesion or melting energy, whichever is relevant. Quantitative results on the exacvt value can only be obtained by detaching the structure through a series of experiments with increasing normal forces. These growing normal forces cause also growing lateral forces which probe the adhesion.

In the case of clusters, where the height is limited to a few atomic layers but the size of the contact area can vary considerably, the energy deposited in the clusters will vary little with size. The small clusters therefore are subject to a higher energy density per area and will detach first. This might be the reason why in earlier experiments[18] no small clusters (size 1nm) were found.

When exceeding the limiting energy, the tip will destroy or detach the clusters. It is usually not possible to determine the exact mode of destruction. Which event will take place depends on the relative magnitudes of the shear strength of the cluster and the shear strength of the adhesive bond. Comparing the limit lateral force as a function of the area of the cluster, the transition from bulk behavior to the behavior of mesoscopic systems can be studied.

The Scanning Force and Friction Microscope

To measure normal and lateral forces simultaneously, the microscope needs to have two channels. These two channels could be either two independent sensors like two optical fibers for two interferometers or two capacitive displacement sensors[9]. The optical lever method described in this article is unique in the sense that one sensor can independently determine the two angles that

describe the orientation of a plane in a surface[10,11]. The optical lever detection scheme also is a remote sensing method.

THE OPTICAL LEVER

This optical lever method is depicted in figure 6. It is basically the same setup as used in light beam deflection galvanometers. A fairly well collimated light beam is reflected off a mirror-like cantilever and projected to a quadrant diode (see figure 6). Any change in the angular orientation of the cantilever will change the location of the light beam on the quadrant diode. Galvanometers typically use optical path lengths of several meters.

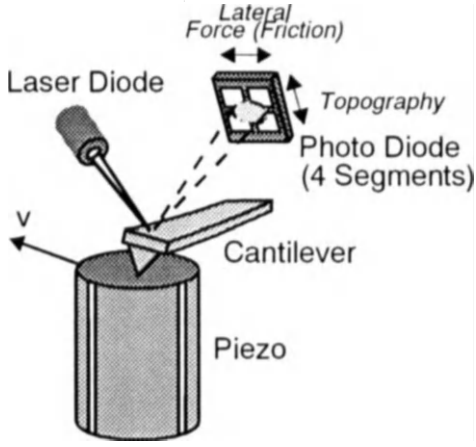

Figure 6. The schematic view of the optical lever force and friction microscope.

Initially, the light ray is set to hit the photo diodes in the center of the four sub-diodes. Any deflection of the cantilever will cause an imbalance of the number of photons reaching the quadrants. Hence the electrical currents in the photo diodes will become unbalanced too. Taking the appropriate sum and difference signals the movement of the cantilever and hence the normal and lateral force are determined.

$$U_{Force} = \alpha\left(\left(I_{Upper_left} + I_{Upper_Right}\right) - \left(I_{Lower_left} + I_{Lower_Right}\right)\right) \quad (7)$$

$$U_{friction} = \beta\left(\left(I_{Upper_left} + I_{Lower_left}\right) - \left(I_{Upper_Right} + I_{Lower_Right}\right)\right)$$

where the parameters α and β are determined by the detector electronics. The signal for the normal force (U_{force}) is fed into a feedback circuit that keeps the normal force constant. The design formulas for a combined scanning force and friction microscope can be found in the literature (see for instance ref. [10]). The deflection of a cantilever due to a normal force is

$$\Delta z = \frac{4Fl^3}{Eh^3b} \tag{8}$$

Similarly the twisting angle of this cantilever is given by[19]:

$$\Theta = \frac{M_t l}{\beta G h^3 b} \tag{9}$$

where $M_t = Fa$ is the external torque due to friction, l is the length of the beam, b and h the sides of the cross section, G the shear modulus and β a constant determined by the value of b/h. For the equation to hold b has to be larger than h.

Inserting the values for a typical micro fabricated lever with integrated tips

$$\begin{aligned} h &= 6*10^{-7}\,\mathrm{m} \\ b &= 10^{-5}\,\mathrm{m} \\ l &= 10^{-4}\,\mathrm{m} \\ a &= 3.3*10^{-6}\,\mathrm{m} \\ G &= 5*10^{10}\,\mathrm{Pa} \\ \beta &= 0.333 \end{aligned} \tag{10}$$

into equation (9) we obtain the relation

$$F = C\Theta = 1.1*10^{-4}\ \mathrm{N} \times \Theta \tag{11}$$

Typical frictional forces are of order 10^{-9} N.

MEASUREMENT PROCEDURES FOR THE DETERMINATION OF ABSOLUTE FORCES

To obtain quantitative results with SFFM normal as well as lateral force measurements have to be calibrated. Unlike piezo sensitivity the sensitivity of the optical lever depends on the geometry of the setup, on the cantilever used and on the intensity on the reflected beam and may vary quite strongly. Therefore a calibration of forces should be performed for each experiment and thus a straightforward and fast method is required. We will describe two independent and complementary procedures.

Figure 7 shows a sketch of the main components of our microscope. The glass plate in front of the photo diode is used for fine adjustment and for calibration. This plate is mounted on a gimbal mount and can be tilted so that the laser spot is moved over the photo diode and a difference signal ΔU is measured. From this signal and from the geometry of the setup, the calibration of forces is obtained as follows:

For calibration of normal forces the plate is tilted such that the beam is moved in an up-down direction (corresponding to the force-signal) by an amount

$$X = T\left(1 - \frac{1}{n}\right)\alpha_{tilt} \tag{12}$$

where T is the thickness and n the index of refraction of the glass plate.

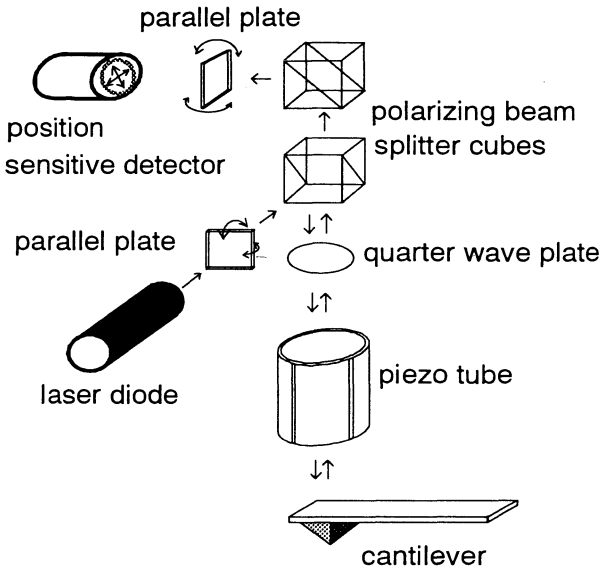

Figure 7. The schematic setup of the light path to do quantitative friction measurements

An equal amount of movement of the laser spot is obtained if the cantilever is bent by the amount Δz:

$$X = 2L\left(\frac{3}{2}\frac{\Delta z}{l}\right) \tag{13}$$

where L is the distance from the cantilever to the photo diode and l is the length of the cantilever. In the linear regime this is proportional to the measured signal ΔU:

$$\Delta z = S_z \Delta U \tag{14}$$

where S_z describes the sensitivity of the setup (small S gives high sensitivity). Combining equations (12), (13), and (14) we obtain

$$\Delta z = \frac{T}{3}\left[1 - \frac{1}{n}\right]\alpha_{tilt}\left(\frac{l}{L}\right) = S_z \Delta U \tag{15}$$

From the tilting of the glass plate by α_{tilt} and the thereby produced signal ΔU we therefore calculate the sensitivity to be

$$S_z = \frac{T}{3}\left[1 - \frac{1}{n}\right]\left(\frac{l}{L}\right)\left(\frac{\alpha_{tilt}}{\Delta U}\right) \tag{16}$$

in [nm/V]. With the compliance k the sensitivity of normal force is thus

$$S_n = k S_z \tag{17}$$

Similarly the calibration of lateral forces is obtained by tilting the glass plate in a left-right direction and recording the corresponding difference signal $\Delta U'$. With equations (9) and (11) we have

$$X' = \Theta L = \frac{F_{lat}}{C} L = T\left(1 - \frac{1}{n}\right)\alpha'_{tilt} \tag{18}$$

again we define a sensitivity by

$$F_{lat} = S_{lat} \Delta U' \tag{19}$$

and with equation (18) we obtain

$$S_{lat} = C \frac{T}{L}\left[1 - \frac{1}{n}\right]\left(\frac{\alpha'_{tilt}}{\Delta U'}\right) \tag{20}$$

where C is defined in equation (11). With 100μW reflected laser power the sensitivities of our microscope are typically S_z = 750 nm/V, S_n = 60 nN/V, and S_{lat} = 5000 nN/V, with the cantilever as described by equation (10). A noise level of 100 μV therefore limits the detection to 6 pN in normal force and to 500 pN in lateral force. With other cantilevers (smaller compliance and longer tips) this limit can be further reduced.

For normal force, an independent calibration can be easily obtained from force versus distance curves. When tip and sample are in contact, tip and piezo movements are equal. The force-signal of the photo diode therefore depends linearly on the piezo movement Δz_{piezo} (for small z) and the sensitivity is simply given by the slope of this force-distance curve in contact:

$$S_z = \frac{\Delta z_{piezo}}{\Delta U} \tag{21}$$

A rough estimate of the calibration for the lateral forces can be obtained if we assume that the laser spot has circular symmetry. From S_z we then obtain

$$S_\gamma = \frac{3}{l} S_z \tag{22}$$

which describes the sensitivity of the system in terms of the deflection angle γ. By assumption this is equal for normal and lateral forces and since

$$F_{lat} = \gamma C = \left(S_\gamma \Delta U\right) C = S_{lat} \Delta U \tag{23}$$

we obtain

$$S_{lat} = \frac{3}{l} C S_z \tag{24}$$

This result, as mentioned, assumes that the laser spot is circular, which is usually not the case.

Careful adjustment of the photo diode with respect to the orthogonal directions of laser movements may be critical for precise results. A misalignment by an angle γ results in a mixing of the movements X_n and X_l corresponding to normal and lateral forces according to:

$$\begin{aligned} X'_n &= \cos(\gamma) X_n - \sin(\gamma) X_l \\ X'_l &= \sin(\gamma) X_n + \cos(\gamma) X_l \end{aligned} \tag{25}$$

If the sensitivities S_n and S_l are comparable, small misalignments may thus be neglected because $X_i \propto 1/S_i$. For commercially available cantilevers, however, the sensitivity for normal forces is higher ($1/S_n > 1/S_l$). Thus for a small misalignement where $X'_n \approx X_n$ and $X'_l \approx X_l$ we obtain for the error angle

$$\gamma \approx \sin(\gamma) = \frac{S_n}{S_l} \tag{26}$$

Hence the misalignement will distort the friction measurement by mixing an equal amount of signal from the normal force channel to the lateral force channel.

In our case the alignment should be better than 1°. If constant force images are recorded this condition becomes less stringent, since the lateral force will add as a constant offset. This offset can be handled numerically or by high-pass filtering the lateral force signal. The cut-off frequency

of the high pass filter or the numerical procedure should be large compared to the time for one line scan. Care has to be taken to include the forward and backward scan data in the analysis.

COMPARISON WITH OTHER FRICTION MEASURING DEVICES

The scanning force and friction microscope is in many respects similar to and a further development of classical friction measuring devices. A widely used design employs a pivoted tip-like rider, whose force on the test surface, the loading force, can be adjusted by a counter weight[17].This loading force is kept constant. Typical values for classical friction apparatus range from 10^{-6} N to 10^{3} N or even more. The contact side of the rider is formed as a spherical asperity with a radius of curvature of 1 μm or more. The lateral force is measured by the deflection of a spring constrained to only lateral movement. The sample is either pulled across the rider on a straight line for strongly interacting systems or it is formed as a rotating disk to obtain long interaction times.

Experimental Results

The Scanning Force Microscope is successfully operated at atomic resolution. As an example we will show a measurement of the mica surface. On a mesoscopic scale the microscope demonstrates a chemical sensitivity for measurements of In on Si. As a last chapter we discuss the imaging of processes on surfaces.

ATOMIC RESOLUTION IMAGING

To understand the interaction of a tip and a sample it is necessary to conduct investigations on an atomic scale. As an example we show in figure 8 a measurement of the mica surface with a resolution of 0.5 nm.

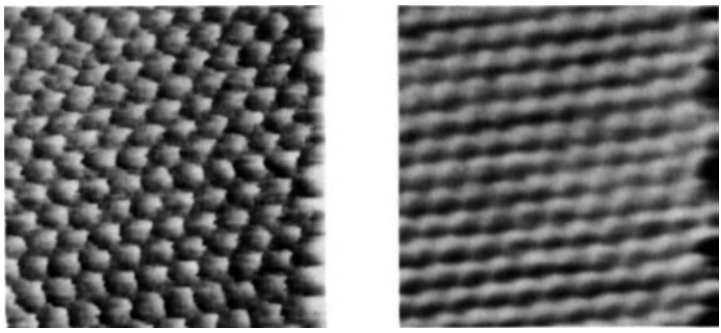

Figure 8. Topographic (left) and lateral force image of mica. The image size is 5 nm x 5 nm. The height modulation in the left image is 0.2 nm. The lateral force varies from black (high lateral force) to white (low lateral force) by 5×10^{-9} N.

Mica was used as model substance for an atomically resolved surface. In the usual topographic mode the unit cell of mica (0.52 nm) is seen, but no further details are visible (see Fig. 8). In the friction mode, however, details as small as ≈0.17 nm are resolved. The typical corrugation of the topographic image was about 0.2 nm and the variation of the friction force was about 0.5 nN. To

study the dependence of the normal force on the images, the loading was varied in the range between 5 and 30 nN, which are typical values for SFM. The features in the images did not change; however, the corrugations in the topographic image increased linearly with loading, while the variation in the friction images seemed to saturate (see figure 9). More experiments with better signal-to-noise ratio are needed to establish the precise dependence of the friction force on the loading, which is important in theoretical studies of friction on an atomic scale.

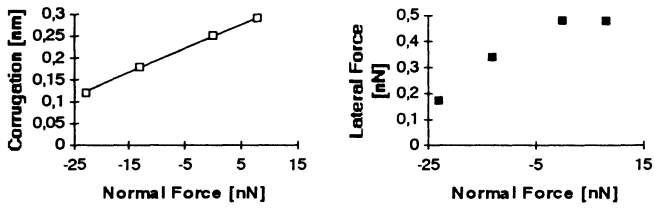

Figure 9. The left part shows the variation of the corrugation with the normal load on a mica surface. The right side displays the variation of the lateral force with the normal force on the same mica surface. The deviation of the rightmost point in the right figure may be due to experimental errors.

CHEMICAL SENSITIVITY OF THE SFFM

On a mesoscopic scale the lateral force is due to friction. On an atomic scale, however, the lateral force has a dissipative as well as a non-dissipative component. It can be shown that the topographic image is related to the variation of the surface potential normal to the sample, while the non-dissipative lateral force is connected with the variations of this potential along the scanning direction[16,20]. The SFFM therefore measures two independent and complementary quantities. The exact nature of friction on an atomic scale is not understood yet. Theoretical work on this subject is starting and the SFFM represents an ideal instrument to test these theories.

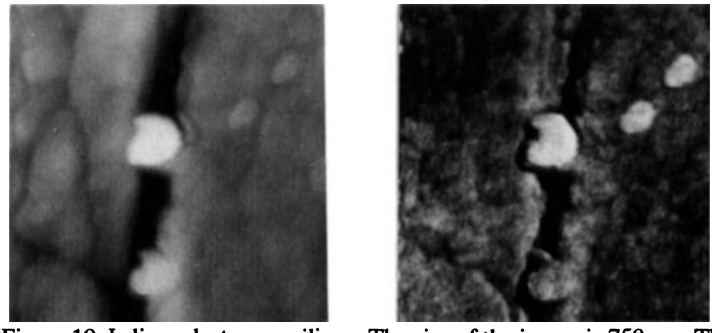

Figure 10. Indium clusters on silicon. The size of the image is 750 nm. The left part shows the topography, with bright parts being high. The right part of the figure shows the friction force. Here bright spots are low friction.

A polished silicon surface on which indium had been deposited was imaged on a mesoscopic scale. The sample was prepared in UHV. An indium film with a nominal coverage of less than one monolayer was evaporated on a silicon sample. The sample was then transported through air to

the scanning force and friction microscope and imaged in air too. In the topographic image, grains and grooves are resolved, but no distinct evidence for indium clusters is seen. In the friction mode, however, the areas corresponding to the indium clusters show a distinct contrast (see figure 10) corresponding to a lower friction coefficient. This demonstrates the ability of the SFFM to extract information about the chemical composition of the sample, which is not possible with a conventional SFM.

Judging from the size of the indium clusters in figure 10 and the relations elaborated in equations (5) and (6) it must be concluded that lateral forces are not destructive.

ROUGHNESS SENSITIVITY OF THE SFFM

In the next experiment we investigated a holographic grating coated with 50 nm of gold. The distance between two ridges is 1 μm. The images were scanned at a constant normal force of 10 nN. The topography and the lateral force image were acquired simultaneously. The lateral force image shows bright colors for large forces and dark colors for small forces. The lateral force is 1 nN everywhere except at the bottom of the holes. There the lateral force is as high as 10 nN. The bright and dark rims in the lateral force image around the holes is a geometrical effect. Since the entire sample is covered by a uniform gold layer, the difference in the friction must be due to the underlying substrate. The holes were anisotropically etched out of a silicon (100) wafer. Therefore the bottom of the holes is a surface affected by the etching process and most likely rougher than the to surface. Hence a possible explanation of this measurement is the different roughness on top and at the bottom of the holes.

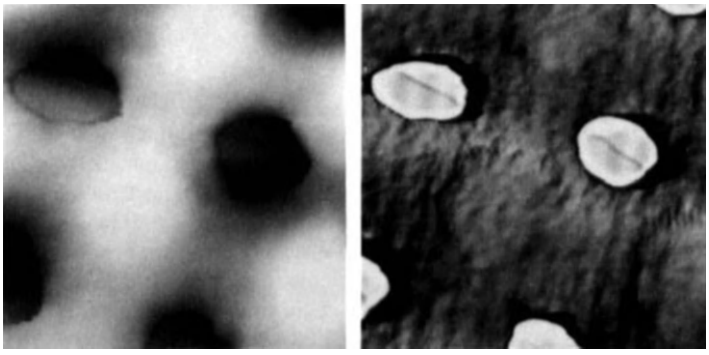

Figure 11. An image of a gold coated test grating. The image size is 1.5 μm x 1.5 μm. The corrugation of the topography in the left image is 200 nm from black to white. The friction image or lateral force image on the right has a force variation of 20 nN from black to white.

SURFACE MODIFICATION BY SFFM

Images done by scanning force and friction microscopy at high loads usually modify the sample or the tip. As an example we show in figure 12 a measurement of a piezo electric polymer foil coated with 0.8 nm gold. The images were scanned with a normal force of 50 nN. The lateral force scale at the right part of figure 12 is not calibrated. Large lateral forces are white and small lateral forces are black.

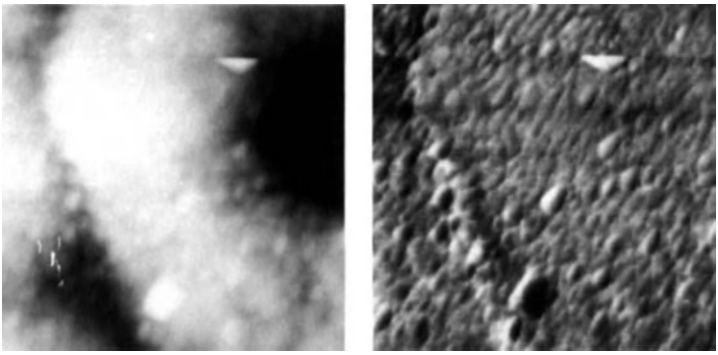

Figure 12. Modification of a polymer surface by the scanning force and friction microscope. The size if the image is 500 nm x 500 nm. The total corrugation in the topography on the left (from black to white) is 20 nm.

The scanning was non destructive except for the cluster at the top right with the half-moon like shape. This cluster was torn apart by the SFFM tip. However, the actual modification took place during the backwards scan, which was not recorded. The size of the reminder of this cluster is 70 nm by 20 nm with a height of 15 nm. Using equations (5) and (6) we can calculate the adhesion energy for this cluster. We find that $E_{adh} \approx 1$ J/m^2. Clearly this value is a very crude approximation and further work, experimental and theoretical, is required to get meaningful quantitative results from this method.

Conclusions and Outlook

The scanning force and friction microscope is a well-suited tool to investigate forces on small to atomic scale structures. Lateral forces are present down to the smallest scale. However a considerable part of the forces is conservative at this level. To understand the exact behavior of the scanning force microscope at this level, theoretical models are indispensable. They are especially necessary to understand the deformation of the tip on this range. On a larger scale, for mesoscopic structures, lateral forces can give a handle to distinguish different chemical species. They can be used to measure the shear stress in the contact range of clusters and can therefore be used to characterize adhesion on a particle by particle scale.

The operation of the scanning force and friction microscope in air can give qualitative insight into physical processes. However to gain a quantitative understanding, the microscope should be operated in ultra-high vacuum[9,21,22] or under electrochemical control[23]. Using single crystalline tips on controlled surfaces will provide the necessary information to understand friction of single contacts. These new insights might also be of value for the understanding of larger scale friction effects involving many small contacts.

Some investigations using scanning tunneling microscopy could also benefit from the combination with lateral force measurements. Especially investigations involving the movement of atoms in high electrical fields would become complete if the direction of the forces applied on the atoms would be known.

ACKNOWLEDGMENTS

The authors would like to thank K Dransfeld, M. Hipp, H. Bielefeldt, J. Mertz, V. Balykin and their other colleges at the University of Konstanz for many useful discussions. The In on Si sample was prepared at the group of G. Schatz by G. Krausch. The polymer sample was prepared by Prof. Lie-Jie. The holographic grating was a gift by Park Scientific Instruments. The interaction with U. Hartmann, H.-J. Kreutzer, H.-J. Güntherodt, and S. Dietrich was important for the further understanding of friction effects.

References

[1] G. Binnig and H. Rohrer, Ch. Gerber, and E. Weibel, Phys. Rev. Lett. 49, 57 (1982).
[2] G. Binnig, C.F. Quate, and Ch. Gerber, Phys. Rev. Lett. 56, 930 (1986).
[3] T.R. Albrecht and C.F. Quate, J. Appl. Phys. 62, 2599 (1987).
[4] O. Marti, B. Drake, and P.K. Hansma, Appl. Phys. Lett. 51, 484 (1987).
[5] O. Marti, H. O. Ribi, B. Drake, T.R. Albrecht, C.F. Quate, and P.K. Hansma, Science 239, 50 (1988).
[6] S. Gould, O. Marti, B. Drake, L. Hellemans, C.E. Bracker, P.K. Hansma, N.L. Keder, M.M. Eddy, and G.D. Stucky, Nature 332, 332 (1988).
[7] G. Meyer and N.M. Amer, Appl. Phys. Lett. 53, 1045 (1988).
[8] S. Alexander, L. Hellemans, O. Marti, J. Schneir, V. elings, P.K. Hansma, M. Longmire, and J. Gurley, J. appl. Phys. 65, 194 (1989).
[9] S.R. Cohen, G. Neubaur, and G.M. McClelland, J. Vac. Sci. Technol. A8, 3449 (1990).
[10] O. Marti, J. Colchero, and J. Mlynek, Nanotechnology 1, 141 (1990).
[11] G. Meyer and N.M. Amer, Appl. Phys. Lett. 56, 2100 (1990).
[12] J.N. Israelachvili, Intermolecular and Surface Forces, Academic Press, London, 66 (1985).
[13] N.A. Burnham, R.J. Colton and H.M. Pollock, Verhandl. DPG (VI) 27, 807 (1992).
[14] G.A. Tomlinson, Phil. Mag. S. 7, Vol. 7, 905 (1929).
[15] Y.I. Frenkel-and T. Kontorova-Zh. Eksp. Teor. Fiz. 8, 1340 (1938).
[16] G. Overney, W. Zhong, and D. Tomanek, J. Vac. Sci. Technol. 9, 479 (1991).
[17] E. Rabinowicz,Friction and Wear of Materials, John Wiley and Sons, New York, (1965).
[18] J. Colchero, O. Marti, J. Mlynek, A. Humbert, C.R. Henry, and C. Chapon, J. Vac. Sci. Technol. B9, 794 (1991).
[19] T. Baumeiser and S.L. Marks, editors, Standard handbook for Mechanical Engineers, 7th edn (McGraw-Hill, New York), 5-29 (1967) .
[20] S. Ciraci, Proc. STM'91 Interlaken, to appear in Ultramicroscopy.
[21] N.A. Burnham, Proc. STM'91 Interlaken, to appear in Ultramicroscopy.
[22] J. Wiecherts, private communication.
[23] A. A. Gewirth, Proc. STM'91 Interlaken, to appear in Ultramicroscopy.

ATOMIC-SCALE ADHESION

U. Dürig and O. Züger*
IBM Research Division
Zurich Research Laboratory
8803 Rüschlikon
Switzerland

ABSTRACT. The interaction of a metal tip with a metal surface is investigated in terms of the known theory of metal adhesion and experimentally by means of force-gradient sensing with scanning tunneling microscopy. Experimental results are presented for the interaction of an Ir tip with an Ir surface, and atomic-scale resolution capability is demonstrated in the *attractive* force regime. Furthermore, we show experimental evidence for adhesion-promoted, entropy-driven local disordering.

1. Introduction

The study of interactions at surfaces has a long history, in particular with regard to adhesion of macroscopic bodies, because of their obvious technological relevance. The topic is also of great importance in modern surface science, which has experienced a tremendous development over the past two decades. Despite all these efforts, adhesion science is still in an empirical stage, since there is a wide gap between our understanding of the fundamental physical processes and the corresponding technological know-how.

One of the reasons for this unsatisfactory situation is that, until recently, it was not possible to investigate interactions in a direct way on an atomic scale. Therefore most experimental work has been devoted to the study of long-range interactions such as Van der Waals forces [1]. The development of scanning tunneling microscopy (STM) and related local probe techniques, in particular, scanning force microscopy, paved the way for a new class of experiments. These techniques allow the gap width between a probe tip and a sample surface to be controlled on an angstrom scale. Consequently, interactions involving electron wave function overlap can be explored. Typical examples are chemical and metallic bond forces. To date, only scant information on these local interactions is available, yet they are of fundamental importance for the understanding of surface interactions such as adhesion and friction on an atomic scale.

*Present address: IBM Research Division, Almaden Research Center, 650 Harry Road, San Jose, Ca 95129-6099, USA

V.T. Binh et al. (eds.),
Nanosources and Manipulation of Atoms Under High Fields and Temperatures: Applications, 271–286.
© 1993 *All Rights Reserved.*

Nanometer-scale mechanics is another important related field that will require increased attention in the near future, since the trend toward miniaturization continues at a rate of approximately one order of magnitude per decade. The ultimate goal is to manipulate individual molecules or atoms. The most spectacular demonstration of the latter has been given by Eigler *et al.* [2], who were able to switch an electrical current by proper positioning of a single Xe atom.

In this paper we will present some aspects of the physics of local interactions from a point of view influenced by our own experimental work. We have concentrated on characterizing tip-sample interactions during normal metal-vacuum-metal tunneling operation of the STM, which allows the correlation of force and tunneling data.

2. Metal-Metal Interaction

The interaction between a metal tip and a metallic sample arises from the quantum mechanical description of the conduction electrons. Two regimes are differentiated according to the separation of the bodies. At large distances, electron wave functions do not overlap and the interaction is dominated by Van der Waals (VdW) forces. The leading term has a power law dependence on distance, and its exponent depends on the geometry. At a gap width on the order of three angstroms, the electron wave functions overlap appreciably and electron exchange becomes important. This gives rise to a different type of attractive interaction: metallic adhesion. The corresponding forces decay exponentially with a characteristic length scale comparable to the screening length.

Interaction theory of metals has so far concentrated on calculating the energy of adhesion of two interacting, parallel half spaces separated by a distance s. Throughout this paper we assume that s is measured with respect to the jellium edges of the interacting bodies. The leading terms of the adhesive energy per unit area due to the nonretarded VdW interaction is given by the well-known Lifshitz formula [3]:

$$W_{\mathrm{ad}}(s) = \frac{\hbar\,\overline{\omega}}{16\,\pi^2\,s^2} \quad , \tag{1}$$

where we use the abbreviation

$$\overline{\omega} = \int_0^\infty \frac{\varepsilon_1(i\xi) - 1}{\varepsilon_1(i\xi) + 1}\,\frac{\varepsilon_2(i\xi) - 1}{\varepsilon_2(i\xi) + 1}\,d\xi \quad . \tag{2}$$

The integration in Eq. (2) is done in the complex ω-plane along the imaginary frequency axis, and $\varepsilon_{1,2}(\omega)$ denote the complex dielectric functions of the two half spaces, respectively. Dielectric properties of simple metals are described fairly well by a free electron approximation. The Lifshitz frequency $\overline{\omega}$ can then be expressed in terms of the plasma frequencies $\omega_{p1,p2}$ of the electron gas in the two half spaces [4]

$$\bar{\omega} = \frac{\sqrt{2}\,\pi}{4} \frac{\omega_{p1}\,\omega_{p2}}{\omega_{p1} + \omega_{p2}} \quad . \tag{3}$$

For simple metals, the order of magnitude of the VdW interaction is adequately represented by Eq. (3). For transition metals, however, $\bar{\omega}$ is underestimated by a factor of approximately two, since additional dissipation channels due to interband transitions must be taken into account. Values of $\hbar\bar{\omega}$ taken from the literature [4] are 8.2 eV and 9 eV for Al and Ag, respectively. The corresponding values estimated by means of Eq. (3) are 7.1 eV and 4.9 eV. The value for Ag is too low by about a factor of two, as expected.

The Lifshitz expression emerges from a local approximation of the dielectric function [5], which means that effects due to finite screening in real metals are neglected. The approximation is valid if the interaction distance is larger than approx. 6 Å. At shorter distances, however, plasmon modes with large wave vectors parallel to the surface contribute substantially to the interaction. Accordingly, the dielectric function must be corrected to account for nonlocal screening effects, and as a result the VdW interaction becomes weaker than the Lifshitz formula would suggest. In particular, the divergence at $s \to 0$ is eliminated. Corresponding theories are rather elaborate, and no simple functional dependence of the interaction potential on distance can be established.

Upon decreasing the gap width further, electron wave functions overlap appreciably, making it necessary to consider exchange effects [6]. Eventually the coupling between the metals becomes so strong that perturbative approaches can no longer be used. Therefore self-consistent density functional formalism [7,8] combined with pseudo-potential methods [9] have been employed for calculating interaction energies. One of the problems with density functional theory is that a local approximation is used for the exchange-correlation functional. As a consequence, binding energies are typically overestimated, and interactions due to correlated electron excitations cannot be treated at all. This means that long-range VdW interactions are not within the scope of such calculations and interaction potentials typically fall off exponentially.

Rose *et al.* [8] calculated the adhesion energy for simple metals using a self-consistent local density formalism and a jellium model. They discovered that the interaction energy as a function of interface separation is accurately represented by the Rydberg function with two scaling parameters, namely, the energy of adhesion E_{ad} and a length l_{sc} approximately equal to the Thomas-Fermi screening length

$$W_{ad}(s) = E_{ad}\,(1 + s/\ell_{sc})\,\exp(-s/\ell_{sc}) \quad . \tag{4}$$

The theory was extended in a semi-phenomenological way to include all metallic elements, whereby the quantities E_{ad} and ℓ_{sc} are inferred from cohesive properties of the bulk [10].

As a typical example, we show in Fig. 1 the interaction potential for two Al half spaces. The respective values of $\hbar\bar{\omega} = 8.2$ eV [4], $E_{ad} = 100$ meV Å^{-2} [8] and $\ell_{sc} = 0.66$ Å [10] are representative for most metals. In the upper panel the different contributions to the adhesion energy are shown on an expanded scale. The dotted

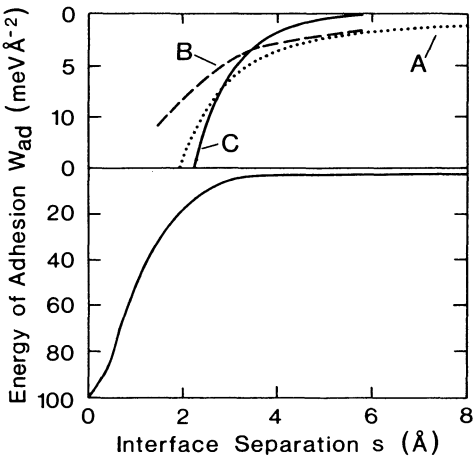

Figure 1. Adhesion energy of two Al half spaces. **Upper panel:** (A) VdW interaction, Lifshitz result; (B) VdW interaction, Inglesfield result; (C) short-range metallic adhesion. **Lower panel:** Overall interaction potential obtained by interpolating curves (B) and (C).

curve (A) corresponds to the non-retarded Lifshitz VdW interaction (Eq. 1). The dashed curve (B), taken from [11], represents the VdW interaction taking into account effects due to finite screening. The short-range metallic adhesion interaction (Eq. 4) is displayed by the solid line (C). The Lifshitz expression is clearly inadequate to describe the VdW interaction for interface separations smaller than 6 Å. The crossover from the VdW to the metallic-adhesion regime occurs at a separation of $\simeq 3$ Å. The overall interaction potential obtained by interpolating curves (B) and (C) is depicted in the lower panel. Most of the adhesive energy (about 95%) is due to short-range interaction.

3. Tip-Sample Interaction

We consider the interaction of a tip with a flat surface. The magnitude of the interaction force as well as its distance dependence are strongly influenced by the geometry of the tip. A simple expression was derived which relates the tip-sample interaction force to the energy of adhesion of two half spaces [12]:

$$F_I(s) = -W_{ad}(s)\,\frac{d\sigma}{dz}(0) - \int_0^\infty W_{ad}(s+z)\,\frac{d^2\sigma}{dz^2}\,dz + \frac{dW_{ad}}{ds}(s)\,\sigma(0)\ . \qquad (5)$$

Here $\sigma(z)$ denotes the cross section of the tip assumed to be rotational-symmetric with respect to the z-axis. The origin of the latter is at the apex of the tip. In deriving Eq. (5), it is implicitly assumed that the interaction can be described in terms of pair

potentials. Moreover, in the spirit of the jellium model, the atomic structure of the tip and sample are neglected, thus justifying the continuum approach. Note that the first term of Eq. (5) corresponds to the so-called Derjaguin approximation [13]

$$F_{\mathrm{I}}(s) = 2\pi R W_{\mathrm{ad}}(s) , \tag{6}$$

where $R = d\sigma/dz(0)$ denotes the radius of curvature of the tip apex.

The notion of pair potentials as well as the continuum approach appear to be somewhat artificial in the context of atomic-scale metal-metal interactions. To develop a more physical picture of the problem, we have looked at the tip-sample interaction from a different point of view. Suppose that the tip consists of atomic layers forming a pattern of parallel terraces (Fig. 2). The spacing between atomic layers d shall be uniform. Let σ_i denote the cross section of the i-th layer. We now simplify matters by considering each terrace to be a subarea of an infinitely extended half space. Hence, effects due to the finite size of the terraces and the influence of steps are ignored. F_{I} may then be expressed as

$$F_{\mathrm{I}}(s) = \sum_{i=0}^{\infty} (\sigma_i - \sigma_{i-1}) F_{\mathrm{ad}}(s + (i-1)\, d) , \tag{7}$$

where $F_{\mathrm{ad}} = -dW_{\mathrm{ad}}/ds$ denotes the interaction force per unit area of two half spaces (note that $\sigma_0 \equiv 0$). Reordering the terms in the sum – corresponding to a partial integration – we obtain

$$\begin{aligned} F_{\mathrm{I}}(s) = {} & (\sigma_2 - \sigma_1) \sum_{j=2} F_{\mathrm{ad}}(s + (j-1)\, d) + \\ & + \sum_{i=3} (\sigma_i - 2\sigma_{i-1} + \sigma_{i-2}) \sum_{j=3} F_{\mathrm{ad}}(s + (j-1)\, d) + \\ & + \sigma_1 F_{\mathrm{ad}}(s) . \end{aligned} \tag{8}$$

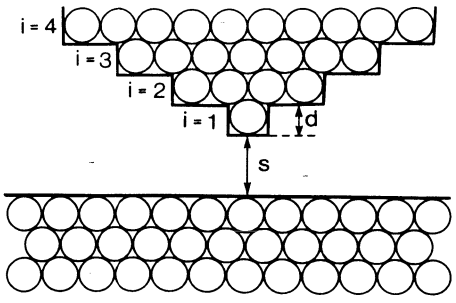

Figure 2. Tip-model considered in this paper.

This equation is the exact analogue to Eq. (5), as is seen by taking the limit $d \to 0$. Hence, we conclude that calculating tip-sample interaction forces either by starting from pair potentials or by summing the contributions of independent, flat terraces is equivalent. In other words, the notion of pairwise interaction emerges as a direct consequence of neglecting the influence of steps.

To see the analogy more clearly, we transform Eq. (7) once more, but this time the difference operator is applied to F_{ad} instead of σ_i. One then obtains

$$F_1(s) = \sum_{i=1} \sigma_i \, \Delta F_{ad}(s + (i-1)\, d) \tag{9a}$$

with

$$\Delta F_{ad}(z) \equiv F_{ad}(z) - F_{ad}(z + d) \ . \tag{9b}$$

Hence, the total tip-sample interaction is simply a linear superposition of the interaction of the substrate with the atomic layers constituting the tip. The interaction of one layer is thereby proportional to its cross section, which in turn is equivalent to the number of atoms N_i in that layer. As a corollary, it follows that $\Delta F_{ad}(z)\, \sigma_a$, where $\sigma_a = \sigma_i / N_i$ denotes the mean area per atom, is the force exerted on a tip-atom that is at a distance z above the plane.

One can go a step further and derive an effective pair potential for the mutual interaction of atoms of the tip and sample, respectively (the derivation is straightforward but somewhat lengthy and will not be given here):

$$U_{pair}(r) \simeq \frac{\sigma_a^2 \, d/dr \, (\Delta W_{ad}(r - d_0) - \Delta W_{ad}(r))}{2 \pi r} \ . \tag{10}$$

The potential is constructed in such a way that W_{ad} is obtained when the interaction energy of two half spaces is calculated, i.e. $W_{ad} = \Sigma_i \Sigma_j \, U_{pair}(r_{ij})$, where r_{ij} denotes the distance between atom i of one half space and atom j of the other. The term d_0 denotes the lattice spacing of close-packed planes. The corresponding values for fcc metals are $d_0 = a/\sqrt{3}$ and $\sigma_a = a^2\sqrt{3}/4$, where a is the lattice constant of the cubic unit cell. Substituting Eq. (1) for W_{ad} and taking the limit $d_0 \ll r$, one recovers the well-known $1/r^6$ dependence of the VdW pair potential.

We wish to make some comments regarding the applicability of the pair-potential approximation. First, we note that a number of theoretical articles dealing with the VdW interaction in scanning force microscopy are based on exactly this assumption [14,15]. However, it must be noted that a potentially important aspect might be missed by this approach. It has been shown that localized surface plasmons are induced by coupling the apex of a sharp tip to a substrate surface [16,17]. One would thus expect that the Lifshitz frequency $\bar{\omega}$ (or, equivalently, the Hamaker constant $H = 3\hbar\bar{\omega}/4\pi$) not only depends on s (to account for finite screening) but also on the local geometry expressed, for example, in terms of an effective radius of curvature. This issue has not yet been addressed — either by theory or by experiments.

It is a well-known fact that metallic cohesion cannot be described by pair-wise atomic interactions. So the question is to what degree do effective pair potentials make sense in the context of short-range adhesion interaction. First, we note that the potentials are derived from a bulk calculation which, according to its sophistication, properly includes many-body effects. Thus we may expect that the pair potentials provide a reasonable approximation if the electron density distribution in an atomic cell at the surface of the tip is not significantly different from that at the surface of the half spaces considered in the reference calculation. By comparison with *ab-initio* calculations [18], we found that our simple model was capable of quite accurately predicting the adhesion between Al(100) planes, including effects due to lattice mismatch. On the other hand, the same *ab-initio* calculation showed that a strong *pz*-like bond is established between an isolated Al atom and a flat Al substrate. Such a bond is not seen between bulk atoms. Accordingly, binding energies predicted by our model are too low in this case. Nevertheless, the effective pair potential model provides a convenient starting point for assessing at least qualitative features of atomic-scale adhesion. For example, lateral tip-sample forces can be easily calculated. It turns out that they are typically an order of magnitude smaller than corresponding perpendicular forces, even in the vicinity of mono-atomic steps on the surface.

Finally we calculate the interaction force F_I and force gradient ∇F_I for the tip shown in Fig. 2. Since it is assumed that the substrate is flat and that the tip is in registry with the atomic lattice of the substrate, either Eq. (7), (8) or (9) may be used for this purpose. The interaction potential is the one discussed in the context of Fig. 1, and $d = 2.3$ Å is taken to correspond to the spacing of Al(111) planes. The micro-tip is assumed to be attached to a support that has a radius of curvature of $R = 100$ Å. The Deryagin approximation is used to account for the interaction of the support with the sample. The result of the calculation is shown in Fig. 3. The dotted curve corresponds

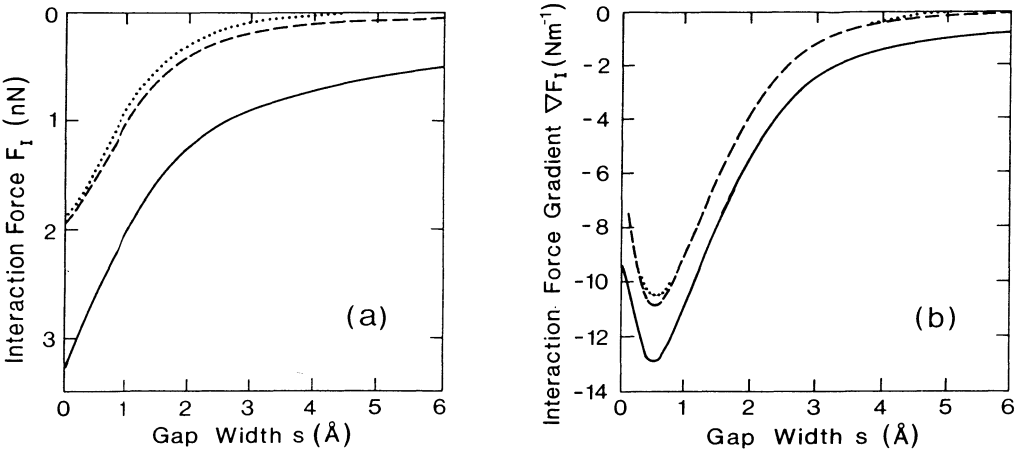

Figure 3. Interaction force (a) and force gradient (b) for the tip in Fig. 2. Dotted line: short-range adhesion interaction; dashed line: short-range plus VdW interaction; solid line: total interaction including a spherical support with radius $R = 100$ Å.

to the short-range metallic-adhesion interaction of the micro-tip with the substrate. The dashed curve is obtained if the VdW interaction is included. The solid line results if in addition the VdW interaction of the support is taken into account. As expected, the VdW interaction has little effect on the interaction of the micro-tip with the substrate. On the other hand, long-range VdW forces that sample a much larger area give rise to a substantial net attractive force (Fig. 3a), which however does not change appreciably with distance. Hence, the shape of the adhesion-force curve at short distances is determined by the atomic structure of the tip apex and the short-range adhesion forces, whereas the net attractive force measured at a distance larger than $\simeq$5 Å provides information on the overall tip shape. Accordingly, the interaction force gradient (Fig. 3b) is only marginally influenced by VdW forces originating from the support. As a final remark, we would like to point out that zero net attractive force does not mean that the tip is not pressing against the sample. In fact, the apex of the tip experiences a repulsive force that is counterbalancing the long-range VdW attraction. Therefore, detection of a negative interaction force gradient is a necessary condition for non-repulsive interaction.

4. Experimental

A comprehensive discussion of interaction force detection in scanning probe microscopy is presented in [19]. Here, we briefly describe the basic principles that are relevant to our study of the short-range tip-sample interaction by means of force-gradient sensing. A flexible cantilever beam (CB) serves as sample stage and spring for sensing the interaction. The tip of the STM is simultaneously used as a force probe and for tunneling. The latter provides a convenient means for adjusting the tip-sample distance and for sensing induced CB vibrations. The CB is coupled to the tunneling tip by the interaction force gradient ∇F_I, which gives rise to shifts of the resonance frequency of the CB. Resonance frequency and force gradient are related as follows:

$$\omega_r \simeq \omega_0 \left(1 + \frac{1}{2} \frac{\nabla F_I}{C} \right) , \tag{11}$$

where ω_0 and C are the resonance frequency and spring constant of the free CB, respectively. The value of ω_r is most effectively measured by using the CB as a mechanical resonator in an oscillator circuit. The oscillation frequency can be measured by any standard technique known from FM radio technology. We used a phase-locked-loop frequency detector for this purpose, since it provides excellent linearity over a wide bandwidth.

Flexible CBs were fabricated from Ir sheet metal approx. 0.05 mm thick. The width and length of the beams were 0.5 mm and 5 mm, respectively. Thus the resonance frequency was typically 1.5 kHz. The spring constant was adjusted by positioning the tip at some fraction ζ from the clamped end of the CB. The resulting effective spring constant scales as $C = \zeta^{-3} C_0$, where $C_0 \simeq 50\ \mathrm{Nm}^{-1}$ is the spring constant at the free

end of the CB. Typical values of ζ were in the range of 0.5 to 0.75, yielding effective spring constants on the order of 400 Nm^{-1} to 100 Nm^{-1}.

The tunneling microscope was mounted in an ultrahigh vacuum (UHV) chamber. Attached to this chamber is a small preparation chamber allowing *in situ* sputtering of the samples. Tunneling tips were made from Ir wire, which was mechanically sharpened. Final tip forming was performed *in situ* by applying a high (100 V) positive potential to the tip for several seconds while tunneling at a constant current of approx. 1 μA. As a result very stable tips were obtained that exhibited neither anomalies of the *I-V* characteristics nor of the barrier height while tunneling on clean metal surfaces.

5. Results and Discussion

We now discuss adhesion results obtained with polycrystalline Ir samples prepared by sputter cleaning the surface of the Ir CB. According to the concepts outlined in Section 2, the interaction-force gradient is expected to be negative and to grow rapidly in magnitude as the point of contact is approached. This behavior is indeed observed. Measured force-gradient characteristics can be interpreted in terms of the universal interaction potential, Eq. (4), using the respective scaling parameters for Ir. Moreover, adhesion and tunneling data are consistent with the notion of a single-atom point contact. A comprehensive description of the experiment is given in [12].

For clean metal surfaces, tip-sample interaction forces are expected to be attractive owing to VdW and short range-adhesion interactions. Since VdW forces are long range, they are relatively insensitive to local (atomic-scale) structural features of the sample [14]. Short-range interactions on the other hand are expected to be extremely surface sensitive, as will be demonstrated in the following example. Figure 4a shows a perspective view of the topography of a representative 100 Å × 100 Å area of the sample. The sputter-cleaned Ir surface exhibits a characteristic microstructure

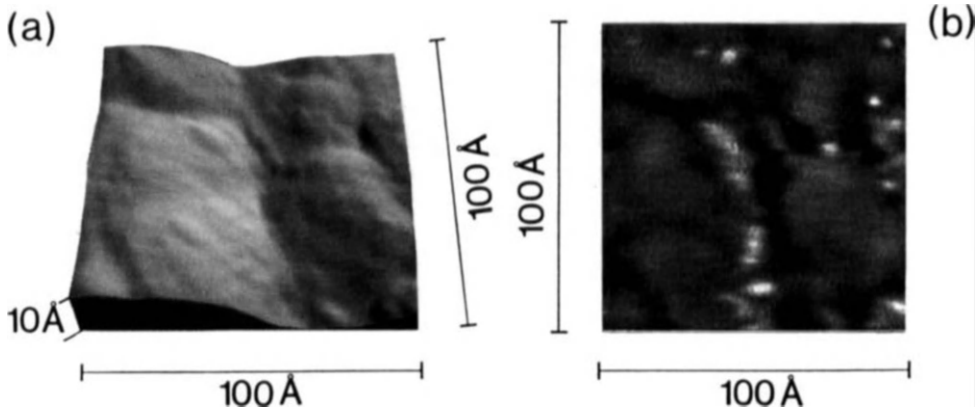

Figure 4. (a) Perspective view of the topography of the sputter-cleaned Ir surface. (b) Interaction-force gradient recorded simultaneously with topography (a); dark and light tones correspond to -8 Nm^{-1} and 0 Nm^{-1}, respectively.

consisting of low, irregularly shaped hills with typical heights and diameters on the order of 5 Å and 30 Å, respectively. Tunneling parameters were $V_T = -20$ mV and $I_T = 2$ nA. The resonance frequency of the CB was measured simultaneously with the topography while raster scanning the surface at a rate of one line per second. The interaction-force gradient shown in Fig. 4b was calculated with Eq. (8). Dark and light shades correspond to $-8\,\mathrm{Nm}^{-1}$ and $0\,\mathrm{Nm}^{-1}$, respectively. The average value of the force gradient is $-3\,\mathrm{Nm}^{-1}$, consistent with metallic-adhesion interaction. However, substantial local variations are also observed. The most striking features are the light spots with lateral dimensions on the order of 5 Å. In accordance with the change of the tip-sample interaction towards weaker adhesion at these sites, we will henceforth also use the term repulsive sites to describe these spots.

Comparing Figs. 4a and 4b, one also recognizes that the adhesive tip-sample interaction is enhanced along trenches formed by adjacent hillocks. The enhancement with respect to the interaction measured on flat areas is typically around 50%. Values as large as 100% can be observed in extreme cases. An example of this is seen close to the center of the image. The area corresponds to a pronounced depression visible in the topographic image. From these observations we conclude that the enhancement is produced mainly by geometry effects, i.e. by the exposure of a larger sample area to the apex of the tip while following V-shaped grooves. The pair potential approach lends itself well to a quantitative analysis of this phenomenon. Investigations are under way, but no definite statements can be made at this point.

The mechanism giving rise to the light spots, i.e. the repulsive sites, on the other hand, must be a different one. Auger analysis revealed that even after extended sputtering of the surface a contamination of carbon (notably being the only one) equivalent to $\simeq 1\%$ of a monolayer persisted. In addition, carbon coverage increased gradually at a rate of 0.2 monolayers per 24 h, if the sample was left in the UHV chamber. We also observed that repulsive sites which did not coincide with pronounced topographic grooves were removed by repetitive scanning of the same sample area. Hence, we are inclined to identify the repulsive sites with adsorbed C atoms. This conjecture is corroborated by complementary observations: Consistent with the Auger results, the density of repulsive sites is substantially higher for samples left in the chamber for an extended period. Furthermore, lateral dimensions of the spots roughly correspond to the size of C atoms observed with STM [20]. By comparing topographic data recorded in subsequent scans, we were able to measure the height contrast created by the adsorbed C atoms. Typical values were on the order of 0.3 Å, which compares favorably with corresponding values reported in [20]. Finally, it is not surprising that adsorbed C atoms are easily removed by the scanning motion of the tip. The bond of atomic C with Ir is not a very strong one, since clusters of monolayer C spontaneously transform into graphite overlayers rather than remaining in the carbidic form [21].

The example presented clearly demonstrates the power of combining interaction force detection and standard tunneling microscopy. The tunneling current is remarkably insensitive to adsorbed atoms or molecules, if there are no states available for resonant tunneling close to the Fermi level. As a result, adsorbed species are difficult to detect if the structure of the substrate surface is not known *a priori* with sufficient accuracy. Interaction forces, on the other hand, can provide a clearly

detectable flag that facilitates identification. However, our present understanding of the physical mechanisms that give rise to the observed interaction contrast is poor. It seems plausible that adsorbed carbon reduces the adhesive tip-sample interaction. Assuming that the atomic electronic states are shifted far away from the Fermi level (which seems to be the case, since only little contrast is observed in tunneling), the adsorbed atom behaves like a closed-shell atom in terms of the interaction with the tip. Hence the atom-induced force on the tip is repulsive because of the increase of the kinetic energy of the conduction electrons due to the Pauli principle.

6. Tip-Sample Interaction and Entropy: Adhesion-Promoted Melting

Short-range adhesion interaction also comes into play in a different context, namely, as the driving force in thermally activated metallurgical processes such as sintering or alloy formation. Here the mutual interaction between surfaces of neighboring grains gives rise to local variations of the surface free energy, which in turn determines the thermodynamics at the interface. Two distinct features make the STM experiments an ideal testing ground for studying related phenomena: First, the interaction can be accurately tuned by proper adjustment of the tunneling gap. Second, experiments are performed on a local scale relating directly to the situation encountered in reality.

We have set up an STM experiment to study metal surfaces close to the melting point. Ga is particularly well suited for this kind of investigation owing to its low melting temperature $T_M = 28.9\,°C$. All low-indexed surfaces were investigated. A rich variety of unexpected phenomena were observed [22], indicating a remarkable stability of the Ga surfaces. One exception, however, is the Ga(111) facet where direct evidence for tip-induced melting was discovered.

First we show a typical image (Fig. 5) of the sputter-cleaned surface. In order to enhance visibility of the steps, the gradient dz/dx is displayed which is computed from

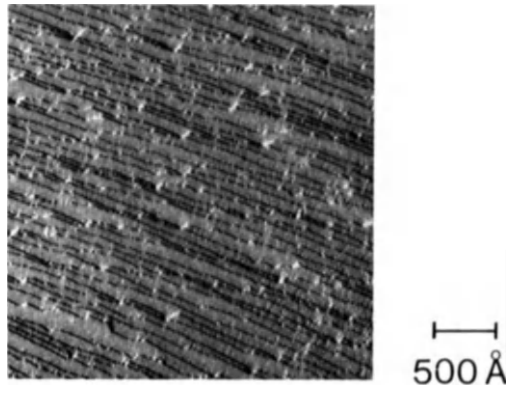

Figure 5. Typical image of the (111) surface (dz/dx displayed). Atomic steps (height $\simeq 3$ Å) preferentially follow the [$\bar{1}$01] direction. The actual step density corresponds to a misalignment of $\simeq 3°$ from the ideal (111) surface.

the measured topography. The crystal was at a temperature of $\simeq 0$ °C and tunneling parameters were $I_T = 0.1$ nA and $V_T = -100$ mV (a negative V_T means tunneling into occupied states of the sample). A large number of mono-atomic steps can be recognized, as a result of the slight misalignment of $\simeq 3°$ from the ideal (111) orientation. The steps are ordered preferentially along the $[\bar{1}01]$ direction.

Gradually the temperature of the crystal was increased. For the settings of the tunneling parameters given above (corresponding to a tunnel resistance $R_T = 10^9\ \Omega$), reproducible images were obtained up to $\simeq 20$ °C. Upon increasing the temperature further, tip-induced surface modifications set in abruptly. However, stable operation of the STM was recovered again by decreasing the tunneling current to 30 pA ($R_T = 3 \times 10^9\ \Omega$). The experiment was repeated several times. It turned out that the critical tunneling resistance R_{crit} at which surface damage set in is clearly correlated with the sample temperature, although a substantial spread was observed. The latter can be attributed to varying experimental conditions due to poor control of the tip geometry. The results are summarized in Table 1, which shows typical values for R_{crit} at three different temperatures corresponding to an undercooling, $\Delta T = T_m - T$, of 30°C, 8°C and 2°C, respectively.

Table 1. Experimental values of the critical tunnel resistance R_{crit} as a function of undercooling ΔT. Tip-induced surface disordering is observed for a tunneling resistance $\lesssim R_{crit}$.

ΔT	30 K	8 K	2 K
R_{crit}	$\lesssim 10^8\ \Omega$	$0.5 \ldots 5 \times 10^9\ \Omega$	$\gtrsim 10^{10}\ \Omega$

For a given tip and sample, temperature switching between destructive and non-destructive imaging was reproducible. An example is shown in Fig. 6 recorded at $\Delta T \simeq 8$ °C. The left panel shows the surface topography of a 1000 Å × 1000 Å area imaged with a tunnel resistance $R_T = 10^9\ \Omega$. The area marked by the box was subsequently raster scanned with R_T decreased by a factor of ten. The right panel shows the deformation induced by the tip (the image was recorded with R_T reset to the initial value). Clearly, the damage extends considerably beyond the area that was raster scanned using the high tunneling current. Another example is shown in Fig. 7. We always observed that a depression was formed by the tip in these experiments. The depth of the depression is on the order of 20 Å to 50 Å. This is distinctively different from the humps produced by literally touching the surface with the tip as has been demonstrated on various metal surfaces. In fact, Taylor-cone-like protrusions can also be created on Ga surfaces in this way.

It is not clear where the material removed from the depression goes since there is no indication that excess material piles up at the borders of the depression. Diffusive material transport along the Ga surface can quite confidently be ruled out, since no surface diffusion was observed on Ga even a few tenths of a degree below melting [22]. Most likely, the excess material was picked up by the tip itself.

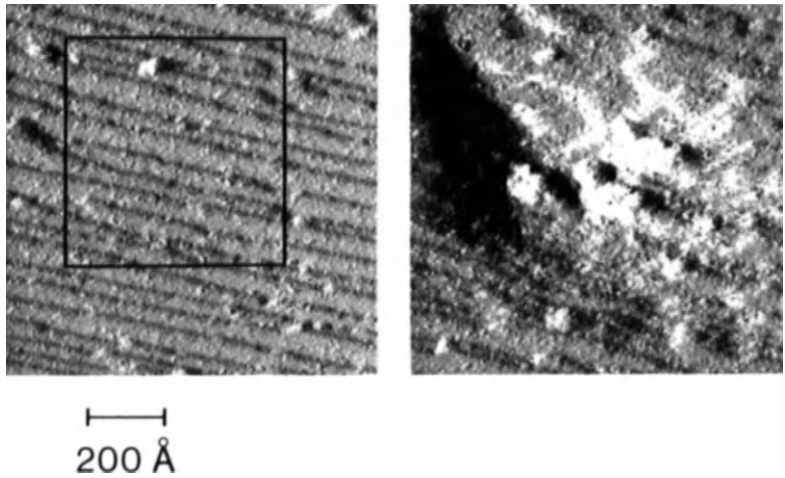

Figure 6. **Left panel:** Gradient image dz/dx of a 1000 Å × 1000 Å area of the sputter-cleaned Ga(111) surface showing mono-atomic steps. Tunneling parameters are $I_T = 0.1$ nA and $V_T = -100$ mV. Sample temperature is 20 °C. **Right panel:** Depression induced by scanning the area marked by the box in the left panel at a tunneling current of 1 nA. After scanning the image was recorded using the same tunneling parameters as for the left panel. The depth of the depression is ≃20 Å.

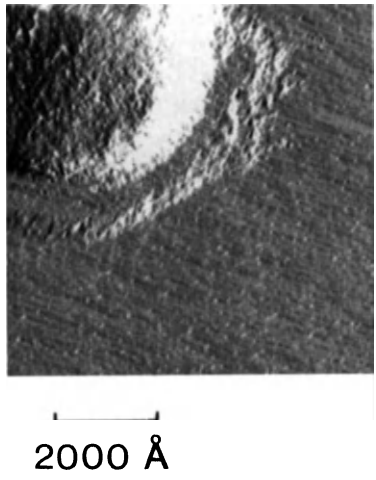

Figure 7. Large-scale image, 7400 Å × 7400 Å, of the Ga(111) surface showing a tip-induced indentation produced in the same way as described in Fig. 6.

The temperature dependence of the observed tip-induced surface damage is a clear indication for a thermodynamic process. In addition the tip-sample interaction plays a subtle role. Tip-induced damage under similar conditions has been observed on those layered materials that also are rather poor conductors, making it very likely that the tunneling tip is actually pressing onto the sample surface. With Ga the situation is different, since its specific resistivity is comparable to that of platinum. We would also like to point out that all the other Ga surfaces could be imaged without difficulty up to the bulk melting point. From this, two conclusions can be drawn: First, the tip is not making mechanical contact at the tunneling conditions used in the experiment. Second, it is unlikely that the (negative) pressure exerted on the sample by the tip is lowering the local ***bulk*** melting temperature (according to the Clausius-Clapeyron equation) sufficiently to produce the observed effect. In fact, the density of liquid Ga is higher than that of the crystal. Hence, a negative pressure would actually cause an increase of the melting temperature. Therefore, we are inclined to interpret the local surface modifications in terms of a tip-induced local ***surface*** melting.

Surface melting is normally discussed in the context of crystal surfaces in contact with vacuum. A prerequisite for the phenomenon is that the liquid phase is wetting the bulk surface, i.e. that the excess surface free energy is positive [23]:

$$\Delta\gamma = \gamma_{SV} - \gamma_{SL} - \gamma_{LV} > 0 \quad . \tag{12}$$

The parameters γ_{SV}, γ_{SL} and γ_{LV} denote the solid-vapor, solid-liquid and liquid-vapor surface free energies. High values of γ_{SV} are normally found in metals for open surfaces which at the same time must be very pure, since by definition any adsorbates will lower the surface energy. The most prominent examples exhibiting surface melting are the Pb(110) and Al(110) facets [24].

In an STM experiment, the excess surface energy is modulated locally by the tip. Correspondingly, the terms γ_{SV} and γ_{LV} must be replaced by the solid-tip, $\gamma_{ST}(s)$, and liquid-tip, $\gamma_{LT}(s)$, free energies, which depend explicitly on the tip-sample distance s. The value of $\Delta\gamma(s)$ is determined by the detailed energetics at the surface. Let us assume that the free surface does not melt, but that at some tip-sample distance s_0 the excess surface energy turns positive. According to mean-field theory [25], a liquid-like layer will grow whose thickness d is proportional to

$$d \propto \ln \frac{\Delta\gamma(s)}{\Delta T} \quad . \tag{13}$$

Disordering sets in if d is on the order of one atomic layer. According to the concepts of short-range adhesion, we may assume that $\Delta\gamma(s) \propto e^{-\kappa_{ad}s}$ increases roughly exponentially with decreasing width s of the tunneling gap. The tunnel resistance $R_T \propto e^{\kappa_T s}$, on the other hand, drops off exponentially with decreasing gap width. Hence, the model predicts that the critical resistance, R_{crit}, and undercooling ΔT are related according to the power law

$$R_{crit} \propto \Delta T^{-\nu}, \tag{14a}$$

with an exponent

$$\nu = \kappa_T/\kappa_{ad}, \tag{14b}$$

equal to the ratio of the inverse decay lengths for tunneling, κ_T and for the short-range adhesion interaction, κ_{ad}. Using $\kappa_T \simeq 1\ \text{Å}^{-1}\ \text{eV}^{-1/2}\sqrt{\Phi}$ and $\kappa_{ad} \simeq 1/l_{TF}$, where Φ and l_{TF} denote the work function and Thomas-Fermi screening length, respectively, the theory of simple metals [26] predicts $1.3 \lesssim \nu \lesssim 1.7$.

From the experimental data, we find that R_{crit} increases roughly by an order of magnitude upon decreasing ΔT by a factor of four, whence $\nu_{exp} \simeq 1.6$ is obtained — in good agreement with the above prediction.

Note that one cannot unambiguously infer from our experimental evidence whether the top-most layer of the Ga is indeed melting in the sense of forming a bulk liquid-like layer. This is, however, not the issue here. Important is that the thermodynamics at a surface can be dramatically influenced on a local scale and that the resulting disordering effects, be it melting or roughening, can be studied *in situ*. Another question remains to be answered, namely, what makes the Ga(111) surface so different from the others? At present we cannot even suggest preliminary arguments, as little is known about either the electronic or the atomic structure of Ga. A peculiarity of Ga is that the crystal consists of covalently bonded dimer molecules that definitely have a substantial effect on the surface energetics. Related theoretical investigations are currently under way [27]. On the experimental side, detailed studies of the adhesive properties would almost certainly provide valuable information. Unfortunately, experiments are difficult to perform, and we do not have conclusive data at present.

ACKNOWLEDGMENTS

The authors wish to thank D. Pohl, S. Ciraci and A. Baratoff for stimulating discussions. We would also like to thank U. Maier for invaluable technical assistance and A. Stalder for his contributions to the development of the data acquisition software.

REFERENCES

[1] See e.g.: Israelachvili, J.N. (1985) *Intermolecular and Surface Forces*, Academic Press, London.
[2] Eigler, D.M., Lutz, C.P. and Rudge, W.E. (1991) Nature **352**, 600.
[3] Lifshitz, E.M. (1956) Soviet Phys. JETP **2**, 73.
[4] Krupp, H. (1967) Adv. Colloid Interface Sci., **1**, 139.
[5] Heinrichs, J. (1973) Solid State Comm. **13**, 1595; Inglesfield, J.E. and Wikborg, E. (1975) J. Phys. F: Metal Phys., **5**, 1475.
[6] Ferrante, J. and Smith, J.R. (1973) Surf. Sci. **38**, 77; Kobelev, A.V., Kobeleva, R.M. and Ukhov, V.F. (1979) Phys. Status Solidi B **96**, 169; Das, M.P. and Nafari, N. (1986) Solid State Comm. **58**, 29.
[7] Vannimenus, J. and Budd, H.F. (1975) Solid State Comm. **17**, 1291.

[8] Rose, J.H., Ferrante J., and Smith, J.R. (1981) Phys. Rev. Lett. **47**, 675; *idem* (1985) Phys. Rev. B **31**, 3427.
[9] Ciraci, S., Baratoff, A. and Batra, I.P. (1990) Phys. Rev. B **41**, 2763; *ibid.* **42**, 7618.
[10] Rose, J.H., Ferrante, J. and Smith, J.R. (1983) Phys. Rev. B **28**, 1835.
[11] Inglesfield, J.E. (1976) J. Phys. F: Metal Phys. **6**, 687.
[12] Dürig, U., Züger, O. and Pohl, D.W. (1990) Phys. Rev. Lett. **65**, 349.
[13] see Ref. 1, p. 130.
[14] Hartman, U., (1991) Phys. Rev. B **43**, 2404.
[15] Goodman, F. and Garcia, N. (1991) Phys. Rev. B **43**, 4728.
[16] Fischer, U.Ch. and Pohl, D.W. (1989) Phys. Rev. Lett. **62**, 458.
[17] Berndt, R. and Gimzewski, J.K. (1991) Phys. Rev. Lett. **67**, 3796.
[18] Ciraci, S., Tekman, E., Gökçedag, M., Batra, I.P. and Baratoff. A. (1992) Ultramicroscopy **42-44**, 163.
[19] Dürig, U., Züger, O. and Stalder, A. (1992) J. Appl. Phys. (to appear Sept. 1992).
[20] Brune, H., Wintterlin, J., Ertl, G. and Behm, R.J. (1990) Europhys. Lett. **13**, 123.
[21] Kholin, N.A., Rut'kov, E.V. and Tontegode, A.Y. (1984) Surf. Sci. **139**, 155.
[22] Züger, O. and Dürig, U. (1992) Ultramicroscopy **42-44**, 520; Züger, O. (1992) PhD Thesis, Swiss Federal Institute of Technology, ETH No. 9658, to be published.
[23] For a review see, e.g., Dash, J.G. (1989) Contemporary Physics **30**, 89.
[24] Frenken, J.W.M., Mareé, P.M. and van der Veen, J.F. (1986) Phys. Rev. B **34**, 7506; van der Gon, A.W.D., Smith, R.J., Gay, J.M., O'Connor, D.J. and van der Veen, J.F. (1990) Surf. Sci. **227**, 143.
[25] Lipowsky, R. and Speth, W. (1983) Phys. Rev. B **28**, 3983; Trayanov, A. and Tosatti, E. (1988) Phys. Rev. B **38**, 6961.
[26] Lang, N.D. and Kohn, W. (1970) Phys. Rev. B **1**, 4555.
[27] Tosatti, E.: private communication.

LOCAL MODIFICATION OF LANGMUIR-BLODGETT FILMS BY ATOMIC FORCE MICROSCOPY

L. F. CHI and H. FUCHS
BASF AG, ZKM/T-J543
D-W-6700 Ludwigshafen
Germany

ABSTRACT. Atomic force microscopy was used to modify locally differing types of Langmuir-Blodgett films. Depending on the interactions between the film and the solid support, as well as between the force sensor and the film surface, thin organic films were locally and irreversibly degraded during scanning. By using this process, defined patterns of a tenth of a micrometer to a few nanometers in size were written into the films. This method was also used to test the binding strength of different types of interfaces of multilayer films. Such experiments are relevant for the understanding of adhesive phenomena in organic compounds as well as adhesive and cohesive delamination phenomena.

1. Introduction

With the advent of the atomic force microscope (AFM) (1) an instrument became available for investigating a variety of insulating organic surfaces, including biological matter such as nucleic acids (2), proteins (3-5), cell surfaces (6-7), and Langmuir-Blodgett (LB) films (8-11). A strong adhesion force between the probed molecules and the substrate is required to allow nondestructive imaging. The force between the AFM tip and the sample surface should be minimized. Calculations indicate that the operating force to study biological samples should not exceed 10^{-11} N (12). Forces of the order of 10^{-8} N can lead to an irreversible damage of the surface (13). On the other hand, efforts have been made by several groups to use the deformation effects to modify organic surfaces locally and to write predefined patterns (14-16). The mechanisms involved allow a better understanding of cohesive and adhesive delamination phenomena.

Here we present the results of local modifications with an AFM tip on differing types of LB films. The advantage of using LB films for this type of study is that the interface parameters can be easily changed by choosing different substrate and amphiphilic molecules to build up mono- or multilayer assemblies. Further more, measurement of the local viscoelastic properties of thin organic films is also of interest for their potential applications.

2. Experiments

The materials used to prepare LB films were obtained from the following sources: arachidic acid (C_{20}) was purchased from Fluka ™ and eicoseneimine ($C_{20}NH_2$) was obtained from Prof.

V.T. Binh et al. (eds.),
Nanosources and Manipulation of Atoms Under High Fields and Temperatures: Applications, 287–292.
© 1993 *Kluwer Academic Publishers.*

Möbius, MPI Göttingen. The spreading solution used was chloroform (HPLC quality, Baker TM). All materials were used without further purification.

The LB films were prepared on a KSV alternating trough TM in a clean room under class 10 conditions. Deionized water from a Christ system TM (19MΩ) was used to prepare the aqueous subphase. Mica, cleaved with Scotch TM - tape shortly before the film deposition, was used as a substrate material for LB films. A transfer speed of 3-5mm/min was used for film deposition. The transfer ratio was between 0.95 and 1 for all the experiments.

AFM imaging was carried out in air with a commercial system (Park Scientific Instruments TM) located in the same clean room as the LB trough. The constant force mode was chosen for all the images. Two kinds of cantilevers with integrated pyramidal tips, exhibiting nominal spring constants of 0.032 N/m and 0.064 N/m, respectively, were used for all the experiments.

3. Results and Discussions

3.1. MONOLAYER FILMS

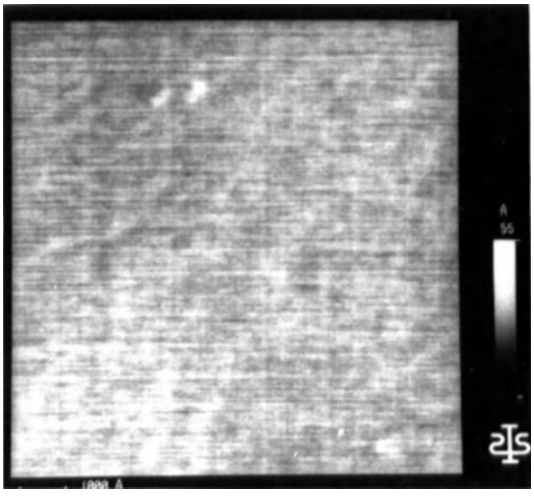

Figure 1. AFM image of a monolayer C_{20} LB film deposited on mica.

LB films of arachidic acid transferred onto mica substrates are homogeneous with a very low defect density, as shown in Fig. 1. During AFM imaging a strong tip-film interaction on this system was observed and the film could be easily degraded even with a low force loading (16). In this way controlled patterns could be written in this system. Fig. 2a shows a rectangular window measuring 300x500 nm^2, which was written with a soft cantilever (0.032 N/m) under a force loading of 1 nN. The window area was previously scanned only once. The zoom-out image was taken at the same force loading (1 nN). The rectangular hole structure was measured to be 16 to 20 Å in depth with respect to the surrounding intact film parts, which is less than the thickness of this film (27 Å). No protruding rim was observed around the window. By scanning smaller areas, again with the same force loading, holes could be made as shown in Fig. 2b. These holes measured 27 Å in depth. In the above images the scanning rate was kept constant (1 Hz), resulting in different absolute scanning speeds. For a constant scanning speed of 2 μm/s over an area of 500x500 nm^2, scanning windows were observed, while over an area of 2000x2000 nm^2 no film degradation was seen.

The mechanism for this type of degradation is not yet well understood. It is likely that the AFM tip deforms the film such that most C_{20} molecules are pushed aside, probably due to the low interaction strength of C_{20} molecules with the mica surface. At high magnification, rather than low magnification, the deformation energy of the moving tip was dissipated into a smaller area and resulted in the film degradation. Since no rim is observed, the molecules from the defect area are either migrating into voids of the intact film or are contaminating the tip.

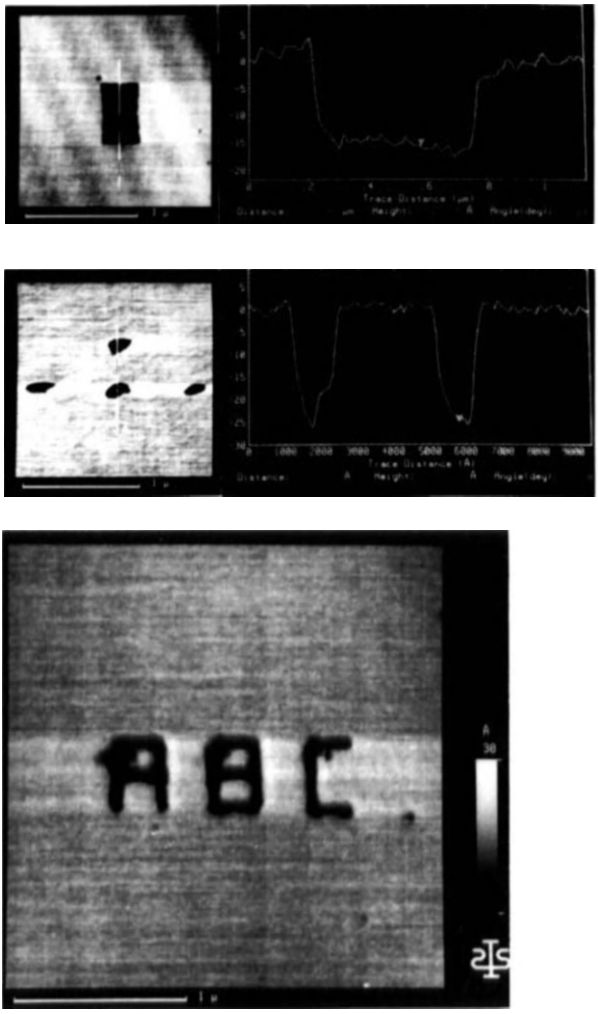

Figure 2. Patterns written into an LB film shown in Fig. 1: a) a scanning window; b) four holes and c) characters. The window and the holes were written by previously scanning the area once with the same force loading as for image a) and b). The cross in a) and b) indicate the location where the height was measured.

By carefully controlling the AFM tip, small structures on the nanometer scale could be written into monolayer films of C_{20} deposited on mica. The scanning area could be set to zero and the AFM tip manually moved via a DC offset voltage. Characters could then be written as shown in Fig. 2c. The width of the finest lines we were able to achieve measured 20 nm using standard pyramidal tips.

The generation of structures in LB films strongly depends on the adhesion force between the sample molecules and the solid substrate. When $C_{20}NH_2$ was deposited instead of C_{20} on the mica, no patterns could be written even with a higher force loading (100 nN). In this case, the binding strength must be increased due to the attractive forces between the $-NH_3^+$ groups and the SiO_3^- groups at the mica surface.

3.2. MULTILAYER SYSTEMS

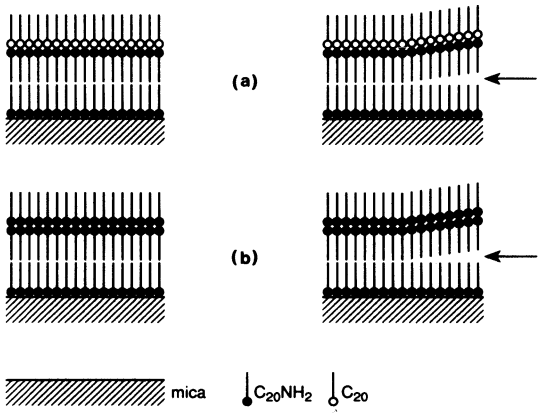

Figure 3. Scheme of different multilayer films on mica (left) and the positions where the delamination occurred (right).

To obtain a strong adhesion between the film and the substrate, $C_{20}NH_2$ was used to prepare the first layer of an LB film on a mica surface. Multilayer systems were built in the way as schematically shown in Fig. 3 (left). Fig. 3a illustrates $C_{20}NH_2$ for the second layer and C_{20} for the third layer, while Fig. 3b shows $C_{20}NH_2$ for both the second and third layers. Cantilevers with a spring constant of 0.064 N/m were used to create structures in these systems. In the first case (Fig. 3a) a force loading of 5 nN was required to create a window of the size 500x500 nm^2, as shown in Fig. 4a.

The window is measured to be 50 Å in depth, which is within 10% of the thickness of a bilayer (54 Å). Note that the molecules were removed in a bilayer formation, as shown in Fig. 3a (right). This indicates that the interaction between the head groups in the adjacent layers (COO^-,$-NH_3^+$) is stronger than that between the methyl groups at the hydrophobic interface. This process is also favored energetically. If only a monolayer is pulled up, the adjacent layer will face toward the air with the hydrophilic head group and the whole system will then become unstable. In the second case (Fig. 3b), the binding strength at the hydrophilic interface between the third and second layers should be weaker as compared to the first case because of the identical headgroups ($-NH_2$,$-NH_2$). Again, however, the depth of structures written was 54 Å, corresponding to the thickness of a bilayer as shown in Fig. 4b.

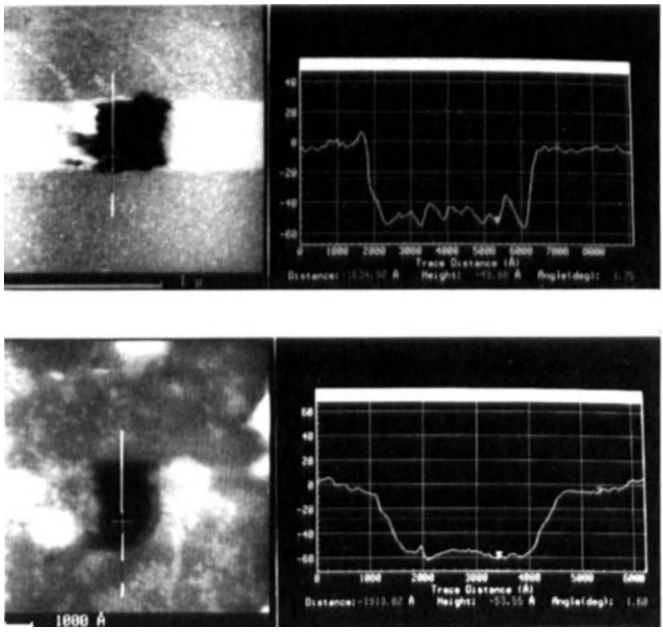

Figure 4. Patterns written in multilayer LB films: a) two layers of $C_{20}NH_2$ and one layer of C_{20} deposited on mica and b) three layers of $C_{20}NH_2$ deposited on mica. In both cases the patterns are about 50 Å in depth, corresponding to the thickness of a bilayer within an accuracy of 10%.

This degradation indicates a hierarchical strength and delamination process in multilayer LB films. Adhesive delamination occurs in the interface with the weaker binding strength. These results indicate that the NH_2-COOH and NH_2-NH_2 interfaces adhere more strongly than the interface between the hydrophobic methyl endgroups.

4. Conclusions

The force between the AFM tip and thin organic films can be used to locally create stable structures. The creation of structures in LB films will depend on the interaction between the tip and the organic molecules and on the adhesion force between organic molecules and the solid substrate. In multilayer systems the structures will be preferentially created with the depth of a bilayer, rather than that of a monolayer.

ACKNOWLEDGMENT. This work were supported by the Federal Ministry of Research and Development under grant of No. 03M4060A0.

References

1. Binnig, G, Quate, C.F. and Gerber, Ch. (1986) 'Atomic force microscope', Phys. Rev. Lett. 56, 930-933.

2. Hansma, P. K., Elings, V. B., Marti, O., Bracker, C.E., (1988) 'Scanning tunneling microscopy and atomic force microscopy: application to biology and technology', Science, 242, 209-216.

3. Drake, B., Prater, C. B., Weisenhorn, A. L., Could, S. A. C., Albrecht, T. R., Quate, C. F., Cannell, D. S., Hansma H. G. and Hansma, P. K. (1989) 'Imaging crystals, polymers, and processes in water with atomic force microscope', Science, 243, 1586-1589.

4. Egger, M., Ohnesorge, F., Weisenhorn, A. L., Heyn, S. P., Drake, B., Prater, C. B., Could, S. A. C., Hansma P. K. and Gaub, H. E. (1990) 'Wet lipid-protein membranes imaged at submolecular resolution by atomic force microscopy', J. Struct. Biol. 103, 89-94.

5. Lin, J. N., Drake, B., Lea, A. S., Hansma, P. K. and Andrade, J. D. (1990) 'Direct observation of immunoglobulin adsorption dynamics using the atomic force microscope', Langmuir, 6, 509.

6. Butt, H.-J., Prater, C. B. and Hansma, P. K. (1991) 'Imaging purple membranes dry and in water with the atomic force microscope', J. Vac. Sci. Technol. B, 9, 1193-1196.

7. Häberle, W., Hörber, J. K. H. and Binnig, G. (1991) 'Force microscopy on living cells', J. Vac. Sci. Technol. B, 1210-1213.

8. Mayer, E., Howald, L., Overney, R. M., Heinzelmann, H., Frommer, J., Güntherodt, H. -J., Wegner, T., Schier, H. and Roth, S. (1991) 'Molecular-resolution images of Langmuir-Blodgett films using atomic force microscopy', Nature, 349, 398-400.

9. Lea, A. S., Pungor, A., Hlady, V., Andrade, J. D., Herron, J. N. and Voss, E. W. Jr. (1992) 'Manipulation of proteins on mica by atomic force microscopy', Langmuir, 8, 68-73.

10. Fuchs, H, Chi, L. F., Eng L. M. and Graf, K (1992) 'Defect structures of Langmuir-Blodgett films investigated by scanning force microscopy', Thin Solid Films, 210/211, 655- 658.

11. Garnaes, J., Schwartz, D. K., Viswanathan R. and Zasadzinski, J. A. N. (1992) 'Domain boundaries and buckling superstructures in Langmuir Blodgett films', Nature, 357, 54-57.

12. Persson, B. P. (1987) 'The atomic force microscope: can it be used to study biological molecules?', Chem. Phys. Lett., 141, 366-368.

13. Abraham F. F. and I. P. S. Batra, I. P. S. (1989) 'Theoretical interpretation of atomic force microscope images of graphite', Surface Sci. 209, L125-L132.

14. Hamada, E. and Kaneko, R. (1992) 'Micro-tribological evaluations of polymer surface by atomic force microscopes', Ultramicroscopy 42/44, 184-190.

15. Leung, On Man and Goh, M. Cynthia (1992) 'Orientational ordering of polymers by atomic force microscope tip-surface interaction', Science, 255, 64-66.

16. Chi, L. F., Eng, L. M., Graf, K and Fuchs, H. (1992) 'Structure and stability of Langmuir-Blodgett films investigated by scanning force microscopy' Langmuir, 8, 2255-2261.

Layered Semiconductors as Materials for (Sub)Nanometer Scale Surface Modification with the STM

H. Fuchs[#], Th. Schimmel[+], S. Akari[*], L. M. Eng[@], M. Anders, M. Lux-Steiner[*] and K. Dransfeld[*]

BASF Aktiengesellschaft, Polymer Research Laboratory, ZKM/T - J 543, W-6700 Ludwigshafen, Germany
[#]Universität Münster, Physikal. Institut, W-4400 Münster, Germany
[+]Universität Bayreuth, Experimentalphysik VI, W-8580 Bayreuth
[*]Universität Konstanz, Fakultät für Physik, W-7750 Konstanz
[@]ETH Zürich, Inst. of Quant. El., CH-8093 Zürich, Switzerland

Abstract

The local surface modifaction of layered dichalcogenides with the tip of an STM results in a novel class of (sub-)nanometer structures. Time-stable as well as spontaneously growing highly symmetric structures can be generated. In the case of tungsten diselenide (WSe_2) the orientation of the structures is strongly related to that of the trigonal lattice of the layered compounds (coherent structures). In contrast, irregular growing structures can be observed on $TaSe_2$. As compared to any other materials reported so far, these layered compounds allow the generation of a remarkable variety of nanometer structures both by tip indentation and by voltage pulsing techniques.

1. Introduction

A variety of novel physical aspects is peculiar to nanometer scale and atomic scale structures which cannot be simply extrapolated from the properties of macroscopic assemblies of the same material. Examples are local electronic properties, local chemical reactivities and the thermodynamic behaviour. In order to investigate these properties of well defined individual nanometer structures rather than averaging over a macroscopic ensemble of them, local techniques are required allowing to generate and to investigate these structures. The invention of near-field scanned probe techniques such as the scanning tunneling microscope (STM) and the scanning force microscope (SFM) made available tools for the direct modification of surfaces and the controlled pattern generation on an unprecedentedly small scale. In addition, these methods allow the

V.T. Binh et al. (eds.),
Nanosources and Manipulation of Atoms Under High Fields and Temperatures: Applications, 293–309.
© 1993 *Kluwer Academic Publishers.*

imaging of the generated structures with the same tip immediately after the modification process and the investigation of their local electronic properties even at the atomic scale.

The different approaches to modify solid surfaces with scanned probe tips. can be classified into two categories.

One strategy to generate nanometer structures with the STM is the local modification of foreign material deposited on substrates and the local deposition of foreign material from the tip to the surface. For example, thin resist layers were structured using the tip of an STM as an electron source [1]. On the atomic scale, atoms adsorbed on well defined surfaces could be rearranged using the STM tip as a nano-tool. The latter experiment requires special environmental conditions such as UHV and low temperatures (4K) [2]. Recently, laser assisted deposition techniques were reported [3].

The other strategy makes use of a direct modification of a free surface. This can be done by mechanical indentation of the STM tip [4], by voltage pulsing [5], by local melting of the surface in the presence of a high electrical field ('taylor cones') [6] or by reactive etching [7]. Most of the previous experiments on free surfaces resulted in a local destruction of the surface, i.e. disruption of the lattice structure within the modified area.

Recently, we reported STM experiments on free surfaces of the dichalocogenide tungsten diselenide (WSe_2) which demonstrated local surface modification on a nanometer scale using different techniques based on mechanical indentation [8] and voltage pulsing [9-11]. All structures have in common that they are in registry with the atomic lattice of the surface. Different types of structures, however, differ with respect to their stabilility. The structures of one class remained stable during the observation period and showed a preserved atomic order within the modified areas of the surface [9, 10] whereas the second class consists of highly symmetric structures of a triangular shape which continuously grow after generation [11]. Concerning the variety of structures which can be generated with the STM on WSe_2, the material is unique as compared to any other material investigated so far.

Here we summarize the various types of nanometer structures and atomic structures generated on dichalcogenides and their properties. The the time dependent behaviour of single atom structures will be addressed.

2. Experimental

Four different STMs were used for our experiment. One is a combined SEM/STM [12] and is equipped with a tripod scanner. The other three instruments are based on tube scanners and are operated either in air or under ultra high vacuum. For the experiments,

both mechanically cut Pt/Ir (80/20) tips and electrochemically etched tungsten tips were used. Only in the case of the triangular structures described in section 4.5 gold tips were used. All images shown in this article represent unfiltered original data and are given in a linear grey scale, increasing brightness corresponding to an increase in the apparent height. The images of Figs. 1b-7 were taken in the constant heigth mode, those of Figs. 8 - 10 were taken in the constant current mode. P-doped crystals of 2H-WSe_2 as well as samples of 1T-$TaSe_2$ were used for our experiments. The samples were grown by the vapor phase transport technique [13, 14]. Freshly-prepared surfaces were obtained by cleaving the samples parallel to the (0001) plane of the crystal lattice.

3. Unmodified Surfaces

The layered dichalcogenides WSe_2 and $TaSe_2$ form sandwich structures of the sequence Se-Me-Se - Se-Me-Se, (here: Me = W,Ta), the layers showing a trigonal symmetry (Fig. 1a). The chalcogenide atoms are threefold coordinated to the metal atoms while the metal atoms have a sixfold coordination. This results in a strong chemical bonding within the sandwich layers whereas different layers interact via van der Waals forces only. Thus, the samples can be easily cleaved parallel to the basal planes of the material. Most of the WSe_2 samples exhibit large well ordered, defect free areas. An example of a high resolution STM image is shown in Fig. 1b.

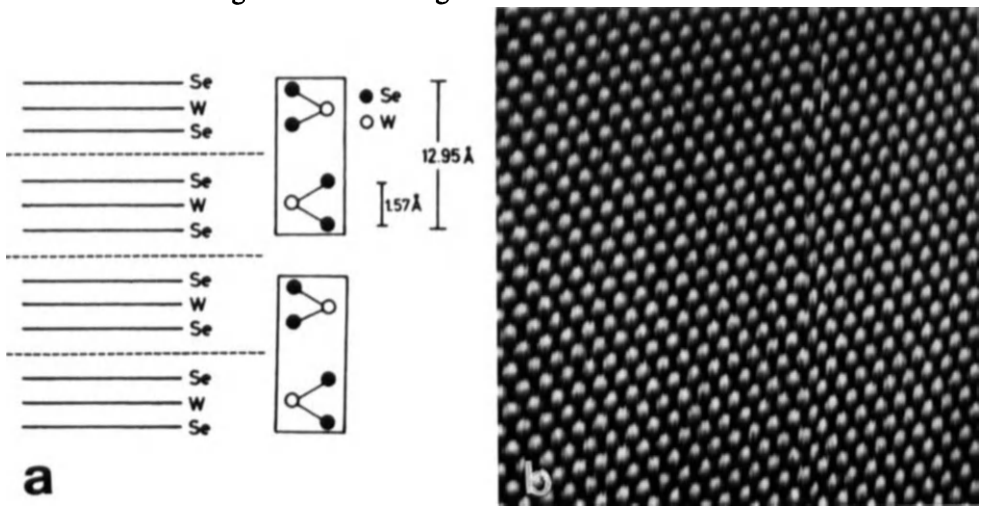

Fig. 1: a) Scheme of the layered structure of WSe_2 (from Ref. [15]). The material consists of sandwich layers of the sequence Se-W-Se. Within each sandwich layer, the atoms are connected by covalent bonds while different layers stick together by van der Waals interaction. In WSe_2, the space group is $P6_3/mmc$, the interatomic distance within a plane is 0.328 nm. b) Atomically resolved STM image of an as-prepared WSe_2 surface. The interatomic distance is 0.33 nm. Image size: 7.5 nm x 7.5 nm.

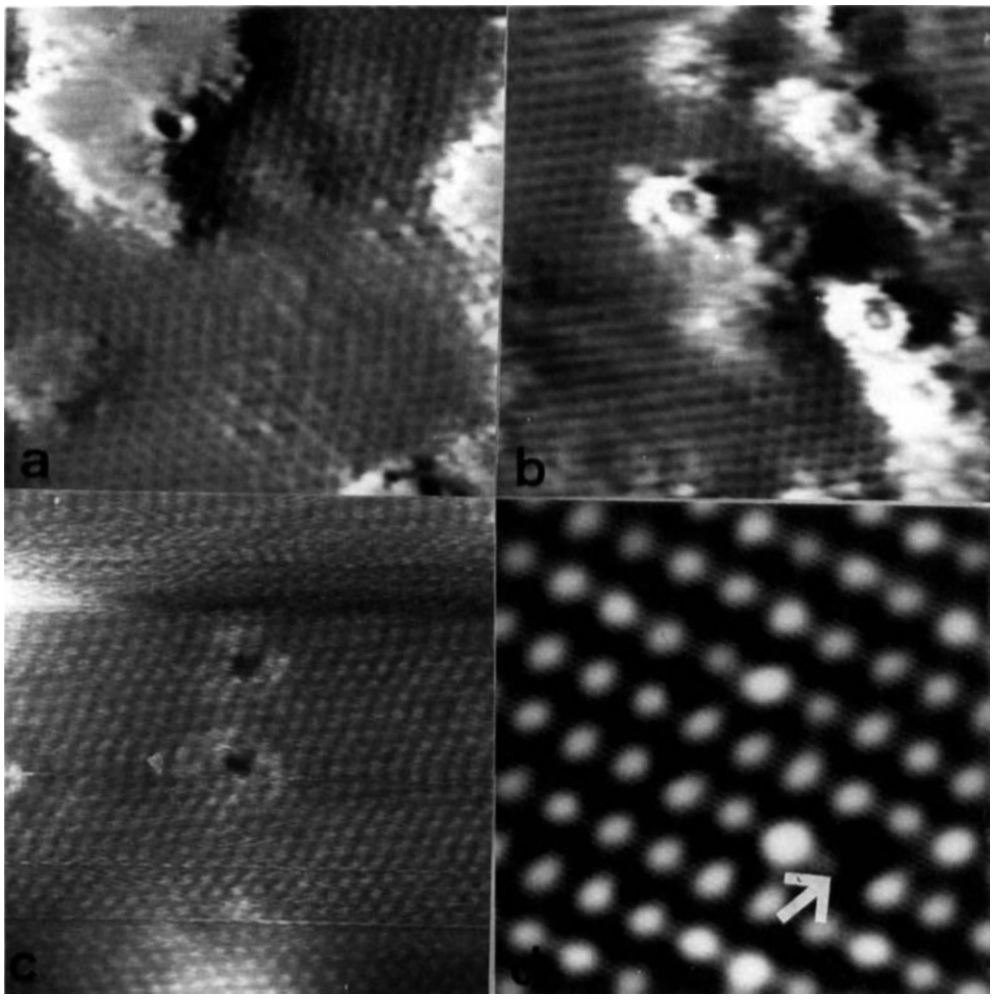

Fig. 2: Intrinsic lattice defects observed on WSe_2. a,b) Amorphous island structures on an atomically resolved lattice showing locally a 3 x 3 superstructure (image sizes: 8 nm x 8 nm and 9 nm x 9 nm, respectively); c) bright ring-like defects with missing central atom (image size: 8 nm x 8 nm); d) point defect (see arrow; image size: 3 nm x 3 nm).

Band structure calculations for WSe_2 [16] indicate that the lower band edge of the conductivity band originates from unoccupied dz^2 states of the tungsten atoms. On the other hand, these caluclations also indicate that the valence band edge is formed by occupied dz^2 states. Thus, depending on the tip bias, tunneling should either occur into unoccupied states (negative tip bias) or from occupied states (positive tip bias) of the

tungsten dz^2 states. However, the influence of the tunneling tip is not considered in these calculations. Thus, the interaction with the tip might result in hybrid states making also the selenium positions visible. In fact, in some experiments there are indications that both types of atoms were observed [15].

Some of the samples investigated showed intrinsic surface defects on a widely differing length scale (Fig. 2) and were therefore discarded. Figs. 2a and 2b show extended island structures on the atomically resolved WSe_2 lattice. The nature of these islands is not clear. No internal structure could be resolved within these areas. They possibly consist of an amorphous contamination layer. The atomically resolved lattice in between shows at some spots a 3 x 3 superstructure.

Another type of intrinsic surface defect is shown in Fig. 2c. Small circular defects occur at some positions with a diameter of less than 1 nm. In the center of the bright rim consisting of six atoms, an individual atom is missing. The smallest intrinsic defects observed are point defects as shown in Fig. 2d. In this case, an individual lattice site exhibits an increased apparent height while a neighbouring atomic position appears to be vacant (see arrow).

4. Surface Modification by STM

Before surface modification, the samples were investigated with atomic resolution and intact areas such as shown in Fig. 1b were selected for performing the modification experiments. Imaging was done at a tip bias of 0.7 to 0.9 V (tip positive) and a tunneling current of 3 nA for the WSe_2 surfaces. In the case of the $TaSe_2$ surfaces a bias of about 60 mV and 130 mV (tip positive) and a tunneling current of about 6 nA were used.

4.1. MECHANICAL INDENTATION EXPERIMENTS

Stable surface modifications on the nanometer scale on WSe_2 can be generated by mechanical tip indentation. Tip excursions of up to several tens of nanometers result in time stable depressions on the sample surface with diameters of typically 3 to 6 nm and a depth of about 0.1 to 0.3 nm. The mechanical deformation process can be performed both in air and under UHV conditions. The resulting structures (Fig. 3a) remained stable in air during the observation time of up to two days. The resulting structures can be resolved atomically with the same tip as used for their generation. The STM images show a preserved atomic order of the lattice even within the deformed surface areas. No microscopic defects are found on the surface which might help to stabilize the deformations. Moreover, most of the depressions are surrounded by a protruding rim which might indicate a transport of material below the surface as the origin of the plastic deformation.

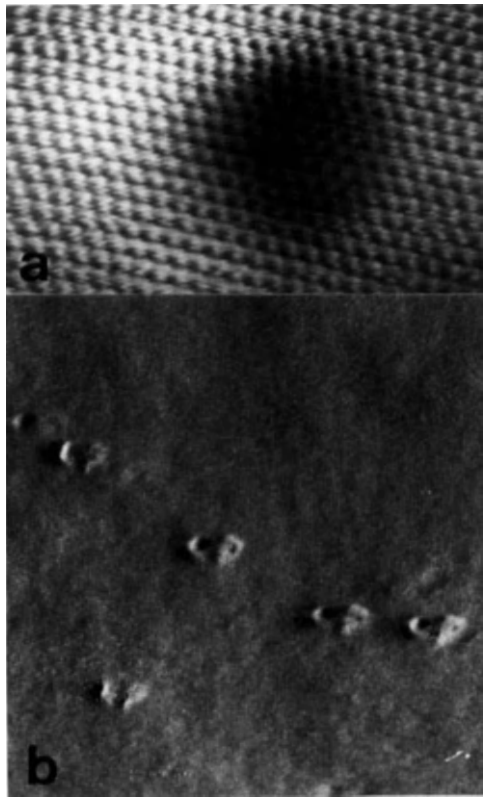

Fig. 3: Nanometer structures induced with the tip of the STM at predefined positions by mechanical indentation. a) Atomically resolved image of a smooth circular indentation induced with an electrochemically etched W tip (image size: 8 nm x 4.5 nm, diameter of the structure: approx. 4 nm). b) Indentation structures generated with a mechanically cut PtIr tip. The structures represent replica of the tip apex (image size: 50 nm x 50 nm, diameter of the structures approx. 5 nm).

The writing mechanism is most likely to be a mechanical deformation of the surface with the STM tip. This is also supported by the fact that no electrical pulses are present during the modification process and that, as a function of the tip excursion, an elastic regime (for excursions below about 10 nm) is followed by a plastic regime (for larger excursions). In addition, the shape of the indentation structures depends on the shape of the tip apex. While electrochemically etched tungsten tips always yield smooth, circular depressions, mechanically cut PtIr tips generate irregular depressions, each tip yielding a characteristic shape of the resulting structure (Fig. 3b). In this way replica of the tip apex can be obtained on a nanometer scale (spatial resolution: 1nm). This also indicates that no material transport occurs from the tip to the surface or vice versa during the

indentation process and that the deformation process is similar to a plastic deformation on a macroscopic scale.

Further experiments in combination with computer simulations [17] showed that the atomic periodicity of the STM images within the modified areas is not originating from imaging artefacts such as Moiré pattern formation. The fact that atomic resolution of the complete structures is easily obtained might be connected with the preserved atomic order of the lattice within the modified surface areas. In this way, the electronic band structure is probably not severely disturbed locally, and the modified areas can be imaged with the same tunneling voltage as the intact areas.

4.2. LOCAL SURFACE DEFORMATION BY VOLTAGE PULSING

A different technique for the generation of structures on the nanometer scale on WSe_2 samples is to apply a transient electrical field between the STM tip and the sample surface. To modify the surface, voltage pulses between 2 and 5 V (tip positive) are added to the tunneling voltage for a period of several milliseconds. As a result, structures are generated whose size and character depend on the pulse amplitude, but not on the shape of the tip apex or on the tip material.

For pulses between 2.7 and 3.5 V structures between 2 and 4 nm in diameter are found which have the shape of circular hillocks, the diameters of the structures increasing monotonically with the pulse amplitude. For larger pulse amplitudes (about 6 V), ring-like structures with diameters of up to 7 nm are found (Fig. 4). Comparable results were obtained when using mechanically cut PtIr tips or etched W tips [9].

These structures were imaged with atomic resolution with the same tip as used for the modification process similar to those induced by the mechanical method. The STM images again show a preserved atomic order of the lattice even within these structures. Similar to the structures generated mechanically, these structures can be generated both under UHV conditions and in ambient air [17]. They are time-stable in UHV as well as in air. Further experiments have shown that a mechanical manipulation of the voltage pulse induced structures is possible. Therefore, these structures represent topographical protrusions rather than mere modifications in the local electronic density of states. Thus, voltage pulsing also results in a mechanical deformation of the surface. Again, the fact that atomic resolution was obtained within the modified areas using the same tunneling parameters as within the unmodified areas indicates that the local band structure remains largely preserved after the deformation.

Interestingly, the shape of these structures is always circular (even for the case of mechanically cut PtIr tips) and does not depend on the shape and the size of the tip used for writing. This indicates that deformation by mechanical contact is not the dominating effect for generating the structures, in contrast to the process discussed in section 4.1.

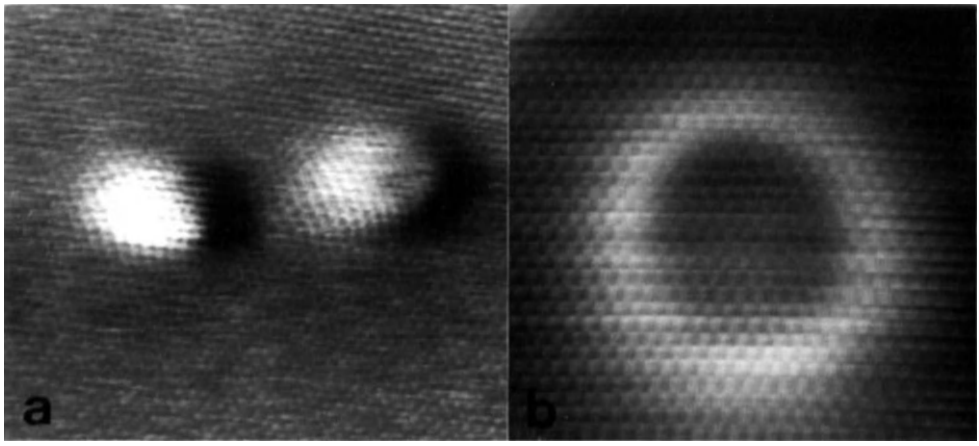

Fig. 4: Surface deformations induced by voltage pulsing (tip positive) on WSe_2. a) STM image of two hillocks generated by voltage pulses of approx. 3.5 V in amplitude (image size: 12 nm x 11 nm, diameter of the hillock: 3 nm). b) Image of a ring-like structure induced by applying a voltage pulse of an amplitude of 5.5 V. Image size: 8 x 7.5 nm, outer diameter of the ring-structure: 6 nm.

4.3. MODIFYING ATOMIC SITES WITH THE STM TIP

A third type of surface modification experiments on WSe_2 also uses voltage pulses of several milliseconds in duration between tip and sample, but does not lead to plastic deformations of the surface as described in sections 4.1 and 4.2, but to the modification of atomic sites of the surface at the locations where the pulses are applied. For this experiment, smaller voltage pulses are used whose amplitude is immediately above the threshold voltage below which no surface modification is observed as a result of the pulsing.

As a result, well-defined and oriented structures are observed which consist of three adjacent atomic sites (Fig. 5). Interestingly, no atoms are missing, and the three atoms of the structure within the accuracy of the measurement remain exactly at their original lateral positions which they occupied before the modification process. Only their apparent height is increased significantly due to the application of the voltage pulse [10].

All structures generated on the same part of a sample surface show the same orientation, an observation that cannot be explained by the sixfold symmetry of the tungsten (W) sublattice or the selenium (Se) sublattice alone. If only one of these two sublattices of 2H-WSe_2 would be involved, both orientations of these three-atom structures should be equivalent. The fact that only one of these orientations is observed shows that both the W and the Se sublattices are involved in the modification process which together result in the threefold symmetry of the WSe_2 lattice, the Se atoms occupying every second

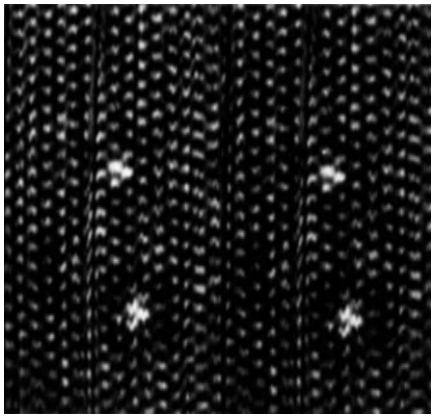

Fig. 5: Pattern of four structures generated with the STM, each structure consisting of three adjacent atoms. The structures were induced by voltage pulses immediately above the threshold voltage for surface modification (in this case approx. 2.3 V). All structures are oriented in the same direction, corresponding to the threefold symmetry of the WSe_2 lattice (see text).

tetrahedral site between the W atoms. These atomic structures have in common with the surface deformations discussed above that they represent time-stable surface modifications which can be induced without disrupting the atomic order of the surface observed with the STM. In contrast to these structures, however, they represent atomic-scale lattice modifications with a well-defined size and orientation rather than plastic deformations.

4.4. DYNAMIC BEHAVIOUR OF A MODIFIED ATOMIC SITE

In an experiment using short voltage pulses we could observe the evolution of atomic-size surface modifications on a time scale of ten seconds. The duration of the pulses of 50 ns was well below the reaction time of the STM feedback loop. Thus, any mechanical tip surface indentation can be excluded. Fig. 6 shows a pattern of four surface atoms of higher apparent height corresponding to an altered vertical position or local electron density. The pattern was created by one pulse with an amplitude of 4V (tip positive). Figs. 6a and 6c were taken 10 seconds and 20 seconds after the pulse had been applied. Figs. 6b and 6d show diagrams of the imaged surface region assigning numbers to the atoms at the highlighted lattice sites.

The surface atom exhibiting an enhanced apparent height in the upper left corner, marked as 1 in Fig. 6b, is part of a defect structure with an enhanced apparent height

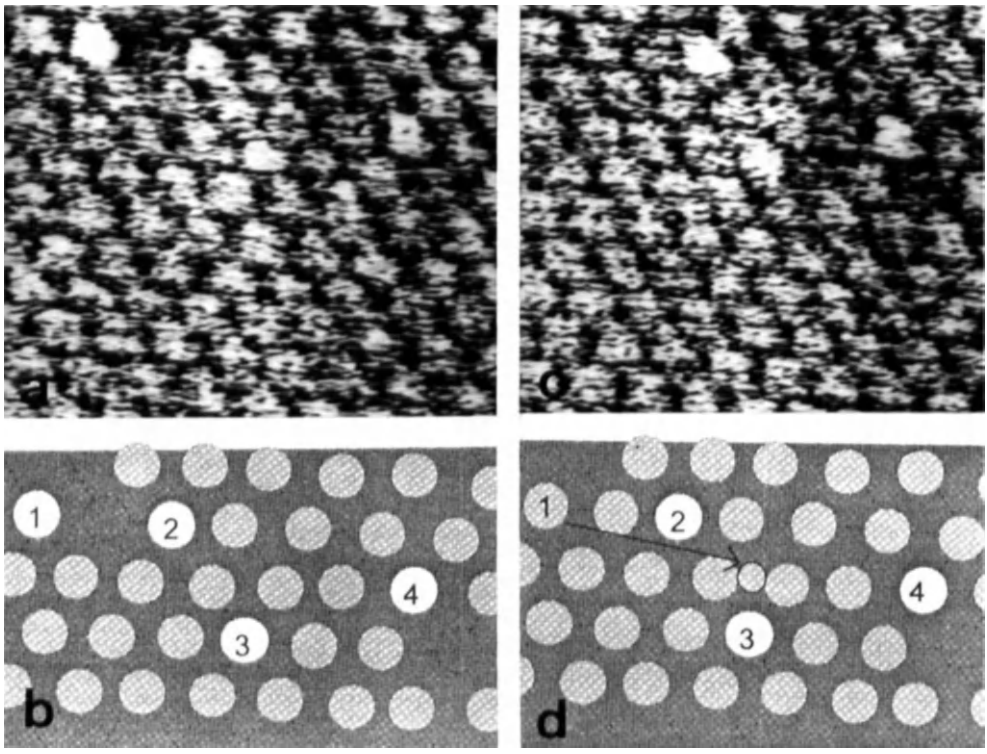

Fig. 6: a) Pattern of atomic sites of increased apparent height. The structure was imaged about ten seconds after generation using a 50 ns pulse with an amplitude of 4V. b) Schematic diagram of Fig. 6a assigning numbers to the highlighted atoms. c) The same surface area imaged 20 seconds after the pulse. Atom 1 is reduced in apparent height, and an occupied localized electron state appears between atom 2 and 3. d) Schematic diagram suggesting diffusion or electron transfer from site 1 to the interstitial lattice site as a possible pathway for the observed evolution of this pattern on tungsten diselenide. Image size in Figs. a) and c): approx. 3 nm x 3 nm.

atom next to a reduced apparent height atom of the type shown in Fig. 2d. In this case, however, the structure was metastable and disappeared about 10 seconds after the measurement. Another structure of this type can be seen at location 4 in the right section of the image. This structure is oriented in diagonal direction from the upper left (bright) to the lower right (suppressed).

The atom at position 2 is a monoatomic defect, which did not loose its increased apparent height during the observation time of several minutes. Note that it remains stable without an adjacent atom of reduced apparent height (see Figs. 6c,d). A close-up

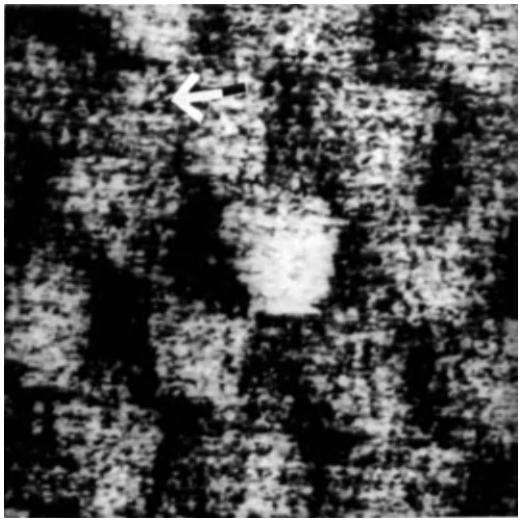

Fig. 7: Magnified view of the atom labelled as number 2 in Fig. 6. In addition, an occupied localized electron state is visible at an interstitial site on the lower right of the atom (arrow). Image size approx. 1.5 nm x 1.5 nm.

image of this atom was taken about one minute after the pulse (Fig. 7). In addition, a localized state appears at an interstitial position shifted by one and a half of a lattice constant (see arrow).

The images of Figs. 6a and 6c show that an occupied localized electron state at the interstitial lattice site is already present in Fig. 6c which was taken 20 seconds after the pulse. The feature is not yet present in Fig. 6a, taken ten seconds after the pulse. Note that the feature appears with the reduction of the increased apparent height at atom 1 and may correspond to diffusion or to a redistribution of charge, stabilizing the enhanced apparent height of atoms 2 and 3.

4.5. GROWTH OF TRIANGULAR STRUCTURES INDUCED BY STM

A different kind of surface modification process can be induced by applying voltage pulses with an amplitude in excess of 4.5 V (tip negative) and a duration of more than 10 ns to a gold tip in air. After the application of the pulse, triangular depressions begin to grow.

Fig. 8 shows a time sequence of STM images taken of the same 120 nm x 120 nm area of a WSe_2 surface. For the images of Fig. 8, a tunneling voltage of 1 V (tip negative) and a tunneling current of 1 nA were used. Fig. 8a shows the intact surface area before the application of the voltage pulse, Fig. 8b the same area approx. 30 s after the pulse

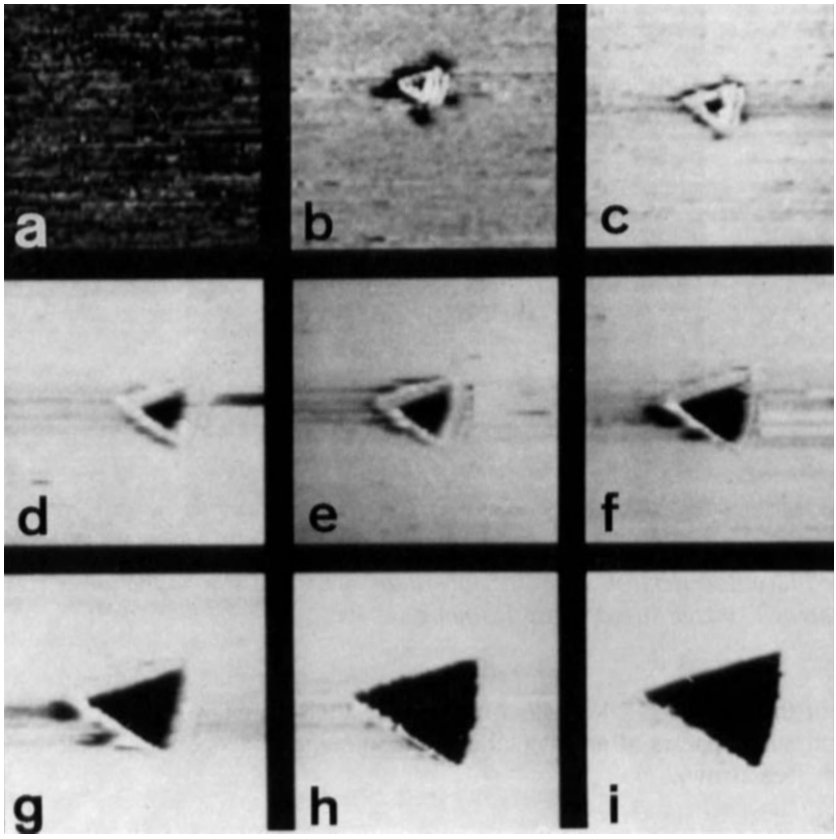

Fig. 8: Evolution of triangular structures on WSe_2 induced by voltage pulsing (tip negative) and subsequent STM enhanced layer decomposition (image size 120 nm x 120 nm). a) STM image of the as-prepared, intact WSe_2 surface. b) Evolution of a triangular structure 30 s after applying a voltage pulse (amplitude > 4.5 V, duration > 10 ns, Au tip). c-i) Growth of this structure during STM imaging. The orientation and shape of the structure reflects the symmetry of the WSe_2 lattice.

was applied. Immediately after pulsing, a small cluster-like structure is observed which within a few seconds develops into a triangular structure. In the image of Fig. 8b this triangle already has a diameter of 5.5 nm, consisting of a central depression surrounded by a protruding rim.

Figs. 8c-e represent images of the same area at intervals of 180 s. Interestingly, the structure continues to grow both laterally and in depth, the lateral growth rate having values of typically 4 nm/min. In Fig. 8i, the edges of the triangle have reached a length

of 75 nm, the depth of the structure being 12 nm. The edges of the triangular rim of the structure are protruding by about 0.5 nm with respect to the plane of the unmodified surface, a value which remains constant within the accuracy of the experiment during the growth of the structure.

The growth of the structure is accelerated significantly by the STM imaging process, although the structures continue to grow even when imaging is stopped for several minutes and the structure is examined by STM afterwards.

The experiment shows that in contrast to the modification processes described in sections 4.1 to 4.3, material decomposition and transport play a significant role in this case. Chemical reactions with surface adsorbates as well as with ambient air could be responsible for this process, an assumption which is supported by experiments performed excluding air. The same sample which showed this phenomenon of the generation and growth of the triangular structures in air did not show this effect when the experiments were repeated under silicon oil and under UHV conditions: in both cases, the triangles generated by voltage pulsing remained much smaller and stopped growing after several minutes.

The fact that triangular structures once generated continue to grow while the spontaneous growth of such triangles is observed only in rare cases, can be explained by the difference in the energies which are necessary to detach an atom from a step edge and from an intact lattice plane.

When several triangular structures are generated on the same region of the surface, they all show the same orientation, a fact which, similar to the orientation of the atomic structures (see section 4.3) is not explained by the sixfold symmetry of the W or the Se sublattice alone, but by the threefold symmetry of the complete WSe_2 lattice.

4.6. STM-INDUCED LAYER DECOMPOSITION OF THE CDW MATERIAL $TaSe_2$

Similar processes of tip-induced layer-by-layer decomposition are also observed on 1T-$TaSe_2$, a layered dichalcogenide which at room temperature exhibits a $\sqrt{13} \times \sqrt{13}$ charge density wave superstructure. When scanning over larger areas, the layered structure of the material becomes evident, the images showing atomically flat terraces separated by steps which are 0.63 nm in height, corresponding to the thickness of individual Se-Ta-Se layers (see Fig. 9a). In high resolution STM images, both the atomic structure and the charge density wave superstructure are observed [18]. An example of such an STM image of the sample surface used for our modification experiments is given in Fig. 9b (image size approx. 10 nm x 10 nm).

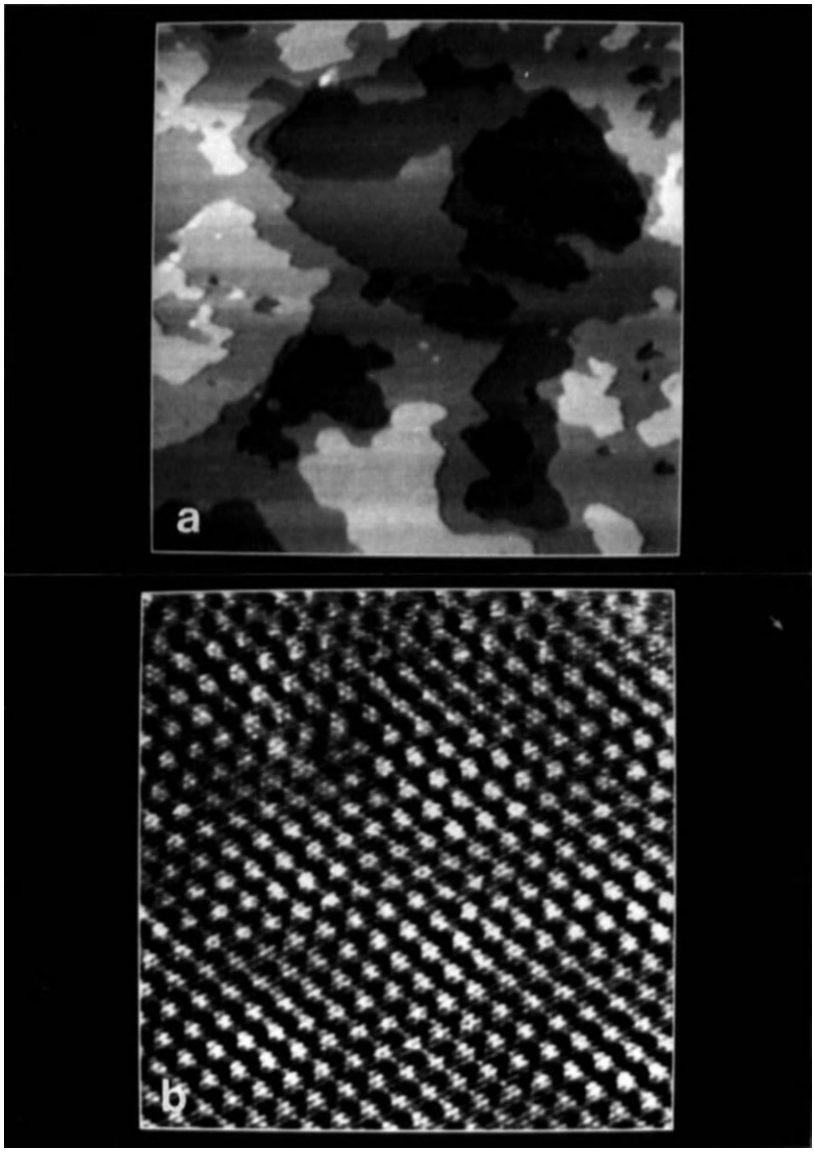

Fig. 9: Constant current STM images of the as-grown 1T-$TaSe_2$ surface used for the modification experiments. While for large scan areas (Fig. 9a, image size approx. 1 μm x 1 μm) atomically flat terraces separated by monolayer steps are observed, high resolution images (Fig. 9b, image size approx. 20 nm x 20 nm) show the atomic structure of the lattice superimposed by the CDW superstructure.

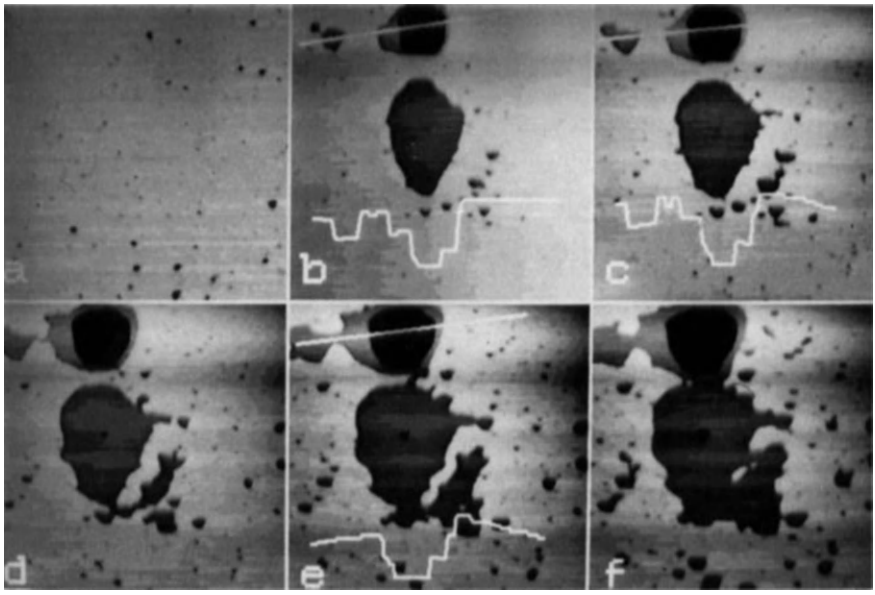

Fig. 10: STM enhanced layer decomposition on 1T-$TaSe_2$. a) STM image (constant current mode) of an as-prepared surface which already exhibits small holes within the topmost layer (black dots). The image size is 600 nm x 600 nm, the diameter of the dots is typically between 5 nm and 15 nm.
b) By applying two voltage pulses (tip positive), two larger holes have been generated on the surface (diameters approx. 100 nm and 150 nm, respectively). c-f) Time sequence of STM images of the same area illustrating the STM enhanced layer decomposition. The white lines within the images represent the cross-section of the upper of the two artificially induced structures. The steps correspond to the thickness of individual Se-Ta-Se sandwich layers (approx. 0.63 nm). In contrast to the structures observed on WSe_2, these structures exhibit an irregular shape.

By applying voltage pulses between STM tip and sample when scanning on one of the flat terraces, holes were induced on the originally flat surface, which were one or several monolayers deep. Similar to the holes induced by pulsing on WSe_2, these structures continue to grow after their generation, the growth rate being significantly increased by the STM scanning process. In contrast to the experiments on WSe_2, however, most of these structures do not show a triangular, but an irregular shape. As in the case of the layer decomposition of WSe_2, the experiments have been carried out in ambient air. Again, chemical reactions with adsorbate layers, with the oxygen of the air or with water could induce the observed layer-by-layer decomposition of the surface. The exact mechanism of the enhancement of the layer decomposition due to the STM imaging process is not yet clear, and further experiments are needed. A plausible explanation is local electrochemistry induced by the tunneling current.

In contrast to the WSe_2 samples, the $TaSe_2$ samples regularly showed natural steps and holes which also continued to grow during imaging. These observations are similar to recent results by Parkinson [19], who reported that nanometer scale etching of transition metal dichalcogenides may be induced with the STM even without applying voltage pulses. This is in good agreement with our observations: when natural surface defects are already present, the decomposition process can continue without voltage pulsing. When no surface defects are available within the scanning area, they can be induced at predefined positions by voltage pulsing. In this way, the etching process will start at the site where the pulse has been applied.

The constant current STM images of Fig. 10 give an example of such an etching process started by voltage pulsing on $TaSe_2$. Fig. 10a is an STM image of the as-prepared $TaSe_2$ surface (image size: 600 nm x 600 nm). The black dots with typical sizes between 5 nm and 15 nm correspond to holes in the topmost Se-Ta-Se layer, which were already present at the beginning of the imaging process. By applying two voltage pulses, each with an amplitude of 4 V and a duration of 0.1 μs, two larger holes (diameters approx. 100 nm and 150 nm, respectively) were generated. Figs. 10c-f demonstrate the growth of these two pulse induced structures and also of the natural holes during the imaging process at a tunneling voltage of 0.9 V and a tunneling current of 0.1 nA.

5. Conclusions

A variety of differing procedures for nanometer-scale and atomic-scale surface modification at predefined locations with the STM was demonstrated on the layered semiconductors 2H-WSe_2 and 1T-$TaSe_2$. All experiments have in common that they do not aim at the manipulation of adsorbed material on a surface but at the (sub)nanometer-scale manipulation of the solid surface itself. We can distinguish between "non-destructive" processes which allow the modification of the surface without decomposing the material locally and "destructive" processes, which involve material decomposition. Three non-destructive processes have been described, i.e. mechanical indentation, surface deformation by voltage pulsing and the manipulation of atomic sites of the solid surface. These processes have in common that the structures are time-stable after modification even when STM imaging of the structures is continued. Destructive processes involve the deliberate generation of surface defects with the STM tip, which act as nucleation centres from which layer decomposition starts and the STM enhanced decompositon starting at natural lattice defects like holes, steps and terraces already present on the surface.

Acknowledgment: We would like to acknowledge Prof. Levy, Lausanne, for the growth of the $TaSe_2$ samples and Prof. Bucher, Konstanz, for stimulating discussions. This work was supported by the Deutsche Forschungsgemeinschaft (SFB 306) and by research programs of the BMFT (grants No. 03M 4008 B0 and No. 0328453-C).

References

[1] *C.R.K. Marrian and E.A. Dobisz, Ultramicroscopy* ***42-44*** *(1992) 1309;*

[2] *D.M. Eigler and E.K. Schweizer, Nature* ***344*** *(1990) 524;*

[3] *S.T. Yau, D. Saltz and M.H. Nayfeh, Appl. Phys. Lett.* ***57*** *(1990) 2913;*

[4] *E.J. van Loenen, D. Dijkkamp, A.J. Hoeven, J.M. Lenssinck and J. Dielemann, Appl. Phys. Lett.* ***55*** *(1989) 1312;*

[5] *R.S. Becker, J.A. Golovchenko and B.S. Swartzentruber, Nature* ***334*** *(1990) 524;*

[6] *U. Staufer, L. Wiesendanger, L. Eng, L. Rosenthaler, H.R. Hidber, H.J. Güntherodt and N. Garcia, J. Vac. Sci. Technol. A* ***6*** *(1988) 537;*

[7] *J.P. Rabe, S. Buchholz and A.M. Ritcev, J. Vac. Sci. Technol. A* ***8*** *(1990) 679;*

[8] *H. Fuchs, R. Laschinski and Th. Schimmel, Europhys. Lett.* ***13*** *(1990) 307;*

[9] *Th. Schimmel, H. Fuchs, S. Akari and K. Dransfeld, Appl. Phys. Lett.* ***58*** *(1991) 1041;*

[10] *H. Fuchs and Th. Schimmel, Adv. Mater.* ***3*** *(1991) 112;*

[11] *S. Akari, R. Möller and K. Dransfeld, Appl. Phys. Lett.* ***59*** *(1991) 243;*

[12] *H. Fuchs and R. Laschinski, Scanning* ***12*** *(1990) 126;*

[13] *M. Ch. Lux-Steiner, "Synthesis, Optoelectronic Properties and Applications of New Semiconductor Crystals", submitted to Springer-Verlag, Heidelberg, 1991;*

[14] *R. Späh, Konstanzer Dissertationen, Vol. 130, Hartung-Gorre Verlag, Konstanz, 1986;*

[15] *S. Akari, Konstanzer Dissertationen, Vol. 346, Hartung-Gorre Verlag, Konstanz, 1992;*

[16] *R. Coehoorn, C. Haas, J. Dijkstra, C.J. Flipse, R.A. de Groot and A. Wold, Phys. Rev. B* ***35*** *(1987) 6195;*

[17] *H. Fuchs, Th. Schimmel, M. Lux-Steiner and E. Bucher, Ultramicroscopy* ***42-44*** *(1992) 1295;*

[18] *B. Giambattista, C.G. Slough, W.W. McNairy and R.V. Coleman, Phys. Rev. B* ***41(14)*** *(1989) 10082;*

[19] *B. Parkinson, J. Am. Chem. Soc.* ***112*** *(1990) 7498;*

MICROMACHINED SILICON TOOLS FOR NANOMETER-SCALE SCIENCE

J. BRUGGER, V.P. JAECKLIN, R.A. BUSER, C. LINDER AND N.F. DE ROOIJ
Institute of Microtechnology, University of Neuchâtel
Breguet 2, 2000 Neuchâtel
Switzerland

ABSTRACT: Silicon microfabrication techniques are well suited for the fabrication of complex integrated microsystems including sensors, actuators and signal processing units. In particular, a high resolution surface scanning microscope such as the atomic force microscope (AFM) is less sensitive to vibrations and thermal drift if it is miniaturized; therefore, these techniques are of special interest for the fabrication of an integrated AFM sensor unit. We present different types of silicon based microstructures for use in surface science instruments, where tip manipulation is required with high accuracy. Micromachined cantilevers and tips in various shapes for force microscopes were reproducibly fabricated in our laboratories by means of processing steps such as dry and wet etching of silicon. They were successfully utilized in commercial AFM's. Furthermore, we present an AFM sensor-head for integrated capacitive read-out consisting of two adjacent silicon cantilevers forming a capacitance of about 0.2 pF. Typical forces in the order of nN induce a bending of the sensing cantilever and change the capacitance in the tens of fF which requires electronics for signal detection. In addition, we developed a polysilicon xy-microstage with submicrometer wide suspension beams driven by electrostatic comb actuators. This device allows with relatively low driving voltage (around 40 V) positioning and scanning of a center stage in the range of 10 μm with a resolution of better than 80 nm. Its main features are quick response time, no hysteresis in the positioning and the feasibility of an integrated capacitive position monitoring.

1. Introduction

Surface profile mapping and manipulation of materials on the nanometer-scale such as scanning tunneling microscopy (STM), atomic force microscopy (AFM), nano-indentation or atomic storage devices require extremely small and accurate handling tools for the tip positioning and manipulation. Microfabricated AFM probes based on silicon technology first utilized thin films of silicon dioxide or nitride as cantilever and tip [1]. Nowadays also single crystalline silicon cantilevers with tips are routinely fabricated by micromachining techniques [2,3]. One advantage of these techniques is that the geometrical dimensions and thus the mechanical properties of the cantilevers can be tailored and reproduced by the photomasks defining the etch areas. For some applications (e.g. surface quality control of integrated circuits) it could be interesting to have a multiprobe array, as described in detail in the next section.

In AFM systems the positioning and scanning unit (piezo), the sensing element (cantilever) and the readout parts (e.g. laser diode and photodetector) have to be assembled. In view of a completely functional AFM sensor head this paper also presents novel silicon structures such as an integrated capacitive cantilever read-out as well as an xy-microstage suitable for minute tip positioning and scanning. The combination of these elements may be used to design a complex AFM microsystem with integrated sensing, measuring, actuating and signal processing units.

V.T. Binh et al. (eds.),
Nanosources and Manipulation of Atoms Under High Fields and Temperatures: Applications, 311–317.
© 1993 *Kluwer Academic Publishers.*

2. Silicon microprobes

The microfabrication of silicon cantilevers with integrated tips needs three photolithography and several dry and wet etching steps as described elsewhere [3,4]. The cantilevers are characterized by the spring constant, the torsional rigidity (for measurements in the friction mode) and the first resonance frequency (for dynamic mode measurements). Cantilevers as shown in Fig. 1 with lengths from 500 to 1000 μm having spring constants from 0.1 to 100 N/m and resonance frequencies ranging from 10 to 150 kHz have been reproducibly fabricated. The cantilever length and width are fully defined by the mask layout, whereas its thickness and the tip height depend on the etch process.

The performance of surface scanning instruments is amongst others dependent on the scan rate, i.e. the scan area versus the scan time. For this reason it is advantageous to have a multiple scan unit with identical parallel scan probes in order to investigate a larger area or the same area several times to enhance image resolution. A prospective application may be the quality control of miniaturized repetitive structures like integrated circuits by designing a scan unit having the same spatial frequency than the structure under investigation. We fabricated such arrays of 10 parallel silicon cantilevers and tips as depicted in Fig. 2. The number and specific requirements for the probe arrangement can be fulfilled by the mask layout.

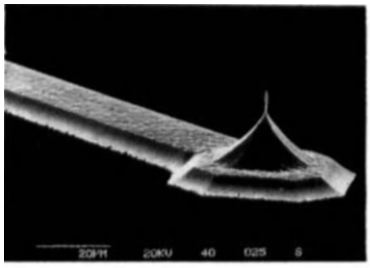

Fig. 1. SEM graph of an microfabricated silicon cantilever with a high protruding tip

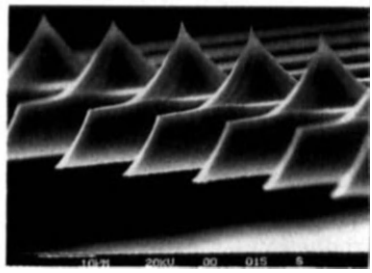

Fig. 2. Micromachined silicon cantilever array for parallel surface probing

The tip design for the various demands in the wide field of applications in AFM or related techniques (i.e. nanometer scale imaging, atomic resolution, friction measurements, indentation) is crucial and we paid special attention to its fabrication. The tip's shape at the micrometer scale (perceptible in a SEM), namely height and sidewall slopes can be controlled to a large degree by adjusting the etch parameters. AFM imaging using such tips in a commercial system were successfully undertaken. Results are shown in Fig. 3, where a three atoms step in graphite is represented. The data were taken by M. Binggeli from the Swiss Center for Electronics and Microtechnology Inc. (CSEM) Neuchâtel.

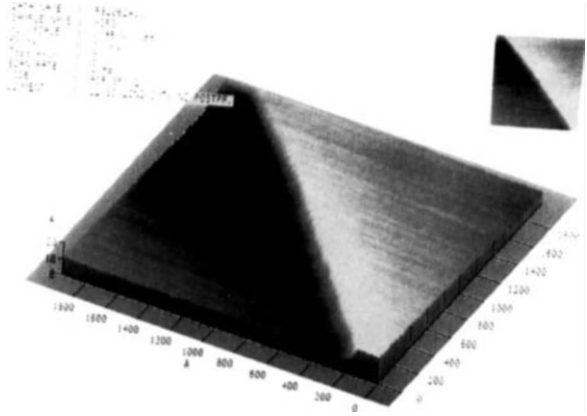

Fig. 3. AFM imaging with a silicon tip; 3 atoms step on graphite. Data raw and unfiltered.

3. AFM micro-probe with integrated capacitive read-out

In AFM the force induced cantilever bending is commonly measured with an assembled setup such as a hovering tunneling tip [5], optical beam deflection [6,7], interferometry [8,9] or a capacitor [10,11]. All these approaches require an accurate alignment of the readout part to the lever. In order to minimize external perturbations like vibrations and thermal drift, it would be advantageous to have a miniaturized integrated readout mechanism; e.g. a piezoresistive cantilever [12] and an electrostatically driven poly-silicon scan-tip obtained by sacrificial layer techniques with optical readout [13] have been presented.

We investigated the feasibility of highly sensitive integrated capacitive AFM probes using micromachining techniques and combining the advantages of silicon as material with the possible integration of the sensing and readout elements. Sensors that use single-crystalline silicon as highly elastic material and capacitance change as readout principle are known to be very reliable and accurate [14]. Additionally, thermal silicon dioxide provides good electrical insulation and allows, in combination with highly doped silicon, to form capacitors with small parasitic effect.

In our case the capacitance structure consists of two adjacent single-crystalline silicon beams, one carrying a sharp tip being the measurement cantilever and the other being the counter-electrode (Fig. 4). Both electrodes are connected to a holder piece, separated by a dielectric layer of dioxide of about 1.5 μm thickness. The process of the integrated capacitive AFM microprobe is based upon the microfabrication steps of simple passive cantilevers extended by additional processing steps such as silicon fusion bonding and additional RIE [15]. The key steps in the processing are the bonding on selective areas and the etching of the bond silicon dioxide as sacrificial layer between the two cantilever electrodes.

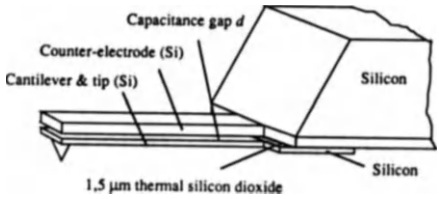

Fig. 4. Schematic representation of the capacitive AFM microprobe

The counter electrode is considerably thicker (> 15 µm) than the sensing cantilever (around 5 µm) in order to make it less influenced by forces due to changes in the electrical field during the measurement.

For the design of a practical system a compromise must be made between the opposing demands of a high sensitivity readout (→ thin cantilever and small gap) and the prevention of snapping, i.e. when cantilever and counter-electrode come into contact due to electrostatic attraction (→ thick cantilever and large gap) [11]. The total capacitance of the probe is the sum of the sensing capacitance C_s (between the electrodes) and the parallel capacitance C_p (of the holder plate). The capacitances can be approximated by $C=\varepsilon A/d$. For A_s=700 x 30 µm^2 and d=1.5 µm being the area and gap of the sensing probes and ε_o=8.85E-12 F/m, the C_s is in the order of 0.2 pF and C_p of 1 pF, with a plate area of about 200 x 200 µm^2 and $\varepsilon = \varepsilon_o\varepsilon_r$ (ε_r=3.9 for thermal SiO_2).The sensitivity of a typical structure can be estimated as dC/dz=3 fF/Å which lies in the detection range of electronic circuits.

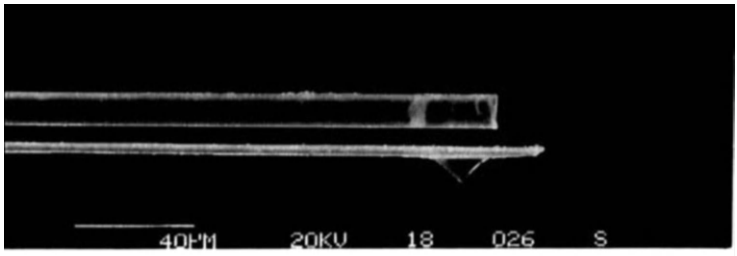

Fig. 5. SEM graph of a micromachined capacitive AFM sensor

4. XY-Microstage

The scanning drive of an AFM unit is less sensitive to vibrations and thermal drift if it is miniaturized [5]. In particular, a micromachined piezoelectrically driven scanner followed this concept [16]. Recently, sacrificial layer technology has gathered much interest as a new method of constructing micromechanical elements using fabrication techniques of the IC-industry [17,18,19]. Some devices based on this technology are driven electrostatically; especially, the comb actuator proved to be a useful driving unit [20,21,22,23]. Its main features are quick response time, IC-compatible driving voltages, no hysteresis in the positioning and the feasibility of an integrated

capacitive positioning detection. These features make the comb actuator an interesting candidate for the positioning of an AFM tip [20, 24].

In the following, micropositioners are discussed which use polysilicon (in the future also silicon) as the structural layer and silicon dioxide as the sacrificial layer. An over view of a typical xy-microstage that we fabricated in collaboration with the Swiss Center for Electronics and Microtechnology Inc. (CSEM) in Neuchâtel, Switzerland, is shown in Fig. 6. The microstage consists of four of such comb actuators assembled around a center stage. The comb actuator itself consists of two electrodes, the fixed electrode and the movable electrode. The functional components of the latter are the suspension, which gives a mechanical guidance for the actuator movement, and the comb, where the force for the actuation is created. The design of the microstage is based on a pull mechanism - the table is moved to any position in the xy-plane by activating two of the four comb drives. The decoupling of the x- and y-position is given by the construction of the suspension. Fig. 7 shows details of the free standing stage; the square table (8 μm by 8 μm) is suspended by four 270 μm long, 0.6 μm wide, and 2 μm high beams.

With this prototype it was possible to displace the table in any direction in the xy-plane. Mechanically, a maximum surface of 30 μm by 30 μm could be covered. For the electrostatic actuation the displacement is a square function of the applied voltage [23]. For example if 20 V is applied on one electrode of the stage shown in Fig. 6, a displacement of 1.3 μm has been measured, while the displacement for 40 V is 5.3 μm. No hysteresis in the positioning has been observed.

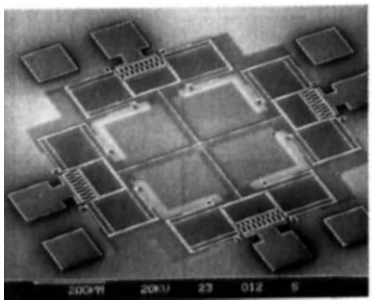

Fig. 6. SEM graph of a complete micro-machined polysilicon xy-microstage comb-drive

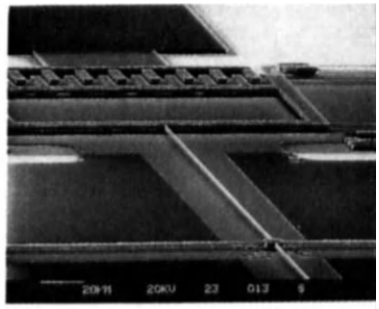

Fig. 7. SEM graph showing the close-up of the free standing xy-microstage with a comb actuator in the background.

FEM simulations of these structures showed that precise positioning can be performed because there is a good common mode rejection ratio of the displacements in x- and in y-direction. For the structure shown in Fig. 6, the simulated ratio is more than 35 dB; hence, this device can be used for two-dimensional positioning in an area of 10 x 10 μm^2 with a precision of better than 80 nanometers.

The resonance behavior of the table has been investigated as well. In x-direction, a resonance frequency of 4.3 kHz has been observed while the amplitude was around 4 μm for a 30 V peak to peak sinusoidal signal. The resonance frequency in z-direction has not been measured yet; however it is believed to be also well above the frequencies of vibrational noise.

The fabrication of these xy-manipulators, in particular, if constructed in single-crystalline silicon, is compatible with the fabrication of the tips; hence, a fully integrated AFM unit may be designed.

5. Conclusion

We have presented several types of micromachined silicon structures suitable for atomic force microscopy or related applications in surface science, where the positioning, scanning and displacement of a sharp tip is required with high accuracy. Silicon cantilevers and tips were successfully utilized in AFM systems. More complex devices like an integrated capacitive read-out AFM sensor and a poly-silicon xy-microstage as scanning unit were successfully fabricated. Future work will focus on the integration of the individual device to microfabricate a completely functional surface scanning system.

6. Acknowledgements

We acknowledge J.-M. Moret from CSEM for valuable contributions, M. Binggeli and R. Christoph for AFM imaging. We are grateful to S. Jeanneret and P.A. Clerc from the IMT and the laboratory staff of the CSEM for technical assistance. This work was supported by the Swiss National Science Foundation and the Swiss Foundation for Microtechnology Research.

---

[1] T.R. Albrecht, S. Akamine, T.E. Carver and C.F. Quate,"Microfabrication of cantilever styli for the atomic force microscope," J.Vac. Sci. Technol. A 8 (4), Jul/ Aug. 1990 p. 3386.

[2] O. Wolter, Th. Bayer and J. Greschner, "Micromachined silicon sensors for scanning force microscopy", J.Vac.Sci.Technol.B9 (2), Mar/Apr 1991

[3] J. Brugger, R.A. Buser, N.F. de Rooij, "Silicon cantilevers and tips for scanning force microscopy", Sensors&Actuators A, 34, No.3 (1992), pp. 193-200

[4] C. Linder, T. Tschan and N. F. de Rooij, "Deep dry etching of silicon - A novel micromachining tool", Sensors and Materials, 3, 6 (1992) pp. 311-324.

[5] G. Binnig, C.F. Quate, and Ch. Gerber, "Atomic Force Microscope", Phys. Rev. Lett., Vol. 56 (9), 1986, pp. 930-933.

[6] G. Meyer and N.M. Amer, "Novel optical approach to atomic force microscopy," Appl. Phys. Lett. 53, 2400 (1988a) and "Erratum: Novel . . .", Appl. Phys. Lett. 53, 1045 (1988b)

[7] D. Rugar, H.J. Mamin, R. Erlandsson, J.E. Stern and B.T. Terris, "Force microscope using fiber-optic displacement sensor", Surf. Sci. 59, 2337, (1988)

[8] G.M. McClelland, R. Erlandson and S. Chiang, "Atomic force microscopy: General principles and a new implementation," Review of progrss in quantitative nondestructive evaluation, Edited by D.O. Thompson and D.E. Chimenti, Plenum, New York, 6B, 307 (1987)

[9] Y. Martin, C.C. Williams and H.K. Wickramasinghe, "Atomic imaging by 'force microscopy' with 1000 Å resolution," Appl. Phys. Lett. 50, 1455 (1987)

[10] T. Goeddenhenrich, H. Lemke, U. hartmann, C. Heiden, "Force microscope with capacitive displacement detection", J.Vac.Sci.Techn. A8 (1), Jan/feb 1990, pp. 383-387.

[11] G. Neubauer, S. Cohen, G. McClelland, D. Horne and M. Mate, "Force microscopy with a bidirectional capacitance sensor," Rev. Sci. Instrum. 61 (9), September 1990. p.2296.

[12] M. Tortonese, H. Yamada, R.C. Barrett and C.F. Quate, "Atomic force microscopy using a piezoresistive cantilever", presented at Transducers '91, June 24-28, 1991, San Francisco

[13] L.C. Kong, B.G. Orr, K.D. Wise, "A Micromachined Silicon scan tip for an Atomic Force Microscope, " Technical digest of the IEEE Solid state sensor and actuator Workshop, Hilton Head Island, South Carolina June 4-7 1990 p.28.

[14] W. Chr. Herens, "Application of capacitance techniques in sensor design", J.Phys.E: Sci.Instrum. 19 (1986), pp. 897-906

[15] J. Brugger, R.A. Buser, N.F. de Rooij, "Micromachined atomic force micropropbe with integrated capacitive read-out", Proc. MME '92, June 1-2, 1992, Leuven, Belgium, pp. 207-210

[16] S. Akamine, T. R. Albrecht, M. J. Zdeblick, and C. F. Quate, "A planar process for microfabrication of a scanning tunneling microscope", Sensors and Actuators, A21-A23, 1990, pp. 964-970.

[17] D. W. Burns and H. Guckel, "Thin films for micromechanical sensors", J. Vac. Sci. Technol., A8 (4), 1990, pp. 3606-3613.

[18] R.T. Howe, "Surface micromachining for microsensors and microactuators", J.Vac.Sci,Technol. B. vol.6, no.6,pp. 1809-1813

[19] C. Linder, L. Paratte, M.-A. Grétillat, V.P. Jaecklin, N.F. de Rooij, "Surface micromachining", Proc. MME '92 Leuven, Belgium, pp. 43-55

[20] C. J. Kim, A. P. Pisano, R. S. Muller, and M. G. Lim, "Polysilicon microgripper", Tech. Dig. IEEE Solid-State Sensor and Actuator Workshop, Hilton Head Island, SC, June 4-7, 1990, pp. 48-51.

[21] T. Hirano, T. Furuhata, K. J. Gabriel and H. Fujita, "Design, fabrication and operation of submicrometer gap comb-drive microactuators", J. MEMS, Vol. 1 , March 1992, pp. 52-59.

[22] V. P. Jaecklin, C. Linder, N. F. de Rooij, J.-M. Moret, R. Bischof, and F. Rudolf, "Novel polysilicon comb-actuators for xy-stages", in Tech. Dig. IEEE Micro Electro Mech. Syst. Workshop, Travemünde, Germany, February 5-7, 1992, pp. 147-149.

[23] V. P. Jaecklin, C. Linder, N. F. de Rooij, and J. M. Moret, "Micromechanical comb actuators with low driving voltage" in Dig. Tech. Papers, Actuator 92, Bremen, Germany, June 24-26, 1992, pp. 40-43.

[24] J. J. Yao, S. C. Arney, and N. C. MacDonald, "Fabrication of high frequency two-dimensional nanoactuators for scanned probe devices", J MEMS, vol. 1, 1992, pp. 14-22.

LIST OF THE PARTICIPANTS

Dr. Robert Baptist
CEA-CENG
LETI-DOPT-SCMM
85X-38041 Grenoble
France

Professor Ernest Bauer
Technische Universität Clausthal
Physikalisches Institut
Leibnizstrabe 4
D-W-3392 Clausthal-Zellerfeld
Germany

Dr. Martin Binggeli
CSCM Centre M
rue Bregnet 2
2007 Neuchâtel
Switzerland

Dr. Pascal Bradu
DRET
Sce des recherches Gpe 3
00460 ARMEES
France

Dr. Jurgen Brugger
Institute of Microtechnology
University of Neuchatel
2 rue A.L. Breguet
CH-2000 Neuchatel
Switzerland

Dr. Jean Pierre Bucher
Institut de Physique Expérimentale
EPFL
PHB-Ecublens
CH-1015 Lausanne
Switzerland

Professor Hans De Raedt
University of Groningen
Institute for Theoretical Physics
P.O. Box 800
9700 AV Groningen
The Netherlands

Professor Klaus Dransfeld
Universität Konstanz
Fakultät für Physik
Universitätsstrasse Postfach 5560
D - 7750 Konstanz 1
Germany

Dr. Urs Dürig
IBM Research Division
Zurich Research Laboratory
Saumerstrasse 4
CH - 8803 Rüschlikon
Switzerland

Dr. Furio Ercolessi
SISSA
Via Beirut 4
I-34014 Trieste
Italy

Dr. Richard G. Forbes
University of Surrey
Dept of Electronic & Electrical Eng.
Surrey GU25XH Guilford
U.K

Dr. H. Fuchs
BASF AG
ZKLIT-J 543
D-6700 Ludwigshafen
Germany

Professor Nicolas Garcia
Universidad Autonoma de Madrid
Depart. de Materia Condensada C-III
Ciudad Universitaria de Canto Blanco
28049 Madrid
Spain

Professor François Gautier
Université Blaise Pascal
IPCMS
4, rue Blaise Pascal
F - 67070 Strasbourg
France

Dr. Titaina Gibert
GREMI
Université d'Orléans
45067 Orléans Cédex 2
France

Dr. J.K. Gimzewski
IBM Research Division
Zurich Research Laboratory
Säumerstrasse 4
CH-8803 Rüschlikon
Switzerland

Dr. Julio Gomez
Universidad Autonoma de Madrid
Depart. de Materia Condensada C-III
Ciudad Universitaria de Canto Blanco
28049 Madrid
Spain

Dr. Peter Güthner
Universität Konstanz
Fakultät für Physik
Universitätsstrasse Postfach 5560
D - 7750 Konstanz 1
Germany

Dr. Harry Heinzelmann
Institut fuer Physik
Universitaet Basel
Klingelbergstr. 82
4056 Basel
Switzerland

Dr. Christian Joachim
Molecular Electronic Group
CEMES-LOE CNRS
29, rue J. Marvig B.P. 4347
31055 Toulouse Cedex
France

Dr. N. D. Lang
IBM Research Division
Thomas J. Watson Research Center
P.O. Box 218
NY - 10598 Yorktown Heights
USA

Dr. John Mamin
IBM Research Division
Almaden Research Center
650 Harry Rd
CA - 95120 San Jose
USA

Dr. O. Marti
Universität Konstanz
Fakultät für Physik
Universitätsstrasse Postfach 5560
D - 7750 Konstanz 1
Germany

Dr. K. Michielsen
Intitut for Theoretical Physics
University of Groningen
Nijenborg 4
9747 AG Groningen
The netherlands

Dr. Nicholas Miskovsky
Penn State University
104 Davey Laboratory
16 802 University Park
USA

Professor Johannes Mitterauer
Technische Universität Wien
Inst. Elektrotechnik & Elektronik
Gusshausstrasse 27-29
A - 1040 Vienna
Austria

Dr. R. Möller
Universität Konstanz
Fakultät für Physik
Universitätsstrasse Postfach 5560
D - 7750 Konstanz 1
Germany

Dr. Hitoshi Nejoh
Aono Atom Projects
JRAC
5-9-9 Tohkohdai Tsukuba
300-26 Ibaraki
Japan

Dr. Ralph M. Nyffenegger
University of Berne
Institute. Inorg. & Phys. Chem.
Freiestrasse 3
CH-3012 Bern
Switzerland

Professor Louis Porte
Ecole Centrale
Lab de Phys-Ch Interfaces
B.P. 163
69131 Ecully Cedex
France

Dr. P.D. Prewett
Central Micro-structure Facility
Rutherford Appleton Laboratory
Building R18, Room G45
OX11 0QX Chilton,Didcot
UK

Dr. Steve Purcell
Dépt de Physique des Matériaux
Université Claude Bernard Lyon 1
69622 Villeurbanne
France

Dr. Christoph Rainer
CSCM Centre M
rue Bregnet 2
2007 Neuchâtel
Switzerland

Professor Ron Reifenberger
Purdue University
Department of Physics
1396 PHYS Building
IN 47907-1396 West Lafayette
USA

Dr. Heinrich Rohrer
IBM Research Division
Zurich Research Laboratory
Saumerstrasse 4
CH - 8803 Rüschlikon
Switzerland

Dr. Juan José Saenz
Universidad Autonoma de Madrid
Depart. de Materia Condensada C-III
Ciudad Universitaria de Canto Blanco
28049 Madrid
Spain

Dr. E.K. Schweizer
Abtl. Oberflächenphysik
Fritz-Haber Institut
Faradayweg 4-6
D-1000 Berlin 33
Germany

Dr. Pedro A. Serena
Universidad Autonoma de Madrid
Depart. de Materia Condensada C-III
Ciudad Universitaria de Canto Blanco
28049 Madrid
Spain

Professor J. Serughetti
Dépt de Physique des Matériaux
Université Claude Bernard Lyon 1
69622 Villeurbanne
France

Dr G.D.W. Smith
Dept Materials
Oxford University
Parks Roads
0XI 3PH Oxford
England

Professor John Spence
Arizona State University
Department of Physics
85287-1504 Tempe,Arizona
USA

Dr. Urs Staufer
Universitat Basel
Institut für Physik
Klingelbergstr. 82
CH-4056 Basel
Switzerland

Professor D.J. Thomson
Dept of Electrical Eng
Univ.of Manitoba
R3TZNZ Winnipeg
Canada

Professor Robert Uzan
Dépt de Physique des Matériaux
Université Claude Bernard Lyon 1
69622 Villeurbanne
France

Professor Vittoria Volterra
Ben Gurion Universityof the Negev
84 105 Beer-Sheva P.O. Box 653
Israel

Professor Binh Vu Thien
Dépt de Physique des Matériaux
Université Claude Bernard Lyon 1
69622 Villeurbanne
France

Dr. Z.Z. Wang
LAM/CNRS
196 Avenue H. Ravera
92220 Bagneux
France

Professor Paul S Weiss
The Pennsylvania State University
University Park
152 Davey Lab
PA16802 Park
USA

Dr. Lloyd J. Whitman
Department of the Navy
Naval Research Laboratory
Code 6177
DC 20375-5000 Washington
USA

INDEX

aberration, chromatic 22, 125
aberration, geometrical 125
aberration, spherical 126
aberrations 20
aberrations coefficients 21
adhesion, atomic scale 271
adhesion-promoted melting 281
adsorbed atom 177, 213
AFM 61, 195, 287, 314
AMIE 20, 63
atom switch 229, 239
atom transfer 229
atom tunneling 230
atomic and ionic potentials 208
atomic markers 220
Au 77, 191, 207, 220, 267

ball-tips 60
benzene 115, 215
brightness 20, 104
build-up tips 106

charge exchange model 207
charge transfer 232
clusters, metallic 77
clusters, moving 215
Co islands 16
coherence 22
coherent electrons 16
computer simulations 45, 185
conductance states 236
constriction 51
convergent beam electron diffraction pattern 25
$CoSi_2$ 14
Coulomb blockade 115
Coulomb staircase 115
Cs 111, 140
Cu 60, 223, 249

deformation by voltage pulsing 297
dissipation mechanisms 255

electron focusing 45
electron optics 103
electronic markers 222
electrostatic force 17
embedded atom method 207
energy dissipation 89
environment dependant potential 207

FEES 66, 79
FEM 59, 64, 77, 89, 111
femtosecond field emission camera 111
field confinement 65
field electron emission 46
field emission 19, 77, 111, 122
field emission guns 20
field emitter arrays 140, 148, 165
field evaporation 207
field penetration 69
field-surface-melting 62
FIM 59, 64, 207
flat displays 165
flat displays, addressing mode 168
flip-flop 71
focused ion beam (FIB) 121, 139
forces, atomic scale 253
Fourier images 19, 28
friction 253, 255
functionalized local probe 8

Ga 123, 283

Hellmann-Feynman theorem 182
hologram, in-line 35
holographic diffraction pattern 38
holography electron 26
holography, Fraunhofer 27
HREM 23

In clusters 266
inelastic tunneling 223
integrated capacitive cantilever 313
integrated circuits repair 133
interaction forces 253
interaction, tip-sample 274
interactions at surfaces 271
interactions, metal-metal 272
ion deposition 130
Ir 271

kendograms 36
kendograms, reconstruction 40
kendroscope, kendroscopy 36

Langmuir-Blodgett films 287
lateral forces 254
layer decomposition 305
layered semiconductors 293
LEEM 13
lensless low energy electron microscopy 35
liquid crystal 115
liquid metal sources (LMIS) 121, 141
liquid metal sources, miniaturized (MILMIS) 139, 153

local probe methods 1, 5
local probes 223
local probes, chemical identity 227
local probes, electromagnetic field 223
low energy beams 102

mechanical indentation 297
MECS 78
mica 265
micro-lenses 101
microcolumn 103
microelectronics technology 156
microfabrication 121
micromachining 128
microtechnology 1
microtips 165
microvolcano 151
miniaturization 1
miniaturized electron microscope 101
molecular dynamics simulations 185
motion of individual surface atoms 111
moving atoms and molecules 213
multiple scattering 39

Na atoms 177
nano-cantilever tips 61
nano-protrusions 63
nanochemics 4
nanometer world 3
nanoprotrusion tips 65
nanoscience 1
nanosources 59
nanostructures 219
nanotechnology 1
nanotips 16, 19, 59
Nottingham effect 70, 90

Peltier heating or cooling 95
phonon excitation 89
photomask repair 132
point sources 36, 101
post-miniaturization 8
protrusion tips 106
pulse power technology 159

quantum switch 229

resonance frequency 61
resonant tunneling 68, 78

scanning thermal profiler 91
scattering theory 36
scattering, elastic 32
scattering, inelastic 32
selective scaling 104
SFFM 253
shadow imaging 23
Si 14, 207, 311
silicon cantilever ,array, 312
silicon tools 311
single-electron manipulation 115
slit emitters 143
space technology 158
spin-polarised electrons 15
spring constant 61
stability, structural 82
step edge 249
STM 89, 115, 177, 195, 213, 219, 229, 239
STM image calculations 239
surface diffusion 60, 220
surface melting 185, 189
surface modification 293
switch structure 240

$TaSe_2$ 293
Taylor cone 123, 142
TED 66, 91
TED peaks 67, 80
TED, clusters 80
TED, size dependant 80
teton tips 64
thin organic films 287
Ti 222
time dependant Schrödinger equation (TDSE) 46
tip apex 245
tip-surface interactions 195
TLEED 19, 26
transfer, field induced 177
triangular structures 303
tunneling barrier 45, 51

ultra-fine beams 101

vacuum microelectronics 140
van der Waals forces 61, 271
virtual sources 21

W 16, 62, 64, 82, 111, 133
WSe_2 293

x-y microstage 314
Xe 215, 229, 239